The development and maintenance of synaptic specificity in the fly visual system

Inaugural-Dissertation

to obtain the academic degree

Doctor rerum naturalium (Dr. rer. nat.)

Submitted to the Department of Biology, Chemistry, Pharmacy

of Freie Universität Berlin

by

Ferdi Ridvan Kiral

born in Bandirma, Turkey

2020

I hereby declare that all experiments and writing contained within this thesis were conducted by myself, all references used are cited accordingly and any personal assistance has been acknowledged by name.

All experiments for this dissertation were conducted from October 2015 to June 2020 at the Division of Neurobiology of Institute of Biology of Freie Universität Berlin under the supervision of Prof. Dr. P. Robin Hiesinger.

1st reviewer: Prof. Dr. P. Robin Hiesinger

Division of Neurobiology, Freie Universität Berlin

2nd reviewer: Prof. Dr. Mathias F. Wernet

Division of Neurobiology, Freie Universität Berlin

Date of defence: 02/10/2020

Table of Contents

1. General Introduction 1
1.1. The brain wiring problem 2
1.1.1. The chemoaffinity hypothesis and molecular tags.......... 2
1.1.2. Algorithmic brain growth: Finding neural partners in space and time.......... 5
1.2. The synaptic maintenance problem 8
1.3. Local protein degradation mechanisms in brain wiring and maintenance 9
1.3.1. Ubiquitous endolysosomal degradation 9
1.3.2. Neuron-specific endolysosomal degradation: Neuronal ‘sort-and-degrade’ 11
1.3.3. Autophagy 12
1.4. The effect of external factors in brain wiring 14
1.5. The *Drosophila* visual system: A model to study brain wiring and maintenance 15
2. Aim 20
3. Manuscript 1: Live observation of two parallel membrane degradation pathways at axon terminals.......... 21
Contribution 21
Manuscript 22
Supplementary information 39
4. Manuscript 2: Autophagy-dependent filopodial kinetics restrict synaptic partner choice during *Drosophila* brain wiring 51
Contribution 51
Manuscript 52
Supplementary information 66
5. Manuscript 3: Temperature-dependent synaptic specificity in the *Drosophila* visual system 83
Contribution 83
Manuscript 84
Supplementary information 104
6. General discussion 108

Local degradation of synaptic vesicle and plasma membrane proteins in distinct endolysosomal compartments 108
Filopodia dynamics restrict synapse formation and synaptic partner choice 111
Brain wiring with combinatorial role of several ‘permissive’ factors 113
7. Outlook and future directions 115
8. Summary 117
9. Zusammenfassung 119
10. References 122
11. Appendix 129
11.1. List of publications from the doctoral work 129
11.2. Curriculum Vitae 130

1. General Introduction

Everything we know, all experience we piled up through human history is the result of our curious nature to learn and know more. Curiosity, the unrestrainable desire to know, is not a characteristic of inanimate matter. Instead, it emerged through millions of years of evolutionary processes to restructure unconscious matter as a substance that produces consciousness, constructs our perception of the external worlds, brings our actions under control and gives rise to inner experience of joy, sorrow, anger and curiosity to know more. Needless to say, it is the brain, an astonishingly complex, biological computational device that can perform remarkably expeditious and accurate deeds owing to harmonious activity of cells –its neurons- that communicate to each other through precise, yet plastic connections.

For earlier generations, the pursuit to unravel the complexity of the brain, or to be precise, to understand the nature of the human mind was in the realm of philosophy. The then philosophers and thinkers placed our mind separately from our body, a result of 'Divine Grace', which was embodied in famous proposition by René Descartes 'I think, therefore I am'. One of the greatest steps forward in the modern era, especially with Charles Darwin's works on the evolution of body structures from animal ancestors, was the realization that Descartes had it backwards that in actuality the proposition should have been 'I am, therefore I think'. As Darwin elaborated in his book, *The Expression of the Emotions in Man and Animals* (Darwin, 1872), our mental processes, much in the same way as other morphological features of the body, evolved from animal ancestors that is evident with conserved structures of the brain through animal kingdom. However, the realization that our mind is not supernal but can be explained in physical terms created even more compelling and challenging questions on the development and maintenance of such a remarkable organ: Where does the information to build a brain come from? How is such information turned into synapse-specific connections between neurons? and as most of the neurons live throughout the entire lifespan of the organism, how do neurons keep themselves and particularly their synapses functional and healthy over a long time?

1.1. The brain wiring problem

The vast number of neurons a brain contains, their spatial segregation into different brain regions and the mature morphology of neurons, i.e., axon terminals and dendrites being positioned spatially distinct from their cell bodies, are suggestive of a robust developmental program for proper assembly of neural circuits. The last century has seen a substantial advance in our understanding of brain development, which can be categorized into sequential developmental steps. First, neurons are born and specified at distinct brain regions by temporally regulated expression of a set of transcription factors (Holguera and Desplan, 2018; Shirasaki and Pfaff, 2002). Next, neurons send out their axons and dendrites that need to be guided to proper, final location where they meet their neuronal partners to form synaptic connections (Chedotal, 2019; Stoeckli, 2018). Finally, once they reach the target area, they need to selectively form synaptic connections with appropriate partners out of plethora of possible synaptic partners physically present in the same area. Then the obvious question arises here how does a developmental program ensure generation of several converging and diverging neural circuits with synaptic precision?

1.1.1. The chemoaffinity hypothesis and molecular tags

Synapse specificity has been classically thought to be regulated by homophilic or heterophilic interactions between adhesion molecules at the synaptic cleft of two connecting neurons and by morphogen gradients of secreted molecules that can promote or inhibit synaptogenesis (Margeta and Shen, 2010). Classic studies by Roger Sperry during 1940s demonstrated that ablated retinal ganglion cell axons regrow to the same target area with functional and behavioral recovery. Interestingly, when he surgically rotated animal’s eyes upside-down, neurons still managed to “home-in” on their original target area causing reversed vision in animals (Sperry, 1943, 1963). These observations led Sperry to develop the chemoaffinity hypothesis stating that neurons carry individual chemical identification tags that lead each neuron connecting only with certain neuronal partners having complementary chemical tags and become selectively attached to them by specific chemical affinities (Sperry, 1963). Later on, he included additional features to the chemoaffinity hypothesis such as the application of morphogen gradients to explain orderly topographic projections of axons (Sperry, 1951).

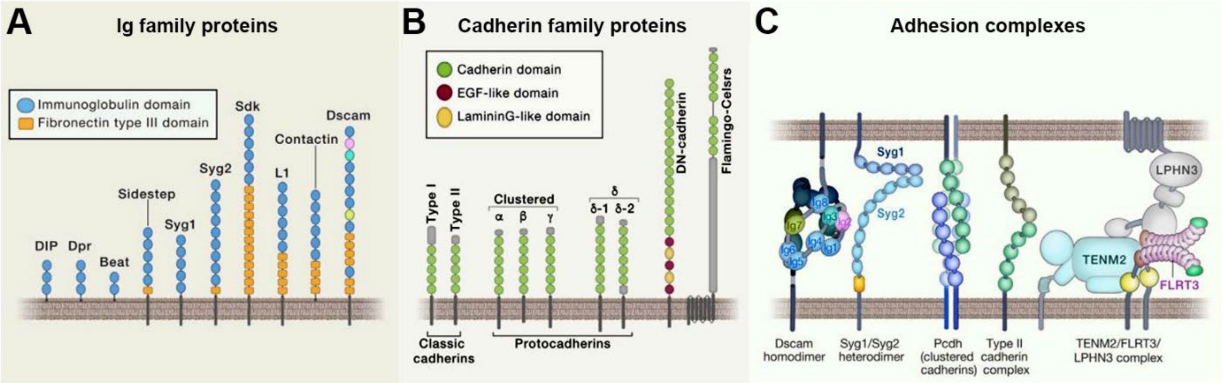
A
Ig family proteins
Immunoglobulin domain
Fibronectin type III domain
DIP
Dpr
Beat
Sidestep
Syg1
Syg2
Sdk
L1
Contactin
Dscam
B
Cadherin family proteins
Cadherin domain
EGF-like domain
LamininG-like domain
Type I
Type II
Clustered
α
β
γ
δ
δ-1
δ-2
DN-cadherin
Flamingo-Celsrs
Classic cadherins
Protocadherins
C
Adhesion complexes
Syg1
Syg2
LPHN3
TENM2
FLRT3
Dscam homodimer
Syg1/Syg2 heterodimer
Pcdh (clustered cadherins)
Type II cadherin complex
TENM2/FLRT3/LPHN3 complex

Figure 1: Different classes of recognition molecules implicated to have role in synaptic specificity. A, Domain structures of Immunoglobulin (Ig) family proteins. Pink, turquoise and yellow Ig domains represent variable domains in invertebrate Dscam1 proteins present (or not) in different isoforms. **B**, Different subclasses of Cadherin family proteins. **C**, Structure of adhesion proteins and binding partners located on pre- and postsynaptic membranes. Adapted from (Sanes and Zipursky, 2020).

The quest for finding molecular tags to account for synaptic specificity traditionally focused on attractive and repulsive molecular interactions between potential partners. Over the years, this approach has blossomed to identify several proteins and protein families required for correct layer targeting in the brain (Figure 1). However, one can easily consider correct layer targeting and synaptic specificity as separate and subsequent developmental steps as the former brings partners in close proximity to initiate synapse formation but the latter requires to discriminate between potential synaptic partners within a restricted, populated area. Among the proteins and protein families found to be required for correct targeting are, for instance, in the vertebrate retina, Immunoglobulin superfamily (IgSF) adhesion molecules Dscam/DscamL and Sidekick-1 and 2 (Sdk-1 and 2), which were found to regulate correct targeting to different sublaminae of inner plexiform layer (Yamagata and Sanes, 2008). In flies, N-cadherin

(Ncad) mediates photoreceptor targeting to correct medulla layers through homophilic attractive interactions. Selective removal of Ncad from *Drosophila* R7 photoreceptors results in R7s mistarget to R8 photoreceptor layer (Lee et al., 2001). Similar to targeting defects seen in Ncad mutants, flies mutant for LAR receptor tyrosine phosphatase, Syd1 and Liprin-α result in retractions and overshootings from the normal targeting layer of R7 photoreceptors (Choe et al., 2006; Clandinin et al., 2001; Holbrook et al., 2012). However, a recent re-evaluation of these mutants in R7 photoreceptors using live imaging in intact, developing *Drosophila* brains revealed that previously reported mistargeting phenotypes are the secondary consequences to growth cone stabilization defect at the correct targeting layer due to failed synapse formation (Ozel et al., 2019).

Sperry's chemoaffinity hypothesis entails unique identification tags for several million individual neurons to form synapse-specific neural circuits. Since a limited number of proteins can be translated by a genome, this seems to be a daunting task for neurons to achieve. One solution to this problem might be using the same molecules to establish neural circuits at different brain regions physically apart from each other. Another solution that was put forward by Sperry himself was that instead of using different molecular tags to define every individual synaptic connection, neurons might express the same molecular tags at different levels and only partners expressing molecular tags at matching levels would recognize each other and form a synaptic connection (Sperry, 1963). This idea was later supported by the discovery of morphogen gradients as in the case of complementary gradients of Eph receptors and their ligands ephrins that has been shown to be required for the topographic organization of the chicken retinotectal map (Drescher et al., 1995). Although morphogen gradients offer a solution to establish laminated, torographically structured regions in the brain, it fails to explain intermingled neural ensembles seen throughout a brain, which still requires qualitatively distinct chemical tags for partner recognition. One possible strategy that neurons use to generate unique identification tags is to express different variants or isoforms of the same protein with different binding affinities. An example of such a protein is the *Drosophila* Down syndrome cell adhesion molecule 1 (Dscam1) with roughly 38,000 different isoforms randomly produced through alternative splicing. Dscam1 proteins show isoform specific homophilic repulsion that each neuron, expressing a unique isoform of Dscam1 protein, recognize itself leading to spread-out axonal and dendritic branching (Chen et al., 2006; Dascenco et al., 2015; Schmucker et al., 2000). In a similar manner, in vertebrates, several isoforms of Neurexin (Nrx) is produced, which have slightly different binding affinities to their receptor Neuroligin (Nlg) (Sudhof, 2017). Such random generation of different isoforms of several distinct proteins can give each neuron a unique identity. However, considering the function of these proteins, as in the case of Dscam1 executing self-avoidance function for neurons to recognize themselves and avoid collapsing of dendrites of the same neuron, this strategy still doesn't offer a solution as to how two neurons recognize each other as partners and form synaptic connections.

1.1.2. Algorithmic brain growth: Finding neural partners in space and time

All cellular interactions during development are restricted in space and time. A prerequisite for synapse formation between two neural partners is the axonal and dendritic projections of these neurons need to 'see each other' at the same time and place. Brain development, like any other tissue growth, is a successive collection of developmental steps in which every developmental step generates a new state based on which the next developmental step runs. The outcome of this developmental growth is correctly patterned, functional brain structures. Here, the notion that neuronal partner recognition is controlled by matching molecular tags is challenged due to the fact that synapse formation is one of the later steps during brain development preceded by several other developmental steps from neurogenesis to correct guidance and branching of axons and dendrites to get into close proximity with other neurons to initiate synapse formation. Then the question arises here: How do neurons know which neuronal partners they will form synaptic contacts in the future?

One way to overcome this hurdle is to consider molecules, which have been previously studied to be part of a code to specify synapses, as a part of a developmental growth program to bring right partners together, while synapse formation itself is a non-selective, promiscuous event (Hassan and Hiesinger, 2015). Over the years, synaptic promiscuity has been supported by several studies. For instance, when neurons are relocated to incorrect target regions in the brain, they readily form synapses with available partners in these new, unfamiliar environment (Berger-Muller et al., 2013; Kulkarni et al., 2016). In fact, when neurons are isolated, i.e., there is no available partner to form synaptic connections, they form synapses with themselves (autapses) that are functionally indistinguishable from other synapses in the brain (Bekkers and Stevens, 1991). These examples support the notion that when precise sorting of right partners is guided, promiscuous synapse formation may still lead to proper assembly of neural circuits.

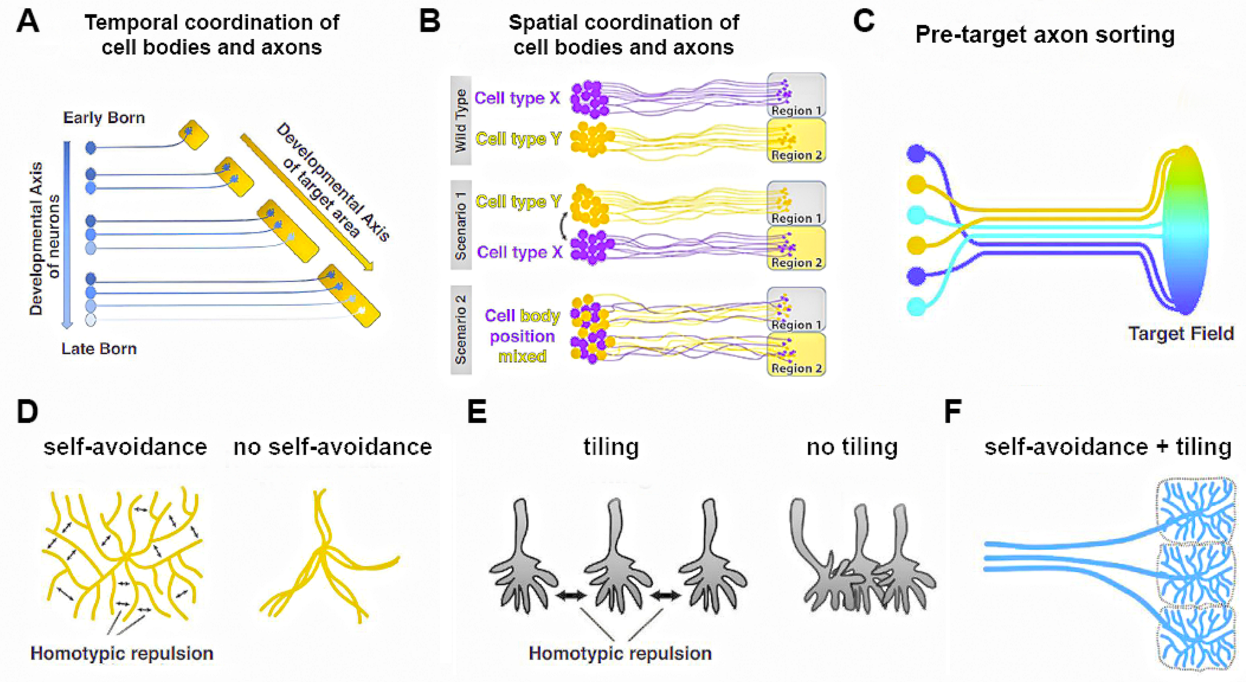
A
Temporal coordination of cell bodies and axons
Early Born
Developmental Axis of neurons
Late Born
Developmental Axis of target area
B
Spatial coordination of cell bodies and axons
Wild Type
Cell type X
Cell type Y
Region 1
Region 2
Scenario 1
Cell type Y
Cell type X
Region 1
Region 2
Scenario 2
Cell body position mixed
Region 1
Region 2
C
Pre-target axon sorting
Target Field
D
self-avoidance
no self-avoidance
Homotypic repulsion
E
tiling
no tiling
Homotypic repulsion
F
self-avoidance + tiling

Figure 2: Developmental growth steps that regulate neuronal encounters prior to synapse formation. A, Temporal coordination of cell body and axon positioning. The temporal order of cell differentiation affects cell body location and eventual innervation of axons to the target area. **B,** Relative position of cell bodies affects axon targeting. Swapping the position of cell body clusters of different neuronal subclasses can alter axon targeting and eventual connectivity pattern (Scenario 1). Similarly, random positional changes in neuronal cell bodies from their original positions might affect regional specificity of axon targeting (Scenario 2). **C,** Pre-target inter-axonal interactions facilitate fasciculation leading to topographic targeting of axons in the target field. **D,** Homotypic repulsion between sister processes causes spread-out arborizations. Loss of self-avoidance results in clumping of arborizations. **E,** Homotypic repulsion between neighbor neuronal processes results in equal spacing (tiling). Loss of repulsion causes disparate neuronal processes to overlap and clump together. **F**, Self-avoidance and tiling mechanisms together can

create patterns that restrict and facilitate specific neuronal encounters. Adapted from (Agi et al., 2020).

There are several cellular mechanisms during brain growth that may contribute to final wiring specificity although these mechanisms themselves do not necessarily need to contain an ‘information’ to specify synapses. Such mechanisms include temporal regulation of neuronal birth, cell body position, axon-axon interaction before reaching the target region, and branch patterning in the target region (Agi et al., 2020). Timing of neuronal birth and subsequent position of the cell body have been shown to influence final target innervation and positioning of neurites. For instance, early born neurons in the vertebrate visual system extend their axons to significantly larger area than late born neurons (Osterhout et al., 2014). In another example, changing the migratory route of cortical interneurons, hence the cell body position, significantly altered axonal arborizations (Lim et al., 2018). Axon-axon interactions before reaching the target area is another cellular mechanism to pre-sort certain neurons together before establishing synaptic connections (Figure 2C). A nice example for this phenomenon is the topographic representation of mouse facial whiskers in the neocortex. Here, thalamocortical axons are pre-sorted as they pass through the basal ganglia primordium and reach to similar target region in the neocortex forming a sensory map (Lokmane et al., 2013). Control of branching pattern in the target region is another important step during brain wiring to establish final synaptic connectivity. As mentioned earlier, in *Drosophila*, every individual neuron expresses a unique isoform of Dscam1 in a non-deterministic manner, which is required for self-avoidance (Schmucker et al., 2000). In the absence of self-avoidance, neurites fail to spread and clump together reducing neurite coverage in the target area for synaptic interactions (Figure 2D). Therefore, such a role played by Dscam isoforms is more akin to pattern formation than a unique synapse specification code. Another similar patterning rule, tiling, is based on repulsion between non-self branches (Figure 2E). Tiling and self-avoidance can be mediated by the same repulsion mechanisms that lead to laminar and columnar organization of neurons in several brain regions including cerebral cortex (Chen et al., 2017; Lefebvre, 2017). The sum of such patterning rules during brain development physically restricts neuronal encounters in time and space where synapses can be formed promiscuously without sacrificing specificity (Figure 2F).

1.2. The synaptic maintenance problem

During brain wiring, axons and dendrites travel long distances to form synaptic connections away from their cell bodies. Once they establish synaptic connections with other neurons, especially during adulthood, they face another challenge, which can be broken down to two points: First, morphological complexity of neurons dictates the necessity of compartmentalized maintenance mechanisms at their axons and dendrites while maintaining the communication with the cell body. Second, unlike the other cells in the body, most neurons live throughout the entire lifespan of the organism that requires robust and possibly unique cellular maintenance mechanisms to keep neurons and particularly their synapses functional and healthy over a long time. Consequently, morphological complexity together with longevity result in a formidable challenge to maintain synapses that defects in maintenance mechanisms often leads to adult-onset neurodegeneration in several neurodegerative disorders including Alzheimer’s disease and Parkinson’s disease (Bezprozvanny and Hiesinger, 2013).

What are the cellular strategies neurons use to maintain themselves and their synapses? First of all, neurons cannot use the most common cellular strategy used by other type of cells, which is the turnover of an entire cell. This is particularly due to the fact that the information required to replace hearth or liver cell is less than to replace, for instance, a pyramidal cell in the hippocampus because of the difficulty to re-establish all synaptic connections of that particular neuron formed with other neurons within the complicated network of the brain. However, at least in principle, neurons can replace entire synapses without losing overall connectivity with other neurons. Such ‘synaptic turnover’ mechanisms have been observed in sensory- and learning-dependent synapse formation and elimination mechanisms (Liston et al., 2013). For instance, in the mice barrel cortex, dendritic spines are eliminated in a sensory input-dependent manner. Animals deprived of sensory input show reduced dendritic spine elimination (Zuo et al., 2005). Another, functional aspect of synaptic maintenance problem is the need for high membrane turnover required for chemical neurotransmission (Sudhof, 2004). At the presynaptic site, synaptic vesicles undergo Ca^{2+}-regulated cycles of fusion and fission that requires tight protein quality control for robust neurotransmission. Failed quality control, i.e., defective rejuvenation of new synaptic vesicle proteins and elimination of old, dysfunctional protein may lead to reduction in neuronal function and health (Esposito et al., 2012).

1.3. Local protein degradation mechanisms in brain wiring and maintenance

Neurons, like any other cell, need continuous synthesis and degradation of proteins both during development and maturity. However, as highly polarized cells with spatially segregated axons and dendrites, neurons are particularly challenged for homeostatic regulation of protein turnover at extremities. The existence of protein synthetic machinery and mRNAs at developing axonal growth cones suggest a local ability of growth cones to react to changing internal and external states during development (Steward, 2002). Similarly, local protein synthesis has also implicated in synaptic plasticity during long-term potentiation and depression events (Steward and Schuman, 2001). On the other side of the coin, protein degradation pathways including proteasomal degradation, endolysosomal degradation and autophagy have been long described in neurons both in development and maintenance (Jin et al., 2018). To date, most studies on local protein degradation in neurons have focused on proteasomal degradation with a special focus on protein turnover at the postsynaptic terminals (Hamilton and Zito, 2013; Yi and Ehlers, 2007). However, proteasomal degradation mainly degrades cytosolic proteins that may not be responsible for the degradation of majority of synaptic membrane proteins at pre- and post-synaptic terminals (Hakim et al., 2016). The candidates of local protein degradation pathways include ubiquitous and neuron-specific endolysosomal degradation pathways and autophagy (Figure 3).

1.3.1. Ubiquitous endolysosomal degradation

Endolysosomal degradation begins with endocytosis of membranes that traffics through transport vesicles to early endosomes that mature into late endosomes or so-called multivesicular bodies (MVBs) and finally these subcellular structures fuse with Golgi-derived vesicles containing degradative machinery to form lysosomes where degradation of proteins take place. The hallmark of maturation process from early endosomes to lysosomes is progressive increase in luminal pH, which is required for activation of proteases including Cathepsins in lysosomes to initiate degradation (Bright et al., 2016). Rab GTPase family proteins play key roles at every steps of endolysosomal degradation (Kiral et al., 2018). Rab5, an early endosomal Rab GTPase, regulates clathrin-mediated endocytosis and endosomal maturation, which has a crucial role in synaptic vesicle retrieval from the pre-synaptic membrane (McLauchlan et al., 1997; Semerdjieva et al., 2008). During development, loss of Rab5 function negatively affects the elongation of retinal axons in *Xenopus* and impairs axon fasciculation, hence leads to mistargeting of L2/L3 callosal projections in rats (Falk et al., 2014; Wu et al., 2014). Other early and recycling endosome Rabs including Rab4 and Rab11 are also likely candidates to regulate synaptic vesicle recycling process. The expression of dominant-negative Rab4 impairs rejuvenation of synaptic vesicles from endocytic intermediates (de Wit et al., 2001). Such intermediate endosomal structures have been implicated as sorting stations for synaptic vesicle proteins also in other studies. Rab35 and its GTPase activating protein (GAP) Skywalker (Sky) regulate synaptic vesicle rejuvenation in *Drosophila* and vertebrate neuronal cultures (Figure 3). Rab35 over-activation in *sky* mutants leads to both increase turnover of synaptic vesicles from the readily releasable pool and increase in neurotransmission. This effect was due to increased degradation rate of dysfunctional synaptic vesicle protein neuronal Synaptobrevin (n-Syb) suggesting that Rab35/Sky function at the interplay between synaptic vesicle recycling and degradation (Fernandes et al., 2014; Uytterhoeven et al., 2011).

There are two distinct paths that endocytosed proteins may follow: they are either recycled back to plasma membrane or sorted into late endosomes/MVBs for degradation. Rab7 is the key regulator of early-to-late endosome maturation and also required for fusion of late endosomes/MVBs with lysosomes (Guerra and Bucci, 2016). Rab7 is ubiquitously expressed in all cells to mediate lysosomal degradation. However, in *Drosophila*, it is expressed in neurons before other cells types and loss of Rab7 in photoreceptors leads to progressive degeneration starting at synapses (Chan et al., 2011; Cherry et al., 2013). Consistently, although Rab7-dependent ubiquitous endolysosomal degradation occurs in all cell types, dysfunctional degradation evokes problems first in tissues with high protein turnover like the nervous system. This may underlie why most lysosomal storage disorders affect the nervous system before any other tissue in the body (Schultz et al., 2011). These findings suggest that neurons, and particularly synaptic terminals, are sensitive to reduced endolysosomal degradation and they may employ several local and cargo-specific endolysosomal degradation for both proper neuronal development and maintenance (Figure 3).

1.3.2. Neuron-specific endolysosomal degradation: Neuronal ‘sort-and-degrade’

Morphological complexity of neurons and high demand for protein turnover especially at axon terminals and dendrites suggest that neurons might have local degradation machineries at synapses. Previous studies have shown abundance of lysosomal proteins including lysosomal associated membrane protein 2 (LAMP2) at axon terminals and recruitment of lysosomes to dendritic spines in an activity-dependent manner suggesting that lysosomal degradation might be regulated locally at synapses possibly independent from lysosomes at the cell body (Frampton et al., 2012; Goo et al., 2017). Here the question becomes whether neurons use the same ubiquitous degradation machinery at axon terminals and dendrites or exploit more and specialized degradation pathways, perhaps also with distinct cargo-specificity to meet high demand for protein turnover? One such neuron-specific endolysosomal degradation mechanism has recently been described, which is operated by neuron-specific synaptic proteins n-Syb and the vesicular ATPase component V100 (Haberman et al., 2012; Williamson et al., 2010a). In *Drosophila*, photoreceptor-specific loss of function of both V100 and n-Syb result in intracellular sorting and degradation defects downstream of endocytosis. Consequently, mutations in both *v100* and *n-syb* lead to slow adult-onset neurodegeneration (Haberman et al., 2012; Williamson et al., 2010a). It is interesting to note that both V100 and n-Syb are located on synaptic vesicles and required for normal neurotransmission suggesting that they likely function at the interface between the synaptic vesicle recycling and synaptic endolysosomal function. Apart from their functions in neuronal maintenance, both n-Syb and V100 have also been shown to degrade guidance receptors during development with the former leading tiling defects in *Drosophila* R7 and R8 photoreceptors (Hiesinger et al., 1999; Williamson et al., 2010b).

1.3.3. Autophagy

Autophagy is a conserved, ubiquitous intracellular degradation pathway used by all cells to clear cytoplasmic entities such as proteins, sugars, lipids and also entire organelles as in the case of mitophagy to degrade damaged mitochondria (Mizushima, 2007). In the nervous system, autophagy has been mainly implicated in neuronal maintenance and neurodegeneration. The conditional loss of core autophagy proteins Atg5 and Atg7 in neurons leads to intracellular protein accumulations and eventual adult-onset neurodegeneration (Hara et al., 2006; Komatsu et al., 2006). Although studies on local roles of autophagy in neurons are still in earlier stages, recent works have demonstrated compartmentalized formation and regulation of autophagy at axon terminals and dendrites. In axons of cultured neurons, autophagosomes continuously form at distal tips containing cargos derived from synapses (Maday et al., 2012). Following formation at axon terminals, autophagosomes travel to the cell body and fuse with lysosomes to degrade their cargos (Maday and Holzbaur, 2016). Although local degradation of synaptic proteins by autophagy has not been demonstrated, a local degradation of mitochondria in axons by a selective autophagy mechanism called mitophagy has been reported. Here, autophagosomes and lysosomes are recruited to damaged mitochondria for local degradation in axons (Ashrafi et al., 2014). With ample evidence on local formation of autophagosomes, recent studies have also shown local regulation of autophagosome formation by synaptic proteins at axon terminals. For instance, a synaptically enriched protein Endophilin A (EndoA), which was previously characterized to have a role in synaptic vesicle endocytosis, has been shown to recruit an early autophagosome protein Atg3 to growing autophagosome membrane that facilitates elongation and enclosure of autophagosomes (Soukup et al., 2016). In addition, another study showed that presynaptic active zone protein Bassoon in mammalian neurons inhibits autophagy interacting with an essential autophagy protein Atg5 (Figure 3). Consequently, loss of Bassoon function in neurons triggers autophagosome formation at pre-synaptic terminals (Okerlund et al., 2017). Collectively these studies point to the fact that autophagy is locally regulated at synapses by synaptic proteins linking autophagy and synaptic homeostasis/dysfunction in mature neurons.

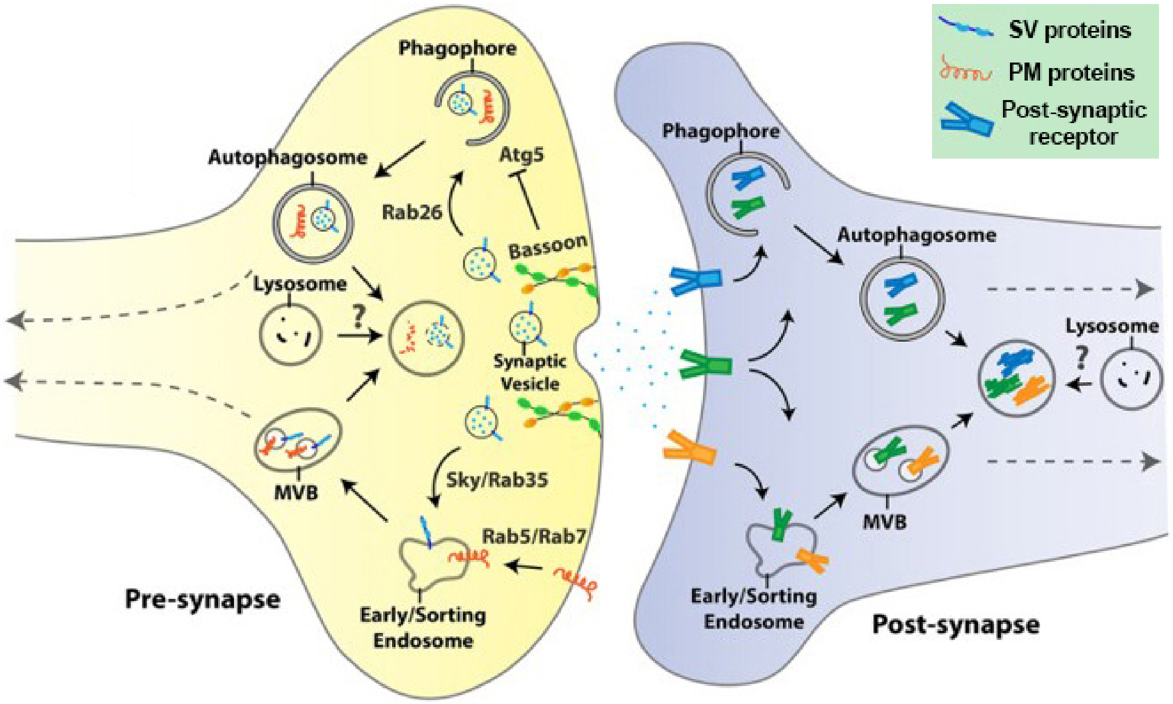
SV proteins
PM proteins
Post-synaptic receptor
Phagophore
Autophagosome
Atg5
Rab26
Bassoon
Lysosome
?
Synaptic Vesicle
MVB
Sky/Rab35
Rab5/Rab7
Early/Sorting Endosome
Pre-synapse
Phagophore
Autophagosome
Lysosome
?
MVB
Early/Sorting Endosome
Post-synapse

Figure 3: Protein sorting and degradation mechanisms at pre- and post-synaptic terminals. Known mechanisms of cargo sorting and degradation by endolysosomal degradation pathways and autophagy and their regulatory proteins in pre- and post-synaptic terminals. Dashed arrows represent retrograde axonal transport of endolysosomal and autophagic organelles from terminals to the cell body. Most mechanisms depicted here have been characterized in developed, functional neurons. MVB = Multivesicular bod. Adapted from (Jin et al., 2018).

Although the role of autophagy in neuronal and synaptic homeostasis is well established, comparably little is known about its role in developing brain. Functional neurons develop in the absence of autophagy (Hernandez et al., 2012; Juhasz et al., 2007). A recent study on the role of autophagy regulating axon pathfinding of thalamocortical neurons in mouse reported no defect in loss of core autophagy protein Atg7 (Wang et al., 2018). Interestingly, in *Drosophila* and *C.elegans*, loss of autophagy in specific neurons leads to reduced synapse development (Shen and Ganetzky, 2009; Stavoe et al., 2016). By contrast, in primary neuronal cultures and in the mouse brain, dysfunctional autophagy leads to increased dendritic spine density due to defective postnatal pruning following synapse formation (Tang et al., 2014). In numerous other studies loss of autophagy function has also been linked to social behavior defects frequently observed in individuals with neurodevelopmental disorders including autism spectrum disorders (Hui et al., 2019; Kim et al., 2017; Yan et al., 2018). However, it still remains unknown whether and how autophagy may contribute neural circuit assembly and synaptic partner choice during brain development.

1.4. The effect of external factors in brain wiring

The nature versus nurture debate is one of the oldest issues in psychology and in the last century it also started to be considered as an investigation question in developmental biology. Simply, nature refers to the genetic traits inherited from parents, while nurture refers to the different environmental factors that have an influence in brain development. Since amniotic, endothermic animals including humans develop in an environmentally controlled amniotic sac, the possible effects of environmental factors on brain development have been mostly studied during early postnatal life during which experiences may shape the way synaptic connections are formed, consolidated or eliminated. However, development of non-amniotes including insects, amphibians and fish mostly occurs while exposed to changing external conditions such as temperature, humidity, sunlight, pH etc. It has been long known that temperature affects the body size of non-amniotes. A phenomenon named temperature-size rule holds that ectothermic animals develop at cold temperature have increased body size as adults (Angilletta et al., 2004). Developmental temperature also affects the growth rate of embryonic, larval and pupal development in insects including the *Drosophila* (Ludwig and Cable, 1933; Powsner, 1935). However, it still remains largely known whether and how developmental temperature affects brain development especially in cellular level. Reports on the effect of developmental temperature in brain development have mostly focused on behavioral repercussion in adult animals developed at different temperatures. For example, adult honey bees experienced different brood temperature during pupal development show distinct learning and memory abilities and change in dancing patterns (Tautz et al., 2003). In another study, researchers demonstrated that development of sensorimotor function in *Xenopus laevis* affected by rearing temperature as the larvae developed at cold temperature show enhanced escape swimming behavior compared to the ones developed at warmer temperatures (Spencer et al., 2019). To what extent such behavioral changes may be explained by brain wiring differences at different development temperatures is subject to further investigation.

1.5. The *Drosophila* visual system: A model to study brain wiring and neuronal maintenance

Since the human brain has an extraordinary complexity that is beyond our understanding with the present biotechnological tools, scientists generally take advantage of a reductionist approach, that is, they use simpler models like murine or insect brains. Although this approach contains a problem in itself like the applicability of findings in simpler models to more complex systems, it has been proven many times that organisms share biological processes throughout the evolutionary hierarchy. The fruit fly *Drosophila* melanogaster has comparably little number of neurons in their brains, yet it is complex enough to reliably study basic principles of intra- and intercellular mechanisms including brain wiring and neuronal maintenance. The *Drosophila* visual system is composed of four neuropils in each optic lobes, namely the lamina, the medulla, the lobula, and the lobula plate, which contain roughly 60,000 neurons of over 70 neuronal substypes (Fischbach and Dittrich, 1989; Morante and Desplan, 2008). Similar to other invertebrate and vertebrate brain structures, axons and dendrites in the fly visual system are spatially arranged into regular layers and columns in a subtype-dependent manner, which allows to study biological principles of pattern formation and assembly of neurons into circuits (Clandinin and Zipursky, 2002).

The adult *Drosophila* eye consists of 750-800 small, hexagonal facets called ommatidia. Each ommatidium contains 8 photoreceptors (R cells), R1 to R8, and 11 accessory cells, including lens secreting cone cells, pigment cells, and bristle cells (Treisman, 2013). Photoreceptors can be categorized into three groups according to the type of Rhodopsin they express and hence the ability to detect different wavelengths of light. R1 to R6 photoreceptors, which are called outer photoreceptors, express Rhodopsin 1 (Rh1). They are specialized for motion detection, hence functional equivalent of rod photoreceptors in vertebrates. The inner photoreceptors, R7 and R8, are involved in color vision being functional equivalent of vertebrate cone cells. They express distinct Rhodopsin molecules that are sensitive to different light spectrum. R7 expresses either Rhodopsin 3 (Rh3) or Rhodopsin 4 (Rh4), which are sensitive to ultraviolet light. On the other hand, R8 expresses Rhodopsin 5 (Rh5) or Rhodopsin 6 (Rh6), which are sensitive to wavelengths in blue and green spectrum, respectively (Yamaguchi et al., 2010). In addition to differential Rhodopsin expression, the inner and outer photoreceptors also differ in connectivity. R1 to R6 axons terminate in the first neuropil lamina forming synaptic connections mainly with lamina monopolar cells, while the inner photoreceptors terminate at distinct layers in the medulla with R8 axons targeting at layer M3 and R7 axons targeting at layer M6 (Figure 4A). Here, they form connections with various types of medulla neurons (Fischbach and Dittrich, 1989; Gao et al., 2008; Meinertzhagen and O'Neil, 1991; Takemura et al., 2015).

Over the years, visual systems of different organisms have become a valuable tool for understanding common and divergent principles of neuronal connectivity. Although the anatomical structures of the visual system can be quite different between invertebrates and vertebrates, they still share similar design principles that manifest itself best in axonal and dendritic patterning in repetitive columns of similar cells and orthogonal divisions of columns into layers, or laminae, that provide anatomically restricted regions where prospective synaptic partners get in close proximity to initiate synapse formation. One seemingly key difference of synapse specification between invertebrates and vertebrates is that, although visual system wiring in *Drosophila* appears to be pre-specified by a genetic program, in vertebrates, activity-dependent synapse pruning plays a key role to determine final connectivity. However, in both systems initial axon and dendrite targeting to certain columns and layers still lay the foundation for mature connectivity patterns and it is likely that in both systems pre- and post-specification events contribute neural circuit assemblies (Hassan and Hiesinger, 2015; Kolodkin and Hiesinger, 2017; Sanes and Zipursky, 2010).

One interesting example of pre-specification of synaptic connections in the fly visual system is neural superposition. The lamina of the fly optic lobe consists of iterative columns, or ‘cartridges’, which are synaptic units where a point in visual space captured by photoreceptors from different ommatidia converge on (Figure 4B). Such an intricate wiring diagram can be explained by simple, successive developmental rules based on growth cone extensions and filopodia dynamics that bring right partners together without a need for individual recognition tags between partners (Langen et al., 2015). Interestingly, when sorting step is disrupted and photoreceptor axons find themselves in wrong cartridges, correct number of synapses form between wrong partners suggesting that pre-specification of partners and synapse formation are separable events and the latter may be executed promiscuously (Hiesinger et al., 2006). Although the columnar restriction, as in the case of neural superposition, is a commonly used strategy during brain wiring to bring right partners in close proximity, there are several examples where neuronal projections are not restricted to columns. One such example is Dm8 dendrites, the main postsynaptic partner of R7 photoreceptors, which span ~13 medulla columns (Gao et al., 2008). However, a highly variable pattern of Dm8 dendritic processes raises questions about synaptic specificity in different columns (Ting et al., 2014). A recent discovery of Ig superfamily cell adhesion molecules Dprs and DIPs show that yellow type R7s and a Dm8 subtype express interacting molecular pairs Dpr11-DIP-γ (Tan et al., 2015). During early development, Dm8 subtypes are produced in excess and following matching with their cognate R7, through a cellular competition, unmatched Dm8s are eliminated by apoptosis suggesting that Dpr11-DIP-γ interaction is required for Dm8 survival (Courgeon and Desplan, 2019). Such molecular interactions might be important for pre-sorting synaptic partners and bias subsequent synapse formation mechanism between certain partners. However, EM reconstruction studies showed that different types of R7s (pale or yellow) form synapses with lateral braches of any Dm8 subtype (Menon et al., 2019; Takemura et al., 2015) again suggesting that brain wiring program uses different strategies to bring right partners together collectively through genetic and stochastic processes that could be sufficient to match right partners together even if synapse formation per se can be promiscuous.

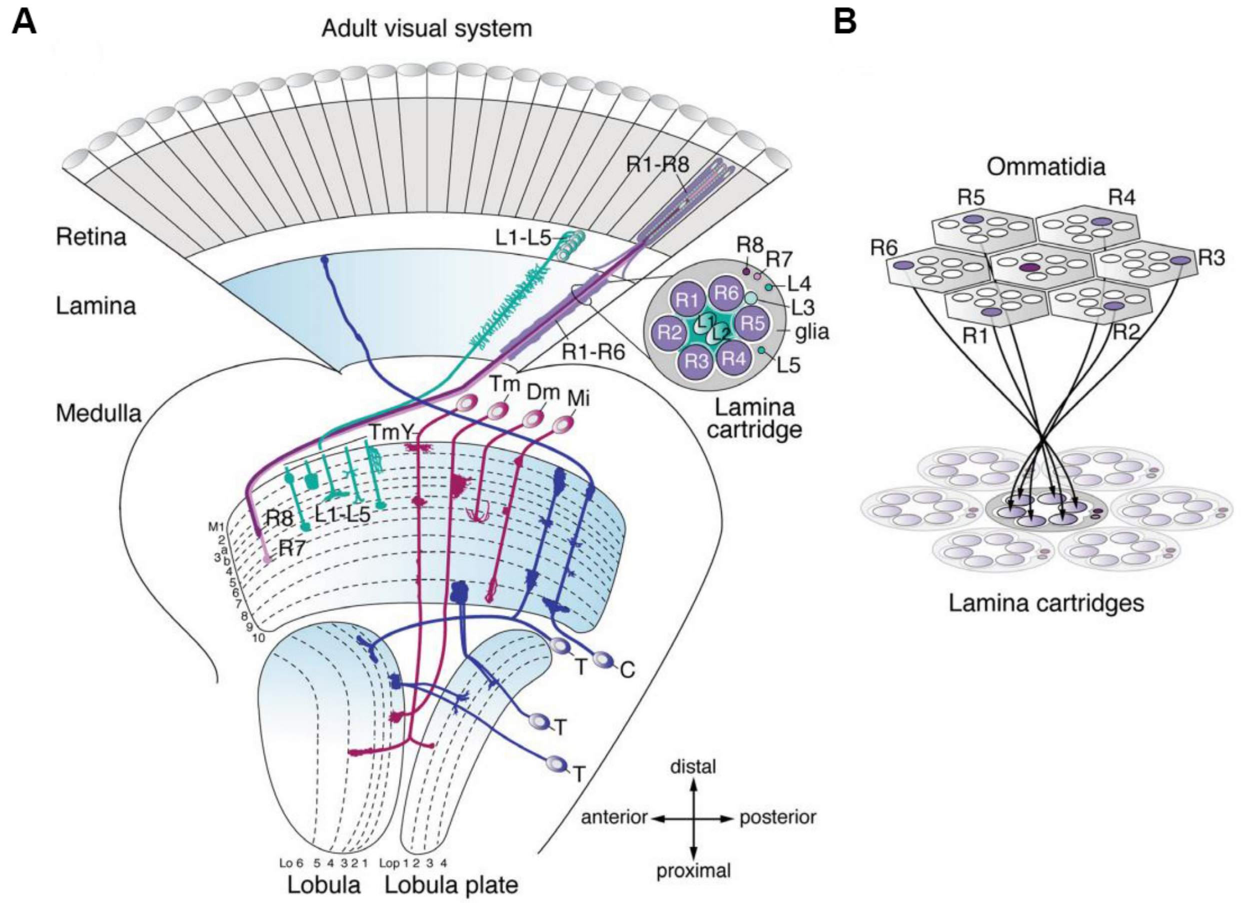
A
Adult visual system
Retina
Lamina
Medulla
R1-R8
L1-L5
R1-R6
R8
R7
L4
L3
glia
L5
R1
R2
R3
R4
R5
R6
L1
L2
Lamina cartridge
Tm
Dm
Mi
TmY
R8
L1-L5
R7
M1
2
a
3
b
4
5
6
7
8
9
10
T
C
T
T
distal
anterior
posterior
proximal
Lo 6 5 4 3 2 1
Lop 1 2 3 4
Lobula
Lobula plate
B
Ommatidia
R5
R4
R6
R3
R1
R2
Lamina cartridges

Figure 4: The adult *Drosophila* visual system. A, The optic lobe consists of the lamina, medulla, lobula and lobula plate. The illustration shows a subset of neurons and their projections in different neuropils. R1-R6 photoreceptors extend their axons from the retina to the lamina where they form synaptic connections with lamina neurons in columnar synaptic units called cartridges. R7 and R8 photoreceptors and lamina neurons, L1 to L5, extend their axons into one or more of ten medulla layers. Transmedullary (Tm and TmY) neuron axons pass through the medulla and terminate in distinct lobula and lobula plate layers. Distal medulla (Dm) neurons form lateral braches spanning several columns at distal medulla layers. Medulla intrinsic (Mi) neurons connect distal and proximal medulla layers. C neurons extend their axons to medulla and lamina. T neurons connect either lobula and lobula plate or lobula and lobula plate to medulla. **B**, R1 to R6 photoreceptors from different ommatidia that see the same point in space innervate the same lamina cartridge following the neural superposition principle. Adapted from (Apitz and Salecker, 2014).

The *Drosophila* visual system and especially photoreceptors have also been extensively used to study cellular neuronal maintenance mechanisms and associated neuronal degeneration. A hallmark of photoreceptor degeneration and eventual cell loss is disrupted ommatidial lattice in the eye, which can be easily assessed by electron microscopic analysis of retina. Furthermore, photoreceptor functions can easily be analyzed through electroretinograms, an extracellular recording to assess response to light stimulus. As light-activated cells, photoreceptors can also be challenged via light stimulus that can be used to distinguish activity-dependent and independent cellular mechanisms for neuronal maintenance. The use of *Drosophila* photoreceptors as a model also led to the discovery of several proteins with functions in intracellular membrane trafficking, which is tightly connected to normal neuronal functions and disease states. The first neuron-specific branch of endolysosomal degradation, which is operated by synaptic proteins V100 and n-Syb, have been described at *Drosophila* photoreceptor axon terminals. The loss of function of both V100 and n-Syb disrupts membrane trafficking at axon terminals that cause slow adult-onset neurodegeneration (Haberman et al., 2012; Williamson et al., 2010a). Also, more than half of Rab GTPases, key regulators of various membrane trafficking mechanisms in all cells, have been shown to be enriched in neurons and are located at synaptic terminals in the *Drosophila* visual system (Chan et al., 2011). Furthermore, genetic screens using the fly eye have led to identification of several genes affecting neuronal functions leading to neurodegeneration (Jackson, 2008). The fly eye has also been effectively used to understand neurotoxic functions of protein aggregates such as amyloid plaques seen in degenerating neurons in Alzheimer's disease (Jeon et al., 2020; O'Keefe and Denton, 2018). The ease of tissue-specific transgenic expression of the toxic proteins in *Drosophila* photoreceptors allowed researchers to easily study affected intracellular functions due to aggregate formation as well as functional state of degenerating neurons with simple electrophysiological and behavioral assays (Deal and Yamamoto, 2018; Jackson, 2008; McGurk et al., 2015).

2. Aim

Neurons are highly polarized cells with their axons and dendrites often located away from the cell body. This morphological complexity results in a formidable challenge both during development as they need to find right neuronal partners to establish a functional circuit and during adulthood as they need to maintain health and function of synapses. The robustness of these biological processes is largely dependent on having proper protein and membrane composition at the right place and time and may be subjected to changes in environmental conditions such as developmental temperature.

The goal of this doctoral work therefore is to address unanswered questions regarding mechanisms and functions of local protein degradation pathways and external factors such as developmental temperature in brain wiring and maintenance: Are there compartmentalized, local protein degradation mechanisms maintaining local pool of functional proteins? If so, what are the molecular machineries regulating local protein degradation pathways? And what are the physiological functions of these pathways during development and function? Finally, to what extent neuronal strategies to find right synaptic partners is affected by environmental factors such as temperature experienced during development? In this context, I investigated the local role of ubiquitous and neuron-specific endolysosomal degradation pathways and autophagy and also the possible effects of rearing temperature on synapse formation, synaptic partner choice and synaptic maintenance.

3. Manuscript 1

Live observation of two parallel membrane degradation pathways at axon terminals

Jin, E.J.*, **Kiral, F.R.*,** Ozel, M.N., Burchardt, L.S., Osterland, M., Epstein, D., Wolfenberg, H., Prohaska, S., and Hiesinger, P.R.

* These authors contributed equally to this work

Current Biology, April 2, 2018; 28(7):1027-1038.

Contribution

Experiments in this manuscript were designed by myself and Eugene Jennifer Jin under the supervision of Prof. Dr. P. Robin Hiesinger. All experiments were performed and analyzed with equal contribution by myself and Eugene Jennifer Jin. Lara S. Burchardt, Daniel Epstein and Heike Wolfenberg helped with experiments and data analysis. Steffen Prohaska and Marc Osterland provided the Markov state model analyses. The paper was written by myself, Eugene Jennifer Jin and Prof. Dr. P. Robin Hiesinger.

The original article including the supplemental information is included on the following pages and available online at:

https://doi.org/10.1016/j.cub.2018.02.032

Current Biology

Live Observation of Two Parallel Membrane Degradation Pathways at Axon Terminals

Highlights

- Membrane protein degradation can occur at axon terminals
- Two parallel mechanisms degrade synaptic vesicle and plasma membrane proteins
- The two mechanisms are molecularly distinct and employ different cathepsins
- Local "hub" compartments bud off retrograde vesicles at any maturation stage

Authors

Eugene Jennifer Jin, Ferdi Ridvan Kiral,
Mehmet Neset Ozel, ...,
Heike Wolfenberg, Steffen Prohaska,
Peter Robin Hiesinger

Correspondence

robin.hiesinger@fu-berlin.de

In Brief

Jin et al. develop a live-imaging method based on acidification-sensing probes in intact *Drosophila* brains to reveal two molecularly distinct endolysosomal degradation pathways at axon terminals. Independent of the canonical Rab7-dependent pathway, synaptic vesicle protein degradation requires n-Syb, V100, and Cathepsin L-like protease Cp1.

Jin et al., 2018, Current Biology *28*, 1027–1038
April 2, 2018 © 2018 The Authors. Published by Elsevier Ltd.
https://doi.org/10.1016/j.cub.2018.02.032

Current Biology
Article

CellPress

Live Observation of Two Parallel Membrane Degradation Pathways at Axon Terminals

Eugene Jennifer Jin,[1,2,5] Ferdi Ridvan Kiral,[1,5] Mehmet Neset Ozel,[1,2] Lara Sophie Burchardt,[1] Marc Osterland,[3] Daniel Epstein,[1,4] Heike Wolfenberg,[1] Steffen Prohaska,[3] and Peter Robin Hiesinger[1,6,*]
[1]Division of Neurobiology, Freie Universität Berlin, Königin Luise Straße 1-3, 14195 Berlin, Germany
[2]Graduate School of Biomedical Sciences, UT Southwestern Medical Center, Dallas, TX 75390, USA
[3]Zuse Institute Berlin, Takustraße 7, 14195 Berlin, Germany
[4]Present address: Department of Surgery, University of Alabama, Birmingham, Birmingham, AL 35233, USA
[5]These authors contributed equally
[6]Lead Contact
*Correspondence: robin.hiesinger@fu-berlin.de
https://doi.org/10.1016/j.cub.2018.02.032

SUMMARY

Neurons are highly polarized cells that require continuous turnover of membrane proteins at axon terminals to develop, function, and survive. Yet, it is still unclear whether membrane protein degradation requires transport back to the cell body or whether degradation also occurs locally at the axon terminal, where live observation of sorting and degradation has remained a challenge. Here, we report direct observation of two cargo-specific membrane protein degradation mechanisms at axon terminals based on a live-imaging approach in intact *Drosophila* brains. We show that different acidification-sensing cargo probes are sorted into distinct classes of degradative "hub" compartments for synaptic vesicle proteins and plasma membrane proteins at axon terminals. Sorting and degradation of the two cargoes in the separate hubs are molecularly distinct. Local sorting of synaptic vesicle proteins for degradation at the axon terminal is, surprisingly, Rab7 independent, whereas sorting of plasma membrane proteins is Rab7 dependent. The cathepsin-like protease CP1 is specific to synaptic vesicle hubs, and its delivery requires the vesicle SNARE neuronal synaptobrevin. Cargo separation only occurs at the axon terminal, whereas degradative compartments at the cell body are mixed. These data show that at least two local, molecularly distinct pathways sort membrane cargo for degradation specifically at the axon terminal, whereas degradation can occur both at the terminal and *en route* to the cell body.

INTRODUCTION

Neurons must regulate the turnover of membrane proteins in axons, dendrites, and the cell body to ensure normal development and function. Defects in membrane protein degradation are hallmarks of neurodegenerative diseases [1–6]. Recent progress has identified several mechanisms that are required at axon terminals to prevent dysfunction and degeneration, including the local generation of autophagosomes and endolysosomes [7–12]. However, it is unclear whether these degradative organelles are principally transported back to the cell body for degradation or whether degradation can occur locally [9, 13–16]. In addition, the cargo specificity of membrane degradation mechanisms at the axon terminals has remained largely unknown, i.e., it is unclear which membrane proteins are degraded by what mechanisms [16].

Several mechanisms have been directly linked to synapse function or degeneration and have raised questions about cargo specificity and the ultimate locale for degradation. These include (1) local generation of autophagosomes at axon terminals [7, 8], (2) maturation of autophagosomes and endosomes that depends on the ubiquitous small guanosine triphosphatase (GTPase) Rab7 [17, 18], (3) endosomal sorting that depends on the GTPase Rab35 and RabGAP Skywalker [11, 12, 19], and (4) endosomal sorting that depends on the neuron-specific synaptic vesicle (SV) proteins neuronal synaptobrevin (n-Syb) and V100 [20–22]. These mechanisms may overlap, and defects in any of them cause neurodegeneration in a variety of neurons [11, 17, 20, 22–25]. In the case of (macro-) autophagy, the formation of autophagosomes occurs at axon terminals [10, 26, 27], whereas degradation is thought to occur during and after retrograde transport back to the cell body [8, 9, 27]. As with both the canonical and neuron-specific endolysosomal mechanisms, it remains largely unknown what cargoes are sorted into autophagosomes at axon terminals [9, 27]. The Rab35/Skywalker-dependent endosomal sorting mechanism was recently reported to selectively sort different SV proteins in an activity-dependent manner [19]. Lysosomes have also been shown to localize to dendritic spines in an activity-dependent manner [28]. In both cases, it remains unknown whether degradation occurs locally at synapses and what cargo proteins are affected. Finally, we have previously described a "neuronal sort-and-degrade" (NSD) mechanism based on the function of the two neuron-specific synaptic genes *n-syb* and *v100* [20, 22]. Similar to the other mechanisms, neither cargo specificity nor the locale of degradation for NSD is known. For all mechanisms, it has remained a challenge to directly observe their local roles in the context of normal development and function in an intact brain.

Current Biology *28*, 1027–1038, April 2, 2018 © 2018 The Authors. Published by Elsevier Ltd. 1027
This is an open access article under the CC BY-NC-ND license (http://creativecommons.org/licenses/by-nc-nd/4.0/).

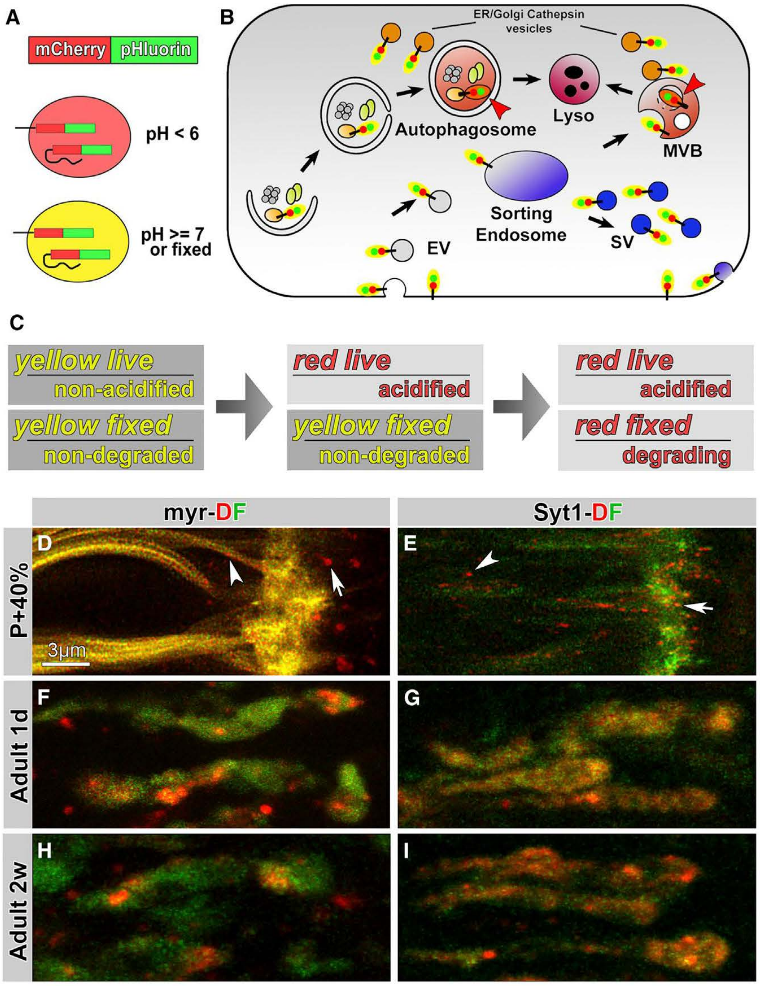

Figure 1. Live Observation of General Plasma Membrane Cargo (myr) and Synaptic-Vesicle-Specific Cargo (Syt1) in Large Acidic Compartments at Axon Terminals

(A) Design of the acidification-sensing dual fluorophore (DF) mCherry-pHluorin tag.

(B) Cytoplasmically DF-tagged proteins "turn red" only in multivesicular bodies (MVBs), lysosomes, and autophagosomes.

(C) The DF tag as acidification and degradation sensor. Acidification sensor: yellow fluorescence live indicates a non-acidic environment; red fluorescence live indicates an acidic environment. Degradation sensor: "yellow fixed" indicates both fluorophores are intact; "red fixed" indicates degradation of the terminal pHluorin tag.

(D–I) Live imaging of myr-DF and Syt1-DF probes in axon terminals of developing (P+40%, 40% pupal development; D and E), 1-day-old (F and G), and 2-week-old adult (H and I) *Drosophila* photoreceptor axon terminals. Arrows, terminal compartments; arrowheads, axonal compartments.

See also Figures S1 and S2 and Movies S1 and S2.

In this study, we report the direct observation of cargo-specific endolysosomal sorting and degradation at axon terminals *in vivo* using live imaging in intact *Drosophila* brains. We define axon terminal "hub" compartments based on their local dynamics, maturation, degradation, continuous mixing through fusion and fission, and budding of retrograde transport vesicles. In addition, we identified two distinct pools of hubs that function locally in two separate endolysosomal pathways based on different cargo specificities, different molecular sorting, and different maturation mechanisms.

RESULTS

We devised a live-imaging approach to directly observe when, where, and with what cargo specificity membrane protein turnover and degradation occur in neurons in an intact brain. Our approach is based on two improved methods that make use of advantages of the *Drosophila* system: first, a recently developed eye-brain culture system for continuous fast live imaging at subcellular resolution in neurons inside an intact brain from early development up to adulthood [29], and second, genetically encoded dual fluorophore live-imaging probes that quantitatively measure when and where they are sorted into degradative compartments.

Live Observation of Large Acidic Compartments at Axon Terminals

Genetically encoded fusions with pHluorin, a pH-sensitive GFP, and mCherry, a particularly pH-resistant red fluorescent protein (RFP), report cargo incorporation into degradative membrane compartments [30, 31] (Figures 1A and 1B). The approach is designed to measure both sorting and degradation: cytosolic fusions of the dual fluorophore (DF) tag to membrane proteins retain yellow fluorescence during normal cycles of exo-/endocytosis, including the entire SV cycle, and shift from yellow to red fluorescence only after engulfment into the strongly acidified environments of multivesicular bodies or autophagosomes (Figure 1B).

In addition, the DF tag can visualize partial degradation if only one of the two fluorophores is degraded (Figure 1C). pHluorin is both more sensitive to fluorescence loss and more exposed to proteases when fused in the terminal position (Figures 1A and 1B). We reasoned that fusion proteins on early endosomal compartments and cytoplasmically exposed membranes should retain yellow fluorescence both live and fixed ("yellow live" in Figure 1C). Engulfment into strongly acidified compartments should initially lead to "red live" fluorescence that can be reverted to yellow when fixed. Finally, initiation of degradation should lead to irreversible damage of pHluorin first and thereby to "red fixed" fluorescence (Figure 1C).

We designed two imaging probes: first, a general membrane cargo by fusing the DF tag to a myristoylated residue with the idea to mark most membranes in an unbiased manner (myr-DF), and second, a fusion of the DF tag to the highly specific SV membrane protein Synaptotagmin 1 (Syt1-DF) [32]. We performed live imaging of the two probes in developing photoreceptor axon terminals starting prior to synaptogenesis (40% of pupal development [P+40%]) and in 1-day- and 2-week-old adults (Figures 1D–1I). The myr-DF probe exhibited widespread membrane labeling, whereas Syt1-DF was more restricted to the axon terminals. Both probes marked clearly discernible intracellular membrane compartments in axons (arrowheads in Figures 1D and 1E) and at axon terminals (arrows). We expected to see both acidified and non-acidified compartments, but surprisingly, yellow or green fluorescence appeared always diffuse or, in the case of myr-DF, on the plasma membrane. Diffuse yellow labeling of terminals in the case of Syt1-DF most likely represents pools of SVs. In contrast, all distinctly recognizable compartments lacked the pHluorin signal and appeared red live, indicating an acidified environment below pH 6 [20, 30] (Figures 1D–1I; Movie S1). We made similar observations in photoreceptor neuron cell bodies and at axon terminals and in cell bodies of class IV sensory neurons in intact larvae (Figures S1A and S1B). We chose P+40% photoreceptor neuron terminals for the majority of wild-type and mutant imaging analyses, because all mutants used in this study exhibited membrane degradation defects starting at this stage (see below). Secondary effects, including an upregulation of autophagy, subsequently mask the primary endolysosomal functions and defects in sorting and degradation of cargo proteins [13, 22].

The presence of large, acidified compartments suggests that packaging of synaptic membrane cargo into degradative compartments, and possibly degradation itself, can occur locally at axon terminals. Furthermore, we were surprised that Syt1-DF may be subject to turnover and degradation before functional synapses exist. We therefore tested whether our imaging probes are faithful reporters of local degradative compartments in a series of experiments as follows.

First, we tested whether expression of either probe alters endomembrane compartments, degradation, or neuronal function. Immunohistochemical analyses indicate that neither probe alters endogenous levels of endosomes, lysosomes, or autophagosomes in either axon terminals or cell bodies based on several markers in quantitative clonal comparisons (Figures S1C–S1G); in addition, neither probe alters neuronal function based on electroretinogram recordings in adult flies (Figures S1H and S1I). Second, Syt1-DF is expressed at levels comparable to endogenous Syt1 at axon terminals (Figures S2A and S2B); similar to the probe, endogenous Syt1 is made and transported to axon terminals as early as P+10% (Figures S2C–S2F; Movie S2) and both endogenous Syt1 and the Syt1-DF probe are sorted into lysosomal compartments indistinguishably (Figures S2G–S2I). Third, we confirmed with electrophysiology, live imaging, and immunohistochemistry that C-terminally tagged Syt1-DF is sorted and degraded indistinguishably from N-terminally tagged DF-Syt1, despite being a less functional protein [33] (Figures S2J–S2N). Importantly, DF-Syt1 is less useful for our purpose, because it is a sensor for SV acidification, similar to numerous probes facing the vesicular lumen, which are prominently used to measure synaptic function and single SV exocytosis [34]. In contrast, cytoplasmically tagged Syt1-DF selectively turns red live only when sorted into a multivesicular body or autophagosome (Figure 1B). Findings were validated in fixed preparations using both Syt1 probes throughout the study. We conclude that both the myr-DF and Syt1-DF imaging probes faithfully report the local incorporation of synaptic membrane proteins into large, acidic compartments at axon terminals. Furthermore, because Syt1 has no developmental function in photoreceptor neurons [22, 35], its early turnover indicates that photoreceptor neurons activate synaptic maintenance machinery prior to synaptic function.

Degradation Starts at Axon Terminals

Fixation of red-live compartments should cause full reversion of intact DF tags to yellow fluorescence due to the reversibility of pHluorin quenching, whereas degradation of pHluorin should lead to red-fixed compartments (Figure 1C). We found that 14% of myr-DF and 8% of Syt1-DF-positive axon terminal compartments did not regain pHluorin fluorescence through fixation (Figures 2A–2E and 2G). To test whether red-fixed compartments represent late-stage degradative compartments, we performed co-labeling with the lysosomal marker Spinster and the early endosomal marker Rab5. Indeed, red-fixed compartments were 2- to 3-fold more positive for the lysosomal marker, whereas yellow-fixed compartments were 2- to 3-fold more positive for the early endosomal marker (Figures 2F and 2H). These results indicate that some pHluorin is degraded in late-stage lysosomal compartments at axon terminals. We conclude that degradation of both probes is initiated in the axon terminal, and we therefore refer to these late-stage endolysosomal compartments as "degradative compartments".

Next, we asked whether trafficking vesicles in the axon are selectively late-stage degradative compartments. Surprisingly, co-labeling of axonal trafficking vesicles with Rab5 and Spin revealed a mixture very similar to axon terminal compartments (Figures 2I–2L). These findings suggest that axonal vesicles for retrograde trafficking are not selected for their degradative state but instead can enter retrograde trafficking at any stage of maturation.

To investigate the nature of degradative compartments, we tested, in addition to Rab5 and Spin, the late endosomal marker Rab7, the recycling endosomal marker Rab11, the synaptic endosomal marker Skywalker, and the autophagosome marker Atg8 [12, 20, 36, 37]. All six markers colocalized 8%–25% with both Syt1- and myr-DF-positive compartments (Figures 2M and S3). Note that low levels of colocalization are expected for dynamically changing markers as compartments mature, e.g., conversion from Rab5 to Rab7 [38, 39]. Importantly, red-fixed compartments predominantly colocalize with degradative compartment markers Rab7 and Atg8, in addition to Spin, but not with the endosomal markers Rab5, Rab11, and Sky, corroborating the local initiation of degradation in late-stage compartments (red bars in Figure 2M). Finally, only late-stage compartments, marked by Rab7 and Atg8, exhibited significantly increased labeling of myr-DF compared to Syt1-DF, suggesting a possible difference between the two probes (Figure 2M).

Local Hub Compartments Are in Continuous Flux and Bud off Retrograde Trafficking Vesicles

To understand their different local dynamics, stability, and retrograde trafficking, we tracked Syt1-DF and myr-DF acidic

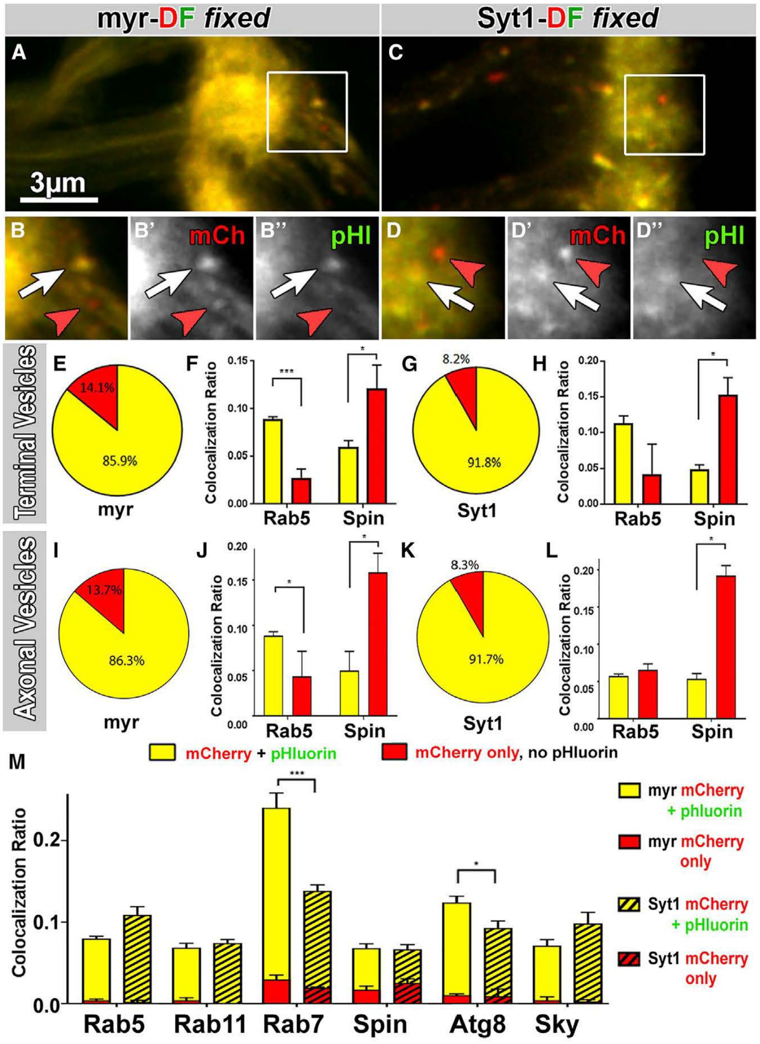

Figure 2. Degradation Starts at Axon Terminals

(A–D″) Some terminal compartments remain "red only" after fixation (red arrowheads), indicating irreversible damage of pHluorin for both myr-DF (A–B″) and Syt1-DF (C–D″). White arrows mark yellow-fixed compartments.

(E–L) Red-only compartments after fixation are late-stage degradative compartments. Pie charts show ratios of mCherry-only versus yellow terminal compartments (E and G) and axonal vesicles (I and K). Bar charts in (F), (H), (J), and (L) show colocalization ratios of yellow-fixed and red-fixed compartments separately with the early endosomal marker Rab5 and the lysosomal marker Spin (F, H, J, and L). Mean ± SEM; brain n = 15 per probe (E, G, I, and K); brain n = 3 per antibody staining (F, H, J, and L); $^{*}p < 0.05$; $^{***}p < 0.001$; unpaired t test.

(M) Colocalization of myr-DF (non-striped) and Syt1-DF (striped) compartments with markers of the endolysosomal system. Shown are ratios for yellow-fixed and red-fixed terminal hub compartments that colocalize with a given antibody divided by the total number of compartments. The yellow-fixed and red-fixed bars are stacked in the bar chart. Mean ± SEM; $^{*}p < 0.05$; $^{***}p < 0.001$; unpaired t test; brain n = 3–5 per antibody staining. See also Figure S3.

compartments live. We found that compartments of both types exhibited restricted mobility within the axon terminals but continuously exchanged membrane cargo and budded off smaller axon trafficking vesicles; we therefore termed these compartments "hubs" (Figures 3A–3J; Movie S3). Specifically, using resonant confocal microscopy, we could track individual hubs at the axon terminal in 4D with a temporal resolution of 7.5 s over the course of several hours in the case of myr-DF (Figures 3A–3C, 3L, and 3M) but typically only for 15 min in the case of the smaller Syt1-DF hubs (Figures 3F–3H). Hubs marked by either probe were locally restricted with a displacement of maximally 2 µm in 5 min (Figures 3E, 3J, and 3K) and maximally 3 µm over 5 hr for myr-DF (Figure 3L). Analysis of the 4D tracking data revealed, unexpectedly, no unequivocal *de novo* appearance or disappearance of individual hubs. Instead, both myr and Syt1 hubs exhibited frequent and balanced fusion and fission events at a rate of 2/min that resulted in continuous enlargements and splits suggestive of continuous cargo flux (Figures 3N and 3O; Table S1; Movie S3).

The budding of smaller vesicles that entered the axon for retrograde trafficking was more frequent for Syt1-DF than for myr-DF (Figures 3A, 3B, 3F, and 3G). Similar to the hubs, the axonal trafficking vesicles were exclusively red live for both probes (Figures 3H, S4A, and S4B; Movie S3). Larger axonal vesicles moved predominantly retrogradely, whereas the smallest discernible axonal vesicles moved in both directions (Figures S4A–S4F). To quantitatively analyze the net movements of axonal trafficking vesicles, we computed Markov state models. Both myr-DF- and Syt1-DF-positive axonal trafficking vesicles exhibited increasing "committor probabilities" toward the cell body, which indicate net retrograde trafficking back to the cell body (Figures 3D and 3I).

To compare the dynamics of hubs and axonal trafficking vesicles with autophagosomes, we co-expressed the autophagosome marker Atg8-mCherry with myr-GFP or Syt1-GFP. Consistent with the colocalization in fixed preparations, live imaging of these two pairs revealed that small subsets of myr-DF and (to a lesser extent) Syt1-DF indeed mark autophagosomes (Figures S4G–S4I). However, Atg8-positive autophagosomes exhibited very different dynamics compared to hub compartments: they (1) form *de novo* at axon terminals (controlled for z movement in 4D data; Movie S4) and exhibit (2) significantly lower fission/fusion rates (Figure S4J); (3) a size distribution distinct from

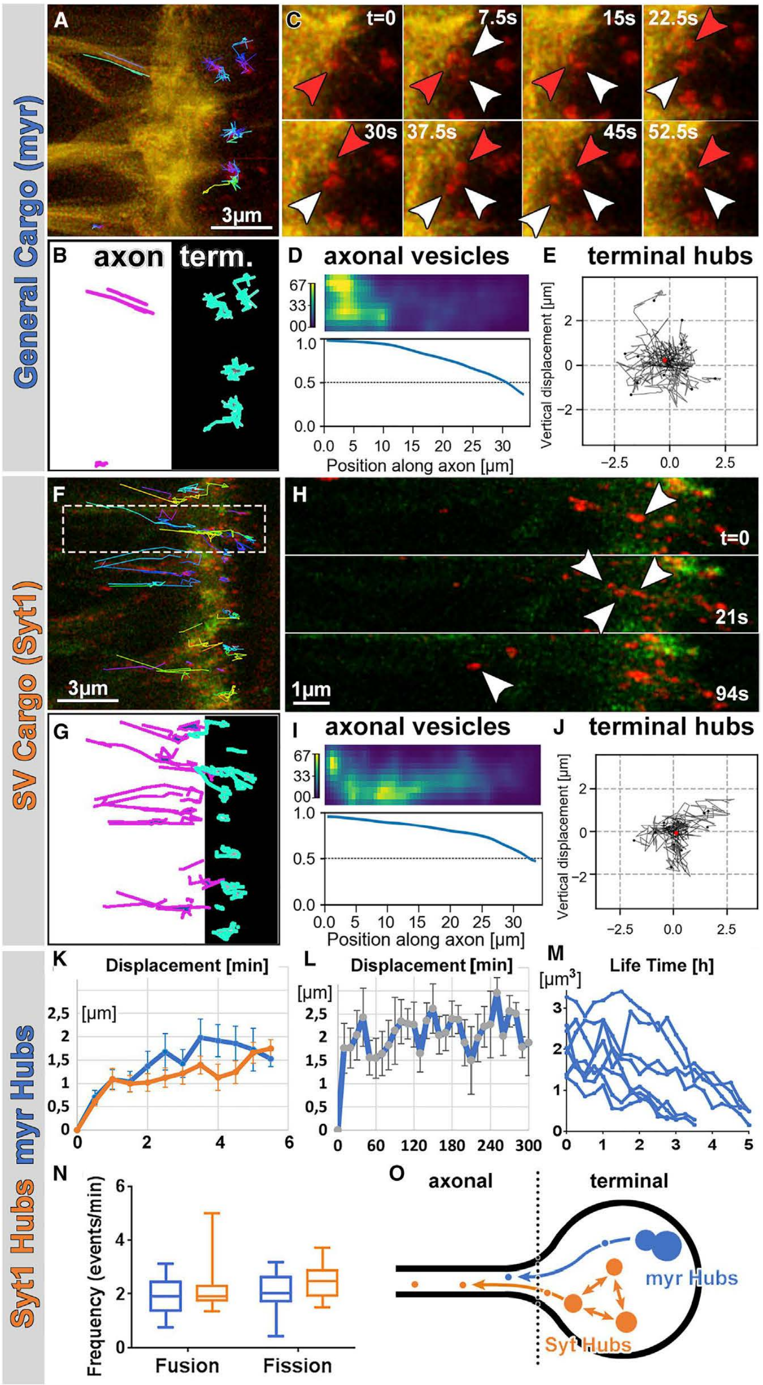

Figure 3. The Hub Compartments: Continuous Flux through Fusion, Fission, and Budding of Retrograde Trafficking Vesicles

(A, B, F, and G) 4D tracking of acidified compartments marked by myr-DF (A and B) and Syt1-DF (F and G) revealed distinct terminal hub compartments and retrogradely trafficking axonal vesicles.

(C) myr-DF-positive hubs undergo multiple fusion (red arrowheads) and fission (white arrowheads) events in seconds.

(D and I) Markov state models of axonal vesicles for myr-DF (hub n = 222; D) and Syt1-DF (hub n = 202; I) revealed high probabilities for trafficking toward the cell body (to the left) and increasing “committor probabilities” along the axon.

(E and J) Trajectories from origin of myr-DF (hub n = 12; E) and Syt1-DF (hub n = 11; J) hubs with mean displacement revealed no directed movements of hub compartments. Red dot indicates the origin of movement.

(H) Example of Syt1-DF hub compartment fission into multiple compartments, including retrograde axonal trafficking vesicle (arrowhead).

(K) Mean ± SEM displacement from origin of myr or Syt1 hubs in 6 min. Mean ± SEM; hub n = 11 per probe.

(L) Mean ± SEM displacement from origin of myr hubs over 5 hr (hub n = 9).

(M) Lifetime of myr hubs represented as volume of hubs over hours (hub n = 8).

(N) Fusion and fission frequencies of myr and Syt1 hubs. Box and whiskers plot shows 5–95 percentiles; hub n = 12–15 per probe.

(O) Schematic of hub compartment dynamics: no *de novo* appearance or disappearance but continuous flux and budding for retrograde trafficking.

See also Figure S4, Table S1, and Movies S3 and S4.

both myr-DF- and Syt1-DF-degradative compartments (Figure S4K); and (4) no budding of axonal trafficking vesicles. Most importantly, in contrast to the Syt1- and myr-containing hubs, Atg8-positive autophagosomes entered the axon directly (Movie S4). We conclude that autophagosomes are largely distinct from endolysosomal hub compartments at axon terminals.

In sum, live imaging revealed flux within a network of continuously splitting and fusing endolysosomal hubs that do not leave the axon terminals, whereas smaller, retrogradely trafficking axonal vesicles provide an exit from this “hub flux” at varying stages of endolysosomal maturity (Figures 2M and 3O; Movie S3).

Two Distinct Pools of Hub Compartments

We next probed the cargo specificity of the hubs marked by our cargo probes. Co-labeling of axon terminal hubs marked by myr-DF and Syt1-DF with a panel of SV and plasma membrane protein antibodies revealed a remarkably clear separation of markers: SV proteins, most prominently Rab3 and CSP, exhibited 6- to 8-fold more colocalization with Syt1-DF compared to myr-DF. In contrast, the t-SNARE Syx1A

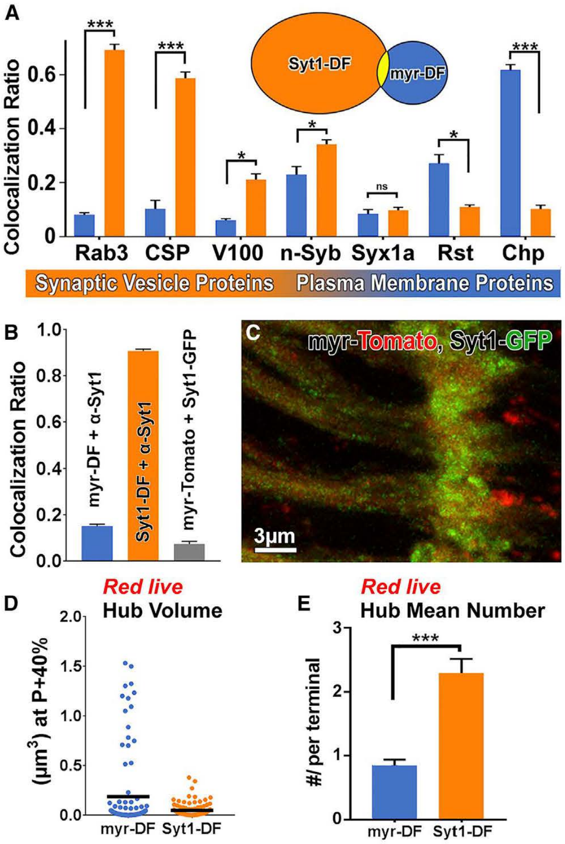

Figure 4. Two Distinct Pools of Hub Compartments

(A) Colocalization ratios of myr-DF- (blue) and Syt1-DF (orange)-marked compartments with antibody labeling against SV and plasma membrane proteins in fixed preparations reveals largely distinct compartment pools. Mean ± SEM; *$p < 0.05$; ***$p < 0.001$; unpaired t test; brain n = 3 per antibody staining.

(B) Colocalization ratios of myr-DF with anti-Syt1, Syt1-DF with anti-Syt1, and myr-Tomato with Syt-GFP. Mean ± SEM; brain n = 3 per colocalization.

(C) Co-expression of myr-Tomato and Syt1-GFP reveals distinct compartments.

(D) Volumes of acidified (red) compartments at axon terminals. Hub n = 100 per probe; black lines indicate mean values.

(E) Mean number of acidified compartments per axon terminal at P+40%. Mean ± SEM; ***$p < 0.001$; unpaired t test; brain n = 3–5 per probe.

See also Figure S5.

colocalized at low levels with both types and the non-SV plasma membrane receptors Rst and Chp colocalized 3–6 times more with myr-DF (Figures 4A, S5A, and S5B). Immunolabeling for Syt1 marked almost all Syt1-DF compartments but only 15% of myr-DF compartments (Figure 4B), indicating that most myr-DF compartments do not contain Syt1. Indeed, live co-expression of myr-Tomato and Syt1-GFP revealed <10% colocalization (Figures 4B and 4C). Quantitative analysis of the red-live axon terminal hubs marked by Syt1-DF revealed 2.5 times more compartments that were on average half the size compared to those marked by myr-DF (Figures 4D and 4E). These data indicate that myr-DF and Syt1-DF mark distinct pools of hub compartments at axon terminals. SV-specific hubs mostly exclude plasma membrane proteins.

Distinct Molecular Mechanisms Sort and Degrade Plasma Membrane Proteins and SV Proteins

As reported above, Rab7 (canonical endolysosomal degradation and autophagy) and Atg8 (autophagy) exhibited significantly increased colocalization with the plasma membrane hubs compared to SV hubs (Figure 2M). In contrast, n-Syb and V100 (NSD) exhibited increased colocalization with SV hubs compared to plasma membrane hubs (Figure 4A). These findings prompted us to probe the functional roles of Rab7, n-Syb, and V100 in the sorting and degradation of the distinct hubs. *rab7* is a ubiquitous key factor required for maturation in the endolysosomal system [38] and at least some types of autophagy [40] and the gene underlying the neuropathy Charcot-Marie-Tooth 2B [17, 23]. The vesicular ATPase component V100 and the vesicle SNARE neuronal synaptobrevin (n-Syb) are both exclusive neuronal proteins that were initially identified as SV proteins with single neuronal orthologs from worms to humans [41, 42]. In flies, V100 and n-Syb function in endolysosomal degradation, and it is this second function that leads to photoreceptor adult-onset degeneration in the mutants [20, 22]. We have previously proposed the term neuronal sort-and-degrade (NSD) for this putative neuronal branch of the endolysosomal system. The neuron-specific functions and cargo specificity of both canonical endolysosomal degradation and NSD have so far remained unknown.

To analyze cell-autonomous, cargo-specific sorting and degradation in mutant neurons, we performed live imaging in mosaic brains in which only a subset of photoreceptor neurons was mutant for *rab7*, *v100*, or *n-syb* in otherwise wild-type brains (Figures 5A–5H). In all three mutants, hub compartments were present at axon terminals, with one exception: myr-DF hub compartments were lost at axon terminals of *rab7* mutant neurons (Figures 5C and 5I). In contrast, Syt1-DF hub compartment numbers were unaltered in the *rab7* mutant and instead significantly decreased in both NSD mutants. Fusion and fission rates between hub compartments were not significantly changed for either probe in NSD mutants and equally reduced for the Syt1-DF probe and hence not likely to be contributors to the changes in hub numbers (Table S1). These surprising observations suggest that the normal formation of hub compartments containing SV cargo requires NSD but is *rab7* independent, whereas the formation of myr-DF hub compartments is *rab7* dependent but NSD independent.

To further test the cargo specificity of the two molecular mechanisms, we overexpressed *rab7*, *v100*, and *n-syb* in the presence of both probes. Overexpression of *rab7* had no significant effect on either compartment type. However, overexpression of *v100* or *n-syb* selectively affected Syt1-DF hub compartments in a manner opposite to their loss of function. myr-DF hub compartments were not affected by either NSD mutant, similar to their loss of function (Figures S6A and S6B). Finally, n-Syb knockdown in the *v100* mutant background further decreased the number of SV hubs, but not myr-DF hubs (Figures 5B, 5F, 5H, 5I, and S6C–S6J), suggesting additive cell biological functions of V100 and n-Syb that are specific to SV hubs.

Next, we assayed endolysosomal progression of both probes from early via late endosomes to lysosomes using Rab5, Rab7,

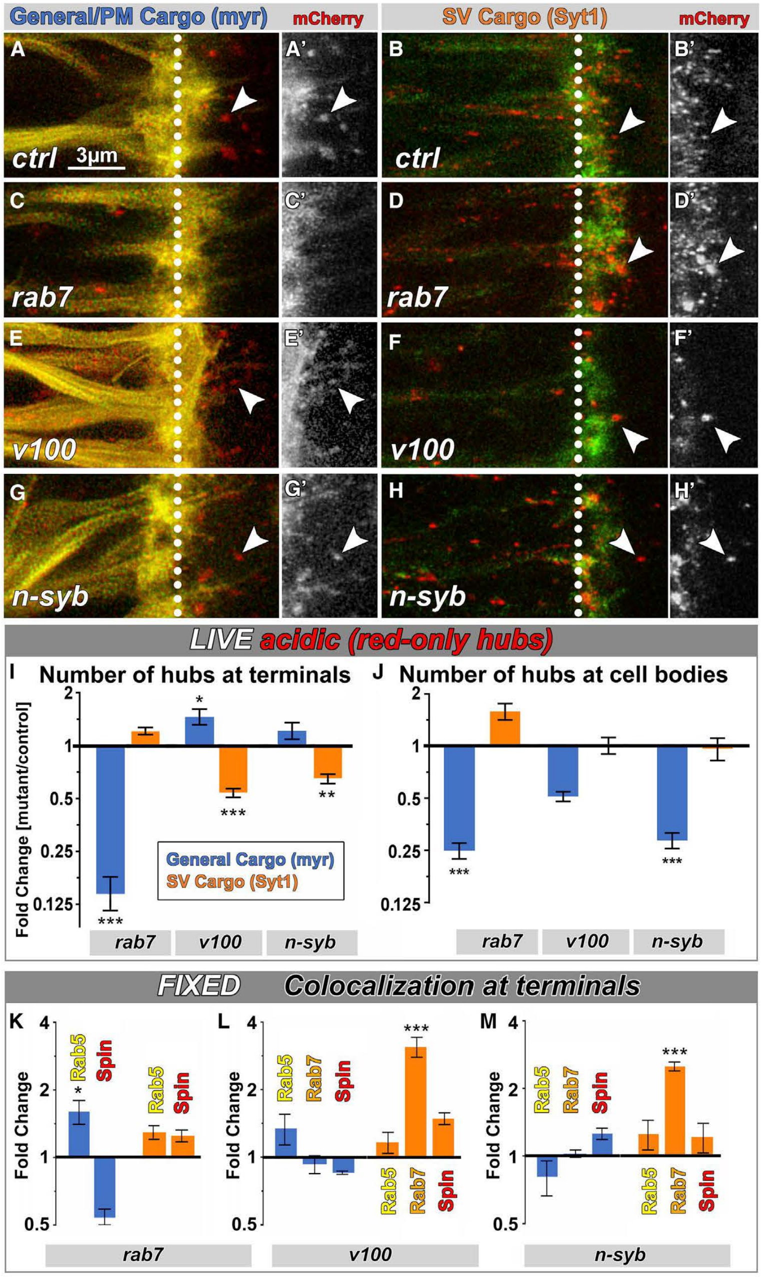

Figure 5. Distinct Molecular Mechanisms Sort and Degrade Plasma Membrane Proteins and SV Proteins

(A–H′) Live imaging of myr-DF and Syt1-DF in wild-type (A–B′), *rab7* (C–D′), *v100* (E–F′), or *nsyb* (G–H′) mutant background in P+40% photoreceptor axon terminals. Arrowheads, examples of acidic (red-only live) compartments at axon terminals. White dotted lines mark the boundaries between axon (left) and axon terminals (right).

(I and J) Relative number of degradative compartments in mutants from live-imaging data in axon terminals (I) and cell bodies (J). Mean ± SEM; $^{*}p < 0.05$; $^{**}p < 0.01$; $^{***}p < 0.001$; unpaired t test; brain n = 4–8 per experimental condition.

(K–M) Relative colocalization ratio changes of yellow-fixed compartments with early endosomes (Rab5), late endosomes (Rab7), and lysosomes (Spin) in *rab7* (K), *v100* (L), and *nSyb* (M) mutant axon terminals. Mean ± SEM; $^{*}p < 0.05$; $^{***}p < 0.001$; brain n = 3 per experimental condition; unpaired t test.

See also Figure S6.

and Spin co-labelings in fixed preparations. As shown in Figure 5K, loss of *rab7* leads to an increase of myr-DF in Rab5-positive compartments and a corresponding reduction in lysosomal compartments, consistent with the known role of Rab7 in endosomal maturation. In contrast, Syt1-DF exhibited no such changes in the *rab7* mutant, corroborating that sorting of Syt1-DF into SV hubs at axon terminals is *rab7* independent (Figure 5K). The opposite cargo specificity was observed in the two NSD mutants *v100* and *n-syb*: whereas myr-DF exhibited no significant alterations in either NSD mutant, the Syt1-DF probe accumulated 3-fold in late endosomal (Rab7-positive) compartments in both NSD mutants (Figures 5L and 5M), suggesting that degradation of Syt1-DF, but not myr-DF, is NSD dependent. Note that Syt1-DF accumulates in a Rab7-positive compartment, even though sorting and maturation of Syt1-DF are *rab7* independent, consistent with a known further role of Rab7 in lysosomal degradation based on interaction with the homotypic fusion and vacuole protein sorting (HOPS) complex [43]. Indeed, we observed an increase of SV hub volume in the *rab7* mutant (Figure S6K) as well as in a mutant for the HOPS complex component Vps33A/Carnation (*car*) (Figures S6L–S6Q), consistent with impaired degradation. In contrast to rab7, loss of *car* affects both probes similarly, effectively singling out a late common role in degradation with no effects on sorting or maturation of either hub compartments (Figures S6K, S6P, and S6Q). We conclude that sorting of SV cargo depends only on NSD (and is Rab7 independent) and sorting of general plasma membrane cargo depends only on Rab7 (and is NSD independent).

CP1 Is a Protease Specific to SV Hubs

Local degradation requires the delivery of proteases to the hub compartments at axon terminals. In *Drosophila* photoreceptors, the Cathepsin-L-like protease CP1 mediates neurodegeneration

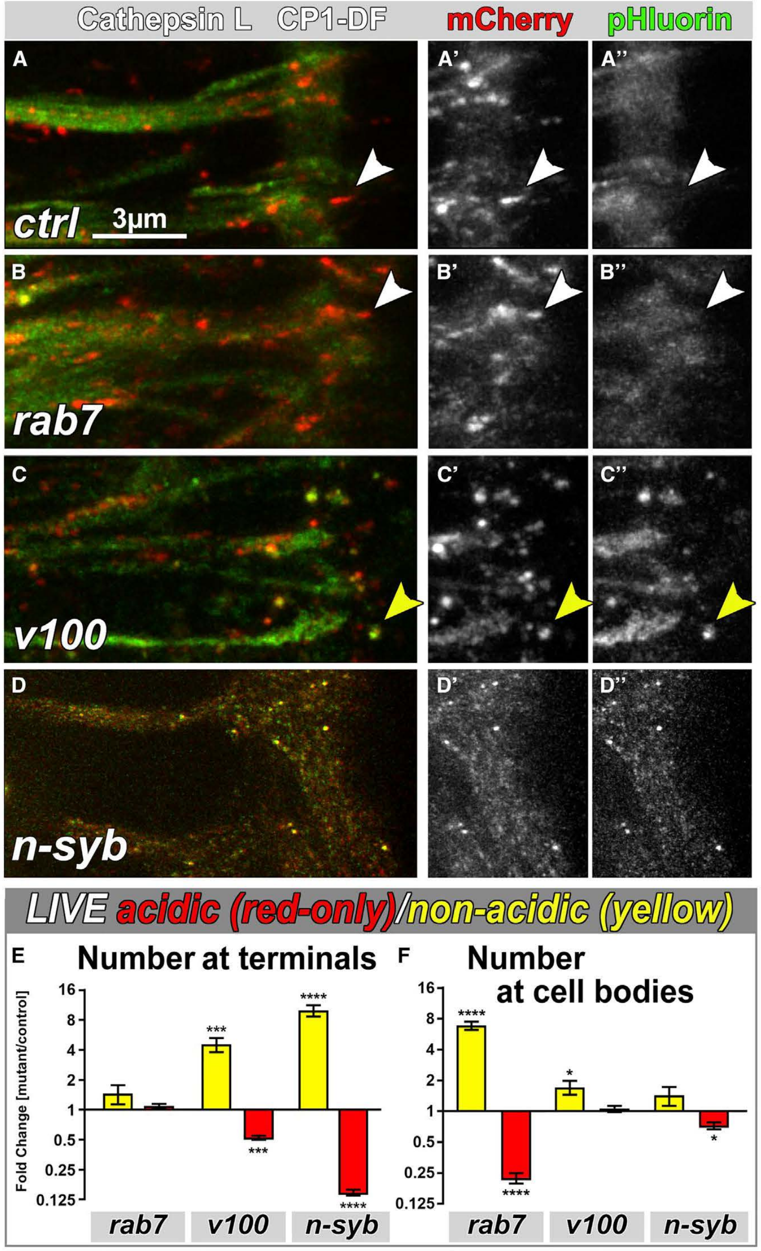

Figure 6. The Cathepsin-L-like Protease CP1 Is Specific to SV Hubs

(A–D″) Live imaging of CP1-DF in wild-type (A–A″), *rab7* (B–B″), *v100* (C–C″), or *nsyb* (D–D″) mutant axon terminals. White arrowhead, acidic (red-only live) compartment; yellow arrowhead, non-acidic (yellow live) compartment.

(E and F) Relative number of acidified (red) or non-acidified (yellow) CP1-DF-positive compartments at axon terminals (E) and cell bodies (F). Mean ± SEM; *$p < 0.05$; ***$p < 0.001$; ****$p < 0.0001$; brain n = 3 per experimental condition; unpaired t test. See also Figure S7.

[44]. To test whether CP1 is a protease that functions in one or both types of hub compartments, we generated a CP1-DF probe for live imaging. CP1-DF is incorporated into red-live hub compartments at axon terminals that appear in size and number more similar to Syt1-DF than myr-DF (Figures 6A, S7A, and S7B). Co-labeling of CP1-DF-positive hub compartments with SV and plasma membrane markers in fixed preparations appeared similar to SV hubs (Figures S7C and S5). As shown in Figures 6A–6D, CP1-DF labeling of acidic compartments is selectively affected in the NSD mutants but unaltered in *rab7*. Because there are almost no myr-positive hubs in *rab7* mutant axon terminals, CP1-DF may specifically supply SV hubs. Indeed, in *n-syb* mutant terminals, CP1-DF labeling of acidified compartments is completely lost and CP1-DF appears trapped in numerous non-acidified, smaller vesicles, indicating a complete failure to reach hub compartments (Figures 6D and 6E). In contrast, in the *v100* mutant, CP1-DF does reach hub compartments, but around 50% remain non-acidified, indicating that *v100* is partially required for acidification of SV hubs (Figures 6C, 6E, and S7D). Correspondingly, n-Syb knockdown in the *v100* mutant background caused an additive effect with both the small yellow CP1-delivery vesicles as well as larger non-acidified hubs (Figures S7E–S7I), i.e., a combination of the *nsyb* and *v100* mutant phenotypes (Figure 6). We conclude that CP1 is sorted specifically into hub compartments of the SV pathway at axon terminals via an *n-syb*-dependent and *rab7*-independent mechanism (Figure 7).

Cargo Separation Occurs Specifically at the Axon Terminal and Not in the Cell Body

Finally, we compared the molecularly distinct endolysosomal sorting of plasma membrane and SV cargo between the cell body and the axon terminal. In cell bodies, myr-DF and Syt1-DF colocalized more similarly with all endolysosomal markers (Figure S6R) as well as all SV markers (Figure S6S). Hence, both probes mostly marked common, mixed compartments in the cell body. In contrast to the axon terminal, the NSD mutants *v100* and *n-syb* did not specifically affect SV proteins in the cell body (Figures 5J and S6T). Instead, *v100* and *n-syb* mutants exhibited a reduction in the numbers of myr-DF compartments in the cell body and no changes to compartments containing Syt1-DF (Figure 5J). Also opposite to phenotypes at axon terminals, CP1-DF

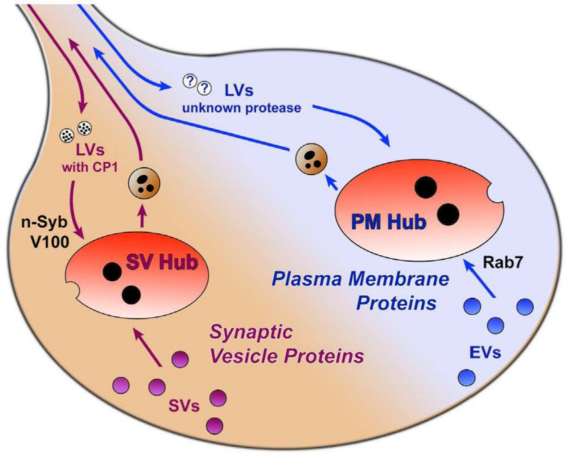

Figure 7. Model: Two Parallel Membrane Degradation Mechanisms at Axon Terminals

Axon terminals harbor at least two types of mostly non-overlapping endolysosomal hub compartments: one for synaptic vesicle (SV) proteins and one for general plasma membrane (PM) proteins. Maturation of SV hubs, but not PM hubs, depends on the n-Syb-dependent delivery of the protease CP1 and acidification by neuronal vATPase component V100. Maturation of PM hubs, but not SV hubs, depends on the small Rab7 GTPase. EVs, endosomal vesicles; LVs, lysosomal vesicles.

accumulated in non-acidified compartments in cell bodies mutant for *rab7*, but not *v100* and *n-syb* (Figures 6E, 6F, and S7J). We conclude that the *rab7*- and NSD-dependent mechanisms sort and degrade in a cargo-specific manner exclusively at the axon terminal. In contrast, the same molecules that function in separate pathways at axon terminals are found in mixed membrane degradation compartments in the cell bodies of the same neuron (Figures S6R, S6S, and S7K). Hence, sorting of SV proteins and plasma membrane proteins for degradation in separate endolysosomal pathways occurs locally at axon terminals (Figure 7).

DISCUSSION

In this study, we investigated neuronal membrane protein degradation *in vivo* from the perspective of different cargo probes and unbiased with respect to sorting and degradation mechanisms. Our key findings are (1) the direct live observation of membrane protein degradation at axon terminals in large, acidified hubs: acidic, degradative endolysosomal compartments that undergo continuous flux and bud of retrograde transport vesicles and (2) the cargo-specific sorting of SV and plasma membrane proteins into different hubs via two molecularly distinct pathways at axon terminals.

"Hub Flux" and Membrane Protein Turnover

It is surprising that the only clearly discernible compartments at axon terminals are red live, large, acidified, and spatiotemporally relatively stable endolysosomal compartments. We named these compartments hubs because of their continuous fission, fusion, and budding of smaller retrograde trafficking vesicles. We never observed appearance or disappearance of an entire hub but only the formation of hubs by fusion of several smaller vesicles and splitting into multiple smaller compartments that underwent renewed cycles of fusion. These dynamics are reflected in hub composition and maturation: at any point in time, some hubs are marked by early endosomal markers and contain undegraded probes, whereas others are marked by lysosomal markers and contain partially degraded probes.

How does this "hub flux" contribute to the sorting and degradation of dysfunctional membrane proteins? A key insight comes from the characterization of retrograde trafficking vesicles: the axonal vesicles exhibit the same composition and a mix of early and late markers and degraded and undegraded probes. These observations are most straightforwardly explained with random mixing of hubs and random budding of axonal vesicles, irrespective of their maturation stage. In this model, sorting into hubs carries a probabilistic chance of degradation that increases with time (either in hubs or in retrograde trafficking vesicles). Sorting into hubs ensures degradation if membrane proteins cannot be recycled back into the axon terminal; alternatively, degradation and recycling may both be probabilistic. The latter would imply that not only dysfunctional proteins are sorted into hubs. Both mechanisms could ensure a pool of functional synaptic proteins that increases with the amount of endolysosomal flux, as previously observed for the Skywalker/Rab35 mechanism [12, 19].

How SV membrane proteins are specifically sorted into SV hubs is unclear. Because sorting of Syt1-DF into SV hubs is Rab7 independent, SV hub maturation bypasses the requirement for Rab5-to-Rab7 conversion [39]. Neither n-Syb (a vesicle SNARE and membrane fusion factor) nor V100 (part of a proton pump) are required for the continuous fusion and fission of SV hubs. However, the reduced axon terminal numbers of SV hubs are consistent with roles in the sorting of SVs to SV hubs. Different SV retrieval mechanisms, including ultrafast endocytosis, clathrin-mediated endocytosis, and bulk endocytosis [45, 46], may account for different mechanisms and routes to local degradative hubs. Preassembled plasma membrane cargo complexes may play a role in promoting the different endocytic routes [46]. Our colocalization measurements revealed a distinction between two membrane degradation mechanisms with enrichments of SV proteins versus plasma membrane proteins between 3- and 8-fold, but not a 100% separation. Hence, if protein complexes facilitate sorting into a specific endocytic pathway or hub compartments, they may do so in a probabilistic fashion.

Continuous flux is a hallmark of endolysosomal compartments and results in low colocalization ratios with dynamically changing molecular markers and difficulties to unambiguously identify a specific compartment at any point in time. Our live observation of dynamic hubs as sorting and degradation stations at axon terminals was only made possible by their integrity over time and may provide an inroad to the study of distinct, cargo-specific mechanisms that keep neurons and their synaptic terminals functional.

Hubs in the Context of Known Membrane Sorting and Degradation Mechanisms

We observed constitutive turnover of SV hubs prior to synaptogenesis and neuronal activity. In contrast, previous work on SV "rejuvenation" focused on turnover that increases in response to neuronal activity [12, 19]. Colocalization of axon terminal hubs with the Rab35 GAP Skywalker (Sky) revealed equal overlap with both hub types. This could indicate an intersection of different endolysosomal pathways; alternatively, Sky may only temporarily localize to hubs depending on their maturation stage. We favor the second possibility, because the early endosomal Rab5 and the lysosomal marker Spin exhibit similar colocalization ratios and all known endolysosomal markers depend in some way on the maturation stage [38, 47]. Our colocalization implies Sky in both the canonical and SV pathway. Consistent with this, *rab7* affects Sky-dependent rejuvenation and the *sky* mutant affects the turnover of an n-Syb imaging probe [11].

Autophagy similarly intersects with axon terminal hub compartments based on colocalization with Atg8, albeit this colocalization is significantly higher for the *rab7*-dependent general PM hubs than for the SV hubs. However, the hubs and axonal trafficking vesicles are distinct from autophagosomes based on their dynamics: Atg8-positive compartments are not part of the "hub flux," emerge *de novo*, and directly enter the axon without prior fission. It is possible that autophagosomes can engulf hub compartments and thus provide an alternative degradative exit to budding of retrograde trafficking vesicles. A Rab26-dependent mechanism was recently proposed for the sorting of SVs to pre-autophagosomal compartments prior to Atg8 recruitment, which may represent a similar hub compartment [48].

Cathepsin L: A Protease with Cargo Specificity

In this study, we showed that cathepsin-L-like protease CP1 has specificity for the SV hubs at axon terminals. This finding is consistent with several cystein cathepsins that have been characterized for their tissue-specific expression [49]. In mammalian systems, cathepsin L selectively degrades polyglutamine (polyQ)-containing proteins, but not other types of aggregation-prone proteins lacking polyQ [50]. In HeLa and Huh-7 cells, cathepsin L was reported to degrade autophagosomal membrane markers, but not proteins in the lumen of autophagosomes [51]. In contrast, the major histocompatibility complex (MHC) class-II-associated invariant chain is specifically degraded by cathepsin S, but not cathepsin L, in CD4$^+$ T cells [52]. Our characterization of cargo-specific membrane degradation machinery with a specific protease raises the question to what extent different membrane degradation mechanisms are characterized and may require specific proteases.

STAR★METHODS

Detailed methods are provided in the online version of this paper and include the following:

- KEY RESOURCES TABLE
- CONTACT FOR REAGENT AND RESOURCE SHARING
- EXPERIMENTAL MODEL AND SUBJECT DETAILS
  - ○ Fly husbandry
  - ○ Flies
- METHOD DETAILS
  - ○ Brain culture and live imaging
  - ○ Immunohistochemistry
  - ○ Image processing
  - ○ Electroretinogram (ERG) Recordings
- QUANTIFICATION AND STATISTICAL ANALYSIS
  - ○ Quantification and Statistical Analysis
  - ○ Markov State Modeling

SUPPLEMENTAL INFORMATION

Supplemental Information includes seven figures, one table, and four movies and can be found with this article online at https://doi.org/10.1016/j.cub.2018.02.032.

ACKNOWLEDGMENTS

We would like to thank all members of the Hiesinger lab, Volker Haucke, Bettina Winckler, Mathias Wernet, Bassem Hassan, Ilya Bezprozvanny, Craig Garner, and Stephan Sigrist for helpful discussions. We further thank Patrik Verstreken, Sergio Grinstein, Helmut Kramer, and the Bloomington Stock Center in Indiana for reagents. This work was supported by the Deutsche Forschungsgemeinschaft (SFB958 and SFB/TRR186), NeuroCure Cluster Berlin, NIH (RO1EY018884 and RO1EY023333), and Muscular Dystrophy Association of the USA to P.R.H. E.J.J. was supported by the NIH (T32 NS069562 and F31 NS084774) and DFG (SFB958).

AUTHOR CONTRIBUTIONS

E.J.J., F.R.K., M.N.O., and P.R.H. designed the experiments and wrote the paper. L.S.B., D.E., and H.W. helped with experiments and data analysis. M.O. and S.P. provided the Markov state model analyses.

DECLARATION OF INTERESTS

The authors declare no competing interests.

Received: October 3, 2017
Revised: January 24, 2018
Accepted: February 14, 2018
Published: March 15, 2018

REFERENCES

1. Arendt, T. (2009). Synaptic degeneration in Alzheimer's disease. Acta Neuropathol. *118*, 167–179.
2. Shankar, G.M., and Walsh, D.M. (2009). Alzheimer's disease: synaptic dysfunction and Abeta. Mol. Neurodegener. *4*, 48.
3. Wong, E., and Cuervo, A.M. (2010). Autophagy gone awry in neurodegenerative diseases. Nat. Neurosci. *13*, 805–811.
4. Morales, I., Sanchez, A., Rodriguez-Sabate, C., and Rodriguez, M. (2015). The degeneration of dopaminergic synapses in Parkinson's disease: a selective animal model. Behav. Brain Res. *289*, 19–28.
5. Bezprozvanny, I., and Hiesinger, P.R. (2013). The synaptic maintenance problem: membrane recycling, Ca2+ homeostasis and late onset degeneration. Mol. Neurodegener. *8*, 23.
6. Wang, Y.C., Lauwers, E., and Verstreken, P. (2017). Presynaptic protein homeostasis and neuronal function. Curr. Opin. Genet. Dev. *44*, 38–46.
7. Maday, S., and Holzbaur, E.L. (2012). Autophagosome assembly and cargo capture in the distal axon. Autophagy *8*, 858–860.
8. Maday, S., and Holzbaur, E.L. (2014). Autophagosome biogenesis in primary neurons follows an ordered and spatially regulated pathway. Dev. Cell *30*, 71–85.
9. Maday, S., and Holzbaur, E.L. (2016). Compartment-specific regulation of autophagy in primary neurons. J. Neurosci. *36*, 5933–5945.
10. Maday, S., Wallace, K.E., and Holzbaur, E.L. (2012). Autophagosomes initiate distally and mature during transport toward the cell soma in primary neurons. J. Cell Biol. *196*, 407–417.

11. Fernandes, A.C., Uytterhoeven, V., Kuenen, S., Wang, Y.C., Slabbaert, J.R., Swerts, J., Kasprowicz, J., Aerts, S., and Verstreken, P. (2014). Reduced synaptic vesicle protein degradation at lysosomes curbs TBC1D24/sky-induced neurodegeneration. J. Cell Biol. *207*, 453–462.
12. Uytterhoeven, V., Kuenen, S., Kasprowicz, J., Miskiewicz, K., and Verstreken, P. (2011). Loss of skywalker reveals synaptic endosomes as sorting stations for synaptic vesicle proteins. Cell *145*, 117–132.
13. Wang, D., Chan, C.C., Cherry, S., and Hiesinger, P.R. (2013). Membrane trafficking in neuronal maintenance and degeneration. Cell. Mol. Life Sci. *70*, 2919–2934.
14. Cai, Q., Lu, L., Tian, J.H., Zhu, Y.B., Qiao, H., and Sheng, Z.H. (2010). Snapin-regulated late endosomal transport is critical for efficient autophagy-lysosomal function in neurons. Neuron *68*, 73–86.
15. Lloyd, T.E., Machamer, J., O'Hara, K., Kim, J.H., Collins, S.E., Wong, M.Y., Sahin, B., Imlach, W., Yang, Y., Levitan, E.S., et al. (2012). The p150(Glued) CAP-Gly domain regulates initiation of retrograde transport at synaptic termini. Neuron *74*, 344–360.
16. Jin, E.J., Kiral, F.R., and Hiesinger, P.R. (2017). The where, what, and when of membrane protein degradation in neurons. Dev. Neurobiol. Published online September 7, 2018. https://doi.org/10.1002/dneu.22534.
17. Cherry, S., Jin, E.J., Ozel, M.N., Lu, Z., Agi, E., Wang, D., Jung, W.H., Epstein, D., Meinertzhagen, I.A., Chan, C.C., and Hiesinger, P.R. (2013). Charcot-Marie-Tooth 2B mutations in rab7 cause dosage-dependent neurodegeneration due to partial loss of function. eLife *2*, e01064.
18. Deinhardt, K., Salinas, S., Verastegui, C., Watson, R., Worth, D., Hanrahan, S., Bucci, C., and Schiavo, G. (2006). Rab5 and Rab7 control endocytic sorting along the axonal retrograde transport pathway. Neuron *52*, 293–305.
19. Sheehan, P., Zhu, M., Beskow, A., Vollmer, C., and Waites, C.L. (2016). Activity-dependent degradation of synaptic vesicle proteins requires Rab35 and the ESCRT pathway. J. Neurosci. *36*, 8668–8686.
20. Williamson, W.R., Wang, D., Haberman, A.S., and Hiesinger, P.R. (2010). A dual function of V0-ATPase a1 provides an endolysosomal degradation mechanism in Drosophila melanogaster photoreceptors. J. Cell Biol. *189*, 885–899.
21. Williamson, W.R., Yang, T., Terman, J.R., and Hiesinger, P.R. (2010). Guidance receptor degradation is required for neuronal connectivity in the Drosophila nervous system. PLoS Biol. *8*, e1000553.
22. Haberman, A., Williamson, W.R., Epstein, D., Wang, D., Rina, S., Meinertzhagen, I.A., and Hiesinger, P.R. (2012). The synaptic vesicle SNARE neuronal Synaptobrevin promotes endolysosomal degradation and prevents neurodegeneration. J. Cell Biol. *196*, 261–276.
23. Verhoeven, K., De Jonghe, P., Coen, K., Verpoorten, N., Auer-Grumbach, M., Kwon, J.M., FitzPatrick, D., Schmedding, E., De Vriendt, E., Jacobs, A., et al. (2003). Mutations in the small GTP-ase late endosomal protein RAB7 cause Charcot-Marie-Tooth type 2B neuropathy. Am. J. Hum. Genet. *72*, 722–727.
24. Hara, T., Nakamura, K., Matsui, M., Yamamoto, A., Nakahara, Y., Suzuki-Migishima, R., Yokoyama, M., Mishima, K., Saito, I., Okano, H., and Mizushima, N. (2006). Suppression of basal autophagy in neural cells causes neurodegenerative disease in mice. Nature *441*, 885–889.
25. Komatsu, M., Waguri, S., Chiba, T., Murata, S., Iwata, J., Tanida, I., Ueno, T., Koike, M., Uchiyama, Y., Kominami, E., and Tanaka, K. (2006). Loss of autophagy in the central nervous system causes neurodegeneration in mice. Nature *441*, 880–884.
26. Vanhauwaert, R., Kuenen, S., Masius, R., Bademosi, A., Manetsberger, J., Schoovaerts, N., Bounti, L., Gontcharenko, S., Swerts, J., Vilain, S., et al. (2017). The SAC1 domain in synaptojanin is required for autophagosome maturation at presynaptic terminals. EMBO J. *36*, 1392–1411.
27. Okerlund, N.D., Schneider, K., Leal-Ortiz, S., Montenegro-Venegas, C., Kim, S.A., Garner, L.C., Gundelfinger, E.D., Reimer, R.J., and Garner, C.C. (2017). Bassoon controls presynaptic autophagy through Atg5. Neuron *93*, 897–913.e7.
28. Goo, M.S., Sancho, L., Slepak, N., Boassa, D., Deerinck, T.J., Ellisman, M.H., Bloodgood, B.L., and Patrick, G.N. (2017). Activity-dependent trafficking of lysosomes in dendrites and dendritic spines. J. Cell Biol. *216*, 2499–2513.
29. Özel, M.N., Langen, M., Hassan, B.A., and Hiesinger, P.R. (2015). Filopodial dynamics and growth cone stabilization in Drosophila visual circuit development. eLife *4*, e10721.
30. Prosser, D.C., Whitworth, K., and Wendland, B. (2010). Quantitative analysis of endocytosis with cytoplasmic pHluorin chimeras. Traffic *11*, 1141–1150.
31. Filimonenko, M., Stuffers, S., Raiborg, C., Yamamoto, A., Malerød, L., Fisher, E.M., Isaacs, A., Brech, A., Stenmark, H., and Simonsen, A. (2007). Functional multivesicular bodies are required for autophagic clearance of protein aggregates associated with neurodegenerative disease. J. Cell Biol. *179*, 485–500.
32. Brose, N., Petrenko, A.G., Südhof, T.C., and Jahn, R. (1992). Synaptotagmin: a calcium sensor on the synaptic vesicle surface. Science *256*, 1021–1025.
33. Han, W., Rhee, J.S., Maximov, A., Lin, W., Hammer, R.E., Rosenmund, C., and Südhof, T.C. (2005). C-terminal ECFP fusion impairs synaptotagmin 1 function: crowding out synaptotagmin 1. J. Biol. Chem. *280*, 5089–5100.
34. Kavalali, E.T., and Jorgensen, E.M. (2014). Visualizing presynaptic function. Nat. Neurosci. *17*, 10–16.
35. Stowers, R.S., and Schwarz, T.L. (1999). A genetic method for generating Drosophila eyes composed exclusively of mitotic clones of a single genotype. Genetics *152*, 1631–1639.
36. Chan, C.C., Scoggin, S., Wang, D., Cherry, S., Dembo, T., Greenberg, B., Jin, E.J., Kuey, C., Lopez, A., Mehta, S.Q., et al. (2011). Systematic discovery of Rab GTPases with synaptic functions in Drosophila. Curr. Biol. *21*, 1704–1715.
37. Sweeney, S.T., and Davis, G.W. (2002). Unrestricted synaptic growth in spinster-a late endosomal protein implicated in TGF-beta-mediated synaptic growth regulation. Neuron *36*, 403–416.
38. Huotari, J., and Helenius, A. (2011). Endosome maturation. EMBO J. *30*, 3481–3500.
39. Rink, J., Ghigo, E., Kalaidzidis, Y., and Zerial, M. (2005). Rab conversion as a mechanism of progression from early to late endosomes. Cell *122*, 735–749.
40. Jäger, S., Bucci, C., Tanida, I., Ueno, T., Kominami, E., Saftig, P., and Eskelinen, E.L. (2004). Role for Rab7 in maturation of late autophagic vacuoles. J. Cell Sci. *117*, 4837–4848.
41. Perin, M.S., Fried, V.A., Stone, D.K., Xie, X.S., and Südhof, T.C. (1991). Structure of the 116-kDa polypeptide of the clathrin-coated vesicle/synaptic vesicle proton pump. J. Biol. Chem. *266*, 3877–3881.
42. Schoch, S., Deák, F., Königstorfer, A., Mozhayeva, M., Sara, Y., Südhof, T.C., and Kavalali, E.T. (2001). SNARE function analyzed in synaptobrevin/VAMP knockout mice. Science *294*, 1117–1122.
43. Balderhaar, H.J., and Ungermann, C. (2013). CORVET and HOPS tethering complexes - coordinators of endosome and lysosome fusion. J. Cell Sci. *126*, 1307–1316.
44. Kinser, R.D., and Dolph, P.J. (2012). Cathepsin proteases mediate photoreceptor cell degeneration in Drosophila. Neurobiol. Dis. *46*, 655–662.
45. Kononenko, N.L., Puchkov, D., Classen, G.A., Walter, A.M., Pechstein, A., Sawade, L., Kaempf, N., Trimbuch, T., Lorenz, D., Rosenmund, C., et al. (2014). Clathrin/AP-2 mediate synaptic vesicle reformation from endosome-like vacuoles but are not essential for membrane retrieval at central synapses. Neuron *82*, 981–988.
46. Cousin, M.A. (2017). Integration of synaptic vesicle cargo retrieval with endocytosis at central nerve terminals. Front. Cell. Neurosci. *11*, 234.
47. Hyttinen, J.M., Niittykoski, M., Salminen, A., and Kaarniranta, K. (2013). Maturation of autophagosomes and endosomes: a key role for Rab7. Biochim. Biophys. Acta *1833*, 503–510.

48. Binotti, B., Pavlos, N.J., Riedel, D., Wenzel, D., Vorbrüggen, G., Schalk, A.M., Kühnel, K., Boyken, J., Erck, C., Martens, H., et al. (2015). The GTPase Rab26 links synaptic vesicles to the autophagy pathway. eLife *4*, e05597.

49. Turk, V., Stoka, V., Vasiljeva, O., Renko, M., Sun, T., Turk, B., and Turk, D. (2012). Cysteine cathepsins: from structure, function and regulation to new frontiers. Biochim. Biophys. Acta *1824*, 68–88.

50. Bhutani, N., Piccirillo, R., Hourez, R., Venkatraman, P., and Goldberg, A.L. (2012). Cathepsins L and Z are critical in degrading polyglutamine-containing proteins within lysosomes. J. Biol. Chem. *287*, 17471–17482.

51. Ueno, T., and Takahashi, K. (2009). A cathepsin L-specific inhibitor preferentially inhibits degradation of autophagosomal LC3 and GABARAP in HeLa and Huh-7 cells. Autophagy *5*, 878–879.

52. Bania, J., Gatti, E., Lelouard, H., David, A., Cappello, F., Weber, E., Camosseto, V., and Pierre, P. (2003). Human cathepsin S, but not cathepsin L, degrades efficiently MHC class II-associated invariant chain in nonprofessional APCs. Proc. Natl. Acad. Sci. USA *100*, 6664–6669.

53. Chinchore, Y., Mitra, A., and Dolph, P.J. (2009). Accumulation of rhodopsin in late endosomes triggers photoreceptor cell degeneration. PLoS Genet. *5*, e1000377.

54. Graf, E.R., Daniels, R.W., Burgess, R.W., Schwarz, T.L., and DiAntonio, A. (2009). Rab3 dynamically controls protein composition at active zones. Neuron *64*, 663–677.

55. Hiesinger, P.R., Fayyazuddin, A., Mehta, S.Q., Rosenmund, T., Schulze, K.L., Zhai, R.G., Verstreken, P., Cao, Y., Zhou, Y., Kunz, J., and Bellen, H.J. (2005). The v-ATPase V0 subunit a1 is required for a late step in synaptic vesicle exocytosis in Drosophila. Cell *121*, 607–620.

56. Wu, M.N., Fergestad, T., Lloyd, T.E., He, Y., Broadie, K., and Bellen, H.J. (1999). Syntaxin 1A interacts with multiple exocytic proteins to regulate neurotransmitter release in vivo. Neuron *23*, 593–605.

57. Deitcher, D.L., Ueda, A., Stewart, B.A., Burgess, R.W., Kidokoro, Y., and Schwarz, T.L. (1998). Distinct requirements for evoked and spontaneous release of neurotransmitter are revealed by mutations in the Drosophila gene neuronal-synaptobrevin. J. Neurosci. *18*, 2028–2039.

58. DiAntonio, A., Parfitt, K.D., and Schwarz, T.L. (1993). Synaptic transmission persists in synaptotagmin mutants of Drosophila. Cell *73*, 1281–1290.

59. Bischof, J., Maeda, R.K., Hediger, M., Karch, F., and Basler, K. (2007). An optimized transgenesis system for Drosophila using germ-line-specific phiC31 integrases. Proc. Natl. Acad. Sci. USA *104*, 3312–3317.

60. Chotard, C., Leung, W., and Salecker, I. (2005). glial cells missing and gcm2 cell autonomously regulate both glial and neuronal development in the visual system of Drosophila. Neuron *48*, 237–251.

61. Mehta, S.Q., Hiesinger, P.R., Beronja, S., Zhai, R.G., Schulze, K.L., Verstreken, P., Cao, Y., Zhou, Y., Tepass, U., Crair, M.C., and Bellen, H.J. (2005). Mutations in Drosophila sec15 reveal a function in neuronal targeting for a subset of exocyst components. Neuron *46*, 219–232.

62. Rigort, A., Günther, D., Hegerl, R., Baum, D., Weber, B., Prohaska, S., Medalia, O., Baumeister, W., and Hege, H.C. (2012). Automated segmentation of electron tomograms for a quantitative description of actin filament networks. J. Struct. Biol. *177*, 135–144.

63. Weber, B., Greenan, G., Prohaska, S., Baum, D., Hege, H.C., Müller-Reichert, T., Hyman, A.A., and Verbavatz, J.M. (2012). Automated tracing of microtubules in electron tomograms of plastic embedded samples of Caenorhabditis elegans embryos. J. Struct. Biol. *178*, 129–138.

64. Scherer, M.K., Trendelkamp-Schroer, B., Paul, F., Pérez-Hernández, G., Hoffmann, M., Plattner, N., Wehmeyer, C., Prinz, J.H., and Noé, F. (2015). PyEMMA 2: a software package for estimation, validation, and analysis of Markov models. J. Chem. Theory Comput. *11*, 5525–5542.

65. Metzner, P., Schütte, C., and Vanden-Eijnden, E. (2009). Transition path theory for Markov jump processes. Multiscale Model. Simul. *7*, 1192–1219.

STAR★METHODS

KEY RESOURCES TABLE

REAGENT or RESOURCE	SOURCE	IDENTIFIER
Antibodies		
rabbit anti-Rab5	Abcam	ab31261, RRID: AB_882240
rabbit anti-Rab7	Gift from Patrick Dolph [53]	N/A
mouse anti-Rab11	BD Transduction Laboratories	Clone 47, RRID: AB_397983
rabbit anti-Syt1	Developmental Studies Hybridoma Bank (DSHB)	3H2 2D7, RRID: AB_528483
rabbit anti-GABARAP+GABARAPL1+GABARAPL2 (ATG8)	Abcam	ab109364, RRID: AB_10861928
guinea pig anti-Spin	Gift from Sean Sweeney [37]	N/A
rat anti-Sky	Gift from Patrik Verstreken [12]	N/A
mouse anti-CSP	DSHB	DCSP-2 (6D6), RRID: AB_528183
rabbit anti-Rab3	Gift from Aaron DiAntonio [54]	N/A
mouse anti-Syx1a	DSHB	8C3, RRID: AB_528484
guinea pig anti-V100	[55]	N/A
rabbit anti-n-Syb	[55]	N/A
rat anti-n-Syb (R29)	Gift from Hugo Bellen [56]	N/A
mouse anti-Chaoptin	DSHB	24B10, RRID: AB_528161
Cy5 AffiniPure Goat Anti-Rabbit IgG (H+L)	Jackson Immunoresearch	111-175-144, RRID: AB_2338013
Cy5 AffiniPure Goat Anti-Mouse IgG (H+L)	Jackson Immunoresearch	115-175-146, RRID: AB_2338713
Cy5 AffiniPure Goat Anti-Rat IgG (H+L)	Jackson Immunoresearch	112-175-143, RRID: AB_2338263
Alexa Fluor 647 AffiniPuree Goat Anti-Guinea Pig IgG (H+L)	Jackson Immunoresearch	106-605-003, RRID: AB_2337446
Cy3 AffiniPure Goat Anti-Rabbit IgG (H+L)	Jackson Immunoresearch	111-165-144, RRID: AB_2338006
Alexa Fluor 488 AffiniPure Goat Anti-Rabbit IgG (H+L)	Jackson Immunoresearch	111-545-144, RRID: AB_2338052
Chemicals, Peptides, and Recombinant Proteins		
TOTO3	Thermo Fisher	T3604
Vectashield	Vector Laboratories	H-1000
PBS	GIBCO	70011-36
Formaldehyde	Merck KGaA	1.03999.1000
Triton X-100	Sigma-Aldrich	T8787
Schneider’s *Drosophila* Medium [+] L-Glutamine	GIBCO	21720-024
Agarose, low gelling temperature	Sigma-Aldrich	A9045-10G
Human insulin recombinant zinc	GIBCO	12585014
Penicillin/Streptomycin	GIBCO	15140122
ES Cell FBS	GIBCO	16141-061
20-Hydroxyecdysone	Sigma-Aldrich	5289-74-7
SilGard and Silicone Elastomer Kit	Dow Corning	184
Sodium Chloride	Merck KGaA	1.06404.1000
Experimental Models: Organisms/Strains		
Drosophila, UAS-myr-mCherry-pHluorin in VK00002	This paper	N/A
Drosophila, UAS-Syt1-mCherry-pHluorin in VK00002	This paper	N/A
Drosophila, UAS-mCherry-pHluorin-Syt1 in VK00002	This paper	N/A
Drosophila, UAS-CP1-mCherry-pHluorin in VK00002	This paper	N/A
Drosophila, GMR-Gal4	Bloomington Drosophila Stock Center (BDSC)	9146
Drosophila, ppk-Gal4	BDSC	32078
Drosophila, ey3.5flp	BDSC	35542

(*Continued on next page*)

Continued

REAGENT or RESOURCE	SOURCE	IDENTIFIER
Drosophila, FRT82b,tub-Gal80	BDSC	5135
Drosophila, FRT80b,tub-Gal80	BDSC	5191
Drosophila, $nsyb^{F33B}$	[57]	N/A
Drosophila, $rab7^{gal4\text{-}knock\text{-}in}$	[17]	N/A
Drosophila, $v100^{4}$	[55]	N/A
Drosophila, syt^{AD4}	[58]	N/A
Drosophila, FRT40A,cl	BDSC	5622
Drosophila, UAS-Atg8-mCherry	BDSC	37749
Drosophila, UAS-Syt1-GFP	BDSC	6926
Drosophila, GMR-myr-GFP	BDSC	7112
Drosophila, GMR-myr-Tomato	Gift from S.Lawrence Zipursky	N/A
Drosophila, $car^{\Delta 146}$,FRT19A	Gift from Helmut Kramer	N/A
Drosophila, UAS-V100	[55]	N/A
Drosophila, UAS-n-Syb	[22]	N/A
Drosophila, UAS-Rab7	Hiesinger lab	N/A
Drosophila, UAS-n-Syb-RNAi	VDRC	104531
Recombinant DNA		
mCherry-SEpHluorin	Addgene	32001
pUASTattB	[59]	Flybase ID: FBmc0003002
Software and Algorithms		
ImageJ	National Institutes of Health (NIH)	N/A
Imaris	Bitplane, Switzerland	N/A
GraphPad Prism	GraphPad Software, La Jolla, USA	N/A
AutoQuant 3x	Media Cybernetics	N/A
Clampfit	Axon Instruments	N/A
Clampex	Axon Instruments	N/A
Python	Python Software Foundation	N/A
Amira	FEI-Thermo Fisher Scientific	N/A

CONTACT FOR REAGENT AND RESOURCE SHARING

Further information and requests for resources and reagents should be directed and will be fulfilled by the Lead Contact, Dr. Robin Hiesinger (robin.hiesinger@fu-berlin.de).

EXPERIMENTAL MODEL AND SUBJECT DETAILS

Fly husbandry

All flies were raised on standard molasses formulation food at either 25°C (most crosses), 29°C (RNAi crosses) or 21°C ($Gal80^{ts}$ crosses).

Flies

For live-imaging and fixed immunostainings, photoreceptor clones expressing the imaging probes were generated using the *ey3.5flp* system [60, 61] in otherwise heterozygous animals. For the analyses of myr-DF and Syt1-DF probes in control and mutant photoreceptors, the following *Drosophila* lines were used: control (ey3.5flp/+;GMR-Gal4/GMR-Gal4,UAS-myr-DF or UAS-Syt1-DF;FRT82B,tub-Gal80/FRT82B), *v100* (ey3.5flp/+;GMR-Gal4/GMR-Gal4,UAS-myr-DF or UAS-Syt1-DF;FRT82B,tub-Gal80/FRT82B,$v100^{4}$; Hiesinger et al., 2005), *n-syb* (ey3.5flp/+;GMR-Gal4/GMR-Gal4, UAS-myr-DF or UAS-Syt1-DF;FRT80B,tub-Gal80/FRT80B,$n\text{-}syb^{\Delta F33B}$; Deitcher et al., 1998), *rab7* (ey3.5flp/+;GMR-Gal4/GMR-Gal4,UAS-myr-DF or UAS-Syt1-DF;FRT82B,tub-Gal80/FRT82B,$rab7^{gal4\text{-}knock\text{-}in}$ [17]). For *syt1* rescue ERG recordings, the following *Drosophila* lines were used: control (eyflp/+; FRT40A,GMR-Gal4/FRT40A,cl^{w+}), *syt1* mutant (eyflp/+;FRT40A,syt^{AD4},GMR-Gal4/FRT40A, cl^{w+}), rescue by C-terminally tagged Syt1 (Syt1-DF) (eyflp/+;FRT40A,syt^{AD4},GMR-Gal4,UAS-Syt1-DF/FRT40A,cl^{w+}), rescue by N-terminally tagged Syt1 (DF-Syt1) (eyflp/+;FRT40A,syt^{AD4},GMR-Gal4,UAS-DF-Syt1/FRT40A,cl^{w+}). For class IV sensory neuron live-imaging: class IV neurons (ppk-Gal4>UAS-Syt1-DF or UAS-myr-DF). For autophagy live-imaging experiments: (GMR-Gal4>UAS-Atg8-mCherry,UAS-Syt1-GFP), (GMR-Gal4>UAS-Atg8-mCherry,GMR-myr-GFP). For co-imaging of fluorescently tagged myr and Syt1 probes: (GMR-Gal4>UAS-Syt1-GFP,GMR-myr-Tomato). For n-Syb knockdown experiments: n-Syb knockdown in v100 mutant background (ey3.5flp/+;GMR-Gal4,UAS-myr-DF or UAS-Syt1-DF/UAS-nSyb-RNAi;FRT82b,*v100*/FRT82b,tub-Gal80), n-Syb knockdown (ey3.5flp/+;GMR-Gal4,UAS-myr-DF or UAS-Syt1-DF/UAS-nSyb-RNAi), control (ey3.5flp/+;GMR-Gal4,UAS-myr-DF or UAS-Syt1-DF/+). For overexpression experiments: (Gmr-Gal4,UAS-myr-DF or UAS-Syt1-DF/UAS-Rab7), (GMR-Gal4,UAS-myr-DF or UAS-Syt1-DF/UAS-V100), (Gmr-Gal4,UAS-myr-DF or UAS-Syt1-DF/UAS-n-Syb), control (GMR-Gal4,UAS-myr-DF or UAS-Syt1-DF/+). For *carnation* mutant experiment: carnation mutant (FRT19A,tub-Gal80,hsflp/FRT19A,car$^{\Delta146}$;GMR-Gal4,UAS-myr-DF or UAS-Syt1-DF/+), control (FRT19A,tub-Gal80,hsflp/FRT19A;GMR-Gal4,UAS-myr-DF or UAS-Syt1-DF/+).

To generate *UAS-myr-mCherry-pHluorin*, we amplified DNA encoding the first 30 amino acids of *Drosophila Src64B* from P[UAS-myr-RFP] (donated from Henry Chang) and PCR amplified the *mCherry-pHluorin* sequence from the mCherry-SEpHluorin vector (addgene, plasmid #32001, donated by Sergio Grinstein), generated the final linear DNA 5′-*NotI-myr-linker-mCherry-pHluorin-XhoI*-3′ by overlap extension PCR, then cloned it into the pUASTattB vector. Linker sequence: GCT GCC. For the generation of UAS-*syt1-mCherry-pHluorin*, UAS-*mCherry-pHluorin-Syt1* and UAS-*CP1-mCherry-pHluorin* (CP1-DF), the same strategy was followed except *syt1* or *cp1* was amplified from a cDNA sample. All constructs were integrated in the same landing site (y^{1}w^{1118}; PBac[y[+]-attP-3B]VK00002) in *Drosophila* genome to equalize expression levels. Transgenic flies were generated using standard procedures through Rainbow Transgenicsm USA.

METHOD DETAILS

Brain culture and live imaging

Pupal eye-brain complexes were dissected in cold Schneider's *Drosophila* Medium and cultured in the culture chambers perfused with culture medium as previously described [29]. For adult photoreceptor live imaging, 1-day and 2-week old adult fly eyes were dissected, with the lamina attached to the retina. To fully expose lamina photoreceptor terminals, pupal brains were mounted dorsal side up and adult eyes were mounted lamina side up in 0.4% dialyzed low-melting agarose. For class IV neuron live imaging, L3 fillet preparation was performed in cold Schneider's *Drosophila* Medium in a SylGard-covered Petri dish.

Live imaging was performed at room temperature using a Leica TCS SP8 X confocal microscope with a resonant scanner, using 63X water objective (NA = 1.2), and optimized settings of minimal white laser excitation and cross-talk avoiding SP detector emission windows. White laser excitation was set to 488 nm for GFP and phluorin, 554 nm for tdTomato, and 587 nm for mCherry signal acquisitions.

Immunohistochemistry

Pupal and adult eye-brain complexes were dissected and collected in cold Schneider's *Drosophila* Medium. The tissues were fixed in PBS with 4% formaldehyde for 30 min and washed in PBST (PBS+0.4% Triton X-100). The following primary antibodies were used: rabbit anti-Rab5 (1:1000), rabbit anti-Rab7 (1:1000), mouse anti-Rab11 (1:1000), rabbit anti-Syt1 (1:1000), rabbit anti-GABARAP (1:100), guinea pig anti-Spin (1:1000), rat anti-Sky (1:200), mouse anti-CSP (1:50), rabbit anti-Rab3 (1:1000), mouse anti-Syx1a (1:50), guinea pig anti-V100 (1:1000), rabbit anti-n-Syb (1:1000), rat anti-nSyb (1:1000), mouse anti-Rst (1:500), mouse anti-Chaoptin (1:500). All samples were mounted in mounting medium (Vectashield; Vector Laboratories) for confocal microscopy. Secondary antibodies used were Cy3, Cy5 (Jackson ImmunoResearch Laboratories), and Alexa 488 (Invitrogen). High-resolution confocal microscopy was performed at room temperature using a Leica TCS SP8 X with 63X Glycerol objective (NA = 1.3). White laser excitation was set to 488 nm for Alexa488, 548 nm for Cy3, and 645 nm for Cy5 signal acquisitions.

Image processing

All 4D live-imaging data were deconvolved with either ImageJ (National Institute of Health) plug-in Microvolution (Microvolution, 2014-2016) or AutoQuant 3X (Media Cybernetics) using adaptive PSF (blind) prior to analysis. Data were processed using Imaris (Bitplane), ImageJ (National Institute of Health), Amira 6.3 (FEI - Thermo Fisher Scientific), Photoshop (CS6, Adobe, Inc) and Python-based software listed in the section 'Markov State Model'.

Electroretinogram (ERG) Recordings

1-day-old adult flies were reversibly glued on slides using nontoxic school glue. Flies were exposed to 1 s pulses of light stimulus provided by computer-controlled white light-emitting diode system (MC1500; Schott) as previously reported [20]. ERGs were recorded using Clampex (Axon Instruments) and measured using Clampfit (Axon Instruments).

QUANTIFICATION AND STATISTICAL ANALYSIS

Quantification and Statistical Analysis

For volume, number, fusion, fission, speed and partition analyses, all 4D live-imaging data were deconvolved with AUTO Quant 3x (Modality: Laser Scanning Confocal; Objective Lens: 1.2 NA; Num. Aperture: 1.2; Imm. Medium (RI): 1.33; Sample Medium (RI) Water (1.33), Dist. From Coverslip: 20; Deconvolution Method: Adaptive PSF (Blind); PSF Settings: Theoretical PSF; Deconvolution

Settings: Adaptive PSF, 10 Iterations, Medium Noise), and analyzed using IMARIS (Bitplane, Switzerland). Binarized datasets were generated semi-automatically, then 4D tracking was performed manually. The following measurements were obtained from the built-in statistics analyses tools of IMARIS: volume, number, speed. The following measurements were obtained manually: fusion and fission frequencies, maximum displacement. For colocalization experiments, the data were obtained in 3D and all co-localization quantification was performed manually on single slices. The following number of compartments were counted: (a) mCherry-only, (b) mCherry-pHluorin, (c) mCherry-only & antibody co-localization, (d) mCherry-pHluorin & antibody co-localization. Only discernible individual compartments were counted. Co-localization ratios were calculated as follows: Co-localization ratios of yellow compartments = d/(a+b), Co-localization ratio of red compartments = c/(a+b). In Figures 2F, 2H, 2J, and 2L, co-localization ratios were calculated as follows: Co-localization ratio of yellow compartments = d/b, Co-localization ratio of red compartments = c/a. All statistical analyses were performed in GraphPad Prism, and the statistical analyses and sample numbers used for each result are indicated in the figure legends.

Markov State Modeling

The image analysis was performed using Python 2.7.12 with scikit-image 0.14 and Amira 6.3. The image stacks were reduced to a single slice with a maximum intensity projection. Each frame was smoothed with a Gaussian kernel and the pHluorin channel was subtracted from the mCherry channel to reduce the background signal. The differential images from each time step were then stacked into a three-dimensional volume. To extract tubular structures in space-time, the normalized cross correlation with a solid cylinder template was performed on this volume [62, 63]. Areas with high correlation were traced to extract the compartment trajectories. To analyze the trajectories from the image analysis, a Markov state model (MSM) was defined with pyEMMA 2.4 [64], where each state represents an area of 8x8 pixels (600 states in a 60 by 10 grid). The state assignment for each compartment was computed with the negative exponential distance to each state, normalized to one. The products of the state vectors between two time points were summed and normalized to generate a stochastic transition matrix. This matrix was then used to compute the committor probabilities for each state [65]. The committor probability was here defined for a compartment to leave the image area retrograde rather than anterograde.

Current Biology, Volume *28*

Supplemental Information

Live Observation of Two Parallel Membrane Degradation Pathways at Axon Terminals

Eugene Jennifer Jin, Ferdi Ridvan Kiral, Mehmet Neset Ozel, Lara Sophie Burchardt, Marc Osterland, Daniel Epstein, Heike Wolfenberg, Steffen Prohaska, and Peter Robin Hiesinger

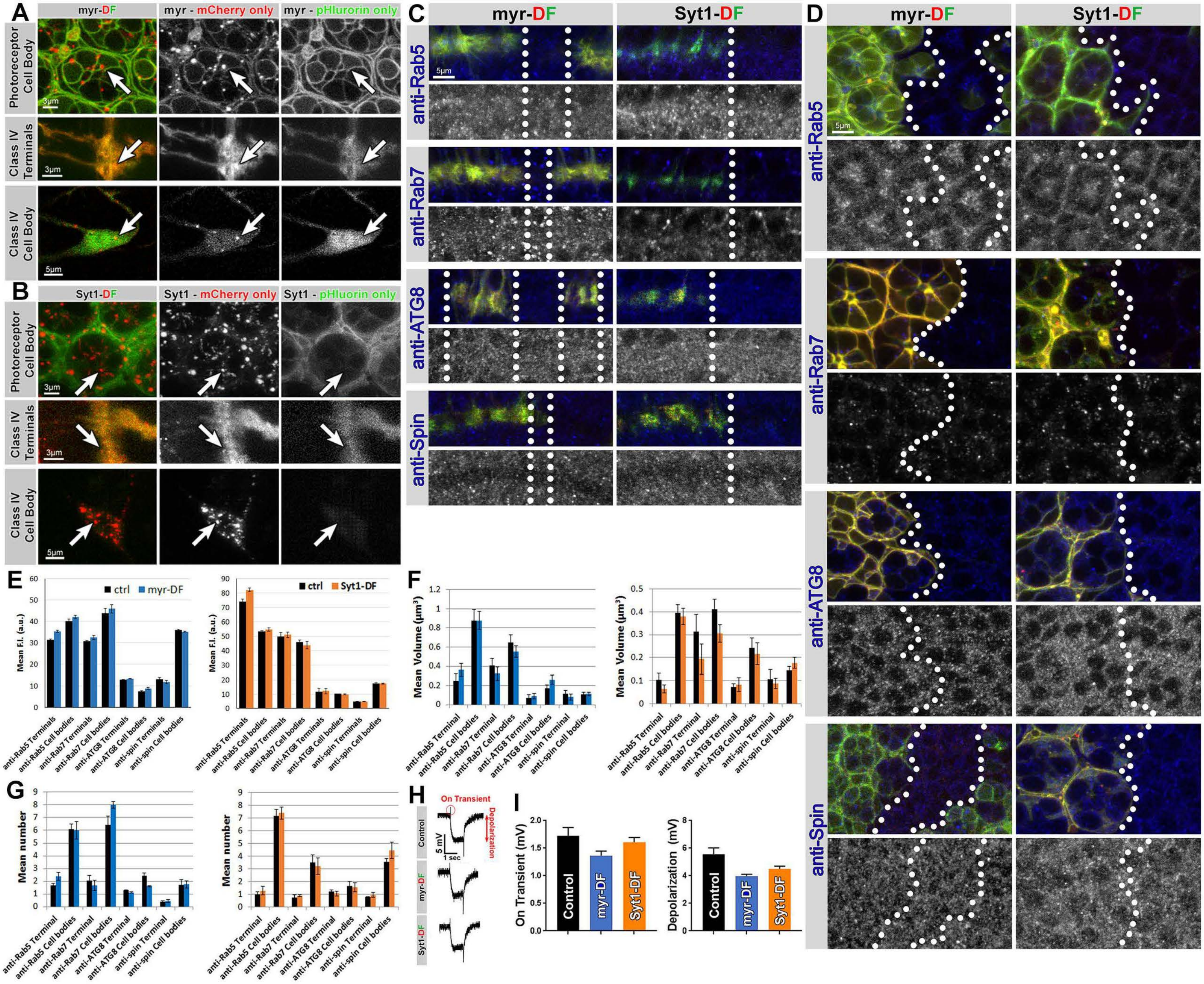
A
myr-DF
myr - mCherry only
myr - pHlurorin only
Photoreceptor Cell Body
Class IV Terminals
Class IV Cell Body
3μm
5μm
B
Syt1-DF
Syt1 - mCherry only
Syt1 - pHluorin only
C
myr-DF
Syt1-DF
anti-Rab5
anti-Rab7
anti-ATG8
anti-Spin
D
E
ctrl
myr-DF
Syt1-DF
Mean F.I. (a.u.)
F
Mean Volume (μm³)
G
Mean number
anti-Rab5 Terminals
anti-Rab5 Cell bodies
anti-Rab7 Terminals
anti-Rab7 Cell bodies
anti-ATG8 Terminals
anti-ATG8 Cell bodies
anti-spin Terminals
anti-spin Cell bodies
H
On Transient
Depolarization
Control
5 mV
1 sec
I
On Transient (mV)
Depolarization (mV)

Figure S1. Myr-DF and Syt1-DF probes mark large acidic compartments in photoreceptor cell bodies, class IV da neuron axon terminals and cell bodies, and expression of neither probe affects endolysosomal and autophagic markers or photoreceptor function. Related to Figure 1.

(A and B) Live imaging of myr-DF (A) and Syt1-DF (B) reveal the presence of large acidic compartments in photoreceptor cell bodies at P+40%, class IV dendritic arborization neuron axon terminals and cell bodies. Arrows: examples of acidic (red-only live) compartments. (C and D) Comparison of the levels of endolysosomal and autophagic pathways markers (Rab5, early endosome; Rab7, late endosome/ multivesicular bodies (MVB); ATG8, autophagosome; Spin, lysosome) in mosaic expression of myr-DF or Syt1-DF at P+40% photoreceptor axon terminals (C) and cell bodies (D). The white dotted lines mark clonal boundaries (with and without probe expression). (E-G) Comparison of mean fluorescence (E), mean volume (F) and mean number (G) of endogenous endolysosomal markers in control (black) and probe-expressing [myr-DF (blue), Syt1-DF (orange)] axon terminals and cell bodies. Mean number per axon terminal was quantified, and mean number per ommatidium was quantified for cell bodies. Mean ± SEM, Unpaired t-test, brain n=3 per antibody staining. (H and I) Electroretinogram (ERG) recordings from adult photoreceptors expressing either myr-DF or Syt1-DF. Representative ERG traces (H), and quantifications of on-transient and depolarization amplitudes (I). Mean ± SEM, fly n=10 per genotype.

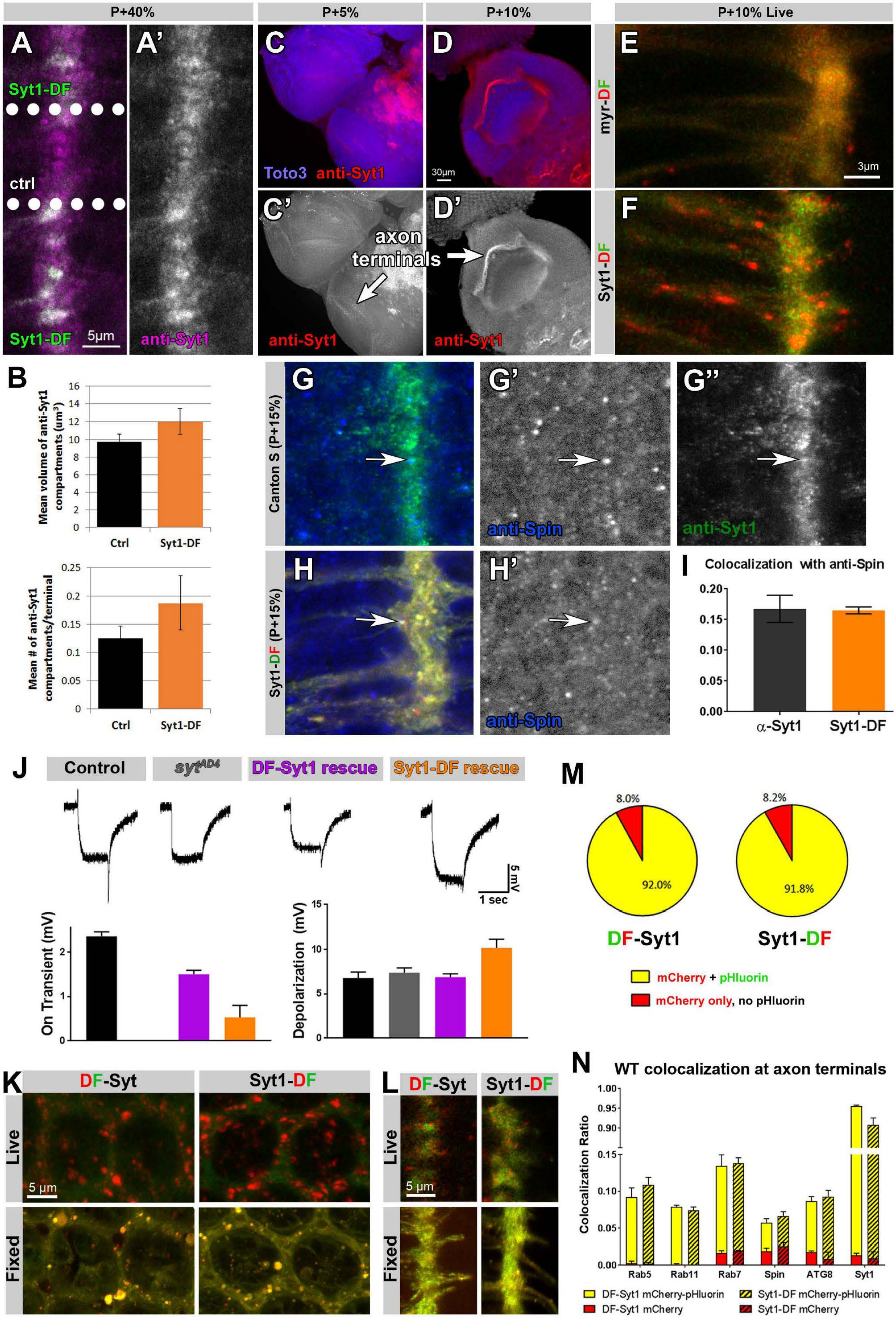
P+40%
P+5%
P+10%
P+10% Live
A
A'
Syt1-DF
ctrl
Syt1-DF
5µm
anti-Syt1
C
Toto3
anti-Syt1
C'
axon
terminals
anti-Syt1
D
30µm
D'
anti-Syt1
E
myr-DF
3µm
F
Syt1-DF
B
Mean volume of anti-Syt1 compartments (um³)
16
14
12
10
8
6
4
2
0
Ctrl
Syt1-DF
Mean # of anti-Syt1 compartments/terminal
0.25
0.2
0.15
0.1
0.05
0
Ctrl
Syt1-DF
G
Canton S (P+15%)
G'
anti-Spin
G''
anti-Syt1
H
Syt1-DF (P+15%)
H'
anti-Spin
I
Colocalization with anti-Spin
0.20
0.15
0.10
0.05
0.00
α-Syt1
Syt1-DF
J
Control
syt^AD4
DF-Syt1 rescue
Syt1-DF rescue
5 mV
1 sec
On Transient (mV)
2
1
0
Depolarization (mV)
15
10
5
0
M
8.0%
92.0%
8.2%
91.8%
DF-Syt1
Syt1-DF
mCherry + pHluorin
mCherry only, no pHluorin
K
DF-Syt
Syt1-DF
Live
5 µm
Fixed
L
DF-Syt
Syt1-DF
Live
5 µm
Fixed
N
WT colocalization at axon terminals
Colocalization Ratio
1.00
0.95
0.90
0.15
0.10
0.05
0.00
Rab5
Rab11
Rab7
Spin
ATG8
Syt1
DF-Syt1 mCherry-pHluorin
DF-Syt1 mCherry
Syt1-DF mCherry-pHluorin
Syt1-DF mCherry

Figure S2. Syt1-DF is expressed at endogenous levels and sorted for degradation indistinguishably from endogenous Syt1, and cytoplasmically tagged Syt1-DF and lumenally tagged DF-Syt1 are indistinguishably localized and degraded in the endolysosomal pathway. Related to Figure 1.
(A-B) Antibody labeling with anti-Syt1 in mosaic expression of Syt1-DF in the P+40% photoreceptor axon terminals (A and A') and quantification of mean volume and number of compartments marked by anti-Syt1 (B). Mean ± SEM, brain n=3, Unpaired t-test. The white dotted lines mark clonal boundaries (with and without probe expression). (C-D') Endogenous Syt1 is localized to axon terminals of photoreceptors starting at 10% pupal development (P+10%). (E and F) Live imaging of myr-DF and Syt1-DF probes at P+10% photoreceptor axon terminals. Note that Syt1 protein turnover starts as soon as it is localized to photoreceptor terminals. (G-H') Syt1-DF colocalizes with lysosomal marker Spin equally as the endogenous Syt1 at P+15%. Arrows: colocalization of Syt1 compartments with anti-Spin. (I) Quantification of colocalization of endogenous Syt1 or Syt1-DF with anti-Spin at P+15%. Mean ± SEM, brain n=3 per experimental condition. (J) Rescue experiment of loss of neurotransmission of sytAD4 null mutant photoreceptors using either C- or N-terminally tagged Syt1 expression (Syt1-DF or DF-Syt1) in 1 day old adult flies. Representative ERG traces, and quantification of on-transient and depolarization amplitudes. Fly n=7 per genotype. (K and L) Live and fixed imaging of Syt1-DF and DF-Syt1 in cell bodies (K) and axon terminals (L) of P+40% photoreceptors. (M) Ratio of mCherry-only Syt1-DF and DF-Syt1 compartments at axon terminals after fixation. Brain n=15 per probe. (N) Colocalization of DF-Syt1 (non-striped) and Syt1-DF (striped) compartments with markers of endolysosomal system, autophagy and Syt1 antibody. Shown are ratios for 'yellow-fixed' and 'red-fixed' terminal hub compartments that colocalize with a given antibody divided by the total number of compartments. The 'yellow-fixed' and 'red-fixed' bars are stacked in the bar chart. Mean ± SEM, brain n=3 per antibody staining.

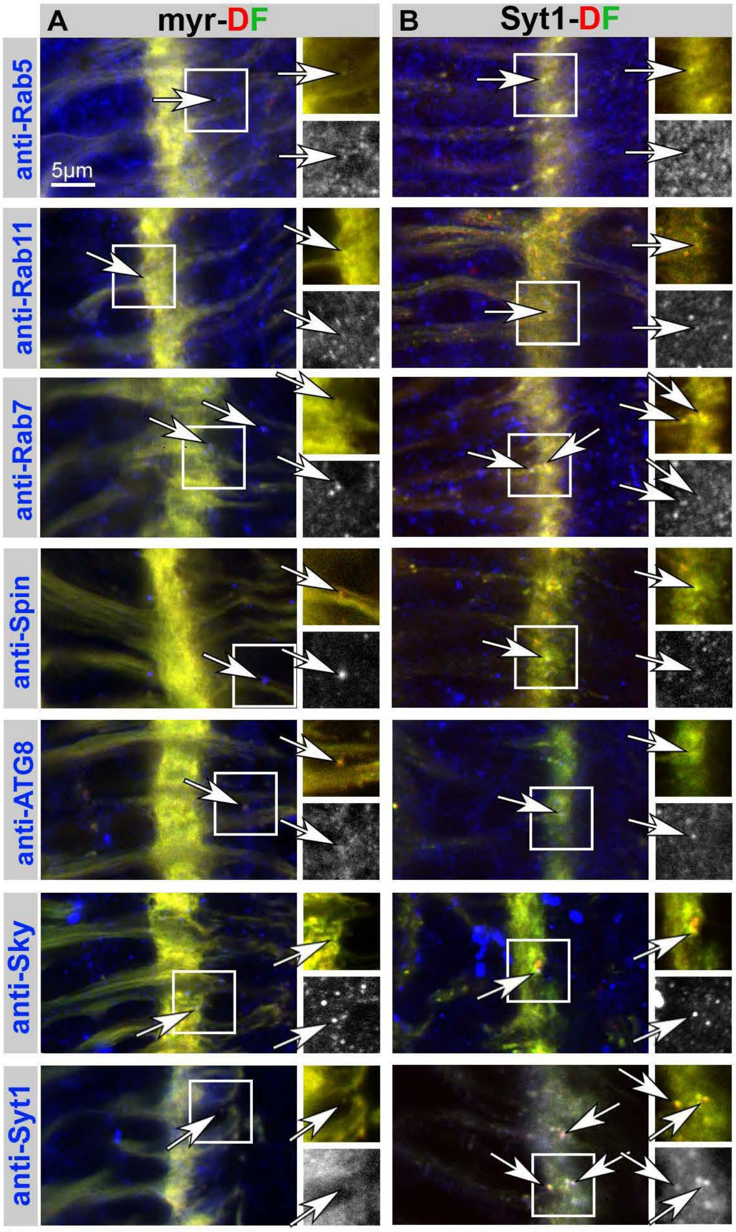
A
myr-DF
B
Syt1-DF
anti-Rab5
5μm
anti-Rab11
anti-Rab7
anti-Spin
anti-ATG8
anti-Sky
anti-Syt1

Figure S3. Colocalization of myr-DF or Syt1-DF probes with endolysosomal and autophagosomal markers at axon terminals. Related to Figure 2.

Representative images for colocalization of myr-DF (A) or Syt1-DF (B) at axon terminals with Rab5, Rab11, Rab7, Spinster (Spin), Atg8, Skywalker (Sky) and Synaptotagmin 1 (Syt1). Arrows: examples of colocalization. Single channels are antibody stainings.

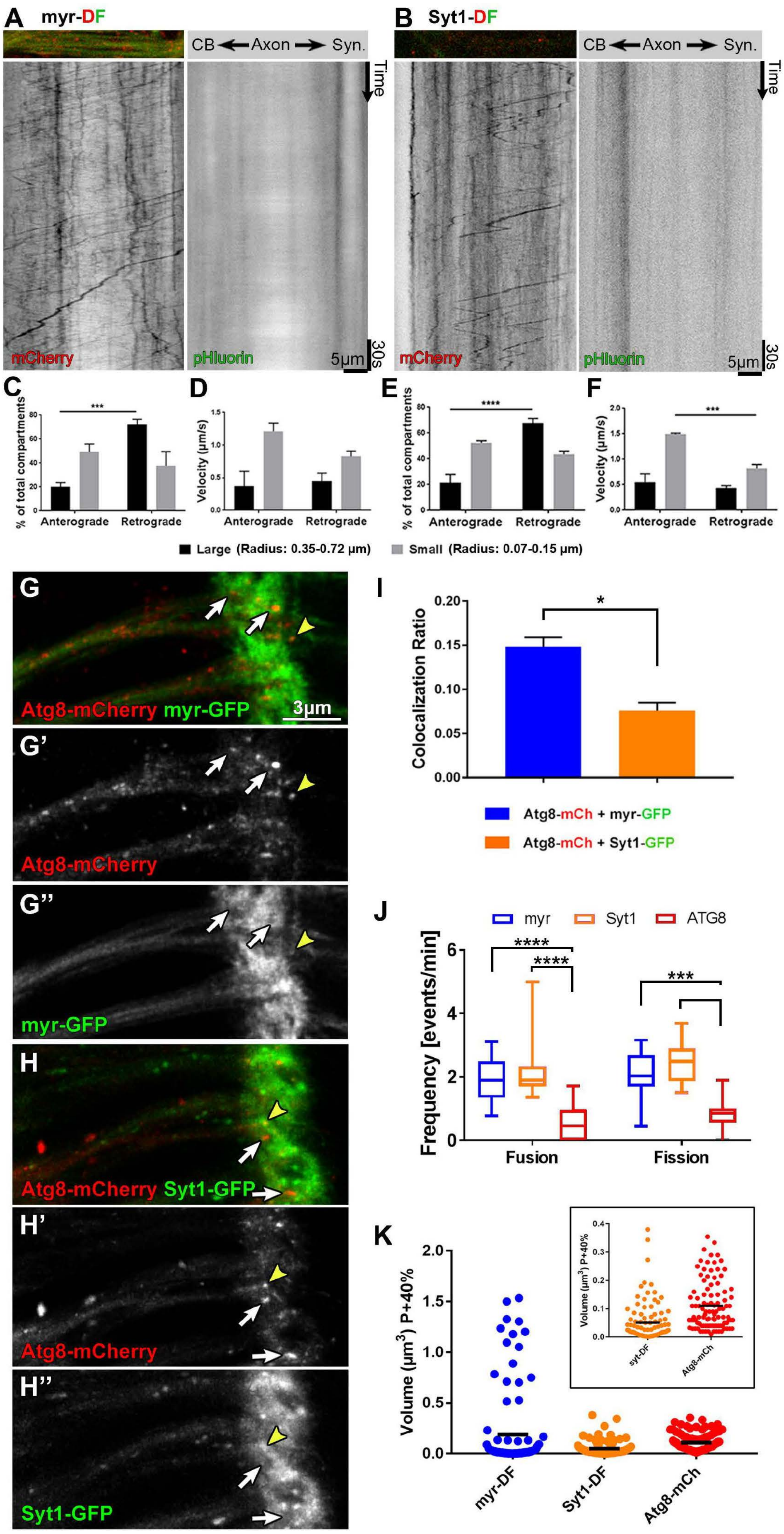
A
myr-DF
CB
Axon
Syn.
Time
mCherry
pHluorin
5μm
30s
B
Syt1-DF
CB
Axon
Syn.
Time
mCherry
pHluorin
5μm
30s
C
% of total compartments
***
0
20
40
60
80
Anterograde
Retrograde
D
Velocity (μm/s)
0.0
0.5
1.0
1.5
Anterograde
Retrograde
E
% of total compartments
****
0
20
40
60
80
Anterograde
Retrograde
F
Velocity (μm/s)
***
0.0
0.5
1.0
1.5
2.0
Anterograde
Retrograde
Large (Radius: 0.35-0.72 μm)
Small (Radius: 0.07-0.15 μm)
G
Atg8-mCherry myr-GFP
3μm
G'
Atg8-mCherry
G''
myr-GFP
H
Atg8-mCherry Syt1-GFP
H'
Atg8-mCherry
H''
Syt1-GFP
I
Colocalization Ratio
*
0.00
0.05
0.10
0.15
0.20
Atg8-mCh + myr-GFP
Atg8-mCh + Syt1-GFP
J
myr
Syt1
ATG8
Frequency [events/min]
****
****
***
0
2
4
6
Fusion
Fission
K
Volume (μm^3) P+40%
0.0
0.5
1.0
1.5
2.0
myr-DF
Syt1-DF
Atg8-mCh
Volume (μm^3) P+40%
0.0
0.1
0.2
0.3
0.4
syt-DF
Atg8-mCh

Figure S4. Axonal transport dynamics of acidified axonal trafficking vesicles, and characteristics of autophagosomes compared to hub compartments. Related to Figure 3.
(A and B) Kymographs showing axonal transport of myr-DF (A) and Syt1-DF (B) positive compartments. (C and E) Net direction of large or small compartments positive for myr-DF (C) and Syt1-DF (E). Quantification for stationary compartments is not shown. Mean ± SEM, *** $p<0.001$, **** $p<0.0001$, Unpaired t-test, brain n=3 per probe. (D and F) Mean velocity of retrogradely or anterogradely trafficked compartments for myr-DF (D) and Syt1-DF (F). Mean ± SEM, *** $p<0.001$, **** $p<0.0001$, Unpaired t-test, brain n=3 per probe. (G-H'') Live imaging of co-expression of Atg8-mCherry and myr-GFP (G-G'') or Syt1-GFP (H-H'') at P+40% photoreceptor terminals and axons. White arrows: autophagosomes that do not co-localize with myr-GFP or Syt1-GFP positive compartments. Yellow arrowhead: autophagosomes that co-localize with myr-GFP or Syt1-GFP positive compartments. Stacks have been checked in 4D data for co-migration of autophagosomes and Syt1-GFP or myr-GFP positive compartments. (I) Quantification of colocalization ratio between Atg8-mCherry and myr-GFP or Syt1-GFP, Respectively. Mean ± SEM, * $p<0.05$, Unpaired t-test, brain n=3 per co-expression. (J) Fusion and fission frequencies of Atg8-mCherry positive autophagosomes compared to myr-DF and Syt1-DF positive acidified compartments. Box and whiskers plot, showing 5-95 percentiles, hub n=12 to 15 per probe, *** $p<0.001$, **** $p<0.0001$, Unpaired t-test. (K) Volumes of Atg8-mCherry compartments at axon terminals at P+40%, compared with acidified myr-DF and Syt1-DF from Figure 4D. Hub n=100 per probe, black lines indicate mean values. Inset compares volumes of Syt1-DF and Atg8-mCherry compartments.

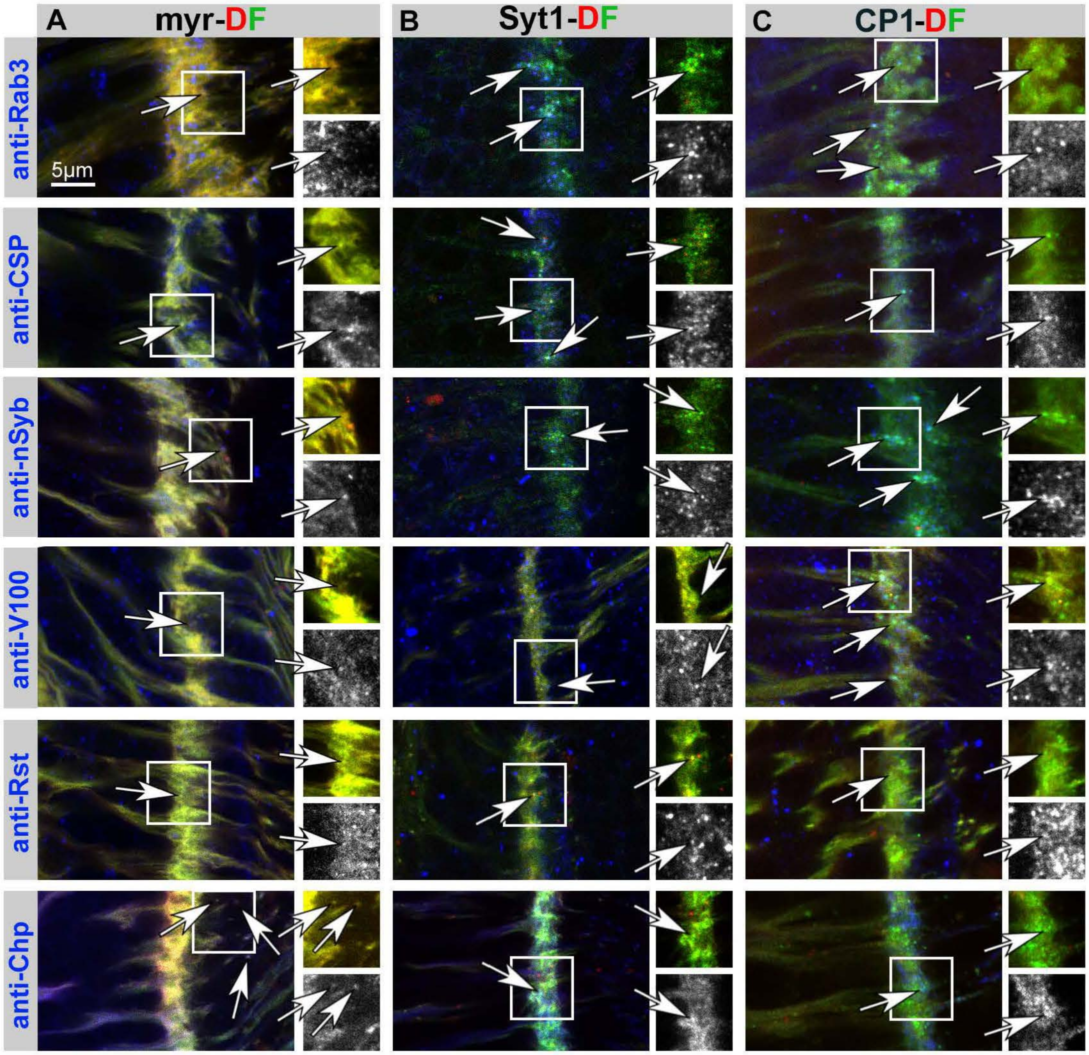
A
myr-DF
B
Syt1-DF
C
CP1-DF
anti-Rab3
anti-CSP
anti-nSyb
anti-V100
anti-Rst
anti-Chp
5μm

Figure S5. Colocalization of hub compartments at axon terminals with synaptic vesicle proteins and plasma membrane proteins. Related to Figure 4.

Representative images for colocalization of myr-DF (A), Syt1-DF (B), and CP1-DF (C) positive compartments with SV markers (Rab3, Cystein String Proteins (CSP)), SV and endolysosomal markers (neuronal Synaptobrevin (n-Syb) and vesicular ATPase component V100), and two photoreceptor plasma membrane receptors (Chaoptin (Chp) and Roughest (Rst)). Arrows: examples of colocalization. Single channels are antibody stainings.

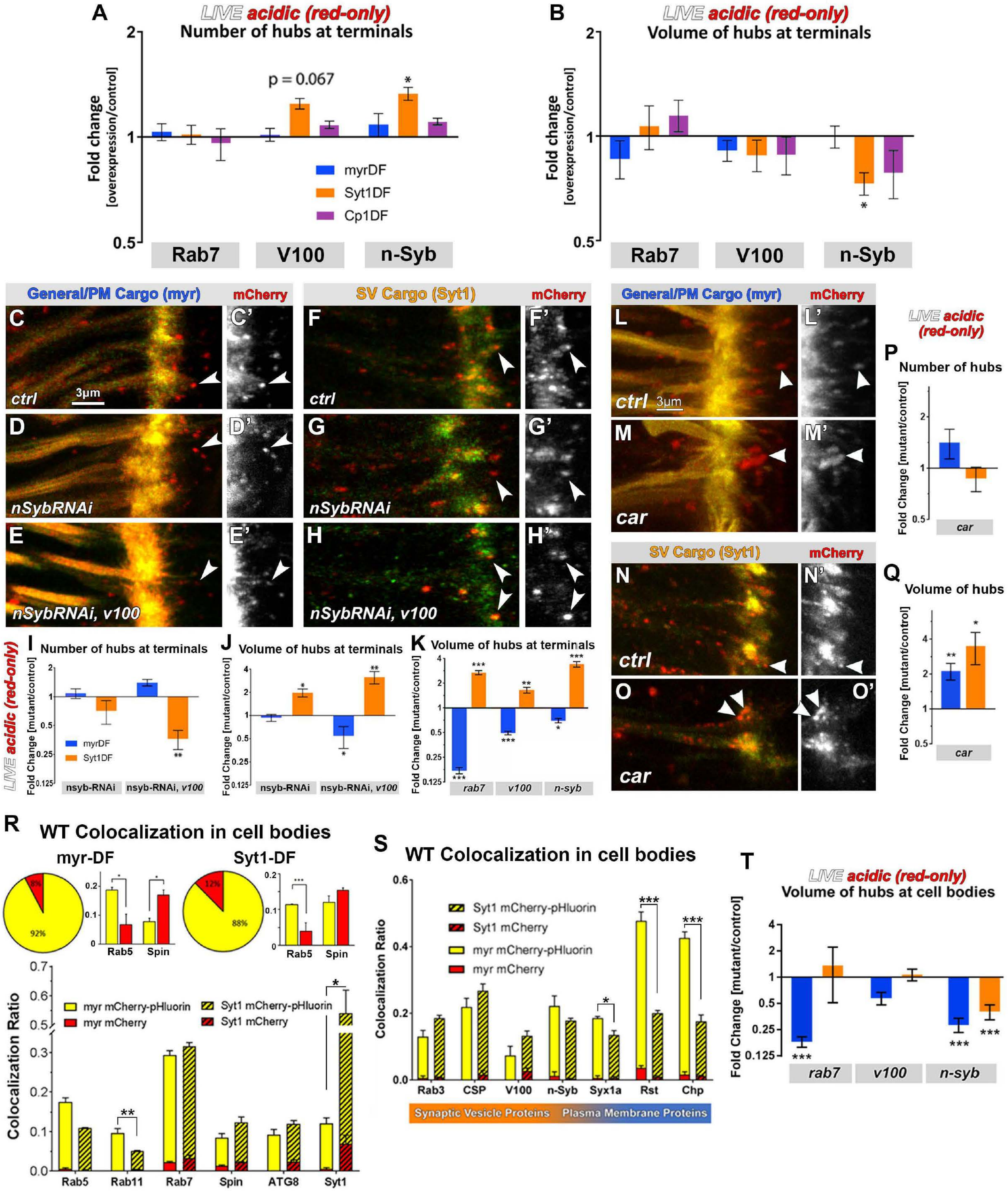
A
LIVE acidic (red-only)
Number of hubs at terminals
Fold change [overexpression/control]
p = 0.067
myrDF
Syt1DF
Cp1DF
Rab7
V100
n-Syb
B
LIVE acidic (red-only)
Volume of hubs at terminals
Fold change [overexpression/control]
Rab7
V100
n-Syb
General/PM Cargo (myr)
mCherry
C
C'
ctrl
3µm
D
D'
nSybRNAi
E
E'
nSybRNAi, v100
SV Cargo (Syt1)
mCherry
F
F'
ctrl
G
G'
nSybRNAi
H
H'
nSybRNAi, v100
General/PM Cargo (myr)
mCherry
L
L'
ctrl
3µm
M
M'
car
LIVE acidic (red-only)
P
Number of hubs
Fold Change [mutant/control]
car
SV Cargo (Syt1)
mCherry
N
N'
ctrl
O
O'
car
Q
Volume of hubs
Fold Change [mutant/control]
car
LIVE acidic (red-only)
I
Number of hubs at terminals
Fold Change [mutant/control]
myrDF
Syt1DF
nsyb-RNAi
nsyb-RNAi, v100
J
Volume of hubs at terminals
Fold Change [mutant/control]
nsyb-RNAi
nsyb-RNAi, v100
K
Volume of hubs at terminals
Fold Change [mutant/control]
rab7
v100
n-syb
R
WT Colocalization in cell bodies
myr-DF
Syt1-DF
8%
92%
12%
88%
Rab5
Spin
Colocalization Ratio
myr mCherry-pHluorin
myr mCherry
Syt1 mCherry-pHluorin
Syt1 mCherry
Rab5
Rab11
Rab7
Spin
ATG8
Syt1
S
WT Colocalization in cell bodies
Colocalization Ratio
Syt1 mCherry-pHluorin
Syt1 mCherry
myr mCherry-pHluorin
myr mCherry
Rab3
CSP
V100
n-Syb
Syx1a
Rst
Chp
Synaptic Vesicle Proteins
Plasma Membrane Proteins
T
LIVE acidic (red-only)
Volume of hubs at cell bodies
Fold Change [mutant/control]
rab7
v100
n-syb

Figure S6. Live and subcellular characterization of myr-DF and Syt1-DF marked compartments at axon terminals and cell bodies. Related to Figure 5.

(A and B) Relative number (A) and volume (B) of degradative compartments in Rab7, V100 or n-Syb overexpressing axon terminals. Mean ± SEM, * $p<0.05$, Unpaired t-test, brain n=3 per experimental condition. (C-H') Live imaging of myr-DF and Syt1-DF in n-Syb knockdown (n-Syb RNAi) or n-Syb knockdown in v100 mutant background at P+40% photoreceptor axon terminals. Arrowheads: examples of acidic (red-only live) compartments at axon terminals. (I and J) Relative number (I) and volume (J) of degradative compartments from live imaging data shown in A-F'. Mean ± SEM, * $p<0.05$, ** $p<0.01$, Unpaired t-test, brain n=3 per experimental condition. (K) Relative volume of acidic compartments in mutants from live imaging data at axon terminals (Figure 5A-5H'). Mean ± SEM, * $p<0.05$, ** $p<0.01$, *** $p<0.001$, Kolmogorov-Smirnov test, hub n=240 to 1314, brain n=3 per experimental condition. (L-O') Live imaging of myr-DF and Syt1-DF in car mutant background at P+40% photoreceptor axon terminals. Arrowheads: examples of acidic (red-only live) compartments at axon terminals. (P and Q) Relative number (P) and volume (Q) of acidic compartments in car mutant live imaging data. Mean ± SEM, * $p<0.05$, ** $p<0.01$, Unpaired t-test, brain n=3 per experimental condition. (R) Wildtype colocalization of myr-DF and Syt1-DF compartments in cell bodies. Pie charts show ratios of 'red-fixed' vs 'yellow-fixed' compartments in cell bodies. Bar charts show colocalization ratios of 'yellow-fixed' and 'red-fixed' compartments separately with early endosomal marker Rab5 and lysosomal marker Spin. Bar chart on the bottom shows wildtype colocalization of myr-DF (non-striped) and Syt1-DF (striped) compartments with markers of endolysosomal system, autophagy and Syt1 antibody in cell bodies. Shown are ratios for 'yellow-fixed' and 'red-fixed' compartments that colocalize with a given antibody divided by the total number of compartments. The 'yellow-fixed' and 'red-fixed' bars are stacked in the bar chart. Mean ± SEM, Unpaired t-test, * $p<0.05$, ** $p<0.01$, *** $p<0.01$, brain n=3 to 5. (S) Wildtype colocalization of myr-DF (non-striped) and Syt1-DF (striped) compartments with markers of SV proteins and plasma membrane proteins in cell bodies. Shown are ratios for 'yellow-fixed' and 'red-fixed' compartments that colocalize with a given antibody divided by the total number of compartments. The 'yellow-fixed' and 'red-fixed' bars are stacked in the bar chart. Mean ± SEM, Unpaired t-test, * $p<0.05$, *** $p<0.001$, brain n=3 per antibody staining. (T) Relative volume of acidic compartments in mutants from live imaging data in cell bodies. Mean ± SEM, *** $p<0.001$, Kolmogorov-Smirnov test, hub n=240 to 1314, brain n=3 per experimental condition.

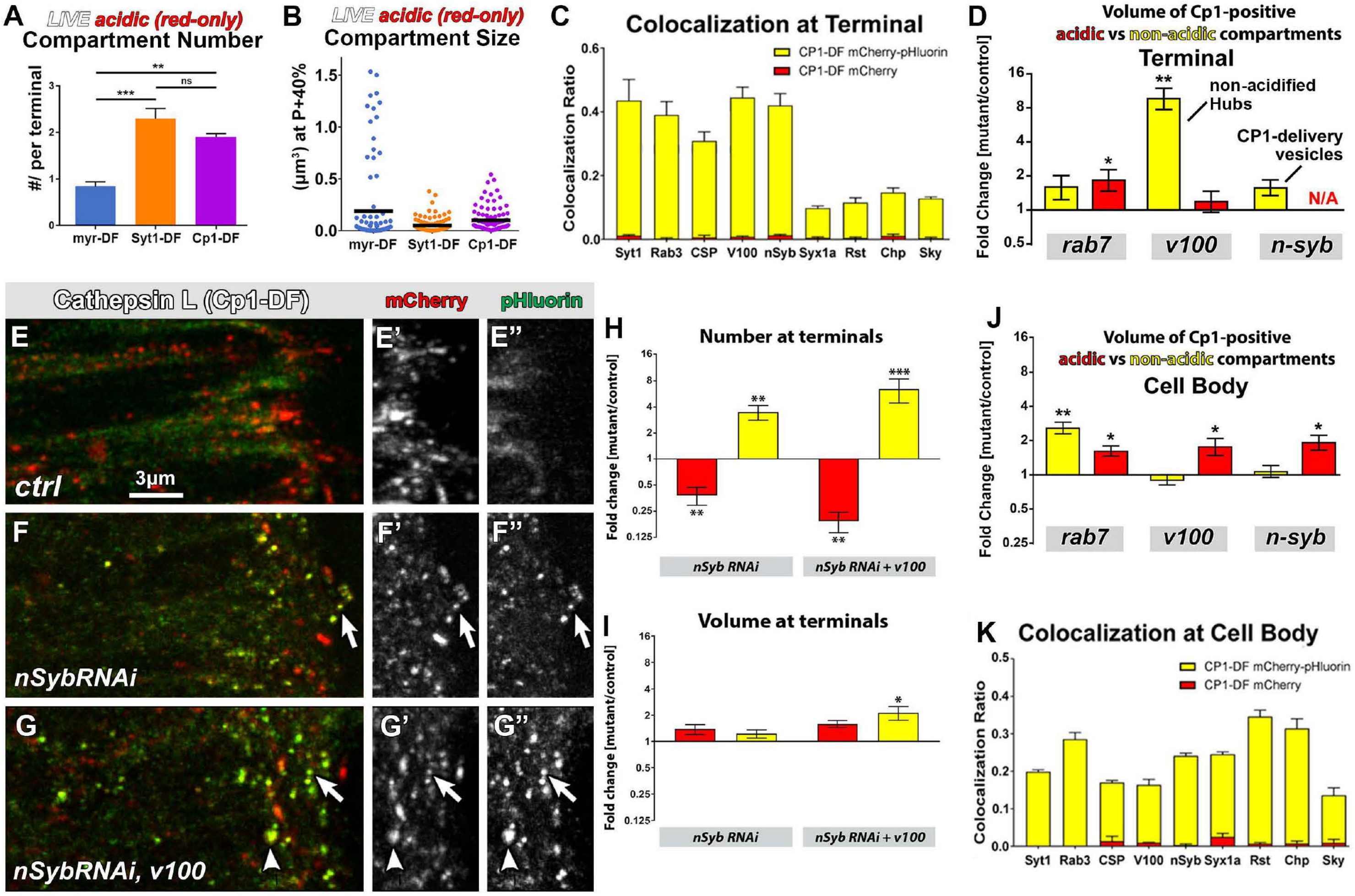

Figure S7. Live and subcellular characterization of CP1-DF marked compartments at axon terminals and cell bodies. Related to Figure 6.

(A and B) Mean number (A) and volume (B) of acidified CP1-DF compartments per axon terminal at P+40% compared to myr-DF and Syt1-DF. n=100 per probe for volume analysis, black lines indicate mean values (B), mean ± SEM (A), $^{**}p < 0.01$, $^{***}p < 0.001$, Unpaired t-test, brain n=3 per probe. (C) Wild-type colocalization of CP1-DF compartments with markers of SV proteins and plasma membrane proteins at axon terminals. Shown are ratios for 'yellow-fixed' and 'red-fixed' terminal compartments that colocalize with a given antibody divided by the total number of compartments. The 'yellow-fixed' and 'red-fixed' bars are stacked in the bar chart. Brain n=3 per antibody staining. (D) Relative volumes of non-acidic (yellow) and acidic (red) compartments containing CP1-DF in rab7, v100 or nsyb mutant backgrounds at axon terminals. Mean ± SEM, * $p<0.05$, ** $p<0.01$, Unpaired t-test, brain n=3 per experimental condition. (E-G") Live imaging of CP1-DF in n-Syb knockdown (n-Syb RNAi) or n-Syb knockdown in v100 mutant background at P+40% photoreceptor axon terminals. Arrows: small CP1-delivery vesicles. Arrowheads: large non-acidified hubs. (H and I) Relative number (H) and volume (I) of non-acidic (yellow) and acidic (red) compartments containing CP1-DF in n-Syb knockdown (n-Syb RNAi) or n-Syb knockdown in v100 mutant background at axon terminals. Mean ± SEM, * $p<0.05$, ** $p<0.01$, *** $p<0.001$, Unpaired t-test, brain n=3 per experimental condition. (J) Relative volumes of non-acidic (yellow) and acidic (red) compartments containing CP1-DF in rab7, v100 or nsyb mutant backgrounds in cell bodies. Mean ± SEM, * $p<0.05$, ** $p<0.01$, Unpaired t-test, brain n=3 per experimental condition. (K) Wild-type colocalization of CP1-DF compartments with markers of SV proteins and plasma membrane proteins in cell bodies. Shown are ratios for 'yellow-fixed' and 'red-fixed' compartments that colocalize with a given antibody divided by the total number of compartments. The 'yellow-fixed' and 'red-fixed' bars are stacked in the bar chart. Brain n=3 per antibody staining.

Probe, Genotype	Fusion			Fission			Speed			Max. displacement (up to 15 min tracks)		
	Mean [/min]	SEM	Range	Mean [/min]	SEM	Range	Mean [/min]	SEM	Range	Mean [/min]	SEM	Range
myr-DF, Control	1.93	0.21	0.77 - 3.11	2.02	0.24	0.44 - 3.16	5.99	0.51	3.39 - 10.3	2.33	0.22	1.3 - 3.7
myr-DF, *rab7 mutant*		--			--		5.88	0.67	2.73 - 12.4	1.99	0.26	0.9 - 3.6
myr-DF, *v100 mutant*	1.93	0.23	1.04 - 3.36	2.58	0.21	1.19 - 3.82	5.20	0.47	2.37 - 8.60	2.43	0.34	0.7 - 5.2
myr-DF, *nsyb mutant*	1.92	0.24	0.92 - 3.39	2.59	0.27	1.42 - 4.88	5.75	0.42	5.03 - 9.54	2.67	0.47	0.9 - 5.9
Syt1-DF, Control	2.21	0.27	1.35 - 5.00	2.47	0.20	1.50 - 3.69	6.00	0.32	4.48 - 8.47	2.74	0.26	1.2 - 4.1
Syt1-DF, *rab7 mutant*	1.36	0.17	0 - 1.98	1.66	0.15	0.55 - 2.44	5.57	0.49	3.16 - 10.50	2.33	0.15	1.4 - 3.1
Syt1-DF, *v100 mutant*	1.62	0.27	0.44 - 3.57	2.04	0.30	0 - 3.57	5.03	0.42	2.70 - 7.77	1.96	0.33	0.7 - 4.1
Syt1-DF, *nsyb mutant*	1.83	0.17	0.55 - 2.65	2.28	0.29	0.73 - 3.97	6.33	0.46	4.14 - 9.34	2.99	0.50	0.5 - 6.2
ATG8-mCherry-GFP	0.51	0.13	0 - 1.71	0.79	0.11	0 - 1.90	5.53	0.45	3.01 - 8.05	1.99	0.36	0.1 - 5.2

Table S1. Quantitative features of hub compartment dynamics. Related to Figure 3.

4. Manuscript 2

Autophagy-dependent filopodial kinetics restrict synaptic partner choice during *Drosophila* brain wiring

Kiral, F.R., Linneweber, G.A., Mathejczyk, T., Georgiev, S.V., Wernet, M.F., Hassan, B.A., von Kleist, M., Hiesinger, P.R.

Nature Communications, March 12, 2020; 11, 1325.

Contribution

I designed, performed and analyzed all experiments in this manuscript under the supervision of Prof. Dr. P. Robin Hiesinger except the Buridan's paradigm and the motion vision assay. Buridan's paradigm experiments were designed, carried out, and analyzed by Gerit Arne Linneweber and Bassem A. Hassan. Motion vision assay experiments were designed, carried out, and analyzed by Thomas Mathejczyk and Mathias F. Wernet. Svilen Veselinov Georgiev helped with 4D tracking analyses of filopodial dynamics. Max von Kleist performed all computational modeling. The paper was written by myself, Prof. Dr. P. Robin Hiesinger, Prof. Dr. Bassem A. Hassan and Prof. Dr. Max von Kleist.

The original article including the supplemental information is included on the following pages and available online at:

https://doi.org/10.1038/s41467-020-14781-4 nature COMMUNICATIONS

ARTICLE

https://doi.org/10.1038/s41467-020-14781-4 OPEN

Autophagy-dependent filopodial kinetics restrict synaptic partner choice during *Drosophila* brain wiring

Ferdi Ridvan Kiral[1], Gerit Arne Linneweber [1,2], Thomas Mathejczyk[1], Svilen Veselinov Georgiev[1], Mathias F. Wernet[1], Bassem A. Hassan[1,2], Max von Kleist [3] & Peter Robin Hiesinger[1]✉

Brain wiring is remarkably precise, yet most neurons readily form synapses with incorrect partners when given the opportunity. Dynamic axon-dendritic positioning can restrict synaptogenic encounters, but the spatiotemporal interaction kinetics and their regulation remain essentially unknown inside developing brains. Here we show that the kinetics of axonal filopodia restrict synapse formation and partner choice for neurons that are not otherwise prevented from making incorrect synapses. Using 4D imaging in developing *Drosophila* brains, we show that filopodial kinetics are regulated by autophagy, a prevalent degradation mechanism whose role in brain development remains poorly understood. With surprising specificity, autophagosomes form in synaptogenic filopodia, followed by filopodial collapse. Altered autophagic degradation of synaptic building material quantitatively regulates synapse formation as shown by computational modeling and genetic experiments. Increased filopodial stability enables incorrect synaptic partnerships. Hence, filopodial autophagy restricts inappropriate partner choice through a process of kinetic exclusion that critically contributes to wiring specificity.

---

[1] Division of Neurobiology, Institute for Biology, Freie Universität Berlin, 14195 Berlin, Germany. [2] Institut du Cerveau et de la Moelle Epinière (ICM) - Hôpital Pitié-Salpêtrière, Sorbonne Université, Inserm, CNRS, Paris, France. [3] MF1 Bioinformatics, Robert Koch-Institute, 13353 Berlin, Germany. ✉email: robin.hiesinger@fu-berlin.de

Synapse formation and synaptic partner choice are based on cellular and molecular interactions of neurons in all animals[1–5]. Brain wiring diagrams are highly reproducible, yet most, if not all, neurons have the ability to form synapses with incorrect partners, including themselves[6,7]. During neural circuit development, spatiotemporal patterning restricts when and where neurons "see each other"[8–10]. Positional effects can thereby prevent incorrect partnerships, even when neurons are not otherwise prevented from forming synapses[7,11,12]. When and where neurons interact with each other to form synapses is a fundamentally dynamic process. Yet, the roles of neuronal interaction dynamics, e.g., the speed or stability of filopodial interactions, is almost completely unknown for dense brain regions in any organism. Our limited understanding of the dynamics of synaptogenic encounters reflects the difficulty to observe, live and in vivo, synapse formation at the level of filopodial dynamics in intact, normally developing brains[13,14].

Fly photoreceptors (R cells) are the primary retinal output neurons that relay visual information with highly stereotypic synaptic connections in dense brain regions, namely the lamina and medulla neuropils of the optic lobe[15–17]. Intact fly brains can develop in culture, enabling live imaging at the high spatiotemporal resolution necessary to measure photoreceptor axon filopodial dynamics and synapse formation throughout the entire developmental period of circuit assembly[13,14,18]. Axonal filopodia inside the developing brain stabilize to form synapses through the accumulation of synaptic building material, but it remains unknown how limiting amounts of building material in filopodia are regulated[14].

Macroautophagy (autophagy hereafter) is a ubiquitous endomembrane degradation mechanism implicated in neuronal maintenance and function[19]. Neuronal autophagy has been linked to neurodegeneration[20] and synaptic function in the mature nervous system[21,22]. Comparably little is known about developmental autophagy in the brain. Functional neurons develop in the absence of autophagy[19,23,24]. In specific neurons in worms and flies, loss of autophagy leads to reduced synapse development[25,26]. By contrast, in the mouse brain, loss of autophagy in neurons leads to increased dendritic spine density due to defective pruning after synapse formation[27,28]. Despite numerous links to neurodevelopmental disorders, it remains unknown whether and how developmental autophagy can contribute to synaptic partner choice and circuit connectivity, especially in dense brain regions.

In this study, we show that loss of autophagy in *Drosophila* photoreceptor neurons leads to increased synapse formation and the recruitment of incorrect postsynaptic partners. Autophagy directly and selectively regulates the kinetics of synaptogenic axon filopodia, a phenotype that could only be revealed through live observation during intact brain development. Autophagic modulation of the kinetics of synaptogenic filopodia restricts what neurons "see each other" to form synapses, thereby critically contributing to the developmental program that ensures synaptic specificity during brain development.

Results

We have previously observed the formation of autophagosomes at the axon terminals of developing photoreceptor neurons R1–R6 in the developing *Drosophila* brain, but their function has remained unknown[29]. Previous analyses of loss of autophagy in fly photoreceptors have not revealed any obvious developmental defects[24,30,31].

Autophagy affects neurotransmission and visual attention. To probe for previously undetected synaptic defects, we blocked autophagy in developing photoreceptor neurons using molecularly well-defined mutants for the essential autophagy proteins Atg7 and Atg6 (fly homolog of Beclin-1)[24,30]. We validated loss of the key autophagosome marker Atg8 in both *atg7* and *atg6* mutants (Supplementary Fig. 1a-b', e). Rescue of *atg6* with the photoreceptor-specific driver GMR-Gal4 reversed this effect and led to a significant increase in Atg8-positive compartments compared with wild type (Supplementary Fig. 1c-c', e).

As expected, the eyes and axonal projections of photoreceptor neurons mutant for *atg6* or *atg7* in otherwise wild-type brains exhibited no obvious defects in fixed preparations (Fig. 1a, b). Photoreceptor neurons are known to exhibit neurodegeneration with aging[31]. To assay photoreceptor function directly following autophagy-deficient development, we therefore recorded electroretinograms (ERGs) from the eyes of newly eclosed flies. Autophagy-deficient photoreceptors exhibited normal depolarizing responses to light, indicating functional phototransduction and healthy neurons (Fig. 1c, d). Surprisingly, "on" transient amplitudes, which are indicative of synaptic transmission and the ability to elicit a postsynaptic response, were increased 30–50% in both mutants (Fig. 1c, e). Conversely, increased autophagy in transgenically rescued *atg6* photoreceptors reversed this effect and resulted in a significant reduction of "on" transients (Fig. 1c, e).

To further validate the effect of loss of autophagy on neurotransmission, we analyzed another autophagy mutant, *atg18*, which is recruited to the phagophore by PI3P (phosphatidylinositol 3-phosphate) and required for LC3 (Atg8) lipidation[32]. The *atg18*-null mutant behaved consistently as a hypomorph for autophagy. Loss of *atg18* in mutant clones reveals a significant, but (in contrast to *atg6* and *atg7*) not complete loss of Atg8-positive compartments (Supplementary Fig. 1d-d', e). Similar to loss of *atg6* and *atg7*, loss of *atg18* in photoreceptors leads to increased neurotransmissions (Fig. 1c–e). We also performed RNA interference (RNAi) knockdown experiments for *atg5* and *atg16*[33,34], validated decreased number of Atg8-positive compartments, and found similar increases in neurotransmission (Supplementary Fig. 2a–g).

Next, we asked whether loss of autophagy selectively in photoreceptors affected fly vision. We used the simple visual choice assay Buridan's paradigm, in which wing-clipped flies walk freely in a circular, uniformly illuminated arena with two high-contrast black stripes placed opposite to each other (Fig. 1f)[35]. In this assay, flies with functional vision walk back and forth between the two high-contrast objects. We chose the parameter "stripe deviation," which measures how much a single fly deviates from an imaginary line between two black stripes, as a behavioral read-out of visual attention (Fig. 1g). Flies with *atg6* or *atg7*-deficient photoreceptors were assayed and compared with their genetic background-matched controls. Surprisingly, in both mutants the flies with autophagy-deficient photoreceptors exhibited increased visual attention behavior (decreased stripe deviation) compared with their genetically matched controls (Fig. 1h, i and Supplementary Fig. 3). Increased autophagy in *atg6*-rescued photoreceptors reversed this effect again in an overcompensatory manner similar to ERG responses (Fig. 1h, i). This increase in autophagy also leads to an overcompensation of "center deviation," i.e., how much a single fly moves away from the center (Supplementary Fig. 4a, b) but does not reduce the total distance walked (Supplementary Fig. 4c, d), leading to the observed increase in time spent walking the circumference of the arena (Fig. 1h). Visual attention is a higher-order behavior that requires functional basic vision. We therefore next tested basic motion vision using an optomotor assay with tethered, flying flies in a virtual flight arena[36,37]. Loss of autophagy in photoreceptors did not significantly affect the ability of flies to follow counter-

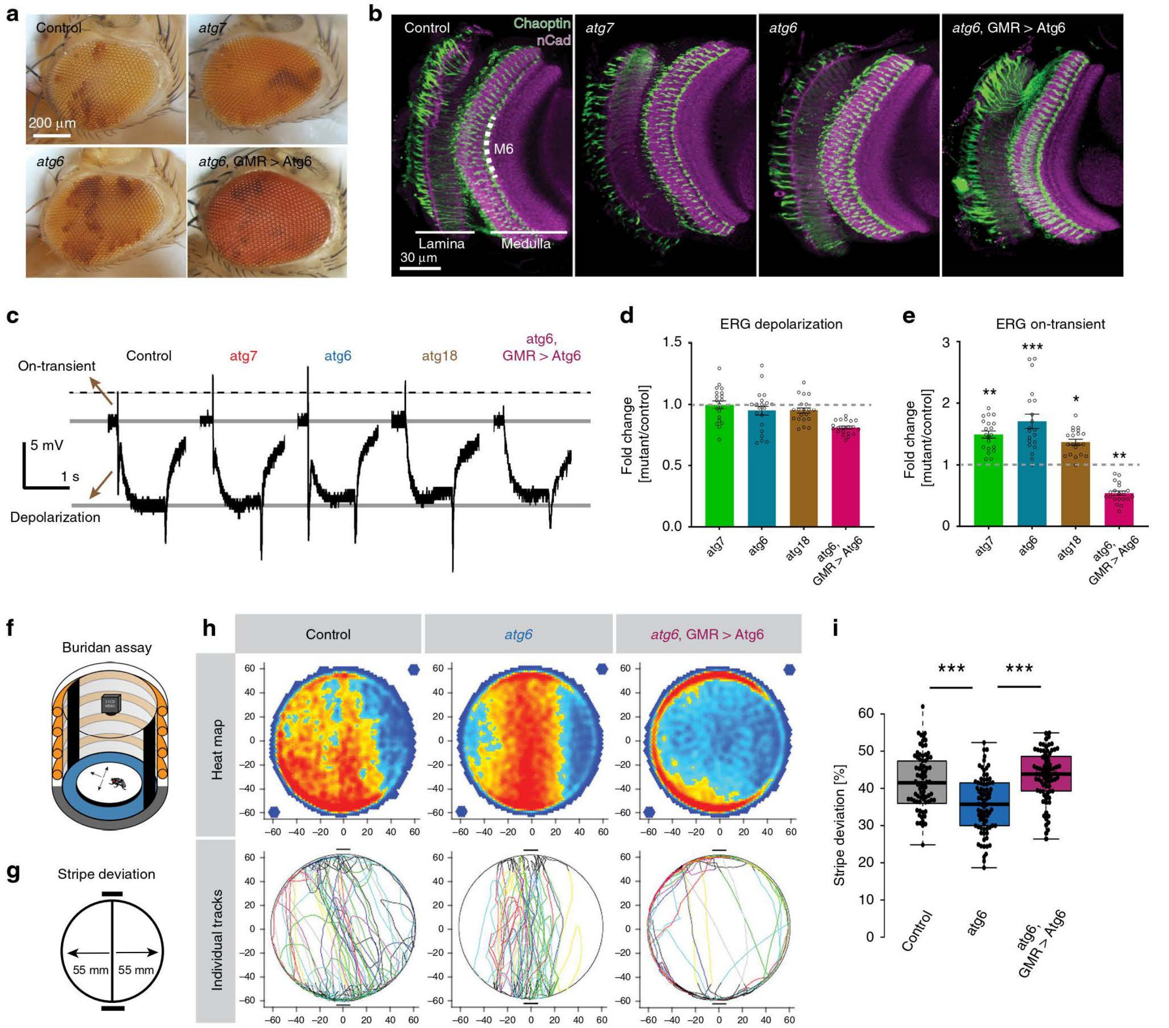

Fig. 1 Autophagy deficiency in *Drosophila* photoreceptors leads to increased neurotransmission and visual attention. a, **b** Newly hatched (0-day-old) genetic mosaic flies with autophagy-deficient (*atg6* and *atg7* mutants) photoreceptors exhibit normal eye morphology (**a**) and axonal projections in the optic lobe (**b**). Repeated three times independently. **c** Representative electroretinogram (ERG) traces. Repeated three times independently. **d**, **e** Quantification of ERG depolarization (**d**) and on-transient (**e**) amplitudes relative to control. Rescue of *atg6* mutant photoreceptors with GMR > atg6 expression leads to overcompensation and increased autophagy (see Supplementary Fig. 1). $n = 20$ flies per condition. Two-tailed unpaired t-test with Welch's correction; $^*p < 0.05$, $^{**}p < 0.01$, $^{***}p < 0.001$. Error bars denote mean ± SEM. **f** Buridan's paradigm arena to measure object orientation response of adult flies, with two black stripes positioned opposite to each other as visual cues. **g** The parameter "stripe deviation"' measures how much a fly deviates from a straight path between the black stripes in the arena. **h** Stripe fixation behavior of adult flies with *atg6* mutant photoreceptors, photoreceptors with upregulated autophagy (*atg6*, GMR > Atg6), and their genetically matched controls are shown on the population level (heatmap) and as individual tracks. Flies with *atg6* mutant photoreceptors show reduced stripe deviation, whereas increased autophagy (*atg6*, GMR > Atg6) leads to increased stripe deviation. **i** Quantification of stripe deviation. The error bars indicate the 25th percentile, the boxed area the 75th percentile, and the middle line of the boxplots indicates the median. $n = 60$ flies per condition, two-way ANOVA and Tukey's HSD as post-hoc test; $^{***}p < 0.001$. Source data are provided as a Source Data file.

clockwise and clockwise motion (see Methods; Supplementary Fig. 4e–l). We conclude that flies with photoreceptors that developed in the absence of autophagy can see, but their vision is characterized by both increased neurotransmission and increased visual attention.

Autophagy-deficient photoreceptors form supernumerary synapses. To assess whether the alterations in neurotransmission and vision were due to altered numbers of synapses, we generated sparse clones of photoreceptors R1–R6 and R7 expressing the active zone marker GFP-Brp$^{\text{short}}$. This marker specifically localizes to presynaptic active zones without affecting synaptic development or function and is suitable for live imaging[14,38]. Loss of *atg6*, *atg7*, or *atg18*, as well as downregulation of *atg5* or *atg16* by RNAi resulted in a 25–80% increase in synapse numbers, whereas increased autophagy in rescued *atg6* mutant photoreceptors reversed this effect and significantly reduced synapse

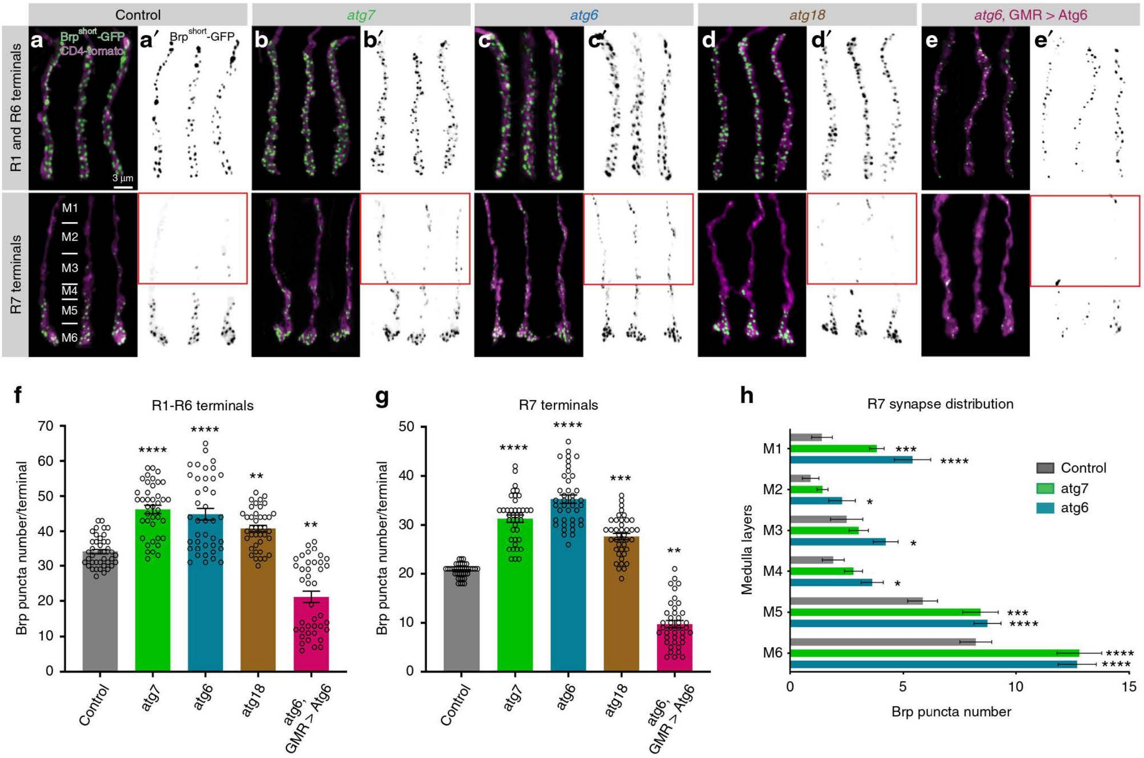

Fig. 2 Autophagy-deficient *Drosophila* photoreceptors form supernumerary synapses. a–e′ Representative images of R1–R6 and R7 photoreceptor axon terminals with Brp^{short}-GFP marked active zones in wild-type (**a**, **a′**), *atg7* mutant (**b**, **b′**), *atg6* mutant (**c**, **c′**), *atg18* mutant (**d**, **d′**), and *atg6*, GMR > Atg6 (**e**, **e′**). R7 axon terminals are shown from distal (top) to proximal (bottom) medulla. Relative thicknesses of medulla layers are shown in Control R7 terminals panel (**a**) along R7 axon terminals. Red boxes show supernumerary synapses in loss of autophagy at distal part of R7 axon terminals. Repeated five to ten times independently with similar results. **f**, **g** Number of Brp puncta per terminal in R1-R6 (**f**) and R7 (**g**) photoreceptors. $n = 40$ terminals per condition. Kruskal–Wallis and Dunn's as post-hoc test; $^{**}p < 0.01$, $^{***}p < 0.001$, $^{****}p < 0.0001$. Error bars denote mean ± SEM. **h** Number of Brp puncta in distinct medulla layers along R7 axon terminals (see Methods for the definition of medulla layers and **a** for relative thicknesses of medulla layers). $n = 22$ terminals for control, $n = 30$ terminals for *atg7*, $n = 27$ terminals for *atg6*. Kruskal–Wallis and Dunn's as post-hoc test; $^{*}p < 0.05$, $^{***}p < 0.001$, $^{****}p < 0.0001$. Error bars denote mean ± SEM. Source data are provided as a Source Data file.

numbers (Fig. 2a–g and Supplementary Fig. 2h, i). In contrast, overexpression of *atg6* did not rescue *atg7* mutant photoreceptors, supporting the notion that *atg7* is absolutely required for autophagy and overexpression of *atg6* has no autophagy-independent effect in this system (Supplementary Fig. 5a, b).

Photoreceptors R1–R6 form columnar terminals in a single layer neuropil, whereas R7 axon terminals span six morphologically distinct layers and form the majority of synapses in the most proximal layer M6[17,39]. We were therefore surprised to see many supernumerary synapses in autophagy-deficient R7 axon terminals at more distal layers M1–M3 (Fig. 2h and red boxes in Fig. 2a–e'). These putative synapses along the distal shaft of autophagy-deficient R7 axons were stable based on live imaging of Brp^{short}-labeled active zones with 15 min resolution over several hours at P70 (70% pupal development; Supplementary Movie 1). Brp stability is indicative of mature synapses and suggests that ectopic Brp puncta in fixed images are not the consequence of axonal transport defects or defective synaptic capture of Brp-positive transport vesicles. These observations raised the question whether loss of autophagy leads to genuine supernumerary synapses and, if so, whether these would be formed with correct postsynaptic partners.

Autophagy-deficient R7s contact incorrect synaptic partners. The synaptic partners of R7 photoreceptors have been quantitatively characterized based on electron microscopy (EM) reconstruction of several medulla columns, revealing highly stereotypic connections[17]. The main postsynaptic target of R7 photoreceptors is the wide-field amacrine neuron Dm8[17,40]. Apart from Dm8s, R7s form fewer connections with Tm5 neuron subtypes that have dendritic fields spanning from M3 to M6[39,40]. To identify the postsynaptic partners of autophagy-deficient R7 photoreceptors, we used the recently developed anterograde *trans*-synaptic tracing method "*trans*-Tango," which labels postsynaptic neurons for a given neuron without a need for previous knowledge about the nature of the connections[41]. In brief, the method is based on a synthetic signaling pathway that is introduced into all neurons in the animal, but only *trans*-synaptically activated by a tethered ligand expressed in a specific presynaptic neuron[41]. We used an R7-specific driver (Rhodopsin4-Gal4) and restricted its expression to mutant R7 photoreceptors, whereas all other neurons, including all postsynaptic partners, are wild type. Consistent with known postsynaptic targets of R7s, *trans*-Tango with wild-type R7s mainly labeled Dm8s and Tm5s (Fig. 3a and Supplementary Fig. 6). By contrast, loss of *atg6* or *atg18* in R7s led to a more

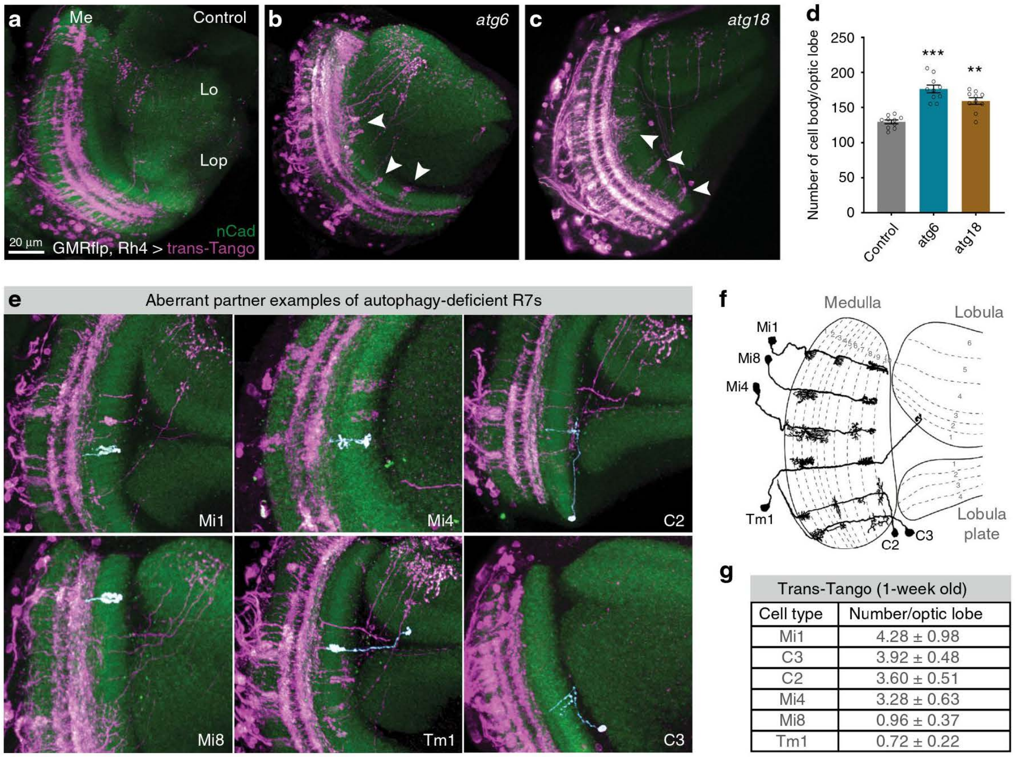

Trans-Tango (1-week old)	
Cell type	Number/optic lobe
Mi1	4.28 ± 0.98
C3	3.92 ± 0.48
C2	3.60 ± 0.51
Mi4	3.28 ± 0.63
Mi8	0.96 ± 0.37
Tm1	0.72 ± 0.22

Fig. 3 Loss of autophagy leads to synaptic connections with aberrant neuronal partners. a–c Neurons postsynaptic to control (**a**), *atg6* mutant (**b**), and *atg18* mutant (**c**) R7s are labeled with *trans*-Tango (see Methods for full genotypes; magenta = postsynaptic neurons, green = CadN, Me = medulla, Lo = lobula, Lop = Lobula plate). Arrowheads show postsynaptic neurons labeled for autophagy-deficient R7s but not for control R7s. Repeated three to five times independently with similar results. **d** Number of postsynaptic neurons per optic lobe for control, *atg6* mutant, and *atg18* mutant R7s based on *trans*-Tango-labeled cell body counts. $n = 10$ optic lobes per condition. One-way ANOVA and Tukey's HSD as post-hoc test $^{**}p < 0.01$, $^{***}p < 0.001$. Error bars denote mean ± SEM. **e** Examples of aberrant neuronal partners of autophagy-deficient R7s, with individual neurons pseudo-colored in white. **f** Schematic of dendritic and axonal arborization of aberrant neuronal partners (redrawn and adapted based on Golgi impregnations from Fischbach and Dittrich[46]). **g** Number of each aberrant neuronal partners per optic lobe from 1-week-old fly brains. Note that only ~10% of R7s are mutant for *atg6* and *trans*-Tango labeling is dependent on synaptic strength between partners and progressively increase through age. See Methods for detailed *Drosophila* genotypes used to perform *trans*-Tango experiments. Source data are provided as a Source Data file.

widespread labeling of postsynaptic neurons (Fig. 3b, c) and an overall increase of the number of postsynaptically connected cells, as expected for supernumerary functional synapses (Fig. 3d). Through application of a sparse-labeling protocol of *trans*-Tango, we further identified several cell types, including Mi1, Mi4, Mi8, Tm1, C2, and C3, which are not normally postsynaptic to R7 based on connectome data[15,17,42,43] (Fig. 3e, f). Mi1 and Mi4, e.g., are part of the motion-detection pathway, to which R7 is not known to provide input[44,45]. Notably, the number of individual neurons detected for these six ectopically connected neurons correlated distinctly with the position of their presumptive dendritic trees: Mi1, C3, and C2 were most often labeled and all three have presumptive dendrites in layers M1 and M5 (Fig. 3f, g)[46]; most ectopic R7 synapses were detected in layer M1, M5, and M6 (Fig. 2h); at the other end of the spectrum, Mi8 and Tm1 were both four-to fivefold less often detected and have presumptive dendrites in layer M2 and M3, where we counted fewer ectopic synapses (Figs. 2h and 3f, g)[46]. These findings suggest that the postsynaptic neurons labeled by *trans*-Tango are incorrect partners connected through axon-dendritic contacts with R7.

Synapses with incorrect postsynaptic neurons are functional. To test whether these contacts are functional synapses, we next used the activity-dependent GRASP method (Green fluorescent protein [GFP] reconstitution across synaptic partners), which is based on *trans*-synaptic complementation of split GFP only when synaptic vesicle release occurs[47,48]. Based on available cell-specific driver lines and the underlying genetics, we could test three of the ectopic pairs identified with *trans*-Tango: potential synapses between R7 and Mi1, C2 or Mi4. For all three cases, wild-type neurons rarely showed isolated synaptic signals (Fig. 4a–c'). In contrast, *atg6* mutant photoreceptors formed abundant synapses in all three cases (Fig. 4d–f'). All three incorrect synaptic pairings were validated for *atg18* mutant photoreceptors, albeit at lower levels (Fig. 4g–i). These findings based on activity-dependent GRASP also indicate that the *trans*-Tango results were not due to an effect of altered autophagy on the ectopically expressed proteins of the *trans*-Tango system. We conclude that loss of autophagy in R7 photoreceptor terminals leads to ectopic synapse formation with inappropriate postsynaptic neurons.

Taken together, our observations reveal that loss of autophagy in photoreceptors does not affect overall axon terminal morphology and transmission of visual input, but selectively leads to increased synapse formation, which includes inappropriate postsynaptic partners, and increased visual attention behavior.

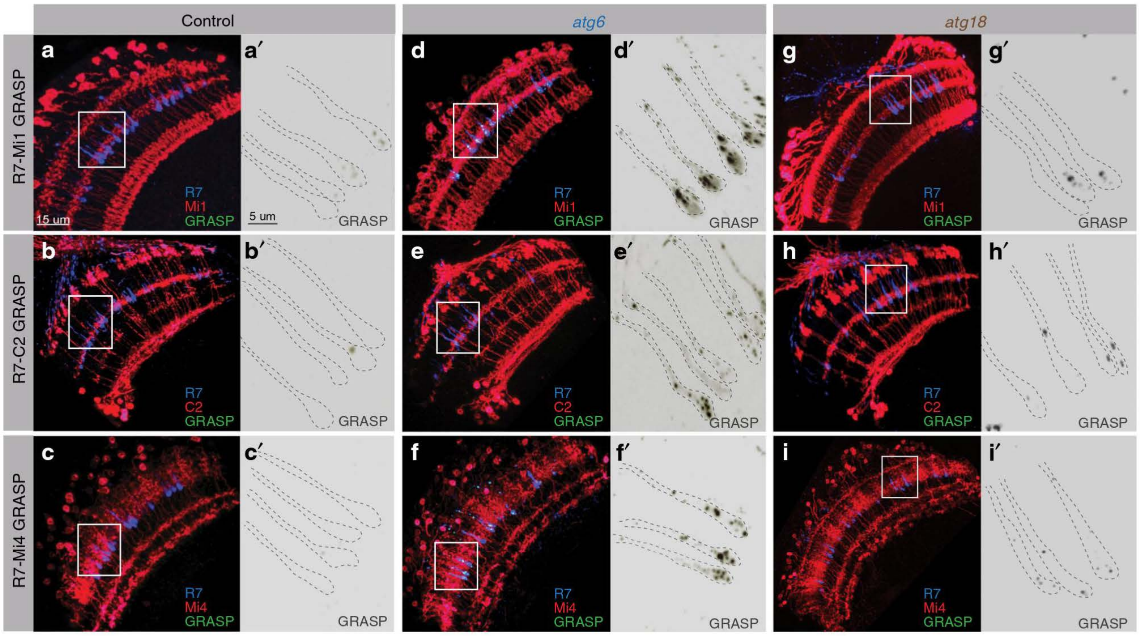

Fig. 4 Synaptic connections between autophagy-deficient R7s and aberrant postsynaptic partners are functional based on activity-dependent GRASP. **a**–**c′** Activity-dependent GRASP between control R7s and Mi1s (**a**, **a′**), C2s (**b**, **b′**), and Mi4s (**c**, **c′**) show that wild-type R7s very rarely form synaptic connections, if any, with Mi1, C2, and Mi4 neurons. **d**–**f′** Activity-dependent GRASP between *atg6* mutant R7s and Mi1s (**d**, **d′**), C2s (**e**, **e′**), and Mi4s (**f**, **f′**) show widespread active synaptic connections between autophagy-deficient R7s and aberrant postsynaptic partners. **g**, **i′**, Activity-dependent GRASP between *atg18* mutant R7s and Mi1s (**g**, **g′**), C2s (**h**, **h′**), and Mi4s (**i**, **i′**) show less frequent active synaptic connections compared with *atg6* mutants. Note that Atg18 loss-of-function does not block autophagosome formation as effective as Atg6 loss-of-function (see Supplementary Fig. 1). Regions inside yellow rectangles are shown in close-up images as single greyscale GRASP channels. See Methods for Mi1, Mi4, and C2-specific LexA drivers and detailed *Drosophila* genotypes used to perform GRASP experiments. Repeated three times independently with similar results.

However, how does defective autophagy at the developing presynapse affect synaptic partner choice mechanistically?

Autophagy modulates the stability of synaptogenic filopodia. To test when and where exactly autophagosomes function during synapse formation, we performed live-imaging experiments of autophagosome formation in developing R7 axon terminals in developing brains. Autophagosomes have previously been shown to form at axon terminals in vertebrate primary neuronal cell culture using the temporal series of autophagosome progression reporters GFP-Atg5 (early) and GFP-Atg8a (late)[49]. We used the same markers to track autophagosome progression after validation that overexpression of neither of these proteins affect development, neurotransmission, or synapse numbers in fly photoreceptors (Supplementary Fig. 7). Surprisingly, we detected autophagosome formation based on these probes selectively at the rare, bulbous tips of synaptogenic filopodia of R7 axon terminals, followed by filopodial collapse (Fig. 5a, Supplementary Fig. 8, and Supplementary Movie 2).

We have recently shown that altered numbers of synaptogenic filopodia lead to changes in synapse numbers[14]. We therefore tested the effects of a loss of autophagy on R7 axon terminal filopodial dynamics during synapse formation (developmental time point P60). Both *atg6* and *atg7* mutants exhibited selectively increased lifetimes of the population of long-lived axonal filopodia compared with wild-type and *atg6*-rescued photoreceptors (Supplementary Fig. 9 and Supplementary Table 1). Wild-type axon terminals only formed one to two synaptogenic filopodia, as characterized by their bulbous tips, at any point in time (Fig. 5b, f–g), which previously led us to propose a serial synapse formation process that slowly spreads out the formation of 20–25 synapses over 50 h[14] (also see Supplementary Movie 3). In contrast, loss of *atg6* or *atg7* in R7 axon terminals led to three to four synaptogenic filopodia at any time point (Fig. 5c, d, f, g and Supplementary Movie 3). As expected for synaptogenic filopodia, almost all supernumerary bulbous tips were stable for more than 40 min (Fig. 5g). Increased autophagy in *atg6*-rescued mutant photoreceptors reversed this effect and lead to a significant reduction and destabilization of synaptogenic filopodia (Fig. 5e–g and Supplementary Movie 3). By contrast, *atg6* overexpression in *atg7* mutant photoreceptors did not alter the increased filopodial stability of *atg7* mutants (Supplementary Fig. 5c), indicating that levels of *atg6* affect filopodia stability in an autophagy-dependent manner. Consistent with selective autophagosome formation in synaptogenic filopodia tips, the changes to filopodial dynamics were remarkably specific to long-lived, synaptogenic filopodia (Fig. 5b–g, Supplementary Fig. 9, and Supplementary Table 1). In sum, analyses of R7 axon terminal dynamics during synapse formation in the intact brain revealed autophagosome formation in synaptogenic filopodia and a specific effect of autophagy function on the kinetics and stability of these filopodia.

A filopodial dynamics model predicts altered synapse numbers. Next we asked whether the observed changes to the kinetics of synaptogenic filopodia are sufficient to quantitatively explain changes in synapse formation throughout the second half of fly brain development. We first counted the numbers of overall filopodia, bulbous tip filopodia, and synapses at time points every 10 h between P40 and P100 in fixed preparations (Fig. 6a–c).

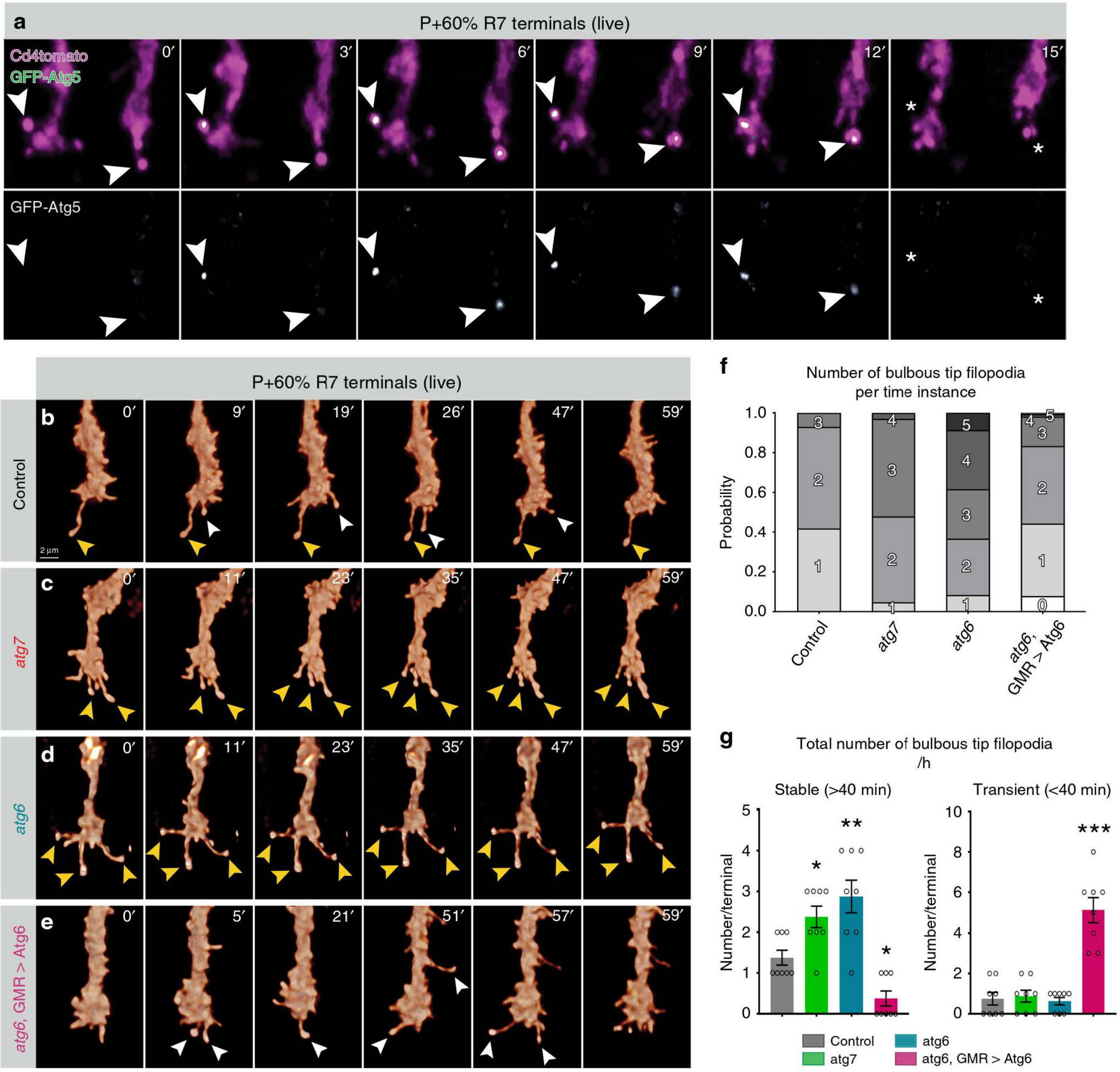
a
P+60% R7 terminals (live)
Cd4tomato
GFP-Atg5
0′
3′
6′
9′
12′
15′
GFP-Atg5
P+60% R7 terminals (live)
b
Control
0′
9′
19′
26′
47′
59′
2 µm
c
atg7
0′
11′
23′
35′
47′
59′
d
atg6
0′
11′
23′
35′
47′
59′
e
atg6, GMR > Atg6
0′
5′
21′
51′
57′
59′
f
Number of bulbous tip filopodia per time instance
Probability
1.0
0.8
0.6
0.4
0.2
0.0
Control
atg7
atg6
atg6, GMR > Atg6
g
Total number of bulbous tip filopodia /h
Stable (>40 min)
Transient (<40 min)
Number/terminal
*
**
*
***
Control
atg7
atg6
atg6, GMR > Atg6

Fig. 5 Autophagy regulates the stability of synaptogenic filopodia at axon terminals. a Live imaging of GFP-Atg5-expressing R7 axon terminals in intact, developing *Drosophila* brain shows formation of autophagosomes at the bulbous tips of synaptogenic filopodia[14] followed by the collapse of filopodia (P + 60%). Repeated three times independently with similar results. **b**–**e** Live imaging of R7 axon terminals at P + 60% (during synaptogenesis) revealed increased stability of synaptogenic filopodia in autophagy-deficient R7 terminals (**c**, **d**) and decreased stability in R7 terminals with upregulated autophagy (**e**) compared with control (**b**). Yellow arrowheads: stable synaptogenic filopodia; white arrowheads: unstable bulbous tip filopodia. Repeated five to ten times independently with similar results. **f** Number of concurrently existing bulbous tip filopodia per R7 axon terminal per time instance. **g** Total number of synaptogenic filopodia per R7 axon terminal per hour. Autophagy-deficient R7 terminals exhibit significantly more stable synaptogenic filopodia (>40 min), whereas upregulated autophagy leads to filopodia destabilization. $n = 8$ terminals per condition. One-way ANOVA and Tukey's HSD as post-hoc test; *$p < 0.05$, **$p < 0.01$, ***$p < 0.001$. Error bars denote mean ± SEM. Source data are provided as a Source Data file.

Compared with control, loss of *atg6* or *atg7* in photoreceptors led to mild increases in overall filopodia, while leaving the rates of change largely unaltered between time points (Fig. 6a). In contrast, numbers of synaptogenic bulbous tip filopodia are increased twofold throughout the main period of synapse formation (P60–P80; Fig. 6b and Supplementary Fig. 10). Synapse numbers, based on presynaptic Brp^{short} labeling, commences indistinguishably from wild type, but then increases at a higher rate throughout brain development (Fig. 6c).

We previously developed a data-driven Markov state model that predicts the slow, serial development of synapses throughout the second half of brain development based on stochastic filopodial exploration and one-by-one selection of synaptogenic filopodia[14]. To test how autophagy-dependent changes of filopodial kinetics affect synapse formation in the model, we used the measured live dynamics of filopodia at P60 (Fig. 5b–g, Supplementary Fig. 9, and Supplementary Tables 1–3) together with the measured fixed time points data for filopodia (Fig. 6a, b

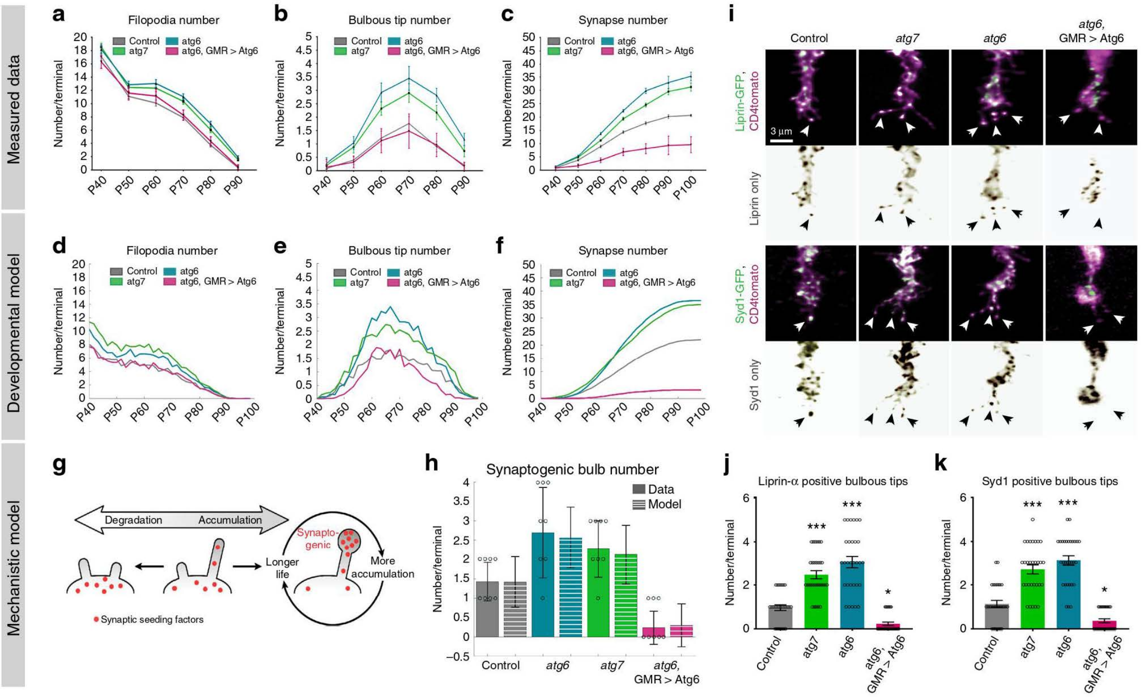

Fig. 6 Loss of autophagy increases the number of synaptogenic filopodia through defective synaptic seeding factor degradation, leading to increased synapse formation throughout development. a–c Quantification of filopodia numbers (**a**), synaptogenic filopodia numbers (**b**), and Brp puncta numbers (**c**) during synaptogenesis (P40–P90) per R7 axon terminal based on fixed data. $n = 40$ terminals per condition. **d–f** Markov State Model simulation based on data in (**a**) and live data at P + 60% (Fig. 5) for filopodia numbers (**d**), synaptogenic filopodia numbers (**e**), and Brp puncta numbers per R7 axon terminal (**f**). **g** The mechanistic model: accumulation of synaptic seeding factors stabilizes synaptogenic filopodia; autophagic degradation of synaptic seeding factors destabilizes filopodia. **h** Measured (solid bars) and simulated (striped bars) synaptogenic filopodia numbers at P + 60% (the simulated data are based on synaptic seeding factor availability, see Supplementary Fig. 6). $n = 8$ axon terminals from independent live-imaging sessions. **i** Representative images of synaptic seeding factors (Syd-1 and Liprin-α) localizing to synaptogenic filopodia. Repeated three times independently with similar results. **j**, **k** Quantifications of the number of Liprin-α (**j**) and Syd-1 (**k**) positive synaptogenic filopodia. $n = 30$ terminals per condition. Kruskal–Wallis and Dunn's as post-hoc test; $^{*}p < 0.05$, $^{***}p < 0.001$. Error bars denote mean ± SEM. Source data are provided as a Source Data file.

and Supplementary Fig. 10) as input. As shown in Fig. 6d–f, the model recapitulates all aspects of synaptogenic filopodial dynamics and synapse formation for both loss and upregulation of autophagy. The model thereby shows that the measured changes in filopodial kinetics, and specifically altered stabilization of synaptogenic filopodia, are sufficient to cause the observed alterations in synapse formation over time (see "Mathematical modeling" in Methods). These findings raise the question how autophagy can specifically regulate the kinetics of synaptogenic filopodia mechanistically.

Degradiation of synaptic proteins tunes filopodia kinetics. We have previously shown that the early synaptic seeding factors Syd-1 and Liprin-α are allocated to only one to two filopodia at any given time point, and that their loss leads to the destabilization of synaptogenic filopodia and a loss of synapses[14]. Autophagy is a protein degradation pathway that affects filopodia stability in opposite ways in loss- vs. gain-of-function experiments. We therefore hypothesized that autophagic degradation may directly regulate the availability of synaptic building material in filopodia. We first tested this idea using a second Markov state model that simulates the stabilization of filopodia as a function of seeding factor accumulation and degradation on short time scales (Fig. 6g and Supplementary Fig. 11a). In this "winner-takes-all" model, synaptic seeding factors are a limiting resources in filopodia that increase filopodia lifetime, which in turn increases the time available for further accumulation of synaptic seeding factors, creating a positive feedback loop[14]. If autophagy plays a role in the degradation of synaptic seeding factors, then decreased autophagic degradation of synaptic seeding factors should lead to more synaptogenic filopodia, whereas increased autophagic degradation should reduce synaptogenic filopodia through further restriction of the limiting resource (Fig. 6g and Supplementary Fig. 11a). The simulations show that the measured number of synaptogenic filopodia (Fig. 6h) and their lifetimes (Supplementary Fig. 11) can be quantitatively explained by degradation and thus availability of synaptic seeding factors for both loss and upregulation of autophagy at P60. Specifically, the number of long-lived filopodia at autophagy-deficient axon terminals was increased compared with control and conversely increased autophagic activity led to a decreased lifespan of filopodia as measured (Supplementary Fig. 9 and Supplementary Table 1). Hence, the mechanistic model predicts that modulation of autophagy affects the degradation and availability of synaptic seeding factors. This primary defect causes secondary changes to filopodial kinetics and synapse formation.

To validate the primary defect, we expressed GFP-tagged versions of the synaptic seeding factors Syd-1 and Liprin-α, and analyzed their restricted localization to synaptogenic filopodia. We use GFP-tagged versions of both proteins that we have previously shown to not affect development or function of fly photoreceptors[14]; furthermore, we validated the function of the tagged proteins by using them to rescue their respective null mutant phenotypes in photoreceptors (Supplementary Fig. 12). Using these probes, we found that autophagy-deficient terminals contain two to three times more synaptogenic filopodia with synaptic seeding factors compared with control; conversely, upregulation of autophagy leads to reduction of seeding factors in filopodia (Fig. 6i–k). In addition, the majority of Atg8a-positive autophagosomes present at filopodia tips colocalizes with with Syd-1 and Liprin-α (Supplementary Fig. 13a–c). Previous work in primary vertebrate neuronal culture as well as *Drosophila* R1–R6 photoreceptors has shown that autophagosomes formed at axon terminals traffic retrogradely to the cell body[29,49]. We therefore analyzed photoreceptor cell bodies and detected large Atg8a-positive compartments containing Syd-1 and Liprin-α (Supplementary Fig. 13d–d"). We previously implicated the upstream receptor Lar and the downstream signaling protein Trio in the kinetic regulation of synaptogenic filopodia[14]. Of these, we only detected the cytosolic protein Trio inside Atg8a-positive compartments, but not the transmembrane receptor Lar, suggesting differential availability to autophagosomal engulfment (Supplementary Fig. 13e, f'). Together, these findings indicate that autophagy controls the amount of synaptic seeding factors in filopodia, while degradation may occur during axonal transport and in cell bodies (Supplementary Fig. 13g).

Autophagy sets a global threshold for kinetic restriction. Autophagy-dependent filopodial kinetics and synapse formation could lead to synapses with incorrect partners through at least two mechanisms. In one scenario, autophagy could be triggered only in specific filopodia, e.g., based on a molecular signal for a contact with an incorrect partner neuron in a wrong layer. Loss of autophagy would then lead to a defect in the specific removal of incorrect synapses. In support of this idea, specific presynaptic proteins have recently been shown to induce autophagy at specific places in the presynapse[50,51]. Alternatively, autophagy could set a global threshold for kinetic restriction for the entire axon terminal, such that only synaptic partners with sufficient spatial availability and molecular affinity can form synapses.

To distinguish between these two models, we quantified the relative increases of all filopodia, synaptogenic filopodia, and synapses along the R7 axon terminal in medulla layers M1–M6 (Fig. 7a–d). Loss of either *atg6* or *atg7* increases the absolute numbers of synaptogenic filopodia and synapses in all medulla layers equally ~1.5-fold (dotted lines in Fig. 7b–d). As a result, the relative levels of synaptogenic filopodia and synapses between layers M1–M6 remain the same as in wild type (solid lines in Fig. 7b–d). These data indicate that autophagy is not differentially triggered in filopodia in specific medulla layers. Instead, loss of autophagy equally increases the stability of synaptogenic filopodia across the R7 terminal, resulting in the stabilization of only few filopodia in layers with low baseline filopodial activity and more pronounced increases in layers with higher baseline filopodial activity. Conversely, destabilization of filopodia along the entire R7 axon terminal in wild type effectively excludes synapse formation in layers with few filopodia, e.g., in layer M2 (Fig. 7a–d). We conclude that autophagy levels set a threshold for kinetic restriction across the R7 axon terminal.

The threshold for kinetic restriction effectively excludes synapse formation with at least six potential postsynaptic partners that are not otherwise prevented from forming synapses with R7 (Fig. 7e). We note that the localization of the presumptive dendritic trees of these six neuron types correlates well with the probabilities to be incorrectly recruited as postsynaptic partners (Figs. 3f and 7e). We speculate that specificity arises through a combination of context-dependent molecular interactions, positional effects, and kinetic restriction rather than any single factor.

Discussion

Brain wiring requires synaptic partner choices that are both specific and robust in time and space[52]. To what extent spatiotemporal vicinity of potential partner neurons facilitates or determines partner choice remains unclear. Our findings suggest that spatiotemporal vicinity is restricted by filopodial kinetics, and that axon terminal autophagy functions as a modulator of these dynamics. Hence, kinetic restriction of synaptogenic filopodia is a means to effectively exclude synapse formation with incorrect partners (Fig. 7e). Conversely, increased stabilization of synaptogenic filopodia is sufficient to recruit as synaptic partners a surprisingly varied population of interneurons that have the principle capacity to form synapses with R7 axon terminals. At least Mi1, Mi4, C3, C2, Mi8, and Tm1 neurons in medulla columns are not prevented by "molecular mismatch" from forming synaptic contacts with R7 in vivo.

Our findings suggest that kinetic restriction sharpens synaptic specificity based on promiscuous synapse formation. Numerous studies have shown that neurons in ectopic locations readily form synapses with incorrect partners, including themselves[6,7,53]. On the other hand, Mi1, Mi4, C3, C2, Mi8, and Tm1 are all likely to express different cell surface proteins that may bias the likelihood of synaptic contacts[10,16,54]. Our data suggest that R7 terminals can form synapses with these incorrect partners simply by slowing down and stabilizing filopodial interactions. We conclude that axonal and dendritic interaction dynamics may greatly facilitate, or restrict, what partner neurons get "to see each other" and initiate synapse formation. This model requires a certain level of promiscuity in the ability to form synapses, while still being consistent with the idea of biasing certain interactions over others based on molecular interactions[1]. Recent evidence highlighted the importance of positional strategies for synaptic partner choice prior to such molecular interactions[7,11,53]. Here we have shown that positional effects are dynamic and subject to stabilization kinetics, not only when and where neuronal processes can be seen in fixed preparations. We propose that an "instruction" for synapse formation may be the product of the composite action of several factors that by themselves appear "permissive" and affect when and where neuronal surfaces meet. For example, positioning and interaction kinetics that are regulated by autophagy restrict which cell surfaces get to engage in adhesive or repellent interactions. Hence, synaptic specificity can emerge from the context-dependent combination of molecular interactions with a cell biological mechanism such as autophagy, which by itself carries no synaptic specificity information. We speculate that different neuronal thresholds for kinetic restriction can critically contribute to sharpen specificity as part of the brain's developmental growth program.

Our findings suggest a novel role for developmental autophagy in synapse formation and brain wiring. Specifically, we report that autophagy indiscriminately destabilizes R7 synaptogenic filopodia in a manner consistent with the local degradation of a limiting resource of proteins required for synapse formation. Specificity of autophagic degradation can be triggered through interactions with proteins that themselves serve as cargo or restrict the time and place where potentially less specific engulfment occurs[19,50,51]. The bulbous tips of synaptogenic filopodia are a small space that may be easily destabilized through autophagic engulfment of proteins and other cargo, even if that engulfment were to occur in a non-selective manner. We therefore speculate that a putative cargo-specificity of autophagy may not be a prerequisite for the developmental function of autophagy described here.

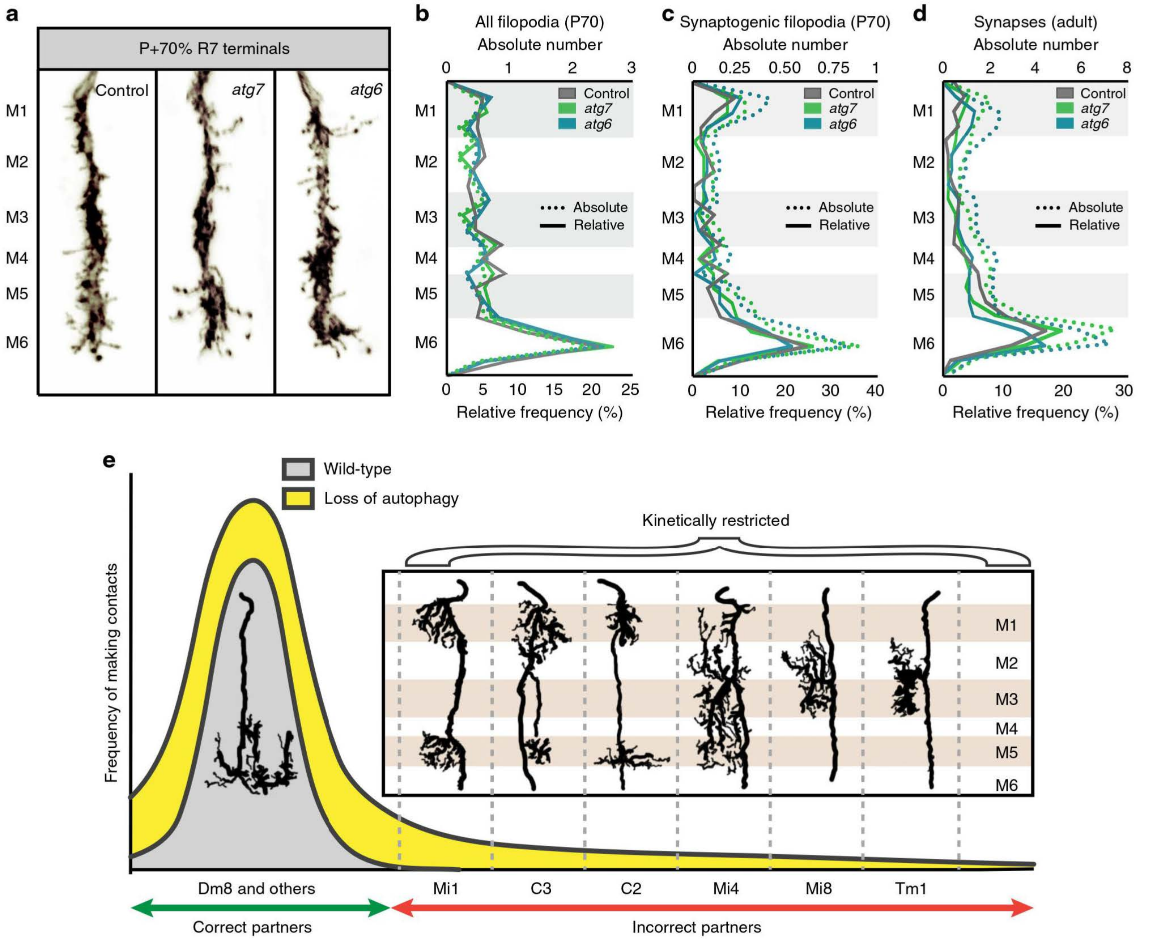

Fig. 7 Loss of autophagy recruits incorrect synaptic partners by lowering an axon terminal-wide threshold for kinetic restriction of synapse formation. **a** Representative R7 axon terminals at P + 70% with medulla layer information. Note that the edge of medulla (M0) is defined as 0 and the end of M6 layer is defined as 100 to calculate relative positions of all filopodia and bulbous tip filopodia, and distributed to medulla layers (M1–M6) using the relative thickness of medulla layers defined by Fischbach and Dittrich[46]. Repeated five to ten times independently with similar results. **b**–**d** Relative frequency (solid lines) and absolute numbers (dotted lines) of all filopodia at P + 70% (**b**), synaptogenic filopodia at P + 70% (**c**), and synapses at 0-day-old adult (**d**). M1–M6 denote medulla layers. $n = 40$ terminals per condition. **e** Model: loss of autophagy during synaptogenesis increases the probability distribution (yellow area) compared with wild-type (gray area) of forming connections with postsynaptic partners through increased filopodial stability. Note that cells with projections at medulla layers where R7s form most of their synapses (Mi1, Mi4, C2, C3) incorrectly synapse with R7s, with higher probability than the cells with projections at medulla layers where R7s form a few, if any, synapses (Mi8, Tm1) (see Fig. 3e, f). Redrawn and adapted based on Golgi impregnations from Fischbach and Dittrich[46]. Source data are provided as a Source Data file.

Autophagy occurs at axon terminals of adult neurons and is required for neuronal maintenance in many neurons, including *Drosophila* photoreceptors[19,31,55,56]. We currently do not know to what extent developmental autophagy and autophagy during neuronal maintenance share the same initiation signals or cargo (un-)specificity. The exclusivity with which autophagosomes form in the tips of synaptogenic filopodia of developing R7 axon terminals suggest a locally restricted trigger that may well be distinct from those found in axon terminals of mature neurons. Given similar roles of autophagy in neuronal maintenance, we think it is likely to be that our observation of a specific role for developmental autophagy in the regulation of filopodial kinetics in *Drosophila* hints at similar roles in other animals and may partially explain the supernumerary dendritic spines observed in mice previously[27].

We have previously shown that spatiotemporally regulated membrane receptor degradation is required for synapse-specific wiring in the *Drosophila* visual system[57]. Degradation and turnover of receptors and synaptic building material restrict synapse formation and contribute to specificity in a context-dependent manner. Developmentally regulated protein synthesis, trafficking, and degradation are likely to differ for different proteins and neurons at different points in time and space, where they form part of composite instructions during the growth program that give rise to specificity.

Based on this combinatorial model for specificity, we speculate that many mutations and single-nucleotide polymorphisms in the genome can result in small cell biological changes that differentially affect neurons during brain wiring. The changes effected through such modulatory, “permissive” mechanisms may not be predictable at the level of circuit wiring and behavior, yet they can cause meaningful changes to behavior that are both selectable and heritable, and thus a means of evolutionary programming of neural circuits.

Methods

***Drosophila* husbandry and strains**. Flies were reared at 25 °C on standard cornmeal/yeast diet unless stated otherwise. For developmental analyses, white pre-pupae (P + 0%) were collected and incubated at 25 °C to pupal stages stated on figures. The following *Drosophila* strains were either obtained from Bloomington *Drosophila* Stock Center (BDSC) or other groups: *atg6*^{1} and UAS-Atg6.ORF.3xHA (E.H. Baehrecke); *atg7*^{d4} (T.Neufeld); *atg18a*^{KG03090}, UAS-Brpshort-GFP, UAS-Syd-1-GFP, and UAS-Liprinα-GFP (S. Sigrist); *Trans*-tango flies (G. Barnea); GRASP flies (BDSC); ey3.5flp, GMRflp, GMR-Gal4, FRT42D, FRT80B, FRT82B, GMR-Gal80, tub-Gal80, UAS-CD4-tdGFP, UAS-CD4-tdtomato, UAS-GFP-Atg5, UAS-GFP-Atg8a, UAS-mCherry-Atg8a, UAS-Atg5RNAi (VDRC, 104461), UAS-Atg16RNAi (VDRC, 105993), GMR22F08-LexA (C2-specific driver), GMR49B06-LexA (Mi4-specific driver), and GMR19F01-LexA (Mi1-specific driver) (BDSC).

***Drosophila* genotypes**. Figure 1a–i: Controls: ey3.5flp; FRT42D/FRT42D, Cl^{w+}, ey3.5flp; GMR-Gal4/+; FRT82B/FRT82B, Cl^{w+}, ey3.5flp; GMR-Gal4/+; FRT80B/FRT80B, Cl^{w+} *atg7*: ey3.5flp; FRT42D, *atg7*^{d4}/FRT42D, Cl^{w+}, *atg6*: ey3.5flp;GMR-Gal4/+; FRT82B, *atg6*^{1}/FRT82B, Cl^{w+}, *atg18a*: ey3.5flp;GMR-Gal4/+; FRT80B, *atg18a*^{KG03090}/FRT80B, Cl^{w+} *atg6*, GMR>Atg6: ey3.5flp;GMR-Gal4/+; FRT82B, *atg6*^{1}, UAS-Atg6.ORF.3xHA /FRT82B, Cl^{w+}.

Figure 2a–h: Controls: GMRflp; FRT42D, GMR-Gal80/FRT42D; GMR-Gal4, UAS-CD4-tdtomato/UAS-Brp^{short}-GFP, GMRflp; GMR-Gal4, UAS-CD4-tdtomato/UAS-Brp^{short}-GFP; FRT80B/FRT80B, tub-Gal80, GMRflp; GMR-Gal4, UAS-CD4-tdtomato/UAS-Brp^{short}-GFP; FRT82B/FRT82B, tub-Gal80, *atg7*: GMRflp; FRT42D, GMR-Gal80/FRT42D, *atg7*^{d4}; GMR-Gal4, UAS-CD4-tdtomato/UAS-Brp^{short}-GFP, *atg6*: GMRflp; GMR-Gal4, UAS-CD4-tdtomato/UAS-Brp^{short}-GFP; FRT82B, *atg6*^{1}/FRT82B, tub-Gal80, *atg18a*: GMRflp; GMR-Gal4, UAS-CD4-tdtomato/UAS-Brp^{short}-GFP; FRT80B, *atg18a*^{KG03090}/FRT80B, tub-Gal80, *atg6*, GMR > Atg6: GMRflp; GMR-Gal4, UAS-CD4-tdtomato/UAS-Brp^{short}-GFP; FRT82B, *atg6*^{1}, UAS-Atg6.ORF.3xHA/FRT82B, tub-Gal80.

Figure 3a–g: Control: GMRflp/UAS-myrGFP, QUAS-mtdtomato(3xHA); Rh4-Gal4/*trans*-Tango; FRT82B/FRT82B, tub-Gal80, *atg6*: GMRflp/UAS-myrGFP, QUAS-mtdtomato(3xHA); Rh4-Gal4/*trans*-Tango; FRT82B, *atg6*^{1}/FRT82B, tub-Gal80, *atg18a*: GMRflp/UAS-myrGFP, QUAS-mtdtomato(3xHA); Rh4-Gal4/*trans*-Tango; FRT80B, *atg18a*^{KG03090}/FRT80B, tub-Gal80.

Figure 4a–c': Control: GMRflp; Rh4-Gal4, UAS-nSyb::splitGFP1-10, LexAop-splitGFP11::GFP/ GMR19F01-LexA (Mi1) or GMR22F08-LexA (C2) or GMR49B06-LexA (Mi4); FRT82B/FRT82B, tub-Gal80. **d-f'**, *atg6*: GMRflp; Rh4-Gal4, UAS-nSyb::splitGFP1-10, LexAop-splitGFP11::GFP/ GMR19F01-LexA (Mi1) or GMR22F08-LexA (C2) or GMR49B06-LexA (Mi4); FRT82B, *atg6*^{1}/FRT82B, tub-Gal80. **g-i'**, *atg18a*: GMRflp; Rh4-Gal4, UAS-nSyb::splitGFP1-10, LexAop-splitGFP11::GFP/ GMR19F01-LexA (Mi1) or GMR22F08-LexA (C2) or GMR49B06-LexA (Mi4); FRT80B, *atg18a*^{KG03090}/FRT80B, tub-Gal80.

Figure 5a: GMRflp; FRT42D, GMR-Gal80/FRT42D; GMR-Gal4, UAS-CD4-tdtomato/UAS-GFP-Atg5. **b-g**, Controls: GMRflp; FRT42D, GMR-Gal80/FRT42D; GMR-Gal4, UAS-CD4-tdGFP, GMRflp; GMR-Gal4, UAS-CD4-tdGFP; FRT82B, tub-Gal80/FRT82B, *atg7*: GMRflp; FRT42D, *atg7*^{d4}/FRT42D, tub-Gal80; GMR-Gal4, UAS-CD4-tdGFP, *atg6*: GMRflp; GMR-Gal4, UAS-CD4-tdGFP; FRT82B, *atg6*^{1}/FRT82B, tub-Gal80, *atg6*, GMR > Atg6: GMRflp; GMR-Gal4, UAS-CD4-tdGFP; FRT82B, *atg6*^{1}, UAS-Atg6.ORF.3xHA/FRT82B, tub-Gal80.

Figure 6a, b: Controls: GMRflp; FRT42D, GMR-Gal80/FRT42D; GMR-Gal4, UAS-CD4-tdGFP, GMRflp; GMR-Gal4, UAS-CD4-tdGFP; FRT82B, tub-Gal80/FRT82B, *atg7*: GMRflp; FRT42D, *atg7*^{d4}/FRT42D, GMR-Gal80; GMR-Gal4, UAS-CD4-tdGFP, *atg6*: GMRflp; GMR-Gal4, UAS-CD4-tdGFP; FRT82B, *atg6*^{1}/FRT82B, tub-Gal80, *atg6*, GMR > Atg6: GMRflp; GMR-Gal4, UAS-CD4-tdGFP; FRT82B, *atg6*^{1}, UAS-Atg6.ORF.3xHA/FRT82B, tub-Gal80. **c**, Control: GMRflp; FRT42D/FRT42, GMR-Gal80; GMR-Gal4, UAS-CD4-tdtomato, UAS-Brp^{short}-GFP, *atg7*: GMRflp; FRT42D, *atg7*^{d4}/FRT42, GMR-Gal80; GMR-Gal4, UAS-CD4-tdtomato, UAS-Brp^{short}-GFP, *atg6*: GMRflp; GMR-Gal4, UAS-CD4-tdtomato, UAS-Brp^{short}-GFP; FRT82B, *atg6*^{1}/FRT82B, tub-Gal80, *atg6*, GMR > Atg6: GMRflp; GMR-Gal4, UAS-CD4-tdtomato/UAS-Brp^{short}-GFP; FRT82B, *atg6*^{1}, UAS-Atg6.ORF.3xHA/FRT82B, tub-Gal80. **i-k**, Controls: GMRflp; FRT42D, UAS-Liprin-α-GFP or UAS-Syd-1-GFP/FRT42D, GMR-Gal80; GMR-Gal4, UAS-CD4-tdtomato, GMRflp; GMR-Gal4, UAS-CD4-tdtomato, UAS-Liprin-α-GFP or UAS-Syd-1-GFP; FRT82B/FRT82B, tub-Gal80, *atg7*: GMRflp; FRT42D, *atg7*^{d4}, UAS-Liprin-α-GFP or UAS-Syd-1-GFP/FRT42D, tub-Gal80; GMR-Gal4, UAS-CD4-tdtomato, *atg6*: GMRflp; GMR-Gal4, UAS-CD4-tdtomato, UAS-Liprin-α-GFP or UAS-Syd-1-GFP; FRT82B, *atg6*^{1}/FRT82B, tub-Gal80; *atg6*, GMR > Atg6: GMRflp; GMR-Gal4, UAS-CD4-tdtomato/ UAS-Liprin-α-GFP or UAS-Syd-1-GFP; FRT82B, *atg6*^{1}, UAS-Atg6.ORF.3xHA/FRT82B, tub-Gal80.

Figure 7a–c: Controls: GMRflp; FRT42D, GMR-Gal80/FRT42D; GMR-Gal4, UAS-CD4-tdGFP, GMRflp; GMR-Gal4, UAS-CD4-tdGFP; FRT82B, tub-Gal80/FRT82B, *atg7*: GMRflp; FRT42D, *atg7*^{d4}/FRT42D, GMR-Gal80; GMR-Gal4, UAS-CD4-tdGFP, *atg6*: GMRflp; GMR-Gal4, UAS-CD4-tdGFP; FRT82B, *atg6*^{1}/FRT82B, tub-Gal80. **d**, Control: GMRflp; FRT42D/FRT42, GMR-Gal80; GMR-Gal4, UAS-CD4-tdtomato, UAS-Brp^{short}-GFP, *atg7*: GMRflp; FRT42D, *atg7*^{d4}/FRT42, GMR-Gal80; GMR-Gal4, UAS-CD4-tdtomato, UAS-Brp^{short}-GFP, *atg6*: GMRflp; GMR-Gal4, UAS-CD4-tdtomato, UAS-Brp^{short}-GFP; FRT82B, *atg6*^{1}/FRT82B, tub-Gal80.

Immunohistochemistry and fixed imaging. Pupal and adult eye–brain complexes were dissected in cold Schneider's *Drosophila* medium and fixed in 4% paraformaldehyde in phosphate-buffered saline for 40 min. Tissues were washed in Phosphate-buffered saline + 0.4% Triton-X (PBST) and mounted in Vectashield (Vector Laboratories, CA). Images were obtained with a Leica TCS SP8-X white laser confocal microscope with a ×63 glycerol objective (c = 1.3). The primary antibodies used in this study with given dilutions were as follows: mouse monoclonal anti-Chaoptin (1:200; Developmental Studies Hybridoma Bank); rat monoclonal anti-nCadherin (1:100; Developmental Studies Hybridoma Bank); rabbit monoclonal anti-Atg8 (1:100; Abcam); mouse monoclonal anti-Trio (1:50; Developmental Studies Hybridoma Bank); mouse monoclonal anti-LAR (1:50; Developmental Studies Hybridoma Bank); goat polyclonal anti-GFP (1:1000; Abcam); rat monoclonal anti-GFP (1:500; BioLegend); rabbit polyclonal anti-CD4 (1:600; Atlas Antibodies); rabbit polyclonal anti-DsRed (1:500; ClonTech); rabbit anti-Syd-1 (1:500; gift from Sigrist Lab). The secondary antibodies Cy3, Cy5 (Jackson ImmunoResearch Laboratories) and Alexa488 (Invitrogen) were used in 1:500 dilution.

Brain culture and live imaging. For all ex vivo live imaging experiments an imaging window cut open removing posterior head cuticle partially. The resultant eye–brain complexes were mounted in 0.4% dialyzed low-melting agarose, covered with a round cover slip stationed on spacers in a culture dish and let it solidify for 15 mins. Modified culture medium was added fully immersing eye–brain complexes and cover slip was sealed with glue on the edges[13]. After 45 mins of incubation at room temperature live imaging was performed using a Leica SP8 MP microscope with a 40X IRAPO water objective (numerical aperture = 1.1) with a Chameleon Ti:Sapphire laser and Optical Parametric Oscillator (Coherent). For single-channel CD4-tdGFP imaging the excitation laser was set to 900 nm and for two-color GFP/tomato imaging lasers were set to 890 nm (pump) and 1090 nm (OPO).

***Trans*-tango and activity-dependent GRASP**. For both *trans*-tango and GRASP experiments, mosaic control and autophagy-deficient R7 photoreceptors were generated by mosaic analysis with a repressible cell marker (MARCM) using the combination of GMRflp and R7-specific driver Rh4-Gal4 (see "*Drosophila* genotypes" section for detailed genotypes). *Trans*-tango flies were raised at 25 °C and transferred to 18 °C on the day of eclosion[41]. After 1 week of incubation at 18 °C, brains were dissected and stained using a standard antibody staining protocol to label postsynaptic neurons of R7 photoreceptors. The number of postsynaptic neurons was counted manually from their cell bodies using cell counter plugin in Fiji including all cell bodies with weak or strong labeling to reveal all potential connections. For activity-dependent GRASP experiments, flies were transferred to UV-transparent Plexiglas vials on the day of eclosion and kept in a custom-made light box with UV light (25 °C, 20-4 light–dark cycle) for 3 days to activate UV-sensitive R7 photoreceptors. Brains were dissected and stained with a polyclonal anti-GFP antibody to label R7 photoreceptors, monoclonal anti-GFP antibody to label GRASP signal, and polyclonal anti-CD4 antibody to label postsynaptic neurons[48].

Electroretinogram recordings. Newly hatched (0-day-old) adult flies were collected and glued on slides using nontoxic school glue. Flies were exposed to alternating 1 s "on" 2 s "off" light stimulus provided by computer-controlled white LED system (MC1500; Schott). ERGs were recorded using Clampex (Axon Instruments) and quantified using Clampfit (Axon Instruments).

Buridan's paradigm object orientation assay. Fly object orientation behavior was tested according to standard protocols using flies grown in low densities in a 12/12 h light–dark cycle[35,58]. The behavioral arena consisted of a round platform of 117 mm in diameter, surrounded by a water-filled moat and placed inside a uniformly illuminated white cylinder. The setup was illuminated with four circular fluorescent tubes (Osram, L 40w, 640 C circular cool white) powered by an Osram Quicktronic QT-M 1 × 26–42. The four fluorescent tubes were located outside of a cylindrical diffuser (DeBanier, Belgium, 2090051, Kalk transparent, 180 g, white) positioned 147.5 mm from the arena center. The temperature on the platform during the experiment was 25 °C and 30 mm-wide stripes of black cardboard were placed on the inside of the diffuser. The retinal size of the stripes depended on the position of the fly on the platform and ranged from 8.4° to 19.6° in width (11.7° in the center of the platform). Fly tracks were analyzed using CeTrAn[35] and custom-written python code[58]. We evaluated several behavioral parameters, including center deviation and absolute distance walked, and focused on absolute stripe deviation as a parameter that gives an estimate of how precise the animals follow an object-orientated path. It is calculated as an average of all points of the fly path away from an imaginary line through the two black vertical bars. For the absolute stripe deviation, it is irrelevant whether the fly deviates to the right or left. The data was statistically analyzed using analysis of variance (ANOVA) and Tukey's honestly significant difference (HSD) as a post-hoc test using R.

Motion vision assay. Four-day-old female flies were immobilized on ice and glued to steel pins (7 mm × 100 µm, ENTO SPHINX s.r.o., Czech Republic) at a 60° angle from horizontal using UV-cured glue (Bondic). After a recovery time of at least 30 min, tethered flies were placed between two vertically aligned magnets. The magnetic field kept flies centered within the arena but allowed them to freely rotate 360° around their yaw-axis. For 5 min, each fly was presented with a rotating 360° panoramic pattern of green vertical bars displayed through an LED matrix (Adafruit), spanning 360° azimuthal and 45° vertical of the visual field (square wave pattern, one period = 45° azimuthal, angular velocity = 50 deg/s). An Arduino controller triggered each recording and also controlled the display of the rotating vertical bars on the LED matrix (Adafruit) surrounding the fly. Each 5 min trial consisted of consecutive iterations of the bars rotating clockwise for 5 s, stopping for 5 s and rotating counter-clockwise for 5 s. Flies were filmed from below with 60 Hz under infrared illumination (880 nm) and each fly's body axis orientation was tracked offline using Fiji (source). For each fly the median rotational velocities during each 5 s period (CW, CCW, Stop) were calculated using circular statistics in Matlab.

Synapse number analysis. All imaging data were analyzed and presented with Imaris (Bitplane). For synapse number analysis, CD4-tomato channel was used to generate Surfaces for individual axon terminals and Brp-positive puncta inside the Surface are filtered using the masking function. Brp-positive puncta in photoreceptor terminals were automatically detected with the spot detection module (spot diameter was set to 0.3 µm) using identical parameters between experimental conditions and corresponding controls. Synapse numbers were taken and recorded directly from statistics tab of Spot function. Graph generation and statistical analyses were done using GraphPad Prism 8.2.0

Analyses of filopodia and synapse distributions. All imaging data were analyzed and presented with Imaris (Bitplane). For synapse distribution analysis, Brp-positive puncta were detected following the same steps in "Synapse number analysis" in R7 axon terminals. Start and endpoints of axon terminals were selected manually with the measurements point module using nCad staining as a reference (start point = beginning of nCad staining at the most distal part of medulla (M0), end point = the beginning of M7, serpentine layer in the medulla). It is noteworthy that M7 layer is devoid of synapses, hence is not labeled by nCad. The length of axon terminals are measured with the measurement point module and normalized as start point = 0 and end point = 100. The actual positions of Brp-positive puncta were exported and relative positions were calculated according to the normalized length of axon terminals. The following equation is used to calculate relative positions of Brp-positive puncta: relative position = (actual position-start point)/ length × 100. For all filopodia and bulbous tip filopodia distribution analysis, the same steps were followed, except that spots were manually placed on the emerging points of all visible filopodia. Graph generation and statistical analyses were done using GraphPad Prism 8.2.0

Filopodia tracing. Filopodia tracing was performed as previously described[14]. Briefly, we previously developed an extension to the Amira Filament Editor[59], in which an individual growth cone is visualized as an annotated skeleton tree where each branch corresponds to a filopodium. In the first time step of four-dimensional (4D) data set, the user marks the GC center, which is automatically detected in the subsequent time steps. Filopodia tips marked by the user are automatically traced from the tip to the GC center based on an intensity-weighted Dijkstra shortest path algorithm[60]. The user visually verifies the tracing and corrects it using tools provided by the Filament Editor if necessary. After tracing all filopodia in the first time step, they are automatically propagated to the next time step with particular filopodia IDs. In every subsequent steps, the user verifies the generated tracings and adds newly emerged filopodia. This process continues until all time steps have been processed. Statistical quantities are directly extracted from the Filament Editor as spreadsheets for further data analysis.

Mathematical modeling. *Developmental model*: We adopted the data-driven stochastic model (developmental model) from ref. [14]. In short, the model structure remained identical, while we estimated genotype-specific parameters from the live-imaging data presented in this manuscript (Fig. 5b-e, Supplementary Movie 3, and Supplementary Table 2). In brief, we modeled synapses (S), short-lived transient bulbous tips (sB) that appeared and disappeared within the 60 min-imaging interval, and stable synaptogenic bulbous tips (synB) that persisted for more than 40 min. We also modeled two types of filopodia, which are distinguished by their lifetime and were denoted short-lived (sF) and long-lived (F) filopodia.

The model's reaction stoichiometries are determined by the following reaction scheme:

$$R_{1,sF} : \emptyset \rightarrow sF, \quad R_{2,sF} : sF \rightarrow \emptyset, \quad R_{1,\ell F} : \emptyset \rightarrow \ell F, \quad R_{2,\ell F} : \ell F \rightarrow \emptyset$$

$$R_3 : F \rightarrow sB, \quad R_4 : sB \rightarrow \emptyset, \quad R_5 : sB \rightarrow synB, \quad R_6 : synB \rightarrow S$$

where reactions $R_{1,sF}$ and $R_{1,\ell F}$ denote the generation of short- and long-lived filopodia, whereas $R_{2,sF}$ and $R_{2,\ell F}$ denote their retraction. Reaction R_3 denotes the formation of a (transient) bulbous tip, whereas R_4 denotes its retraction. Reaction R_5 denotes the stabilization of a transient bulbous tip and, finally, a stable bulb forms a synapse with reaction R_6.

It is noteworthy that in R_3 we denote by F any filopodium (short-lived and long-lived) and in R_4 we have ignored the flux back into the filopodia compartment $sF + \ell F$, as it insignificantly affects the number of filopodia (small number of bulbous tips, small rate r_4).

Similar to the published model[14], reaction rates/propensities of the stochastic model are given by

$$r_{1,sF}(t) = f_F(t) \cdot c_{1,sF}, \quad r_{2,sF}(sF) = sF \cdot c_{2,sF}$$

$$r_{1,\ell F}(t) = f_F(t) \cdot c_{1,\ell F}, \quad r_{2,\ell F}(sF) = \ell F \cdot c_{2,\ell F}$$

$$r_3(t, sF, \ell F, B) = c_3(sF + \ell F) \cdot f_1(synB, B_{50}) \cdot f_{FB}\left(t, t_{\frac{1}{2}}\right), \quad r_4(sB) = c_4 \cdot sB$$

$$r_5(sB) = c_5 \cdot sB, \quad r_6(synB) = c_6 \cdot synB,$$

where $c_1 \ldots c_6$ are reaction constants (estimated as outlined below). The feedback function $f_1(synB, B_{50}) = (synB + B_{50})/B_{50}$ models bulbous auto-inhibition due to limited resources and synaptic seeding factor competition as introduced before[14]. The functions $f_F(t)$ and $f_{FB}\left(t, t_{\frac{1}{2}}\right)$ model slow-scale dynamics of filopodia- and bulbous dynamics, with previously determined parameters[14]:

$f_{FB}(t)$ is a tanh function with

$f_{FB}(t, t_{1/2}) = \frac{1}{2}\left(1 + \tanh\left[\frac{3}{t_{1/2}}\left(t - t_{1/2}\right)\right]\right)$, which models a time-dependent increase in the propensity to form bulbous tips with $t_{1/2} = 1000$ (min). The time-dependent function $f_F(t) = \max\left(0, \sum_{i=0}^{5} p_i \cdot t^i\right)$ is a fifth-order polynome with coefficients $p_5 = -2.97 \times 10^{-14}$, $p_4 = 3.31 \times 10^{-13}$, $p_3 = -1.29 \times 10^{-9}$, $p_2 = 2.06 \times 10^{-6}$, $p_1 = -1.45 \times 10^{-3}$, and $p_0 = 1$, which downregulates the generation of new filopodia at a slow time scale. It is noteworthy that t denotes the time in (min) after P40 (e.g., $t_{P40} = 0$ and $t_{P60} = 60 \times 20$).

Parameter estimation: Using the methods explained below, we derived the parameters depicted in Supplementary Table S2. We first estimated $c_{2,sF}$, $c_{2,\ell F}$ from the filopodial lifetime data, whereby $c_{2,sF}$ was approximated as the inverse of the lifetimes of all filopodia that lived <8 min and $c_{2,\ell F}$ from all filopodia living at least 8 min. We realized that the number of filopodia per time instance was Poisson distributed (Supplementary Fig. 9, solid black lines), i.e., $sF \sim \mathcal{P}(\lambda_{sF})$ and $\ell F \sim \mathcal{P}(\lambda_{\ell F})$, where λ denotes the average number of filopodia per time instance. Given the first-order retraction of filopodia (≈exponential lifetime), the Poisson distribution can be explained by a zero-order input with rate $c_{1,sF}$ and $c_{1,\ell F}$, and $\lambda_{sF} = r_{1,sF}/c_{2,sF}$ and $\lambda_{\ell F} = r_{1,\ell F}/c_{2,\ell F}$, respectively. Using the mean number of sF, ℓF at P60 we then estimated $c_{1,sF} = \lambda_{sF}(P60) \cdot c_{2,sF}/f_F(P60)$ and $c_{1,\ell F} = \lambda_{sF}(P60) \cdot c_{2,\ell F}/f_F(P60)$.

Next, we investigated the lifetimes of bulbous tip filopodia (Supplementary Fig. 11b–e). We realized that akin to the wild type, the *atg6* and *atg7* exhibited almost no transient bulbous tips. We therefore set $c_4 = 1/120$ (min^{-1}) according to the published model[14]. Furthermore, we determined c_6 from the steepest slope in Fig. 6c (control data) divided by the average number of Bulbs ($5 \approx \int_t^{t+\Delta t} r_6(s)\, ds = \int_t^{t+\Delta t} synB(s) \cdot c_6\, ds \Rightarrow c_6 \approx \frac{5}{1.1 \cdot 10 \cdot 60} = 1/133\ \text{min}^{-1}$). We then estimated the three parameters c_5, B_{50}, and $r_3(t)$ for $t = $ P60. To do so, we used the number distribution of short-lived and synaptogenic bulbous tips (Fig. 5f, g), and set up the generator matrix

$$G([i,j],[i-1,j]) = i \cdot c_4, \qquad G([i,j],[i,j-1]) = j \cdot c_6$$
$$G([i,j],[i+1,j]) = r_3(t) \cdot f_1(j, B_{50}), \qquad G([i,j],[i,j+1]) = j \cdot c_5$$

with diagonal elements such that the row sum equals 0. In the notation above, the tupel $[i, j]$ denotes the state where i short-lived bulbous tips sB and j synaptogenic bulbous tips $synB$ are present. The generator above has a reflecting boundary at sufficiently large N (maximum number of bulbous tips). Above, $r_3(t)$ is auto-inhibited by the number of stable bulbous tips through function f_1. The stationary distribution of this model is derived by solving the eigenvalue problem

$$G^T \cdot v = v \cdot \lambda$$

and finding the eigenvector corresponding to eigenvalue $\lambda_0 = 0$. From this stationary distribution, we compute the marginal densities of sB and $synB$ (e.g., summing over all states where $i = 0, 1, \ldots$ for sB) and fit them to the experimentally derived frequencies by minimizing the Kullback–Leibler divergence between the experimental and model-predicted distributions. Lastly, parameter c_3 is derived by calculating

$$c_3 = \frac{r_3(t)}{(sF(t) + \ell F(t)) \cdot f_{FB}\left(t, t_{1/2}\right)} \qquad (1)$$

where $sF(t) = sF(t_{p60})$, $\ell F(t) = \ell F(t_{p60})$, and $f_{FB}(t) = f_{FB}(t_{P60}, t_{1/2})$.

Mechanistic model: This model explains autophagy mutant phenotypes as a consequence of increased seeding factor abundance. We adopted the mechanistic model from ref. [14]. This model essentially assumes a dynamic pool of a limited resource of bulbous tip-stabilizing factors (Fig. 6g and Supplementary Fig. 11a). The model consists of four types of reactions: new filopodia emerge (reaction G_1), accumulate resources (reaction G_2), retract (reaction G_3), or release resources (reaction G_4).

$$G_1 : \emptyset \to F, \qquad G_2 : \quad FS_{i-1} + S \to FS_i,$$

$$G_3 : \; FS_i \to S_i, \qquad G_4 : \; FS_i \to FS_{i-1} + S,$$

where F denotes an "empty" filopodium, S denotes the seeding factor, and FS_{i} denotes a filopodium with i seeding factor proteins in it. The reaction rates (propensities) were modeled as

$$g_1 = const, \quad g_2(i-1) = FS_{i-1} \cdot S \cdot c_{in},$$

$$g_3(i) = FS_i \cdot \frac{1}{i}, \quad g_4(i) = FS_i \cdot c_{out},$$

where we set g_1 equal to the average rate of transient bulbous tip emergence in the control experiments at P60, i.e., $g_1 = r_3(t_{P60}, WT)$. Reaction rate g_3 implements a competitive advantage: the lifetime of bulbous filopodia is increased proportionally to the number of seeding factors it accumulated. The parameters c_{in} and c_{out} were set to values 0.07 and 1.5 (time^{-1}), and as initial condition we set $S(t_0) = \left\| n \cdot \overline{B}(t_{P60}) \right\|$, where n is the number of states (we used $n = 120$), $\overline{B}(t_{P60})$ denotes the genotype-specific average number of bulbous tips at P60 and $|| \cdot ||$ denotes the next integer function.

Importantly, in the model, the wild-type and the *atg6*- and *atg7*-knockout mutants only differ in the total number of seeding factors available.

We stochastically ran the model 100,000 time steps to reach a steady state and discarded the first half as a burn-in period (pre-steady state). Subsequently, we analyzed the number of bulbous tips and their lifetimes from the remaining time steps as shown in Supplementary Fig. 11b–i. Thereby, we assumed that filopodia would be recognized as bulbous tips only if they contained at least $n/4$ seeding factors.

In summary, these computational experiments highlight that the phenotype of the *atg6*- and *atg7*-knockout mutants can be solely explained by an increased abundance of seeding factors (= compromised ability to degrade seeding factors).

In the case of autophagy upregulation *(atg6*, GMR > Atg6), we observed a different phenotype: from the data-driven model, we could see that bulbous tips were destabilized (parameter r4 in Supplementary Table S2) and also that the feedback was lost (parameter E[f1] close to 1 in Supplementary Table S2). We tested different parameter- and model alterations to reproduce both the number and lifetime distribution of bulbous tips. Finally, we found that if seeding factors no longer stabilized bulbous tips (loss in the competitive advantage), both the lifetime and the number distribution of bulbous tips can be accurately reproduced. Thus, we set reaction rate g_3 to $g_3 = FS \cdot const$, for autophagy upregulation, where $const = c_4$ (time^{-1}; Supplementary Table 3).

Statistical analysis. Individual data in the same group were first checked for normal distribution using D'Agostino and Pearson normality test. If all distributed normal, one-way ANOVA and Tukey's HSD as post-hoc tests were used. If at least one data shows non-normal distribution, then non-parametric Kruskal–Wallis and Dunn's as post-hoc tests were used. All significance values are denoted on the graphs and in their respective legends. Data were analyzed using GraphPad Prism 8.2.0 (GraphPad Software, San Diego, CA).

Lead contact and materials availability. All reagents used in this study are available for distribution. Requests for resources and reagents should be directed to Robin Hiesinger (robin.hiesinger@fu-berlin.de).

Reporting summary. Further information on research design is available in the Nature Research Reporting Summary linked to this article.

Data availability

Raw (.lif format) and processed (.ims and.am format) imaging datasets are available on request. The filopodia-tracking software is an extension of the commercial software Amira, which is available from Thermo Fisher Scientific. The filopodia-tracking software is available from the corresponding author upon request in source code and binary form. Executing the binary requires a commercial license for Amira. The source data underlying Figs. 1d, e, i, 2f, g, h, 3d, g, 5g, 6h, j, k, 7b–d and Supplementary Figs. 1e, 2d, 2f, 2g, 2i, 3b, 4b, 4d, 4h, 4l, 5b, 7b, 7c, 7e, 12f, 13c are provided as a Source Data file.

Code availability

MATLAB codes for model parameter inference for model simulation have previously been published[14] and are available through https://github.com/vkleist/Filo2.

Received: 6 September 2019; Accepted: 31 January 2020;
Published online: 12 March 2020

References

1. Sudhof, T. C. Towards an understanding of synapse formation. *Neuron* **100**, 276–293 (2018).
2. Sando, R., Jiang, X. & Sudhof, T. C. Latrophilin GPCRs direct synapse specificity by coincident binding of FLRTs and teneurins. *Science* **363**, 6429 (2019).
3. Hart, M. P. & Hobert, O. Neurexin controls plasticity of a mature, sexually dimorphic neuron. *Nature* **553**, 165–170 (2018).
4. Hong, W., Mosca, T. J. & Luo, L. Teneurins instruct synaptic partner matching in an olfactory map. *Nature* **484**, 201–207 (2012).
5. Apostolo, N. & de Wit, J. Compartmentalized distributions of neuronal and glial cell-surface proteins pattern the synaptic network. *Curr. Opin. Neurobiol.* **57**, 126–133 (2019).
6. Van Der Loss, H. & Glaser, E. M. Autapses in neocortex cerebri: synapses between a pyramidial cell's axon and its own dendrites. *Brain Res.* **48**, 355–360 (1972).
7. Hassan, B. A. & Hiesinger, P. R. Beyond molecular codes: simple rules to wire complex brains. *Cell* **163**, 285–291 (2015).
8. Petrovic, M. & Schmucker, D. Axonal wiring in neural development: Target-independent mechanisms help to establish precision and complexity. *Bioessays* **37**, 996–1004 (2015).
9. Courgeon, M. & Desplan, C. Coordination of neural patterning in the *Drosophila* visual system. *Curr. Opin. Neurobiol.* **56**, 153–159 (2019).
10. Hadjieconomou, D., Timofeev, K. & Salecker, I. A step-by-step guide to visual circuit assembly in *Drosophila*. *Curr. Opin. Neurobiol.* **21**, 76–84 (2011).
11. Balaskas, N., Abbott, L. F., Jessell, T. M. & Ng, D. Positional strategies for connection specificity and synaptic organization in spinal sensory-motor circuits. *Neuron* **102**, 1143–1156.e4 (2019).
12. Hiesinger, P. R. et al. Activity-independent prespecification of synaptic partners in the visual map of *Drosophila*. *Curr. Biol.* **16**, 1835–1843 (2006).
13. Ozel, M. N., Langen, M., Hassan, B. A. & Hiesinger, P. R. Filopodial dynamics and growth cone stabilization in *Drosophila* visual circuit development. *Elife* **4**, 50447–461.e8 (2015).
14. Ozel, M. N. et al. Serial synapse formation through filopodial competition for synaptic seeding factors. *Dev. Cell* **50**, 447–461.e8 (2019).
15. Takemura, S. Y. et al. A visual motion detection circuit suggested by *Drosophila* connectomics. *Nature* **500**, 175–181 (2013).
16. Kolodkin, A. L. & Hiesinger, P. R. Wiring visual systems: common and divergent mechanisms and principles. *Curr. Opin. Neurobiol.* **42**, 128–135 (2017).
17. Takemura, S. Y. et al. Synaptic circuits and their variations within different columns in the visual system of *Drosophila*. *Proc. Natl Acad. Sci. USA* **112**, 13711–13716 (2015).
18. Zschatzsch, M. et al. Regulation of branching dynamics by axon-intrinsic asymmetries in tyrosine kinase receptor signaling. *Elife* **3**, e01699 (2014).
19. Stavoe, A. K. H. & Holzbaur, E. L. F. Autophagy in neurons. *Annu. Rev. Cell Dev. Biol.* **35**, 477–500 (2019).
20. Menzies, F. M. et al. Autophagy and neurodegeneration: pathogenic mechanisms and therapeutic opportunities. *Neuron* **93**, 1015–1034 (2017).
21. Nikoletopoulou, V. & Tavernarakis, N. Regulation and roles of autophagy at synapses. *Trends Cell Biol.* **28**, 646–661 (2018).
22. Vijayan, V. & Verstreken, P. Autophagy in the presynaptic compartment in health and disease. *J. Cell Biol.* **216**, 1895–1906 (2017).
23. Hernandez, D. et al. Regulation of presynaptic neurotransmission by macroautophagy. *Neuron* **74**, 277–284 (2012).
24. Juhasz, G., Erdi, B., Sass, M. & Neufeld, T. P. Atg7-dependent autophagy promotes neuronal health, stress tolerance, and longevity but is dispensable for metamorphosis in *Drosophila*. *Genes Dev.* **21**, 3061–3066 (2007).
25. Stavoe, A. K., Hill, S. E., Hall, D. H. & Colon-Ramos, D. A. KIF1A/UNC-104 transports ATG-9 to regulate neurodevelopment and autophagy at synapses. *Dev. Cell* **38**, 171–185 (2016).
26. Shen, W. & Ganetzky, B. Autophagy promotes synapse development in *Drosophila*. *J. Cell Biol.* **187**, 71–79 (2009).
27. Tang, G. et al. Loss of mTOR-dependent macroautophagy causes autistic-like synaptic pruning deficits. *Neuron* **83**, 1131–1143 (2014).
28. Lieberman, O. J., McGuirt, A. F., Tang, G. & Sulzer, D. Roles for neuronal and glial autophagy in synaptic pruning during development. *Neurobiol. Dis.* **122**, 49–63 (2019).
29. Jin, E. J. et al. Live observation of two parallel membrane degradation pathways at axon terminals. *Curr. Biol.* **28**, 1027–1038 e1024 (2018).

30. Shravage, B. V., Hill, J. H., Powers, C. M., Wu, L. & Baehrecke, E. H. Atg6 is required for multiple vesicle trafficking pathways and hematopoiesis in *Drosophila*. *Development* **140**, 1321–1329 (2013).
31. Wang, T., Lao, U. & Edgar, B. A. TOR-mediated autophagy regulates cell death in *Drosophila* neurodegenerative disease. *J. Cell Biol.* **186**, 703–711 (2009).
32. Polson, H. E. et al. Mammalian Atg18 (WIPI2) localizes to omegasome-anchored phagophores and positively regulates LC3 lipidation. *Autophagy* **6**, 506–522 (2010).
33. Harada, K. et al. Two distinct mechanisms target the autophagy-related E3 complex to the pre-autophagosomal structure. *Elife* **8**, https://doi.org/10.7554/eLife.43088 (2019).
34. Walczak, M. & Martens, S. Dissecting the role of the Atg12-Atg5-Atg16 complex during autophagosome formation. *Autophagy* **9**, 424–425 (2013).
35. Colomb, J., Reiter, L., Blaszkiewicz, J., Wessnitzer, J. & Brembs, B. Open source tracking and analysis of adult *Drosophila* locomotion in Buridan's paradigm with and without visual targets. *PLoS ONE* **7**, e42247 (2012).
36. Bender, J. A. & Dickinson, M. H. Visual stimulation of saccades in magnetically tethered *Drosophila*. *J. Exp. Biol.* **209**, 3170–3182 (2006).
37. Mathejczyk, T. F. & Wernet, M. F. Heading choices of flying *Drosophila* under changing angles of polarized light. *Sci. Rep.* **9**, 16773 (2019).
38. Schmid, A. et al. Activity-dependent site-specific changes of glutamate receptor composition in vivo. *Nat. Neurosci.* **11**, 659–666 (2008).
39. Karuppudurai, T. et al. A hard-wired glutamatergic circuit pools and relays UV signals to mediate spectral preference in *Drosophila*. *Neuron* **81**, 603–615 (2014).
40. Gao, S. et al. The neural substrate of spectral preference in *Drosophila*. *Neuron* **60**, 328–342 (2008).
41. Talay, M. et al. Transsynaptic mapping of second-order taste neurons in flies by trans-tango. *Neuron* **96**, 783–795 e784 (2017).
42. Takemura, S. Y., Lu, Z. & Meinertzhagen, I. A. Synaptic circuits of the *Drosophila* optic lobe: the input terminals to the medulla. *J. Comp. Neurol.* **509**, 493–513 (2008).
43. Takemura, S. Y. et al. The comprehensive connectome of a neural substrate for 'ON' motion detection in *Drosophila*. *Elife* **6**, https://doi.org/10.7554/eLife.24394 (2017).
44. Strother, J. A. et al. The emergence of directional selectivity in the visual motion pathway of *Drosophila*. *Neuron* **94**, 168–182 e110 (2017).
45. Borst, A., Haag, J. & Mauss, A. S. How fly neurons compute the direction of visual motion. *J. Comp. Physiol. A Neuroethol. Sens. Neural Behav. Physiol.* (2019).
46. Fischbach, K. F. & Dittrich, A. P. M. The optic lobe of *Drosophila melanogaster*. I. A Golgi analysis of wild-type structure. *Cell Tissue Res.* **258**, 441–475 (1989).
47. Feinberg, E. H. et al. GFP reconstitution across synaptic partners (GRASP) defines cell contacts and synapses in living nervous systems. *Neuron* **57**, 353–363 (2008).
48. Macpherson, L. J. et al. Dynamic labelling of neural connections in multiple colours by trans-synaptic fluorescence complementation. *Nat. Commun.* **6**, 10024 (2015).
49. Maday, S. & Holzbaur, E. L. Autophagosome biogenesis in primary neurons follows an ordered and spatially regulated pathway. *Dev. Cell* **30**, 71–85 (2014).
50. Soukup, S. F. et al. A LRRK2-dependent endophilin A phosphoswitch is critical for macroautophagy at presynaptic terminals. *Neuron* **92**, 829–844 (2016).
51. Okerlund, N. D. et al. Bassoon controls presynaptic autophagy through Atg5. *Neuron* **93**, 897–913 e897 (2017).
52. Hiesinger, P. R. & Hassan, B. A. The evolution of variability and robustness in neural development. *Trends Neurosci.* **41**, 577–586 (2018).
53. Kulkarni, A., Ertekin, D., Lee, C. H. & Hummel, T. Birth order dependent growth cone segregation determines synaptic layer identity in the *Drosophila* visual system. *Elife* **5**, e13715 (2016).
54. Melnattur, K. V. & Lee, C. H. Visual circuit assembly in *Drosophila*. *Dev. Neurobiol.* **71**, 1286–96 (2011).
55. Birdsall, V. & Waites, C. L. Autophagy at the synapse. *Neurosci. Lett.* **697**, 24–28 (2019).
56. Lee, W. & Kim, S. H. Autophagy at synapses in neurodegenerative diseases. *Arch. Pharm. Res.* **42**, 407–415 (2019).
57. Williamson, W. R., Yang, T., Terman, J. R. & Hiesinger, P. R. Guidance receptor degradation is required for neuronal connectivity in the *Drosophila* nervous system. *PLoS Biol.* **8**, e1000553 (2010).
58. Linneweber, G. et al. A neurodevelopmental origin of behavioral individuality. *Science* 2020, in press.
59. Dercksen, V. J., Hege, H. C. & Oberlaender, M. The filament editor: an interactive software environment for visualization, proof-editing and analysis of 3D neuron morphology. *Neuroinformatics* **12**, 325–339 (2013).
60. Sato, M., Bitter, I., Bender, M. A. & Kaufman, A. E. TEASAR: Tree-structure extraction algorithm for accurate and robust skeletons. In *Proc. 8th Pacific Conference on Computer Graphics and Applications* (IEEE, 2000).

Acknowledgements

We thank all members of the Hiesinger, Wernet, and Hassan labs for their support and helpful discussions. We thank Eric Baehrecke and Stephan Sigrist for reagents. F.R.K. acknowledges Gizem Sancer for her help to design "*trans*-Tango" experiments. This work was supported by the NIH (RO1EY018884) and the German Research Foundation (DFG, SFB958, SFB186), and FU Berlin. B.H. was supported by an Einstein BIH Fellowship. M.v.K. acknowledges financial support from the German ministry for education and science (BMBF) through grant number 031A307 and from the Einstein Stiftung Berlin and the DFG, provided through the excellence cluster Math+. M.F.W acknowledges the Deutsche Forschungsgemeinschaft (DFG) through grants WE 5761/2-1 and SFB958 (Teilprojekt A23), as well as AFOSR grant FA9550-19-1-7005.

Author contributions

F.R.K. and P.R.H. designed the project. F.R.K. performed all experiments, except the Buridan's paradigm and the motion vision assay. Buridan's paradigm experiments were designed, carried out, and analyzed by G.A.L. and B.A.H. Motion vision assay experiments were designed, carried out, and analyzed by T.M. and M.F.W. S.V.G. performed 4D tracking analyses of filopodial dynamics. M.v.K. performed all computational modeling. F.R.K., B.A.H., M.v.K., and P.R.H. wrote the paper.

Competing interests

The authors declare no competing interests.

Additional information

Supplementary information is available for this paper at https://doi.org/10.1038/s41467-020-14781-4.

Correspondence and requests for materials should be addressed to P.R.H.

Peer review information *Nature Communications* thanks Gabor Juhász, and the other, anonymous, reviewer(s) for their contribution to the peer review of this work. Peer reviewer reports are available.

Reprints and permission information is available at http://www.nature.com/reprints

Publisher's note Springer Nature remains neutral with regard to jurisdictional claims in published maps and institutional affiliations.

Open Access This article is licensed under a Creative Commons Attribution 4.0 International License, which permits use, sharing, adaptation, distribution and reproduction in any medium or format, as long as you give appropriate credit to the original author(s) and the source, provide a link to the Creative Commons license, and indicate if changes were made. The images or other third party material in this article are included in the article's Creative Commons license, unless indicated otherwise in a credit line to the material. If material is not included in the article's Creative Commons license and your intended use is not permitted by statutory regulation or exceeds the permitted use, you will need to obtain permission directly from the copyright holder. To view a copy of this license, visit http://creativecommons.org/licenses/by/4.0/.

© The Author(s) 2020

Supplementary Information

Autophagy-dependent filopodial kinetics restrict synaptic partner choice during *Drosophila* brain wiring

Kiral et al.

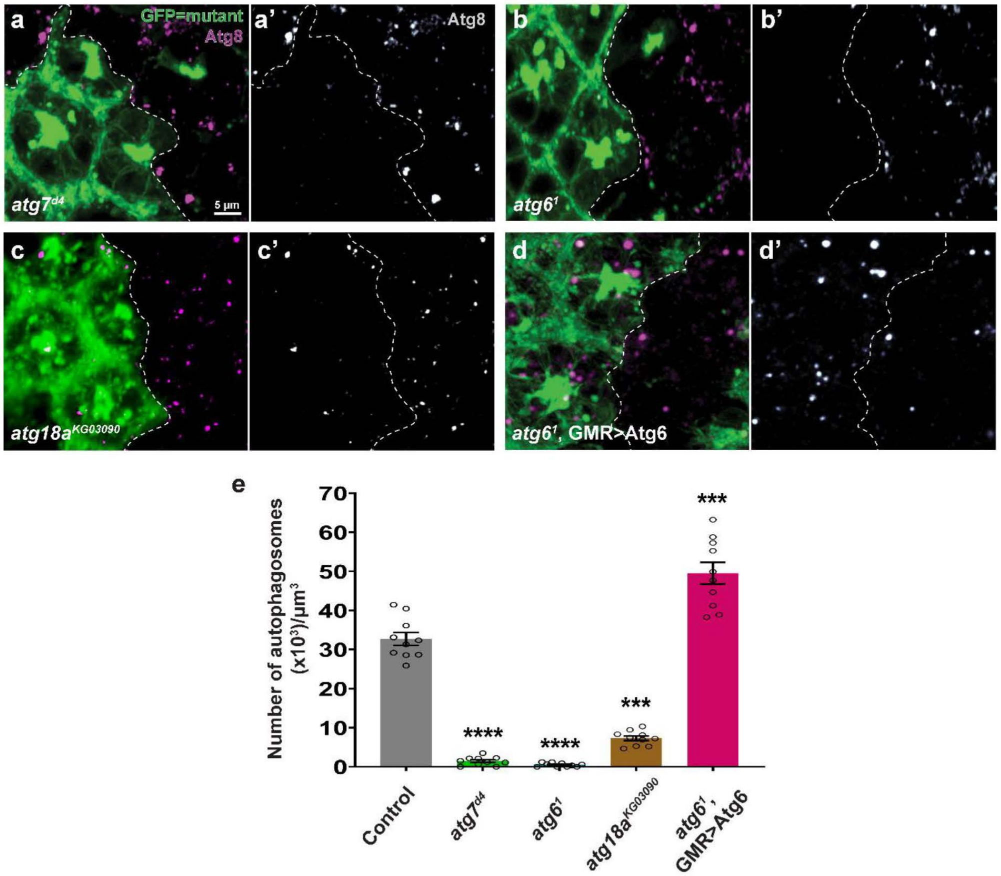
a
GFP=mutant
Atg8
atg7d4
5 µm
a'
Atg8
b
atg61
b'
c
atg18aKG03090
c'
d
atg61, GMR>Atg6
d'
e
Number of autophagosomes (x10³)/µm³
0
10
20
30
40
50
60
70
****
****
***
***
Control
atg7d4
atg61
atg18aKG03090
atg61, GMR>Atg6

Supplementary Figure 1. Atg6, Atg7 and Atg18 are required for developmental autophagy in *Drosophila* photoreceptors. a-d', Atg8 immunolabelled autophagosomes in GFP-positive photoreceptor clones of *atg7*^{d4} **(a-a')**, *atg6*^{1} **(b-b')**, *atg6*^{1}, GMR>Atg6 **(c-c')** and *atg18a*^{KG03090} **(d-d')** versus non-GFP control clones in genetic mosaics of P+50% pupal retina. Repeated 3 times independently with similar results. **e,** Number of autophagosomes in a given volume. Note almost complete abolishment of autophagosomes in *atg7*^{d4} and *atg6*^{1} mutant photoreceptors, milder decrease in autophagosome number in *atg18a*^{KG03090} mutant photoreceptors and a significant increase in autophagosome number in *atg6*^{1}, GMR>Atg6 photoreceptors. n=10 retinas per condition, one region of interest is randomly selected per retina. One-way ANOVA and Tukey HSD as post hoc test; ***$p<0.001$, ****$p<0.0001$. Error bars denote mean ± SEM. Source data are provided as a Source Data file.

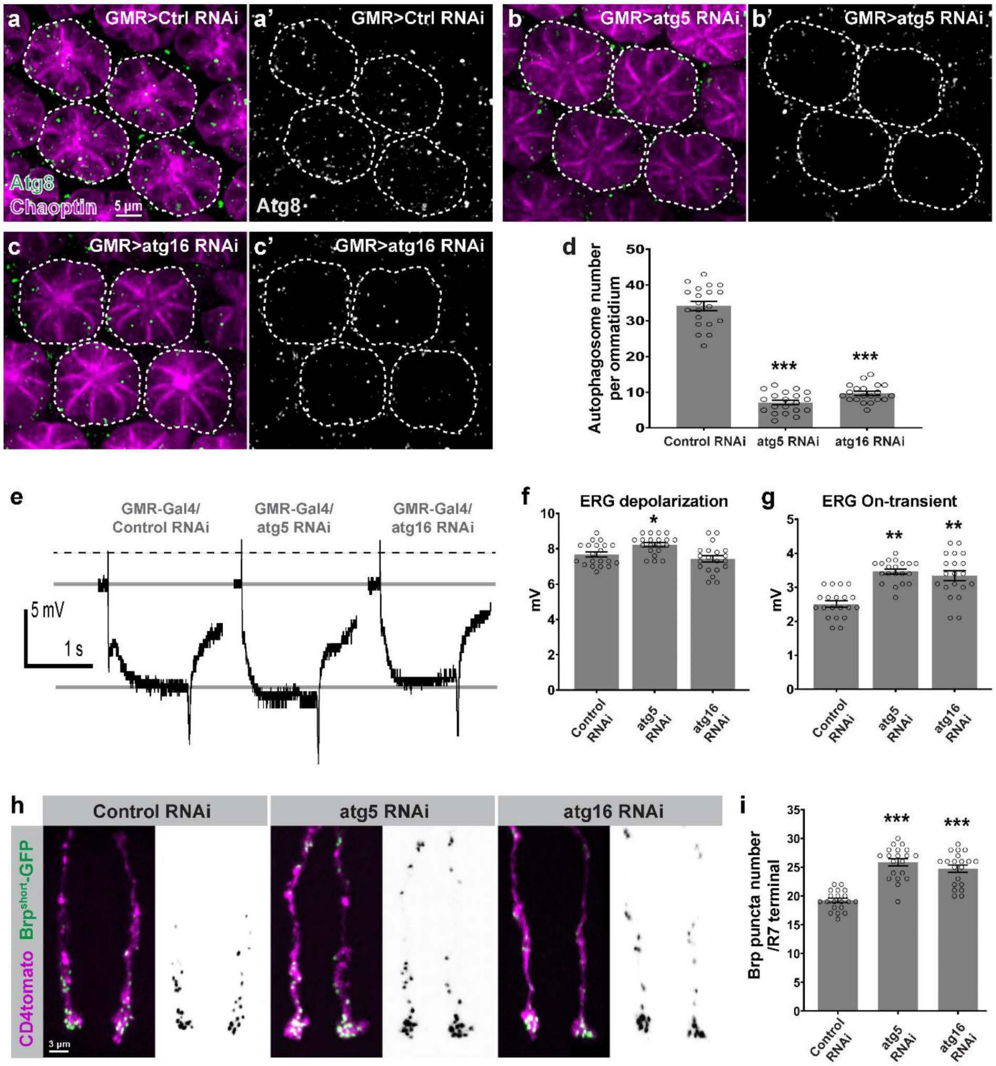

Supplementary Figure 2. Downregulation of autophagy by Atg5 and Atg16 knockdown leads to increased neurotransmission and synapse number. a-c', Atg8 labelled autophagosomes in Chaoptin labelled photoreceptor cell bodies of GMR-Gal4 driven control RNAi **(a-a')**, Atg5 RNAi **(b-b')** and Atg16 RNAi **(c-c')**. Dashed lines encircle photoreceptor cell bodies in individual ommatidium. Repeated 3 times independently with similar results. **d,** Number of autophagosomes per ommatidium. n=20 ommatidia per condition. **e,** Representative ERG traces recorded from control (GMR-Gal4/Control RNAi), Atg5 knockdown (GMR-Gal4/Atg5 RNAi) and Atg16 knockdown (GMR-Gal4/Atg16 RNAi) photoreceptors. Repeated 3 times independently with similar results. **f-g,** Quantifications of ERG depolarization (**f**) and ERG on-transient (**g**). n=20 flies per condition. **h,** Representative images of Brp^{short}-GFP labelled active zones in control, Atg5 knockdown and Atg16 knockdown R7 axon terminals. Repeated 3 times independently with similar results. **i,** Number of Brp puncta in control, Atg5 knockdown and Atg16 knockdown R7 axon terminals. n=20 terminals per condition. One-way ANOVA and Tukey HSD as post hoc test; *p<0.05, **p<0.01, ***p<0.001. Error bars denote mean ± SEM. Source data are provided as a Source Data file.

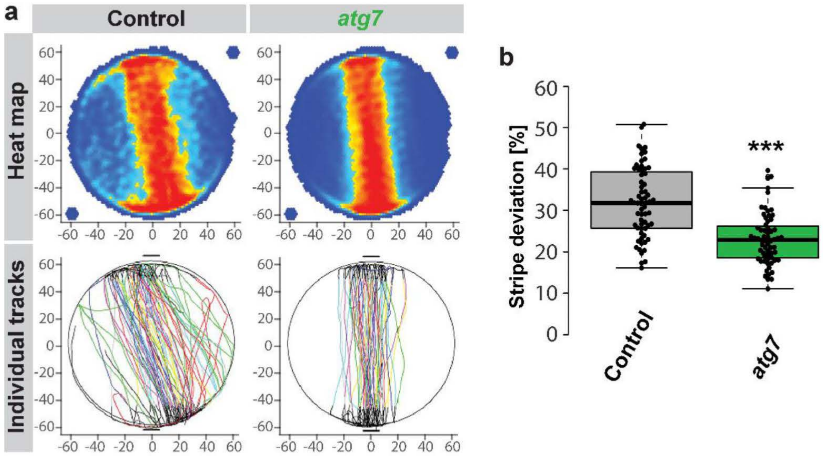

Supplementary Figure 3. Loss of *atg7* in *Drosophila* photoreceptors leads to increased visual attention behavior. a, Stripe fixation behavior of adult flies with control and *atg7* mutant photoreceptors is shown on the population level (heatmap) and as individual tracks. **b,** Quantification of stripe deviation. The bottom-most and top-most horizontal lines, the lower and upper hinges, and the middle line of the boxplots indicate the minimum and maximum values, the 25th and 75th percentiles, and the median, respectively. n=60 flies per condition, two-way ANOVA and Tukey HSD as post hoc test, ***p<0.001. Note that similar to flies with *atg6* mutant photoreceptors (see Fig. 1h), flies with *atg7* mutant photoreceptors show increased stripe fixation behavior and repetitive walks between stripes. Source data are provided as a Source Data file.

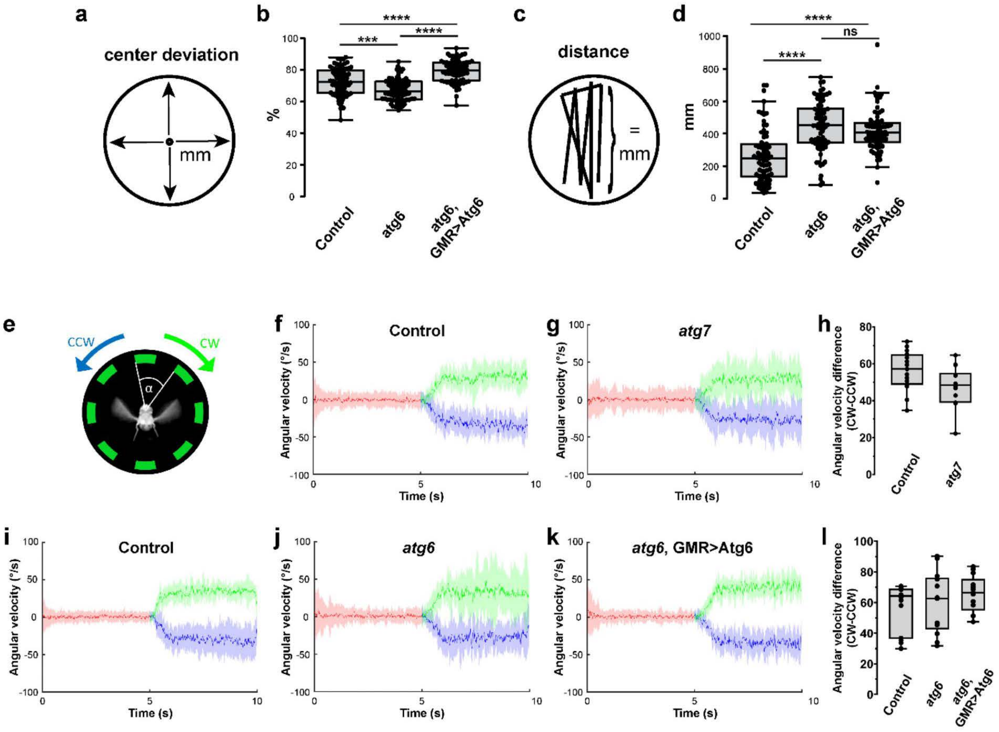

Supplementary Figure 4. Optomotor behavior is unaffected in flies deficient of autophagy in photoreceptors. a, The parameter 'center deviation' measures how much a fly deviates from the center point of the arena. **b,** Quantification of center deviation. n=60 flies per condition, two-way ANOVA and Tukey HSD as post hoc test; ***p<0.001, ****p<0.0001. **c,** The parameter 'distance' measures the total distance travelled by a fly during the imaging window. **d,** Quantification of distance. n=60 flies per condition, two-way ANOVA and Tukey HSD as post hoc test; ****p<0.0001. **e,** Schematic representation of the optomotor setup. A tethered fly is presented with moving green vertical stripes (α = 45°, rotational velocity either 0°/s, or 50°/s CCW or CW, respectively). **f-g** and **i-k**, Averaged optomotor responses of all flies of the tested groups for periods of the vertical stripes not moving (red), moving CW (green) or moving CCW (blue), respectively. Shaded areas indicate the standard deviation. **h** and **l**, Box plots depict the average difference in angular velocity (mean CW - mean CCW) for all tested flies of each individual group. n=15 (control for *atg7*), n=14 (*atg7*), n=14 (control for *atg6* and atg6, GMR>Atg6), n=13 (*atg6*), n=13 (GMR>Atg6). Wilcoxon rank sum test. No significant difference found between groups. The bottom-most and top-most horizontal lines, the lower and upper hinges, and the middle line of the boxplots indicate the minimum and maximum values, the 25th and 75th percentiles, and the median, respectively. Source data are provided as a Source Data file.

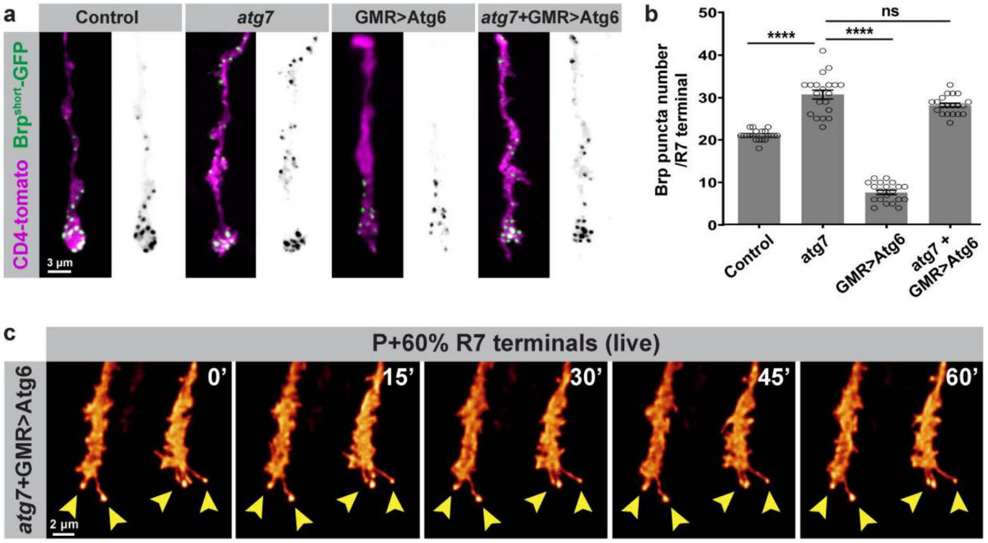
a
Control
atg7
GMR>Atg6
atg7+GMR>Atg6
CD4-tomato Brp^short-GFP
3 µm
b
Brp puncta number /R7 terminal
50
40
30
20
10
0
****
****
ns
Control
atg7
GMR>Atg6
atg7 + GMR>Atg6
c
P+60% R7 terminals (live)
atg7+GMR>Atg6
0'
15'
30'
45'
60'
2 µm

Supplementary Figure 5. Decreased filopodial stability and synapse number in Atg6 overexpression is due to upregulation of autophagy. a, Representative images of control (same as in fig.2a), *atg7*; GMR>Atg6; and *atg7*, GMR>Atg6 R7 photoreceptor axon terminals with Brp^{short-}GFP marked active zones. Repeated 5 times independently with similar results. **b,** Number of BRP puncta in control, *atg7*, GMR>Atg6, and *atg7*, GMR>Atg6 R7 photoreceptor axon terminals. n=20 terminals per condition. Kruskal-Wallis and Dunn's as post hoc test; ****p<0.0001. Error bars denote mean ± SEM. **c,** Live imaging of *atg7*, GMR>Atg6 R7 axon terminals at P+60%. Note that Atg6 overexpression on *atg7* mutant background still shows increased number of stable bulbous tip filopodia similar to *atg7* mutant alone (see fig. 5c). Repeated 2 times independently with similar results. Source data are provided as a Source Data file.

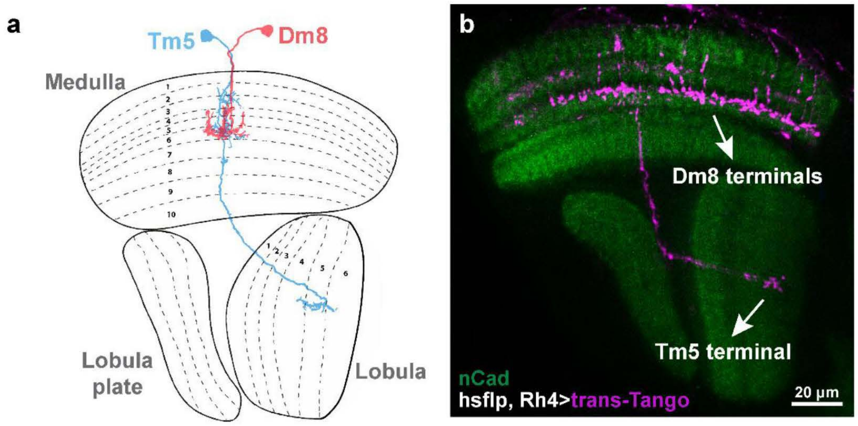
a
Tm5
Dm8
Medulla
1
2
3
4
5
6
7
8
9
10
Lobula plate
Lobula
1
2
3
4
5
6
b
Dm8 terminals
Tm5 terminal
nCad
hsflp, Rh4>trans-Tango
20 µm

Supplementary Figure 6. Dm8 and Tm5 neurons are the main postsynaptic targets of R7 photoreceptors. a, Schematic of Dm8 and Tm5 neuronal morphology in *Drosophila* optic lobe. **b,** Sparse trans-Tango labelling protocol with R7-specific Rh4-Gal4 revealed that R7 photoreceptors mainly connect to Dm8 and Tm5 neurons in wild-type brains. Repeated 3 times independently with similar results.

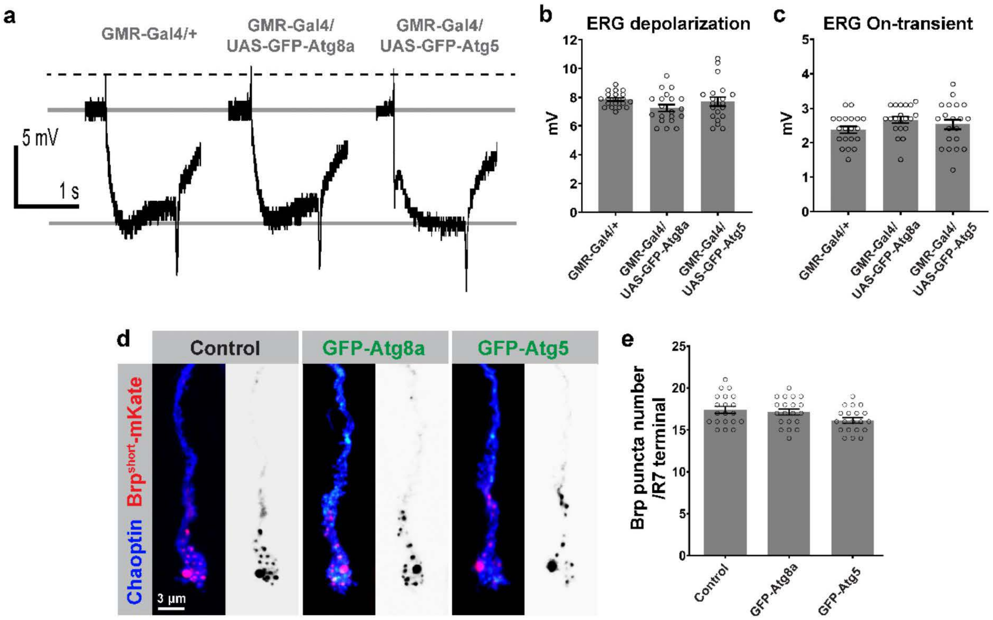

Supplementary Figure 7. Atg5 or Atg8a overexpression does not alter neurotransmission or synapse number. a, Representative ERG traces recorded from control (GMR-Gal4/+), GFP-Atg8a expressing (GMR-Gal4/GFP-Atg8a) and GFP-Atg5 expressing (GMR-Gal4/GFP-Atg5) photoreceptors. Repeated 3 times independently with similar results. **b-c,** Quantifications of ERG depolarization (**b**) and ERG on-transient (**c**). n=20 flies per condition. **d,** Representative images of Brp^{short}-mKate labelled active zones in control, GFP-Atg8a expressing, GFP-Atg5 expressing R7 axon terminals. Repeated 5 times independently with similar results. **e,** Number of Brp puncta in control, GFP-Atg8a expressing, GFP-Atg5 expressing R7 axon terminals. n=20 terminals per condition. One-way ANOVA and Tukey HSD as post hoc test. Error bars denote mean ± SEM. No significant difference found between groups. Source data are provided as a Source Data file.

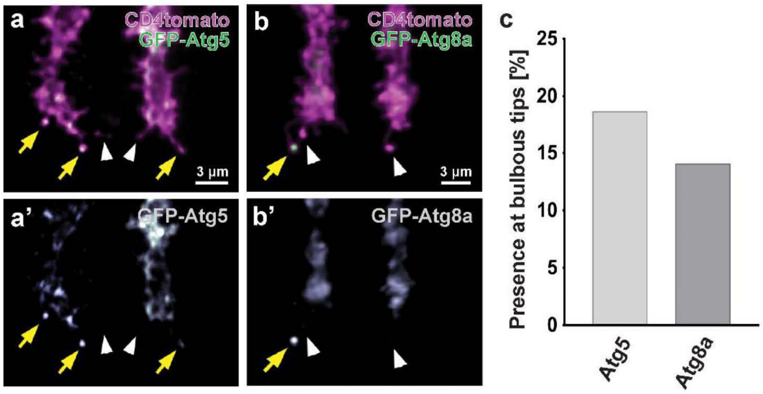
a
CD4tomato
GFP-Atg5
3 µm
b
CD4tomato
GFP-Atg8a
3 µm
a'
GFP-Atg5
b'
GFP-Atg8a
c
Presence at bulbous tips [%]
25
20
15
10
5
0
Atg5
Atg8a

Supplementary Figure 8. The essential autophagy proteins Atg5 and Atg8a localize to synaptogenic filopodia tips. a-b', Localization of autophagy essential proteins Atg5 (**a-a'**) and Atg8a (**b-b'**) to bulbous tip filopodia (P+60%). Yellow arrows show the presence of Atg5 and Atg8a at bulbous tips, while white arrowheads show bulbous tips without Atg5 and Atg8a. Repeated 5-10 times independently with similar results. **c,** Percentage of bulbous tip filopodia with Atg5 and Atg8a signal to all bulbous tip filopodia. n=30 terminals. All bulbous tip filopodia from 30 axon terminals were pooled for quantification.

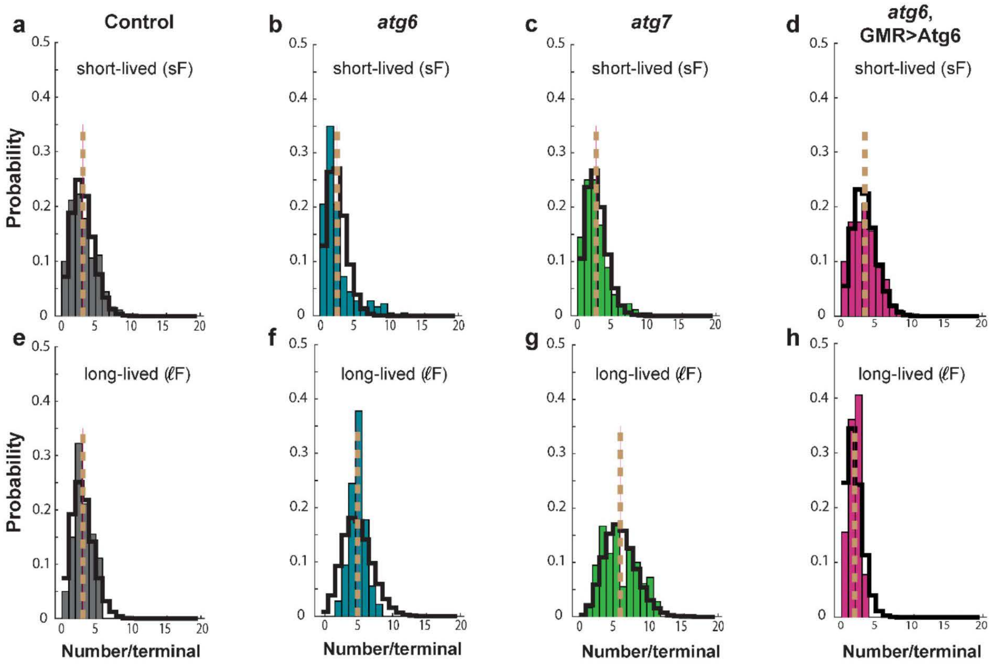

Supplementary Figure 9. Number of short-lived and long-lived filopodia at P60. Bars denote the observed numbers during live imaging and the dashed vertical line indicates the average numbers. The solid black trace depicts a Poisson distribution with expectation value equal to the average number of observed filopodia. short-lived filopodia = filopodia exist shorter than 8 mins, long-lived filopodia = filopodia exist longer than 8 mins. Values for lifetimes and numbers are shown in Supplementary Table 1.

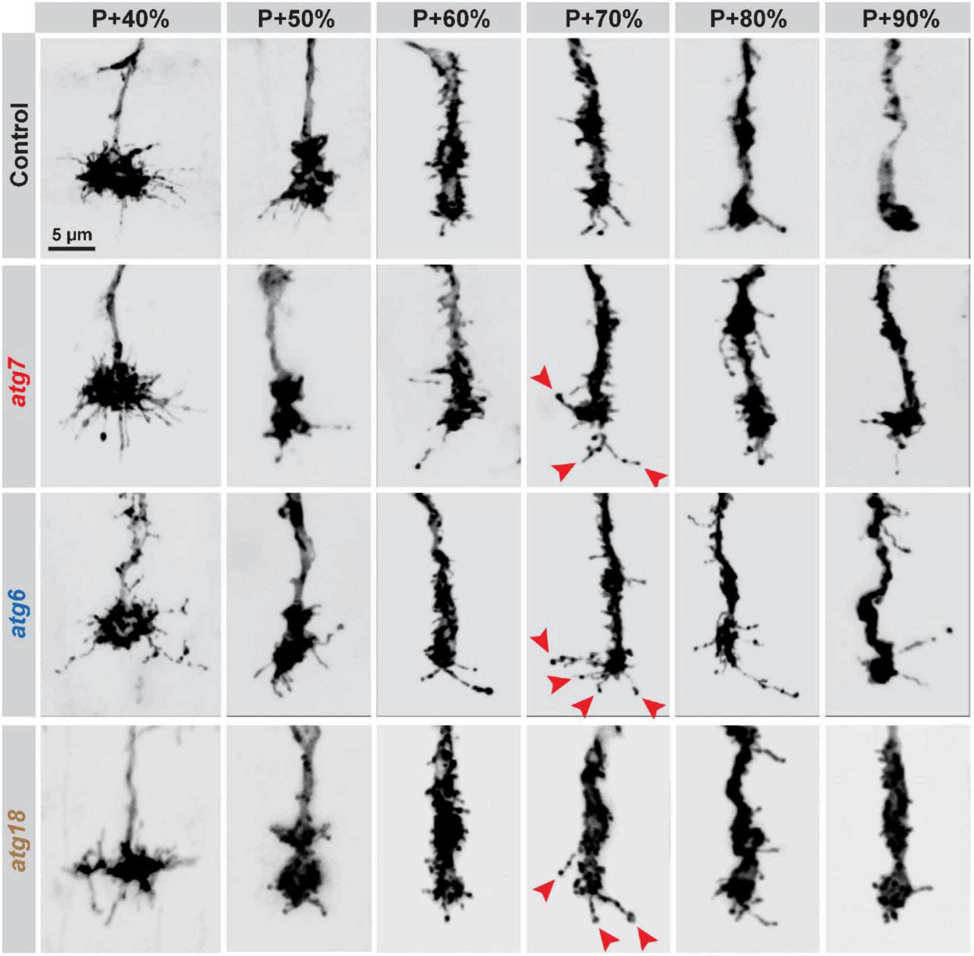

Supplementary Figure 10. Morphology of R7 photoreceptor axon terminals throughout the second half of pupation (the period of synapse formation). Representative images of control, *atg7*, *atg6* and *atg18* mutant R7 axon terminal morphologies at P+40%, P+50%, P+60%, P+70%, P+80%, and P+90% pupal development. Red arrowheads show examples of supernumerary bulbous tip filopodia at P+70%. Note that loss of autophagy leads to increased numbers of bulbous tip filopodia especially during the peak time of synaptogenesis (P+60%-P+80%). Repeated 5-10 times independently with similar results.

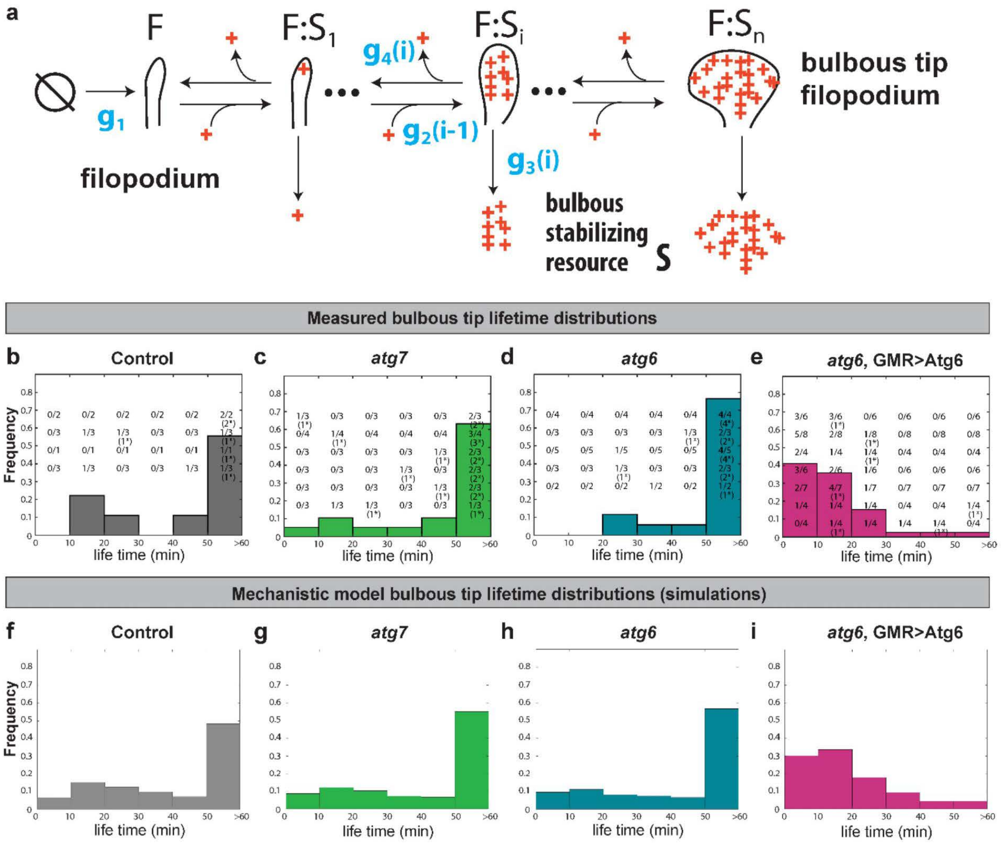

Supplementary Figure 11. The Mechanistic Model: Lifetimes of synaptogenic bulbous tip filopodia as a function of a limiting resource of synaptic seeding factors. a, Graphical depiction of the mechanistic model. **b-e,** Measured data: Histograms depicting the observed frequency of the respective bulbous tip life times during live imaging at P60. The numbers on histograms indicate the number of observations in the respective life time category per growth cone. Numbers in brackets with a star, e.g. (1*), indicate that the bulbous tip either already existed in the first imaging frame, or persisted until the last image. Thus, these life times might actually be longer than indicated here. **f-i,** Model output: Histograms depicting the frequency of the respective bulbous tip lifetimes according to simulations using the mechanistic model. Note that the mechanistic model successfully recapitulates the observed lifetimes of bulbous tip filopodia.

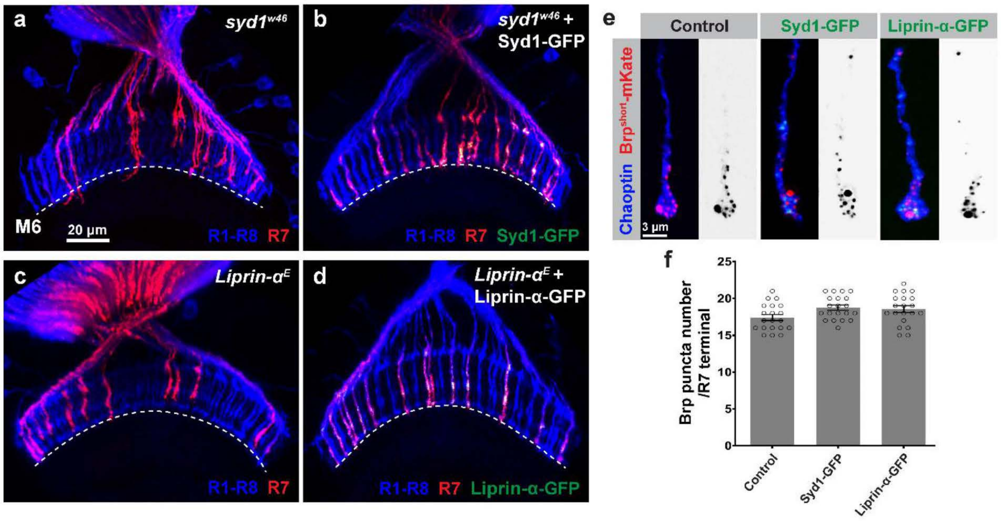
a
syd1^{w46}
M6
20 µm
R1-R8 R7
b
syd1^{w46} +
Syd1-GFP
R1-R8 R7 Syd1-GFP
c
Liprin-α^{E}
R1-R8 R7
d
Liprin-α^{E} +
Liprin-α-GFP
R1-R8 R7 Liprin-α-GFP
e
Control
Syd1-GFP
Liprin-α-GFP
Chaoptin Brp^{short}-mKate
3 µm
f
25
20
15
10
5
0
Brp puncta number
/R7 terminal
Control
Syd1-GFP
Liprin-α-GFP

Supplementary Figure 12. Syd1 or Liprinα overexpression does not alter synapse number. a, *syd1* mutant R7 photoreceptors fails to target their correct medulla layer, M6. **b**, Syd1-GFP overexpression in *syd1* mutant R7 photoreceptors rescues mistargeting phenotypes. **c,** *liprinα* mutant R7 photoreceptors fails to target their correct medulla layer, M6. **d,** Liprinα-GFP overexpression in *syd1* mutant R7 photoreceptors rescues mistargeting phenotypes. Repeated 2 times independently with similar results. **e,** Representative images of Brp$^{\text{short}}$-mKate labelled active zones in control, Syd1-GFP expressing and Liprinα-GFP expressing R7 axon terminals. Repeated 3 times independently with similar results. **f,** Number of Brp puncta in control, Syd1-GFP expressing and Liprinα-GFP expressing R7 axon terminals. n=20 terminals per condition. One-way ANOVA and Tukey HSD as post hoc test. Error bars denote mean ± SEM. No significant difference found between groups. Source data are provided as a Source Data file.

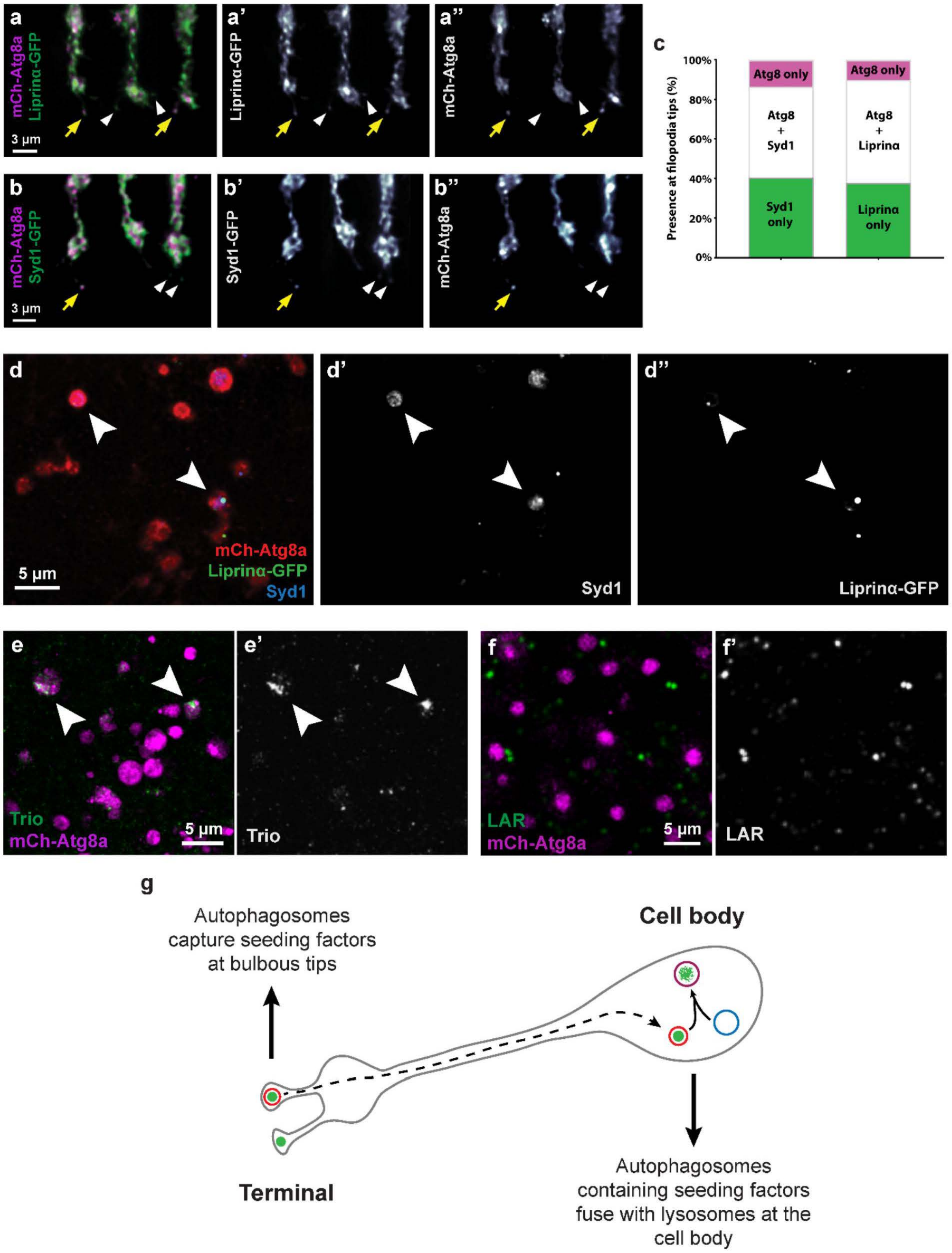
a
mCh-Atg8a
Liprinα-GFP
3 µm
a'
Liprinα-GFP
a''
mCh-Atg8a
b
mCh-Atg8a
Syd1-GFP
3 µm
b'
Syd1-GFP
b''
mCh-Atg8a
c
Presence at filopodia tips (%)
100%
80%
60%
40%
20%
0%
Atg8 only
Atg8 + Syd1
Syd1 only
Atg8 only
Atg8 + Liprinα
Liprinα only
d
5 µm
mCh-Atg8a
Liprinα-GFP
Syd1
d'
Syd1
d''
Liprinα-GFP
e
Trio
mCh-Atg8a
5 µm
e'
Trio
f
LAR
mCh-Atg8a
5 µm
f'
LAR
g
Autophagosomes capture seeding factors at bulbous tips
Cell body
Terminal
Autophagosomes containing seeding factors fuse with lysosomes at the cell body

Supplementary Figure 13. Autophagosomes colocalize with synaptic seeding factors at filopodia tips and contain synaptic seeding factors in autolysosomes at cell bodies. a-a'', Representative R7 axon terminals expressing Liprin-α-GFP and mCherry-Atg8a. **b-b'',** Representative R7 axon terminals expressing Syd-1-GFP and mCherry-Atg8a. Yellow arrows: co-localization of Atg8a with synaptic seeding factors Liprin-α and Syd-1 at filopodia tips; white arrowheads: Liprin-α and Syd-1 at filopodia tips without apparent Atg8a colocalization. Repeated 5-10 times independently with similar results. **c,** Percentages of Syd-1 only, Liprin-α only, Atg8a and Syd-1 together (Atg8a + Syd-1), Atg8a and Liprin-α together (Atg8a + Liprin-α), and Atg8a-only filopodia tips. n=30 terminals per condition. Note that most Atg8a-positive compartments are also positive for the synaptic seeding factors. All filopodia from 30 terminals were pooled for quantification. **d-d'',** Atg8a-positive autolysosomes contain Syd1 (detected with anti-Syd1 antibody) and Liprinα (UAS-Liprin-GFP) at photoreceptor cell bodies. **e-f',** Atg8a-positive autolysosomes at photoreceptor cell bodies contain Trio (**e-e'**) but not membrane receptor LAR (**f-f'**). Repeated 3 times independently with similar results. **g,** Schematic of proposed mechanism of degradation of synaptic seeding factors by autophagy in photoreceptor neurons, including capture at axon terminal filopodia tips and degradation during retrograde transport to the cell body, as first shown in vertebrate cell culture [1]. Source data are provided as a Source Data file.

Supplementary Tables

	Short lived (sF)		Long-lived (ℓF)	
	Life time	Number	Life time	Number
wild type	2.3 (1.6)	2.6 (1.8)	15 (10)	2.6 (1.4)
atg6	2.7 (1.9)	2 (2.3)	21 (16)	4.8 (1.2)
atg7	2.4 (1.6)	2.2 (1.9)	20 (15)	5.6 (2.6)
atg6, GMR>Atg6	2.2 (1.7)	2.9 (1.9)	13 (7)	1.4 (0.84)

Supplementary Table 1: Lifetimes (min) and average numbers of short- and long-lived filopodia at P60. Mean ± (standard deviation). Number distributions are shown in Supplementary Fig. 9.

	r3	r2B	E[f1]	r4	r5	Avg. bulbs
wild type	0.0122	0.0948	0.1291	0.0014	0.0108	1.653
atg6	0.0229	0.0932	0.2463	0.0025	0.0205	3.028
atg7	0.0189	0.1985	0.0955	0.0019	0.0170	2.501
atg6, GMR>Atg6	0.1032	0.1085	0.9515	0.1010	0.0018	1.644

Supplementary Table 2: Measured average rates of the data-driven model at P60.

The denotation is taken from the original model in Figure 3A of [2] and refer to the following filopodial transitions:

Filopodia $\underset{r4}{\overset{r3=r2B*f1}{\leftarrow\!-}}$ Transient Bulbs $\overset{r5}{\rightarrow}$ Stable Bulbs

r3: measured rate of bulb formation, contains r2B * f1, unit: 1/min
r2B: propensity to form bulbs, cannot be measured, because feedback f1 reduces r2B, shown is the only possible fit of r2B, unit: 1/min
f1: negative feedback on bulb formation, cannot be measured, see r5, shown is the only possible fit of the data (r2B; smaller f1 indicates stronger feedback; f1=1 indicates no feedback
r4: measured rate of bulb disappearance, unit: 1/min
r5: measured rate of bulb stabilization, unit: 1/min
Avg. bulbs: average number of bulbs per time instance (min) over an hour (P60)
In blue: direct measurements

	$c_{1,sF}$	$c_{2,sF}$	$c_{1,\ell F}$	$c_{2,\ell F}$	c_3	c_4	c_5	c_6	B_{50}	$t_{1/2}$
wild type	1.82	0.43	0.28	0.07	0.024	1/120§	0.063	1/133	0.078	1000§
atg6	1.19	0.37	0.37	0.05	0.018	1/120§	0.068	1/133	0.716	1000§
atg7	1.48	0.42	0.45	0.05	0.033	1/120§	0.075	1/133	0.162	1000§
atg6, GMR>Atg6	2.13	0.45	0.17	0.08	0.033	0.071	0.001	1/133	3.733	1000§

Supplementary Table 3: Parameters of the data-driven model. All parameters in units min^{-1} except for B_{50} (unitless) and $t_{1/2}$ (min). §previously determined [2].

Supplementary References

1 Maday, S. & Holzbaur, E. L. Autophagosome biogenesis in primary neurons follows an ordered and spatially regulated pathway. *Dev Cell* **30**, 71-85, (2014).

2 Ozel, M. N. *et al.* Serial Synapse Formation through Filopodial Competition for Synaptic Seeding Factors. *Dev Cell*, (2019).

5. Manuscript 3

Temperature-dependent synaptic specificity in the *Drosophila* visual system

Kiral, F.R. and Hiesinger, P.R.

This manuscript is in preparation.

Contribution

All results presented in this chapter were designed, performed, and analyzed by myself. I wrote this chapter with the supervision of Prof. Dr. P. Robin Hiesinger.

Abstract

During brain development, neurons use several molecular and cellular strategies to identify correct synaptic partners that is fundamental to the proper assembly and function of neuronal circuits. Although the contribution of genetic factors for synapse-specific brain wiring is well established, to what extent environmental factors play a role in circuit assembly and synaptic precision still remains elusive. Here, using *Drosophila* R7 photoreceptors, we show that developmental temperature affects synapse formation and synaptic partner choice during the assembly of neuronal circuits. Specifically, low developmental temperature increases R7 axonal filopodial stability and dendritic branching of R7's potential postsynaptic partners that eventually leads to increased number of synapses and recruitment of more synaptic partners. This temperature induced synaptic promiscuity can be mimicked by the cellular ablation of R7's main synaptic partner Dm8 in which R7s synapse with alternative partners. We propose that neurons have the capacity to form synaptic connections with a broad range of cell types but prevented from doing so by the control of axonal filopodia kinetics, dendritic reach and synaptic partner survival.

Introduction

Proper brain wiring during development is largely based on the ability of neurons to recognize appropriate partners and initiate synapse formation. A prerequisite to establish a synaptic connection is that axonal and dendritic projections of two neurons need to be in close proximity in time and place. Such spatiotemporal patterning of neuronal projections in a dynamically changing environment during development may restrict neuronal encounters that could be sufficient to ensure right partnerships even if synapse formation is a promiscuous process. Evidently, many neurons readily form synapses with incorrect partners when projected to wrong target fields or form synapses with themselves when no other choice is given (Berger-Muller et al., 2013; Kulkarni et al., 2016; Van der Loos and Glaser, 1972). Recent years have seen a remarkable progress to identify positional strategies used by neurons during development to establish proper neuronal circuits. Such strategies include axon pre-sorting, dendritic self-avoidance and tiling, axo-dendritic approach angles that determines the degree of synaptic contacts and also the regulation of filopodia dynamics to dynamically restrict neuronal encounters (Balaskas et al., 2019; Hassan and Hiesinger, 2015; Kiral et al., 2020; Petrovic and Schmucker, 2015).

To date, brain wiring studies have mostly focused on genetic and molecular factors determining precision and variability of neuronal circuits despite a generally accepted notion that environmental factors may equally contribute to final wiring pattern. Non-amniotic animals are especially susceptible to changing environmental conditions including fluctuations in environmental temperature during their development. For instance, it is well established that temperature affects the rate of embryonic, larval and pupal development of insects including the *Drosophila* (Ludwig and Cable, 1933; Powsner, 1935). A few studies on the effect of environmental temperature during development have shown behavioral differences in adults reared at different temperatures (Spencer et al., 2019; Tautz et al., 2003). However, it still remains elusive whether and how developmental temperature affects nervous system development, especially synaptic partner choice and synapse formation during the establishment of neuronal circuits.

In this study, using *Drosophila* R7 photoreceptors as a model, we show that developmental temperature affects filopodia speed and stability in R7 axon terminals leading to changes in neuronal connectivity. Particularly, low developmental temperature decreases filopodia speed leading to stabilization of more filopodia that eventually increases R7 synapse number and number of postsynaptic partners they recruit including incorrect partners. Interestingly, killing R7's main synaptic partner Dm8 neurons by DIPγ loss-of-function leads to similar promiscuous synapse formation with aberrant synaptic partners. Our findings argue against the idea that synapse specificity is established through specific molecular interactions between neuronal partners and support a model whereby instead, a developmental growth program that brings right partners together in time and space leading to precise ensembles of neuronal circuits by allowing promiscuous synapse formation.

Results

We have previously shown that the level of autophagy in developing R7 photoreceptors influences filopodia speed and stability. Particularly, loss of autophagy in developing R7 terminals decreased the filopodia speed allowing stabilization of more filopodia, which eventually led to ectopic synapse formation and recruitment of aberrant synaptic partners. This observation led us to propose that neurons use filopodia kinetics as a means to restrict synapse formation and synaptic partner choice that are not otherwise prevented from forming synapses with incorrect partners.

Developmental temperature influences R7-Dm8 connectivity

Ectotherms including the *Drosophila* are particularly susceptible to environmental temperature during development. Although previous studies showed the effect of rearing temperature on adult behaviors, it is still largely unknown whether or how developmental temperature affects brain wiring (Spencer et al., 2019; Tautz et al., 2003). In physical terms, temperature affects the motion of molecules that may have a direct effect on biological processes. Therefore, we first tested the effect of temperature on R7 axon terminal filopodia dynamics during synapse formation (60% of pupal development – P+60%). We performed fast, high-resolution live imaging of R7 axon terminals (1 min time lapse for 1h periods) at 18°C, close to low end of physiologically relevant rearing temperature for *Drosophila* and at 29°C on the warm side. R7 axon terminals imaged at low temperature showed decreased filopodia speed and increased formation of stable, synaptogenic filopodia (Figure 1a), while axon terminals exposed to high temperature had faster filopodia and mostly fail to stabilize synaptogenic filopodia (Figure 1b). Consistently, quantification of synaptogenic filopodia lifetime showed that most synaptogenic filopodia of R7 axon terminals exposed to low temperature were stable throughout the 1-hour imaging window (filopodia lifetime >60min), while oppositely, most filopodia of R7 axon terminals exposed to high temperature lived shorter than 30 mins (Figure 1c). These results demonstrate that environmental temperature affects filopodia dynamics of developing neurons and raises the question of whether changes in filopodia speed and stability due to temperature have an influence on synapse formation and synaptic partner choice.

To address this question, we first generated sparse clones of R7 photoreceptors expressing the active zone marker Brp^{short}-GFP that is specifically localized to presynaptic active zones without affecting synaptic development (Ozel et al., 2019; Schmid et al., 2008). Also, we exposed developing animals to different temperatures only between 40% to 100% of pupal development (P+40%-100%) since P+40% marks the end of layer-specific targeting and the onset of synaptogenesis in developing R7 photoreceptors (Kiral et al., 2020; Ozel et al., 2019; Ozel et al., 2015). R7s developed at 25°C, usual laboratory temperature for *Drosophila* rearing, formed around 20-25 synapses. However, R7s developed at low temperature formed significantly higher synapses and oppositely R7s developed at high temperature formed significantly less synapses suggesting that synapse formation is affected by developmental temperature possibly through changes in filopodia speed and stability (Figure 1d-g). R1-R6 photoreceptor synapse numbers were also similarly affected by developmental temperature, which was reflected in electroretinogram (ERG) recording as the flies developed at low temperature showed increased ERG on-transient amplitudes that is indicative of increased neurotransmission between photoreceptors and their synaptic partners (Supplementary Figure 1).

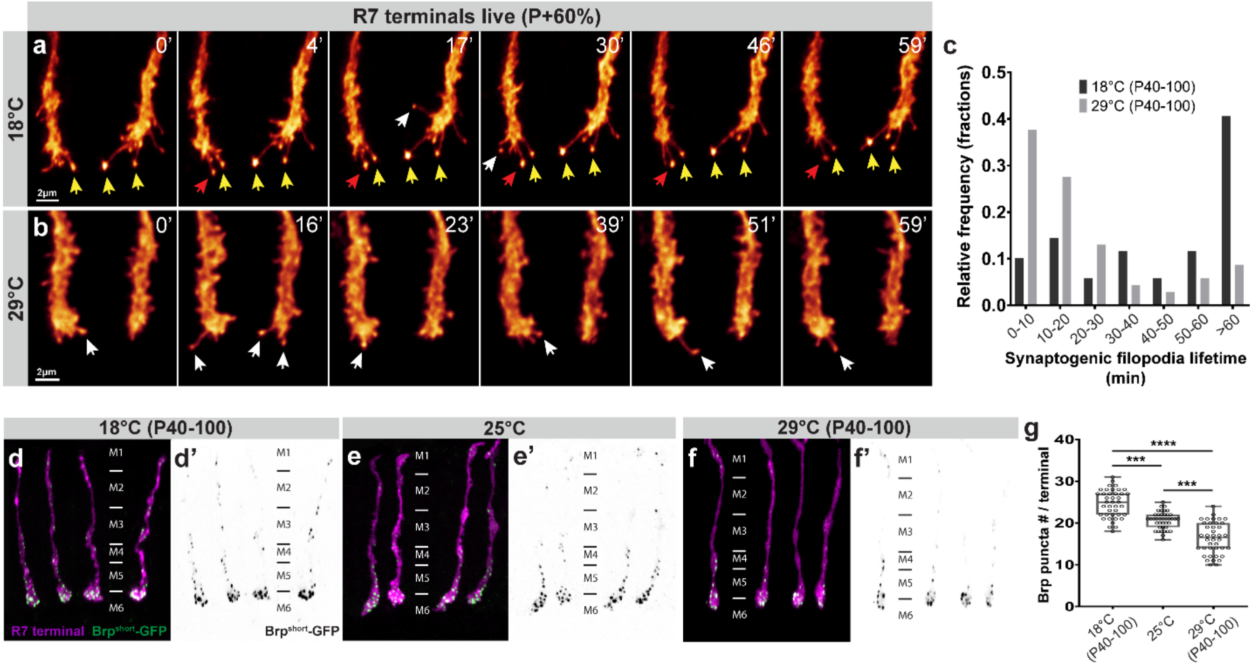
R7 terminals live (P+60%)
a
0'
4'
17'
30'
46'
59'
18°C
2μm
b
0'
16'
23'
39'
51'
59'
29°C
2μm
c
Relative frequency (fractions)
0.5
0.4
0.3
0.2
0.1
0.0
18°C (P40-100)
29°C (P40-100)
0-10
10-20
20-30
30-40
40-50
50-60
>60
Synaptogenic filopodia lifetime (min)
18°C (P40-100)
25°C
29°C (P40-100)
d
d'
e
e'
f
f'
M1
M2
M3
M4
M5
M6
R7 terminal
Brp^short-GFP
Brp^short-GFP
g
Brp puncta # / terminal
40
30
20
10
0
****
***
***
18°C (P40-100)
25°C
29°C (P40-100)

Figure 1: Developmental temperature influences R7s synapse number through altered filopodia stability. a-b, Live imaging of R7 terminals at P+60% (during synaptogenesis) at 18°C (a) and 29°C (b). white arrows: unstable bulbous tip filopodia, yellow arrows: stable bulbous tip filopodia throughout the live imaging window, red arrows: bulbous tip filopodia that appear during imaging and stay stable until the end of imaging. See 'Materials and methods' for live imaging protocol details. **c,** Synaptogenic filopodia lifetime distribution at 18°C and 29°C shown as fractions of 10 min increments. n=23 terminals per condition. **d-f',** Representative images of R7 photoreceptor axon terminals with Brp^{short}-GFP marked active zones developed at 18°C between P+40%-P+100% (synaptogenesis phase) (d-d'), at 25 °C (e-e'), and 29°C between P+40%-P+100% (f-f'). **g,** Number of Brp puncta per R7 terminals at different developmental temperatures. n=40 terminals per condition. Kruskal-Wallis and Dunn's as post-hoc test; ***p<0.0002, ****p<0.0001. The bottom-most and top-most horizontal lines, the lower and upper hinges, and the middle line of the boxplots indicate the minimum and maximum values, the 25th and 75th percentiles, and the mean, respectively.

Previous electron microscopy reconstruction studies have identified the synaptic partners of R7 photoreceptors developed at 25°C revealing highly stereotypic connections (Takemura et al., 2015). The main synaptic partner of R7s is the wield-field amacrine neuron Dm8 (Gao et al., 2008; Takemura et al., 2015). To a lesser extent, R7s also form synaptic connections with Dm9, Dm11 and Tm5 neuron subtypes (Gao et al., 2008; Karuppudurai et al., 2014; Takemura et al., 2015). Here, to address the question whether and how R7 connectivity is affected by temperature, first we investigated the effect of temperature on R7's main synaptic partner Dm8. Since there is no developmental Dm8-specific driver to reliably perform live imaging on these neurons, instead we generated single cell clones of Dm8s and exposed developing animals to low and high temperatures during synaptogenesis between P+40%-100%. Dm8s developed at low temperatures had increased number of dendritic branches and total branch length while mean branch length was not affected compared to the ones developed at high temperature (Figure 2a-e, Supplementary Figure 2). Consistently, occupying a larger area, Dm8s developed at low temperature contacted with more R7s (Figure 2f). Following the effects of temperature on R7s' filopodia stability and synapse numbers and also Dm8's dendritic branching, we performed activity-dependent GRASP, which is based on *trans*-synaptic reconstruction of GFP fragments only when synaptic vesicle release occurs (Feinberg et al., 2008; Macpherson et al., 2015), between R7s and Dm8s developed at low and high temperatures during synaptogenesis to assess the changes in strength of R7-Dm8 connectivity. As shown in Figure 2g-i, R7s and Dm8s form stronger connections when developed at low temperatures.

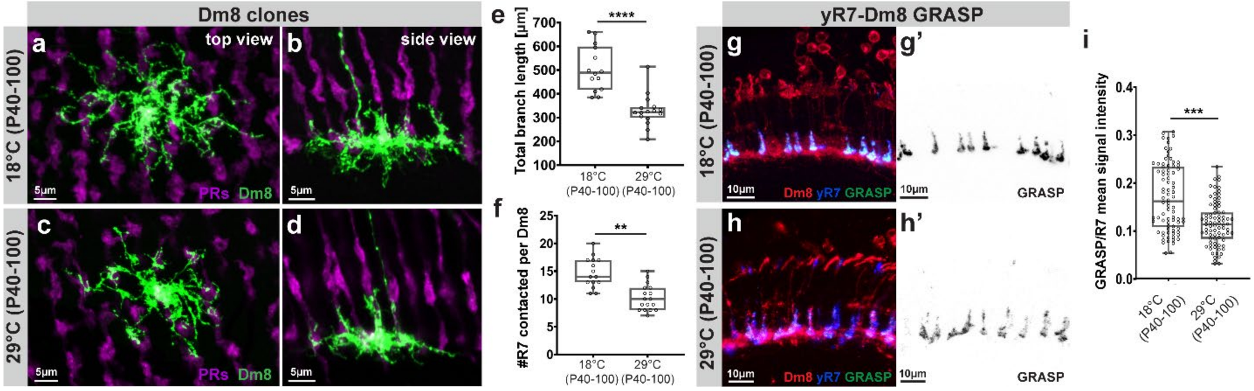
Dm8 clones
a
top view
b
side view
18°C (P40-100)
29°C (P40-100)
5µm
PRs Dm8
c
d
e
Total branch length [µm]
700
600
500
400
300
200
100
****
18°C (P40-100)
29°C (P40-100)
f
#R7 contacted per Dm8
25
20
15
10
5
0
**
yR7-Dm8 GRASP
g
g'
h
h'
10µm
Dm8 yR7 GRASP
GRASP
i
GRASP/R7 mean signal intensity
0.4
0.3
0.2
0.1
0.0
***

Figure 2: Low developmental temperature increases Dm8 branching and R7-Dm8 contacts. **a-b,** Dorsoventral (top view) (a) and proximodistal (side view) (b) views of a single Dm8 cell developed at 18°C between P+40%-P+100%. **c-d,** Dorsoventral (top view) (a) and proximodistal (side view) (b) views of a single Dm8 cell developed at 29°C between P+40%-P+100%. **e,** Total branch length of Dm8s developed at different temperatures during synaptogenesis. n=14 cells for 18°C (P+40%-P+100%), n=16 cells for 29°C (P+40%-P+100%). Kolmogorov-Smirnov test; ****p<0.0001. **f,** The number of R7s contacted per Dm8 developed at different temperatures during synaptogenesis. n=14 cells for 18°C (P+40%-P+100%), n=16 cells for 29°C (P+40%-P+100%). Kolmogorov-Smirnov test; **p<0.0021. **g-h',** Activity-dependent GRASP between yellow R7s (yR7) and Dm8s developed at 18°C between P+40%-P+100% (g-g') and at 29°C between P+40%-P+100% (h-h'). **i,** GRASP signal intensity (normalized to R7 signal intensity) between yR7s and Dm8s developed at different temperatures during synaptogenesis. n=85 terminals per condition. Kolmogorov-Smirnov test; ***p<0.0002. The bottom-most and top-most horizontal lines, the lower and upper hinges, and the middle line of the boxplots indicate the minimum and maximum values, the 25th and 75th percentiles, and the mean, respectively.

Low developmental temperature leads aberrant synaptic connections

Stronger R7-Dm8 synaptic connectivity in brains developed at low temperatures suggest that environmental factors may have a role in shaping the strength of connectivity between normal synaptic partners. An interesting question arises here whether these changes in filopodia dynamics and dendritic branching will be enough to create a different wiring pattern through promiscuous synapse formation between incorrect partners. To address this question, we made use of an anterograde trans-synaptic tracing method called *trans*-Tango. This method unbiasedly labels all postsynaptic neurons connected to a neuron of interest (Talay et al., 2017). Here, we used a yellow-type R7-specific driver (Rhodopsin4-Gal4) to reveal neurons synaptically connected to R7s at different developmental temperatures. Consistent with previous electron microscopy connectome studies performed with flies raised at 25°C, *trans*-Tango mainly showed Dm8 connections and to a lesser degree Tm5 connections in fly brains raised at 25°C (Figure 3b). At higher temperatures, the general wiring pattern stayed the same although with apparent, but not statistically significant, decrease in the number of postsynaptic partners (Figure 3c-d). However, remarkably, R7s in brains developed at low temperature connected to higher number of postsynaptic partners and more importantly it led to R7s connect to extra, morphologically recognizable cell types including Mi neurons, C2-C3 neurons and Tm9 neurons (Figure 3a and d). To test whether these synaptic contacts between R7s and aberrant partners are functional, we next used activity-dependent GRASP between R7s and some aberrant partners we identified from *trans*-Tango. Activity-dependent GRASP between R7s-Mi1s, R7s-Mi4s, and R7s-Tm9s in brains developed at low temperature revealed active connections between these cells, while expectedly brains developed at 25°C did not show active synaptic signals (Figure 3e-j’). Furthermore, similar to the effect of developmental temperature on Dm8 branching, Mi4 neurons developed at low temperature showed increased branch number and total branch length leading their branches to invade M6 layer where R7s are synaptically most active (Supplementary Figure 3). This suggests that altered filopodia activity and dendritic branching pattern at different developmental temperatures not only change the strength of synaptic connections between usual partners but also may induce synapse formation between incorrect partners simply increasing visibility of them to each other in time and space.

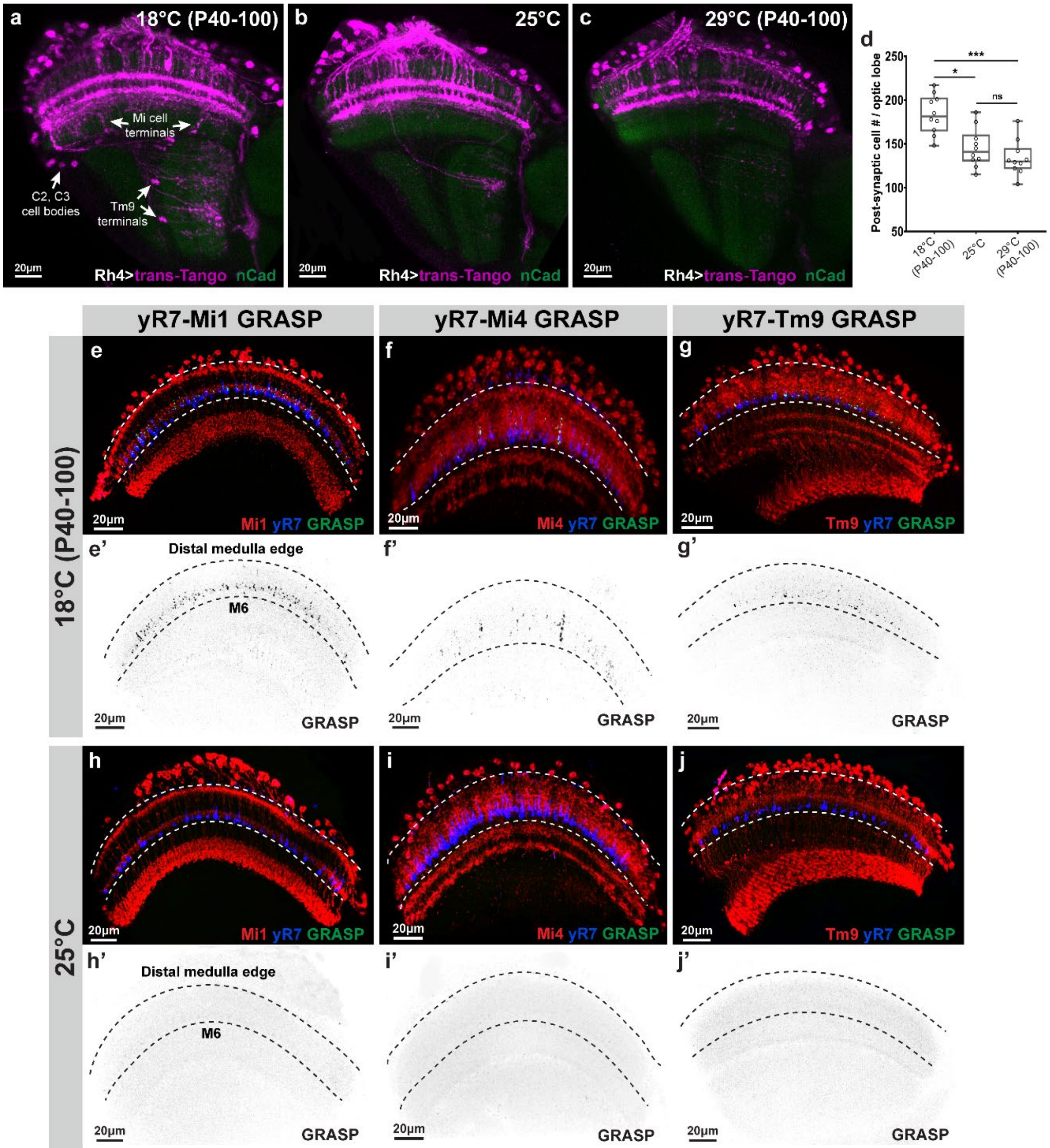
a
18°C (P40-100)
b
25°C
c
29°C (P40-100)
Mi cell terminals
C2, C3 cell bodies
Tm9 terminals
20µm
Rh4>trans-Tango nCad
d
Post-synaptic cell # / optic lobe
250
200
150
100
50
***
*
ns
18°C (P40-100)
25°C
29°C (P40-100)
yR7-Mi1 GRASP
yR7-Mi4 GRASP
yR7-Tm9 GRASP
18°C (P40-100)
25°C
e
f
g
h
i
j
Mi1 yR7 GRASP
Mi4 yR7 GRASP
Tm9 yR7 GRASP
e'
f'
g'
h'
i'
j'
Distal medulla edge
M6
GRASP

Figure 3: Developmental temperature influences R7's synaptic partner choice. **a-c,** Representative images of neurons connected to yR7s in brains developed at 18°C between P+40%-P+100% (a), 25°C (b), and 29°C between P+40%-P+100% labelled with *trans*-Tango. Arrows point examples of cell types aberrantly connect to yR7s at low developmental temperature. Magenta=postsynaptic neurons, green=CadN. **d,** Number of postsynaptic neurons per optic lobe connected to yR7s in brains developed at different temperatures during synaptogenesis. n=10 optic lobes per condition. Kruskal-Wallis and Dunn's as post-hoc test; *p<0.0332, ***p<0.0002, ns=not significant. The bottom-most and top-most horizontal lines, the lower and upper hinges, and the middle line of the boxplots indicate the minimum and maximum values, the 25th and 75th percentiles, and the mean, respectively. **e-j',** Activity-dependent GRASP between yR7s and some aberrant partners shown in *trans*-Tango (a) demonstrate active promiscuous synapses formed at low developmental temperature (18°C between P+40%-P+100%). Dashed lines mark the region between the edge of the medulla and M6 layer where R7axon terminals extend along.

Taken together, our observations revealed that low developmental temperature during synaptogenesis changes dynamic neuronal encounters both through increased filopodia dynamics and increased dendritic branching, which lead to increased synapse formation between appropriate partners but also change brain wiring pattern leading to promiscuous synapse formation between inappropriate partners. These findings support the notion that brain wiring is under control of both genetic and environmental factors especially for non-amniotic animals subjected to fluctuations in environmental temperature during development.

Dm8 cell death due to DIPγ loss-of-function does not affect R7 synapse number

A great progress has been made over the last couple of decades in the study of molecular mechanisms contributing to the development of neuronal circuits and the focus has been mainly on identifying molecularly encoded instructions that specify synaptic connections (Kolodkin and Tessier-Lavigne, 2011; Sanes and Zipursky, 2020). This view interprets synapse specification process as a molecular key-and-lock mechanism in which synaptic partners express matching molecular codes to recognize each other and initiate synapse formation. A recent discovery of a family of interacting cell surface proteins, Dprs and Dpr interacting proteins (DIPs), have been investigated in the context of synapse specification due to the observations showing that interacting pairs of Dpr/DIPs are expressed in synaptic partners in the *Drosophila* brain with a remarkable specificity (Carrillo et al., 2015). However, so far, loss of different Dpr/DIP pairs interactions have been primarily implicated in branch arborization and cell survival (Courgeon and Desplan, 2019; Xu et al., 2019; Xu et al., 2018). Particularly, a recent study showed that Dpr11/DIPγ interaction between yellow subtypes of R7s and Dm8s (yR7 and yDm8) before synapse formation starts is required for survival of yDm8s. In DIPγ loss-of-function, the majority of yDm8s die and the surviving yDm8s lack their home-columns sprigs, a distally extended membrane protrusion that wraps R7 axon terminal from medulla layers M4 to M6 where R7s and Dm8s form majority of their synaptic connections (Courgeon and Desplan, 2019). Therefore, DIPγ loss-of-function phenotypes give us the opportunity to address two questions: First, Do R7s still form synaptic contacts with surviving Dm8s despite lacking Dpr11/DIPγ interaction, which was proposed to be required for synapse specification between these neuronal partners? and second, what happens to R7s when they lose majority of synaptic contacts with their main synaptic partners? Will they only form synapses with other usual partners where Dpr11/DIPγ interaction is not required? Or will they find alternative/incorrect partners and promiscuously form synaptic contacts?

To address these questions, we first set out the experiments to reproduce previously shown effects of DIPγ loss-of-function on Dm8 survival and home-column sprig morphology (Courgeon and Desplan, 2019). As shown in Figure 4a-e', DIPγ loss-of-function leads to partial lethality of Dm8s and surviving Dm8s lack their home-column sprigs only maintaining membrane contacts with yR7s at M6 medulla layer. Next, we sought to address the question whether yR7s can still form synaptic contacts with surviving Dm8s. Here, activity-dependent GRAPS between yR7s and Dm8s in DIPγ mutant background revealed that yR7s still form synaptic contacts with surviving Dm8s although the GRASP signal is mostly confined to M6 layer due to the absence of Dm8 home-column sprigs at medulla layers M4 and M5 (Figure 4f-h). Therefore, we concluded that Dpr11/DIPγ interaction is not required to specify synapses between R7s and Dm8s but required for Dm8 survival and proper home-column sprig morphology.

During synaptogenesis, R7 photoreceptors form the majority of their synapses between medulla layers M4-M6 where they are in direct membrane contact with Dm8s. Since DIPγ loss-of-function leads partial Dm8 lethality and the survivors lack membrane protrusion at medulla layers M4 and M5, the majority of R7-Dm8 synaptic contacts are lost. This raises the question of whether R7s will have reduced number of synapses when they lost the majority of synaptic contacts with their main partners or will they compensate this loss contacting with other potential partners. To address this question, first, we labelled active zones in yR7s driving Brp^{short}-GFP with a yR7s-specific driver Rh4-Gal4 in controls and DIPγ mutants. Suprisingly, the number of synapses R7s form was not significantly different between controls and DIPγ mutants (Figure 4i-k). In fact, previous analysis of R7 synapse number in Dpr11 loss-of-function also showed no effect (Xu et al., 2018). These results collectively suggest that the number of synapses R7s form during development is independent of Dpr11/DIPγ interaction and the presence of R7's main synaptic partner Dm8s and they possibly compensate the loss synaptic contacts with their main partner by contacting with other potential partners.

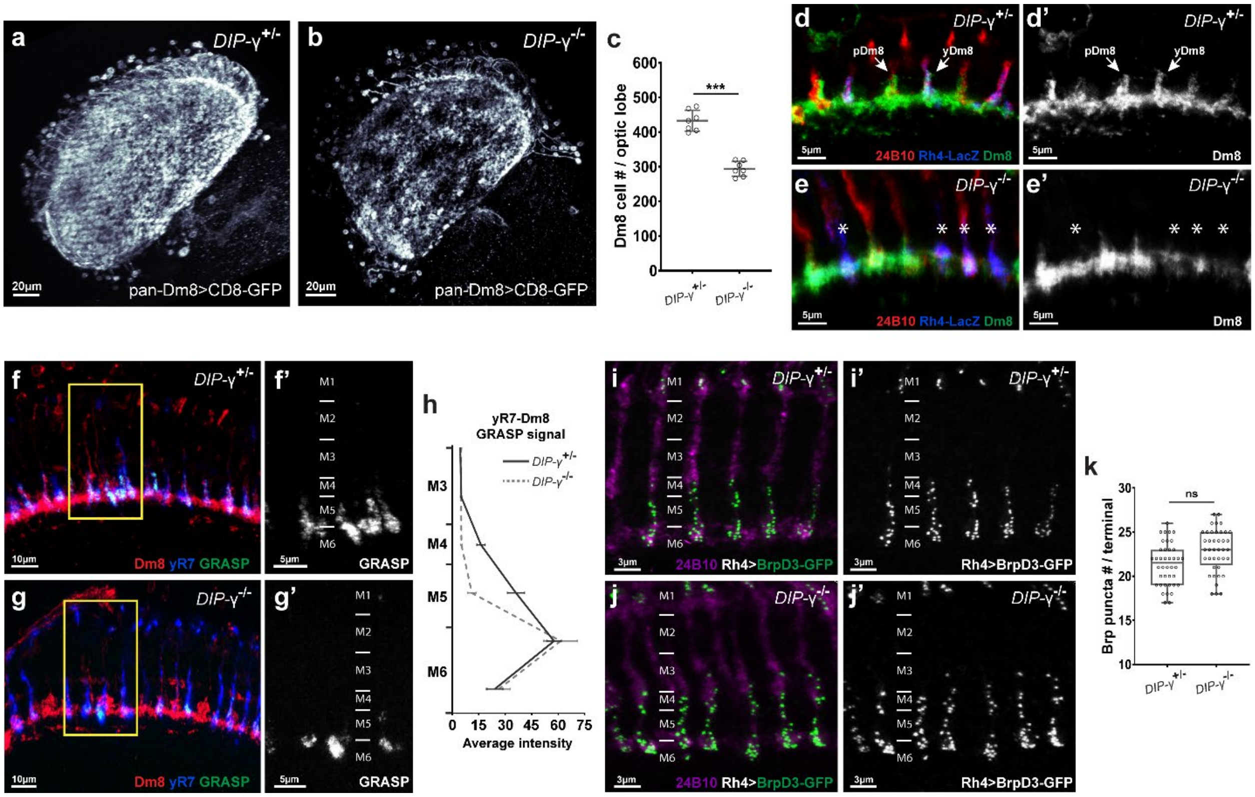
a
DIP-γ+/-
20μm
pan-Dm8>CD8-GFP
b
DIP-γ-/-
20μm
pan-Dm8>CD8-GFP
c
Dm8 cell # / optic lobe
600
500
400
300
200
100
0
***
DIP-γ+/-
DIP-γ-/-
d
DIP-γ+/-
pDm8
yDm8
5μm
24B10 Rh4-LacZ Dm8
d'
DIP-γ+/-
pDm8
yDm8
5μm
Dm8
e
DIP-γ-/-
* * * *
5μm
24B10 Rh4-LacZ Dm8
e'
DIP-γ-/-
* * * *
5μm
Dm8
f
DIP-γ+/-
10μm
Dm8 yR7 GRASP
f'
M1
M2
M3
M4
M5
M6
5μm
GRASP
g
DIP-γ-/-
10μm
Dm8 yR7 GRASP
g'
M1
M2
M3
M4
M5
M6
5μm
GRASP
h
yR7-Dm8
GRASP signal
DIP-γ+/-
DIP-γ-/-
M3
M4
M5
M6
0 15 30 45 60 75
Average intensity
i
DIP-γ+/-
M1
M2
M3
M4
M5
M6
3μm
24B10 Rh4>BrpD3-GFP
i'
DIP-γ+/-
M1
M2
M3
M4
M5
M6
3μm
Rh4>BrpD3-GFP
j
DIP-γ-/-
M1
M2
M3
M4
M5
M6
3μm
24B10 Rh4>BrpD3-GFP
j'
DIP-γ-/-
M1
M2
M3
M4
M5
M6
3μm
Rh4>BrpD3-GFP
k
Brp puncta # / terminal
30
25
20
15
10
ns
DIP-γ+/-
DIP-γ-/-

Figure 4: Dm8 partial cell death and home-column sprig morphology defects in DIPγ mutants does not affect R7 synapse number. a-b, Proximodistal view of Dm8s in control (DIPγ$^{+/-}$) (a) and DIPγ mutants (DIPγ$^{-/-}$) (b). Note partial Dm8 cell death caused by DIPγ loss-of-function. **c,** Number of Dm8s per optic lobe. n=7 optic lobes per genotype. Kolmogorov-Smirnov test; ***p<0.0002. **d-e',** Dorsoventral view of Dm8s (green), yR7s (blue) and all photoreceptor terminals (red) in control (DIPγ$^{+/-}$) and in DIPγ mutants (DIPγ$^{-/-}$). Arrows show both yellow and pale type of Dm8s have home-column sprigs extending between medulla layers M4-M6 in controls (e-e'). Asterisks mark morphological defects in surviving yDm8 home columns in DIPγ mutants (DIPγ$^{-/-}$) as sprigs through M4-M5 layers are lost. **f-g',** Activity-dependent GRASP between yR7 and Dm8s in control (DIPγ$^{+/-}$) (f-f') and in DIPγ mutants (DIPγ$^{-/-}$) (g-g'). **h,** GRASP signal intensity between yR7s and Dm8s at medulla layers M3 to M6. Error bars denote mean ± SEM. Note that yR7s form active synaptic connections with surviving Dm8s although mostly confined to M6 layer due to lack of home-column sprigs in DIPγ mutants. **i-j',** Representative images of yR7 synapses (Brp^{short}-GFP marked active zones) in control (DIPγ$^{+/-}$) (i-i') and in DIPγ mutants (DIPγ$^{-/-}$) (j-j'). **k,** Number of Brp puncta per R7 terminals in control (DIPγ$^{+/-}$) and in DIPγ mutants (DIPγ$^{-/-}$). n=40 terminals. Kolmogorov-Smirnov test; ns=not significant. The bottom-most and top-most horizontal lines, the lower and upper hinges, and the middle line of the boxplots indicate the minimum and maximum values, the 25th and 75th percentiles, and the mean, respectively.

R7s compensate for loss of Dm8 contacts by forming stronger connections with other usual partners and forming connections with aberrant partners

The fact that R7s largely preserve their synapse number and distribution (Figure 4i-k) in the loss of the majority of synaptic contacts with their main partner Dm8s suggest that they may compensate for this loss by increasing contact numbers with their other usual partners or start forming synapses with other potential partners in the vicinity or both. Apart from Dm8s, R7s also form synaptic contacts with Dm9s, Dm11s and Tm5 subtypes (Gao et al., 2008; Karuppudurai et al., 2014; Takemura et al., 2015). To assess the strength of synaptic connections between R7s and their other usual partners, we performed activity-dependent GRASP between yR7s and Dm9s and yR7s and Dm11s. Although the GRASP signal in controls were largely uniform across R7 terminals in the medulla, in DIPγ loss-of-function roughly half of yR7s terminals showed stronger GRASP signal with both Dm9s and Dm11s (Figure 5a-g). Unfortunately, the direct visualization of which R7s lack Dm8s in their columns was not possible in this background but we may speculate that R7s with stronger synaptic connections with Dm9s and Dm11s might be the ones lacking their main partner Dm8s in those columns. Therefore, this data suggests that R7s may compensate for loss of Dm8 contacts by forming stronger connections with their other usual synaptic partners.

Loss of Dm8 cells in DIPγ loss-of-function may increase the synaptic availability of other usual partners but also may make other potential partners available, which R7s normally do not form synapse with. To probe for such promiscuous synaptic connectivity between R7s and potential partners in close proximity, we performed unbiased trans-synaptic tracing method *trans*-Tango in controls and DIPγ mutants with yR7s-specific driver Rh4-Gal4. Expectedly, controls brains mainly showed Dm8 labelling at M4-M6 medulla layers and Tm5 connections were also visible in the lobula (Figure 6a). However, in DIPγ mutant brains, several other neurons were also labelled demonstrating that R7s start to form synaptic connections with aberrant partners when they lose their main synaptic partner (Figure 6b). Also, although in decreased numbers, some Dm8 projections were still visible at M4-M6 medulla layers corroborating our result that yR7s still form synaptic connections

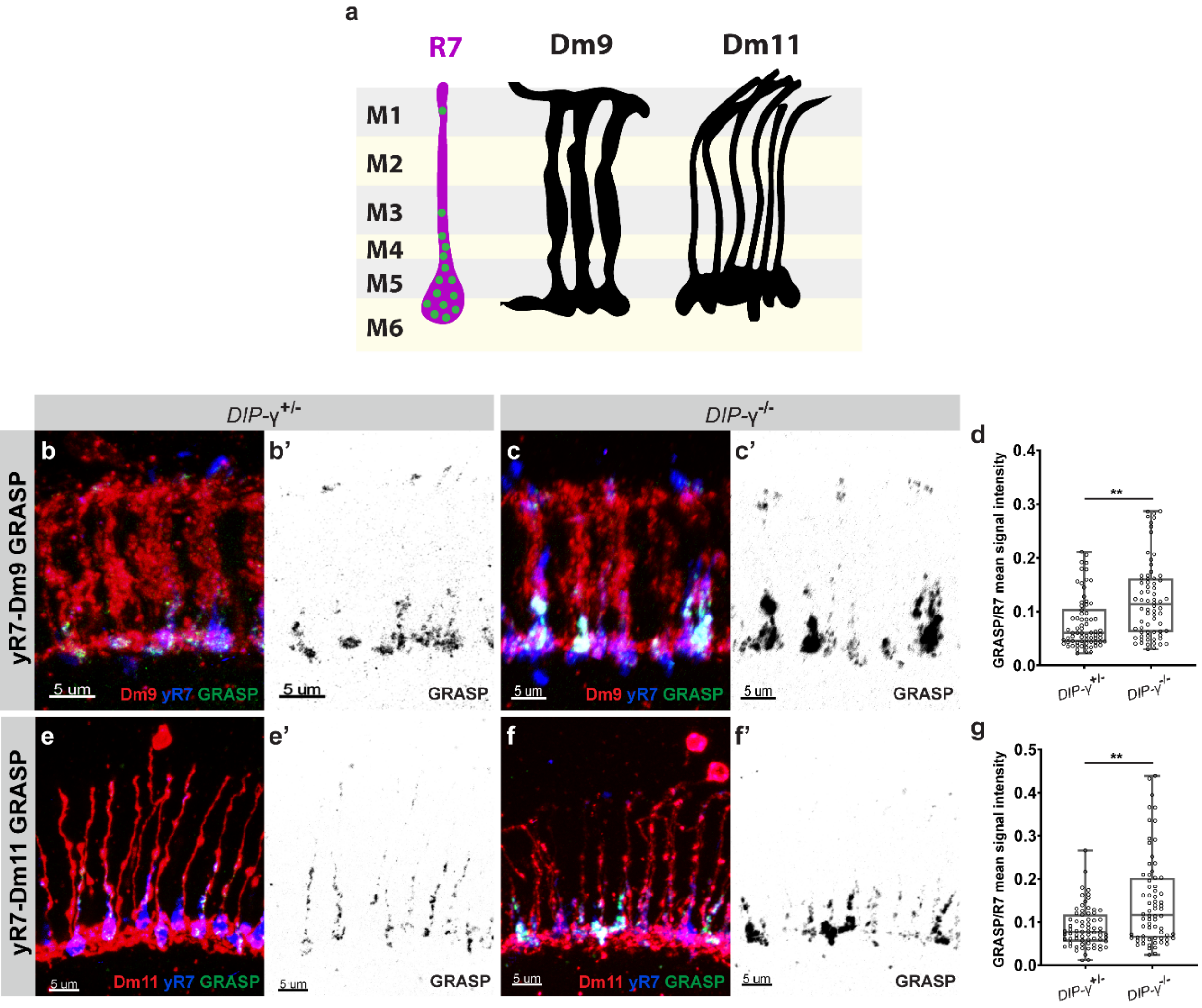
a
R7
Dm9
Dm11
M1
M2
M3
M4
M5
M6
DIP-γ+/-
DIP-γ-/-
yR7-Dm9 GRASP
b
b'
c
c'
5 um
Dm9 yR7 GRASP
GRASP
d
GRASP/R7 mean signal intensity
0.0
0.1
0.2
0.3
0.4
**
DIP-γ+/-
DIP-γ-/-
yR7-Dm11 GRASP
e
e'
f
f'
Dm11 yR7 GRASP
g
0.5

Figure 5: R7s compensate for loss of Dm8 contacts by forming stronger connections with other usual synaptic partners. **a,** Schematic representations of R7, Dm9 and Dm11 morphologies with R7 synapse distribution (green dots) through medulla layers M0-M6. **b-c',** Activity-dependent GRASP between yR7s and Dm9s in control (DIPγ$^{+/-}$) (b-b') and in DIPγ mutants (DIPγ$^{-/-}$) (c-c'). **d,** GRASP signal intensity (normalized to R7 signal intensity) between yR7s and Dm9s. n=70 terminals per genotype. Kolmogorov-Smirnov test; $^{**}p<0.0021$. **e-f',** Activity-dependent GRASP between yR7s and Dm11s in control (DIPγ$^{+/-}$) (e-e') and in DIPγ mutants (DIPγ$^{-/-}$) (f-f'). **g,** GRASP signal intensity (normalized to R7 signal intensity) between yR7s and Dm11s. n=70 terminals per genotype. Kolmogorov-Smirnov test; $^{**}p<0.0021$. The bottom-most and top-most horizontal lines, the lower and upper hinges, and the middle line of the boxplots indicate the minimum and maximum values, the 25th and 75th percentiles, and the mean, respectively.

with surviving Dm8s in DIPγ loss-of-function (Figure 6b). Furthermore, to show that these aberrant connections were active synapses, we performed activity-dependent GRASP between yR7s and Mi1s, yR7s and Mi4s, and yR7s and Tm9s. Expectedly, we observed active connections between these cells and yR7s in DIPγ mutant brains whereas control brains lacked these connections (Figure 6c-h'). We therefore concluded that R7s lacking

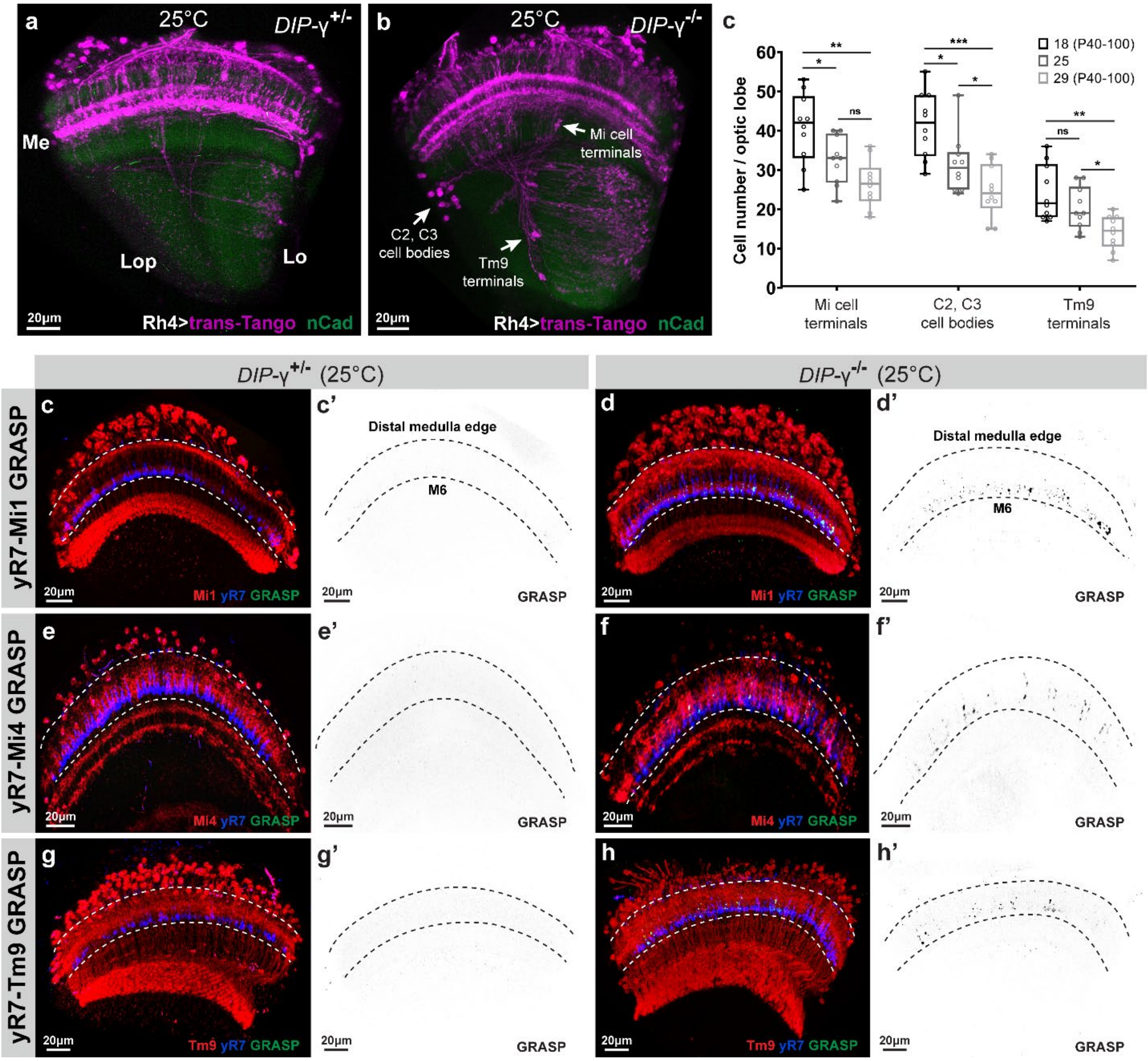
a
25°C
DIP-γ+/-
Me
Lop
Lo
20μm
Rh4>trans-Tango nCad
b
25°C
DIP-γ-/-
Mi cell terminals
C2, C3 cell bodies
Tm9 terminals
20μm
Rh4>trans-Tango nCad
c
Cell number / optic lobe
60
50
40
30
20
10
0
*
**
ns
***
*
*
ns
**
*
18 (P40-100)
25
29 (P40-100)
Mi cell terminals
C2, C3 cell bodies
Tm9 terminals
DIP-γ+/- (25°C)
DIP-γ-/- (25°C)
yR7-Mi1 GRASP
c
c'
Distal medulla edge
M6
20μm
Mi1 yR7 GRASP
20μm
GRASP
d
d'
Distal medulla edge
M6
20μm
Mi1 yR7 GRASP
20μm
GRASP
yR7-Mi4 GRASP
e
e'
20μm
Mi4 yR7 GRASP
20μm
GRASP
f
f'
20μm
Mi4 yR7 GRASP
20μm
GRASP
yR7-Tm9 GRASP
g
g'
20μm
Tm9 yR7 GRASP
20μm
GRASP
h
h'
20μm
Tm9 yR7 GRASP
20μm
GRASP

Figure 6: R7s lacking their main partners (Dm8s) in DIPγ mutants form promiscuous synapses with aberrant partners. **a-b,** Representative images of neurons connected to yR7s in control (DIPγ$^{+/-}$) (a) and in DIPγ mutants (DIPγ$^{-/-}$) (b). Arrows point examples of cell types aberrantly connect to yR7s at low developmental temperature. Magenta=postsynaptic neurons, green=CadN. **c**, Number of aberrant partners per optic lobe in DIPγ mutant brains developed at different temperatures. Note the additive effects of DIPγ loss-of-function and developmental temperature on synaptic promiscuity. n=10 optic lobe per condition. Kruskal-Wallis and Dunn's as post-hoc test; *$p<0.0332$, **$p<0.0021$, ***$p<0.0002$, ns=not significant. The bottom-most and top-most horizontal lines, the lower and upper hinges, and the middle line of the boxplots indicate the minimum and maximum values, the 25th and 75th percentiles, and the mean, respectively. **c-h',** Activity-dependent GRASP between yR7s and some aberrant partners shown in *trans*-Tango (b) demonstrate active promiscuous synapses formed in DIPγ mutants (DIPγ$^{-/-}$). Dashed lines mark the region between the edge of the medulla and M6 layer where R7 axon terminals extend along.

their main synaptic partners not only strengthen synaptic connections with other usual partners but also start connecting with neuronal partners that they normally do not form synapse.

Lastly, given the fact that both low developmental temperature and DIPγ loss-of-function lead to synaptic promiscuity but the former through affecting filopodia stability and dendrite branching and the latter through making other partners more visible by the loss of main synaptic partner, we sought after a possible additive effect of these two phenomena on synaptic promiscuity. Here, DIPγ mutant brains developed at different temperatures showed varying number of aberrant partners connected to yR7s. Specifically, we observed the highest number of aberrant partners in DIPγ mutant brains developed at low temperature (at 18°C between P+40%-100%) and oppositely the lowest number in DIPγ mutant brains developed at high temperature (at 29°C between P+40%-100%) (Figure 6c and Supplementary Figure 4). Collectively, our results suggest that synapse-specific brain wiring can be established through composite instructions of several factors including the control of partner survival, the extent of axo-dendritic overlap, and dynamic neuronal interactions. Alterations in such biological mechanisms may result in recruitment of more or less synaptic partners which are not otherwise prevented from forming synaptic contacts.

Discussion

Brain wiring has long been thought as a process that appropriate synaptic partners express complementary molecular tags that allow them to recognize each other and form synaptic contacts. Such a molecular key-and-lock mechanism favors precise, hardwired assembly of neuronal networks but prevents individual variability, which contributes to the evolvability of biological systems. In fact, individuals with identical genes often have variable neuronal ensembles suggesting that non-heritable factors play important roles in neurodevelopment and synaptic connectivity. However, it remains unclear to what extent this is due to inherently imprecise development, i.e., stochastic and noisy neuronal development or environmental factors. In this study, using the *Drosophila*, a non-amniotic and ectothermic organism whose development is more susceptible to environmental factors, we showed that developmental temperature affects synapse formation and synaptic partner choice leading to different brain wiring patterns in adults. Specifically, low developmental temperature leads to increased filopodial stability and axo-dendritic overlap between potential partners that are sufficient for the formation of not only stronger synaptic connections between usual synaptic partners but also the recruitment of other, aberrant synaptic partners. Interestingly, killing the main synaptic partner before synapse formation leads to a similar synaptic promiscuity suggesting that neurons have a capacity to form synaptic connections with most, if not all, neurons in the vicinity and factors including filopodia kinetics, axo-dendritic overlap and the survival of synaptic partners restrict the partner choice in time and space.

We and others previously showed that neurons use several positional strategies, i.e., axo-dendritic overlap and approach angles of axons and dendrites, and filopodia kinetics to exclude potential partners in the close proximity and to define the degree of synaptic connections between usual partners. It is also likely that differential molecular composition of neuronal surfaces contributes to final connectivity biasing certain synaptic partnerships over others. Such combinatorial activity of several factors during brain wiring suggests a ‘composite instruction’ including many minor contributors to the precision of neuronal assemblies that can each be labelled as ‘permissive’ rather than a molecularly encoded instruction that specifies synaptic contacts between certain partners. For example, our previous analysis of developmental autophagy restricting synaptic partner choice by the regulation of filopodia kinetics is one such example of a ‘permissive‘ factor. Autophagy, a ubiqutious protein degradation mechanism in all cell types, carries no synaptic specificity information yet leads to meaningful and predictable changes in which neurons get to see each other in time and space during the assembly of neuronal circuits. Likewise, in the present study, temperature, a physical property of outside world, leads to changes in neuronal characteristics that directly affect the synaptic availability of partners to each other. In this view, a plethora of molecular and cellular mechanisms, possibly under the influence of environmental conditions, work hand in hand to bring the right synaptic partners together in time and space although synapse formation per se may be a promiscuous event. Restrictions of which partners get to see each other in time and space ensure a level of pre-specification by excluding most incorrect partnerships. The more encounters are restricted, the more synaptic promiscuity may be permissible.

Materials and Methods

Experimental model and subject details

Flies were reared at 25°C on standard cornmeal/yeast diet unless stated otherwise. For developmental analyses white pre-pupae (P+0%) were collected and staged to pupal developmental stages shown on figures. The following Drosophila strains were either obtained from Bloomington Drosophila Stock Center (BDSC) or other groups: UAS-Brpshort-GFP (S.Sigrist); Trans-tango flies (G.Barnea); DIPγ^{null} (C.Desplan); Rh4-Gal4, Rh4-LacZ (M.Wernet); GRASP flies, hsflp, GMRflp, GMR-Gal4, GMR(FRT.stop)Gal4, FRT82B, GMR-Gal80, tub-Gal80, UAS-CD4-tdGFP, UAS(FRT.stop)CD4-tdGFP, GMRmyrtomato, GMR49B06-LexA (Mi4-specific driver), GMR19F01-LexA (Mi1-specific driver), GMR25F10-LexA (Tm9-specific driver), GMR42H01-LexA (Dm9-specific driver), GMR20D11-LexA (Dm3-specific driver), GMR38H06-LexA (Dm6-specific driver), GMR11C05-LexA (Dm11-specific driver), ortC1-3-LexADBD, ortC2B-dVP16AD (Dm8-specific driver), GMR24F06-Gal4 (Dm8-specific driver), GMR19F01-Gal4 (Mi1-specific driver), GMR24C08-Gal4 (Tm9-specific driver), R48A07-p65ADZp(attP40); R79H02-ZpGdbd(attP2) (Mi4-specific driver) (BDSC).

Immunohistochemistry and fixed imaging

Pupal and adult eye-brain complexes were dissected in cold Schneider's Drosophila medium and fixed in 4% paraformaldehyde (PFA) in PBS for 40 minutes. Tissues were washed in PBST (0.4% Triton-X) and mounted in Vectashield (Vector Laboratories, CA). Images were obtained with a Leica TCS SP8-X white laser confocal microscope with a 63X glycerol objective (NA=1.3). The primary antibodies used in this study with given dilutions were as follows: rat monoclonal anti-nCadherin (1:100; Developmental Studies Hybridoma Bank); goat polyclonal anti-GFP (1:1000; Abcam); rat monoclonal anti-GFP (1:500; BioLegend); rabbit polyclonal anti-CD4 (1:600; Atlas Antibodies); rabbit polyclonal anti-DsRed (1:500; ClonTech). The secondary antibodies Cy3, Cy5 (Jackson ImmunoResearch Laboratories) and Alexa488 (Invitrogen) were used in 1:500 dilution.

Brain culture and live imaging

For all ex vivo live imaging experiments an imaging window cut open removing posterior head cuticle partially. The resultant eye-brain complexes were mounted in 0.4% dialyzed low-melting agarose in a modified culture medium. Live imaging was performed using a Leica SP8 MP microscope with a 40X IRAPO water objective (NA=1.1) with a Chameleon Ti:Sapphire laser and Optical Parametric Oscillator (Coherent). The excitation laser was set to 900 nm for single channel CD4-tdGFP imaging. Live imaging of R7 axon terminals at different temperatures was performed as follows: white pre-pupae (P+0%) were collected and staged to P+60% at 25°C. After eye-brain complexes were mounted in 0.4% dialyzed low-melting agarose in a modified culture medium, they were incubated 1 hour in imaging chamber at given temperatures on figures and scanned live for another hour with 1-min time resolution at the same incubation temperature.

Trans-tango and activity-dependent GRASP

Trans-tango and GRASP experiments were performed with yellow R7-specific driver Rh4-Gal4. Trans-tango flies were raised at 25°C until P+40% and moved to 18°C or 29°C for temperature shift experiments. On the day of eclosion, flies were transferred back to 25°C and dissected after 1 week. The number of postsynaptic neurons was counted manually from their cell bodies using cell counter plugin in Fiji including all cell bodies with weak or strong labelling to reveal all potential connections. For activity-dependent GRASP experiments, the same experimental flow was followed as in Trans-tango temperature shift experiments. Flies were transferred to UV-transparent Plexiglas vials on the day of eclosion and kept in a custom-made light box with UV light (25°C, 20-4 light-dark cycle) for 4 days to activate UV-sensitive R7 photoreceptors. Brains were dissected and stained with a polyclonal anti-GFP antibody to label R7 photoreceptors, monoclonal anti-GFP antibody to label GRASP signal, and polyclonal anti-CD4 antibody to label postsynaptic neurons (Feinberg et al., 2008).

Electroretinogram (ERG) recordings

Newly-hatched (0-day old) adult flies were collected and glued on slides using nontoxic school glue. Flies were exposed to alternating 1s “on” 2s “off” light stimulus provided by computer-controlled white LED system (MC1500; Schott). ERGs were recorded using Clampex (Axon Instruments) and quantified using Clampfit (Axon Instruments).

Quantification and statistical analysis

Synapse number analysis

All imaging data were analyzed and presented with Imaris 9.0.1 (Bitplane). For synapse number analysis, CD4-tomato channel was used to generate Surfaces for individual axon terminals and Brp-positive puncta inside the Surface are filtered using the masking function. Brp-positive puncta in photoreceptor terminals were automatically detected with the spot detection module (spot diameter was set to 0.3 µ) using identical parameters between experimental conditions and corresponding controls. Synapse numbers were taken and recorded directly from statistics tab of Spot function.

Dendritic branch analysis

All imaging data were analyzed and presented with Imaris 9.0.1 (Bitplane). Dendritic branches were detected automatically with Filament tracer using identical parameters between experimental conditions and corresponding controls (largest dendrite diameter: 3.0 µm, thinnest dendrite diameter: 0.2 µm). Inconsistencies in automatic detection were checked and corrected manually. The resultant values of branch numbers and dendrite lengths were taken and recorded directly from statistics tab of Filament tracer.

Statistical Analysis

Statistical comparison of two groups was performed with non-parametric Kolmogorov-Smirnov test. Statistical comparison of more than two groups was performed with non-parametric Kruskal-Wallis test and corrected for multiple comparisons with Dunn’s as a post-hoc test. All significance values are denoted on the graphs and in their respective legends. Graph generation and statistical analyses were done using GraphPad Prism 8.

Supplementary information

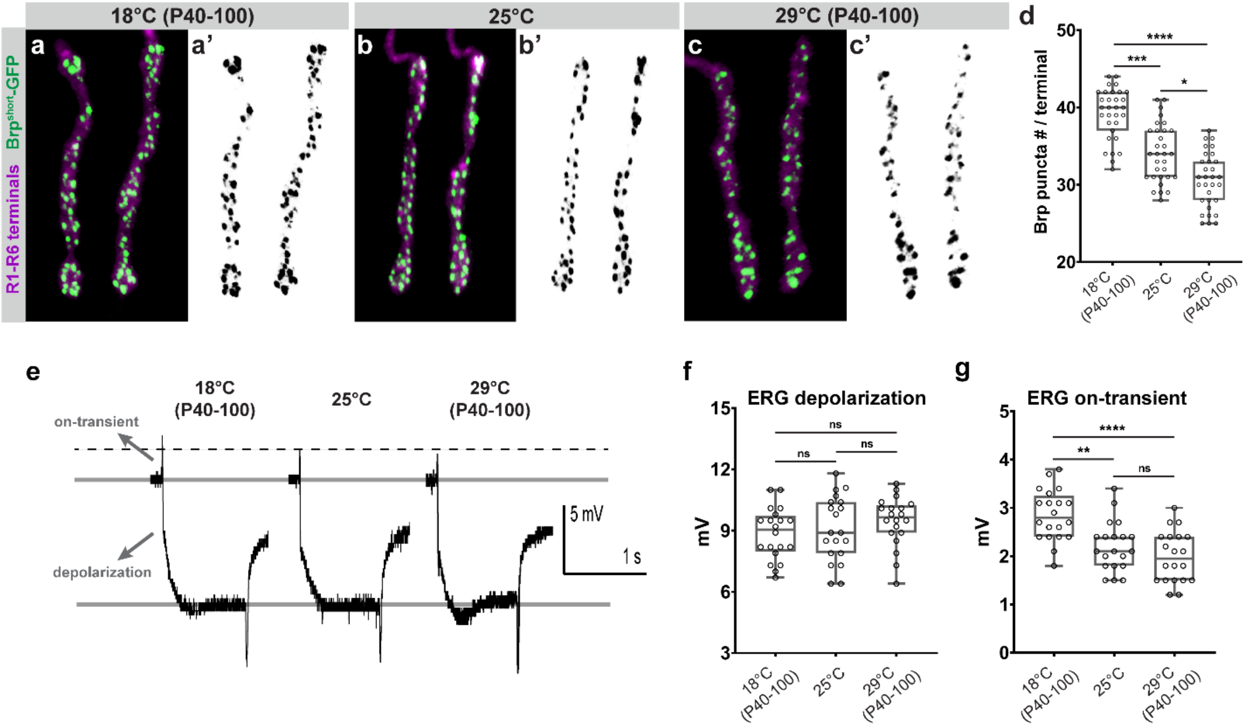

Supplementary Figure 1: Developmental temperature influences R1-R6 photoreceptors synapse number and neurotransmission. a-c', Representative images of R1-R6 photoreceptor axon terminals with Brp^{short}-GFP marked active zones developed at 18°C between P+40%-P+100% (synaptogenesis phase) (a-a'), at 25 °C (b-b'), and 29°C between P+40%-P+100% (c-c'). **d,** Number of Brp puncta per R1-R6 terminals at different developmental temperatures. n=40 terminals per condition. Kruskal-Wallis and Dunn's as post-hoc test; *p<0.0332, ***p<0.0002, ****p<0.0001. **e,** Representative electroretinogram (ERG) traces recorded from fly eyes developed at 18°C between P+40%-P+100%, at 25 °C, and at 29°C between P+40%-P+100%. **f-g,** Quantification of ERG depolarization (f) and on-transient (g) amplitudes. n=20 flies. Kruskal-Wallis and Dunn's as post-hoc test; **p<0.0021, ****p<0.0001, ns=not significant. The bottom-most and top-most horizontal lines, the lower and upper hinges, and the middle line of the boxplots indicate the minimum and maximum values, the 25th and 75th percentiles, and the mean, respectively.

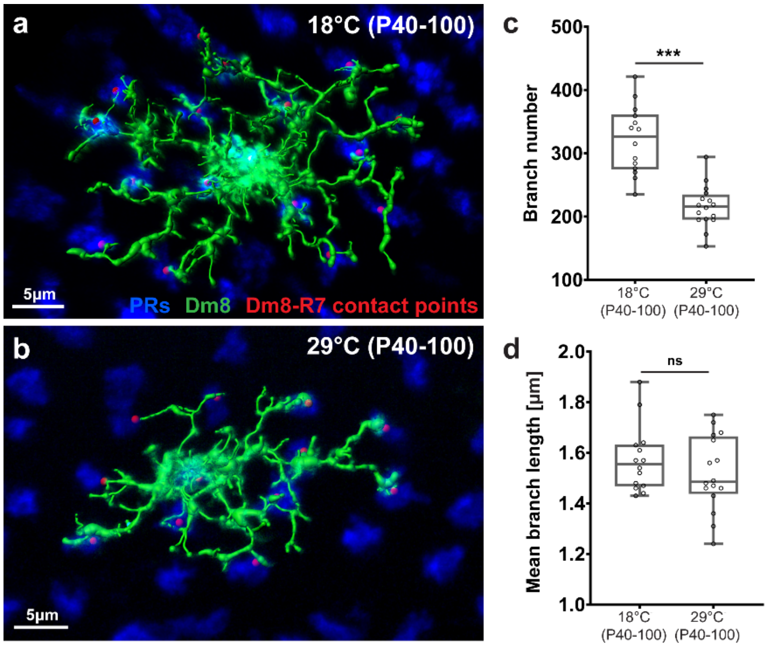

Supplementary Figure 2: Developmental temperature affects Dm8 branching. a-b, Skeletons reconstructed from Dm8 cells developed at 18°C between P+40%-P+100% (a) and at 29°C between P+40%-P+100% (b). Red dots represent contact points between R7s and Dm8s. **c,** Branch number of Dm8s developed at different temperatures during synaptogenesis. n=14 cells for 18°C (P+40%-P+100%), n=16 cells for 29°C (P+40%-P+100%). Kolmogorov-Smirnov test; ***p<0.0002. **d,** Mean branch length of Dm8s developed at different temperatures during synaptogenesis. n=14 cells for 18°C (P+40%-P+100%), n=16 cells for 29°C (P+40%-P+100%). Kolmogorov-Smirnov test; ns=not significant. The bottom-most and top-most horizontal lines, the lower and upper hinges, and the middle line of the boxplots indicate the minimum and maximum values, the 25th and 75th percentiles, and the mean, respectively.

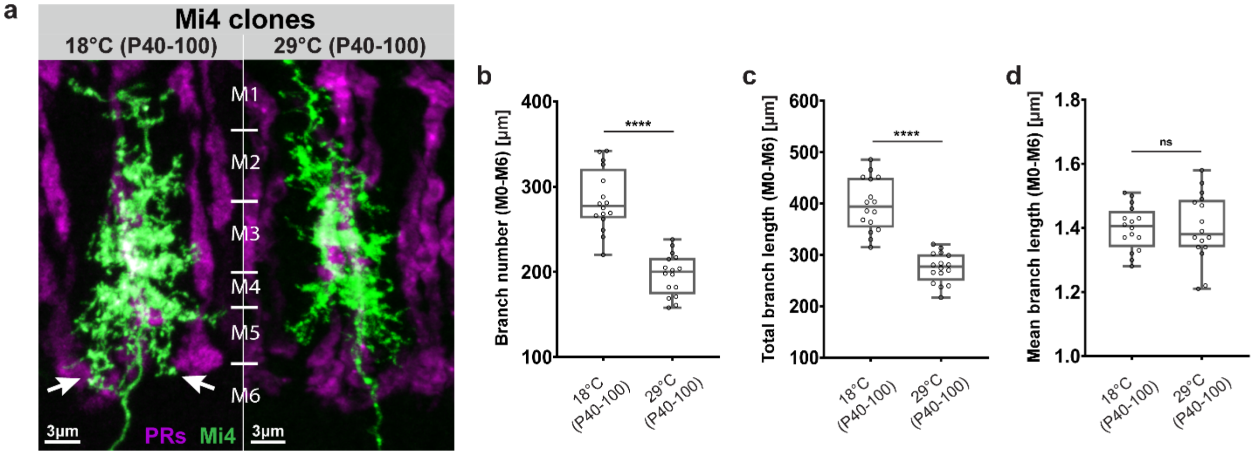

Supplementary Figure 3: Developmental temperature affects Mi4 branching. a, Dorsoventral view of a single Mi4 cell developed at 18°C between P+40%-P+100% and at 29°C between P+40%-P+100%. Arrows point branches from an Mi4 cell developed at 18°C between P+40%-P+100% occupying M6 medulla layer where R7s are synaptically most active. **b-d,** Branch number (b), total branch length (c), and mean branch length (d) of Mi4s between medulla layers M0-M6 developed at different temperatures during synaptogenesis. n=16 cells per condition. Kolmogorov-Smirnov test; ****p<0.0001, ns=not significant. The bottom-most and top-most horizontal lines, the lower and upper hinges, and the middle line of the boxplots indicate the minimum and maximum values, the 25th and 75th percentiles, and the mean, respectively.

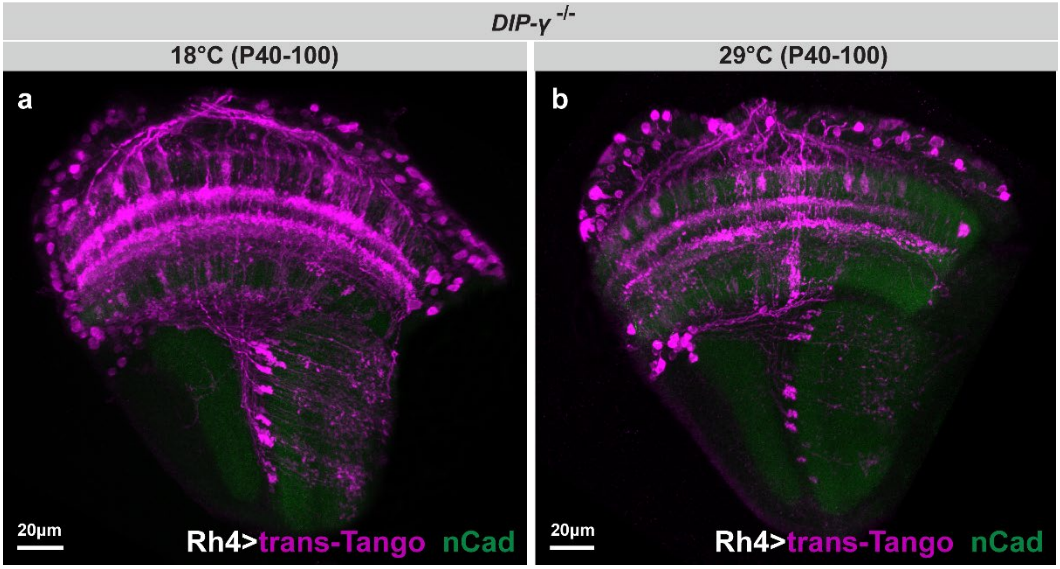
DIP-γ -/-
18°C (P40-100)
29°C (P40-100)
a
b
20μm
Rh4>trans-Tango nCad
20μm
Rh4>trans-Tango nCad

Supplementary Figure 4: Additive effect of main partner loss and developmental temperature on R7's synaptic promiscuity. a-b, Representative images of neurons connected to yR7s in DIPγ mutant (DIPγ$^{-/-}$) brains developed at 18°C between P+40%-P+100% (a) and at 29°C between P+40%-P+100% (b) labelled with *trans*-Tango. Note increased labelling of neurons aberrantly connected to yR7s at low developmental temperature showing the additive effects of DIPγ loss-of-function and developmental temperature on synaptic promiscuity. Magenta=postsynaptic neurons, green=CadN.

6. General Discussion

The aim of my doctoral work has been on contributing to answer the long-lasting and challenging questions in neurobiology such as "How do neurons form specific synaptic contacts with only some neuronal partners while avoiding others during brain development?" and once they establish these contacts and become mature neurons, "How do they keep themselves and particularly their synapses functional and healthy over a long period of time?". I approached these questions from the perspective of possible local roles of lysosomal degradation pathways including endocytic and autophagic routes and also possible effects of developmental temperature. Both in development and function, neurons need robust ways to ensure to maintain protein quality and proper membrane turnover, which are particularly challenging at axon terminals and dendrites generally situated away from the cell body. Previous studies showed the presence of local translation machineries and mRNAs at axon terminals and dendrites suggesting rapid production of proteins locally without communicating with the cell body (Sachdeva et al., 2016; Steward, 2002; Steward and Schuman, 2001). However, to date, local protein degradation studies have particularly focused on proteasomal degradation that mainly degrades cytosolic proteins (Hakim et al., 2016; Hamilton and Zito, 2013; Yi and Ehlers, 2007). This leaves unanswered questions regarding possible local roles of other protein degradation pathways including endolysosomal degradation and autophagy both in developing and functional neurons. Also, to date, studies on the effect of environmental temperature on brain wiring mainly focused on behavioral changes in adult animals leaving the question whether and how developmental temperature may affect formation of neuronal circuits in cellular level. In the following sections, the results obtained during my doctoral work will be discussed in relation to previously published studies.

Local degradation of synaptic vesicle and plasma membrane proteins in distinct endolysosomal compartments

Neurons need compartmentalized regulation of membrane protein turnover in axons, dendrites and the cell body to ensure normal development and function. Recent studies have shown local generation of autophagosomes and endocytic compartments and identified several synaptically enriched proteins regulating their formation (Maday and

Holzbaur, 2016; Maday et al., 2012; Okerlund et al., 2017; Uytterhoeven et al., 2011). Particularly, previous discovery of neuron-specific endosomal sorting mechanism operated by synaptic vesicle proteins n-Syb and V100 at axon terminals suggests that neurons may exploit local, neuron-specific protein quality control pathways (Haberman et al., 2012; Williamson et al., 2010a). However, the exact locale that degradation occurs, i.e., whether these locally generated organelles are transported back to the cell body for degradation or whether degradation can occur locally is still unclear. In addition, it still remains largely unknown whether different degradation mechanisms exert distinct cargo-specificity.

In the first study (Chapter 1), we addressed these questions in an unbiased way by live observation of cargo sorting and degradation at different locales of *Drosophila* photoreceptors using mCherry-pHluorin acidification-sensing degradation probes. Our key findings in this study were: (1) Both general plasma membrane proteins and synaptic vesicle proteins are sorted and degraded locally at axon terminals and (2) different types of cargos (plasma membrane proteins vs synaptic vesicle proteins) are sorted for degradation into distinct endolysosomal compartments or ‘hubs’ at axon terminals and are degraded by molecularly distinct pathways. We named these distinct sort-and-degrade compartments as hubs because we never observed appearance or disappearance of these structures although smaller compartments constantly fuse and bud off. The composition of hub compartments at a given time finely reflects their dynamic nature: although some are enriched in early endosomal markers, others are marked by lysosomal markers. This finding blurs the spatial distinction of endocytic compartments and suggest that the same compartment, though possibly according to its maturation state at different times, may be used as a general sort-and-degrade station.

The hub compartments as sort-and-degrade stations at axon terminals clearly show that proteins are sorted and degraded locally at axon terminals. However, in order to address the question of cargo-specificity, i.e., which membrane proteins are degraded by what mechanisms, we designed two mCherry-pHluorin probes: first, a general membrane cargo by fusing myristoylated residue with mCherry-pHluorin that is located on most membrane in an unbiased manner and second, fusing a synaptic vesicle protein

Synaptotagmin 1 (Syt1) with mCherry-pHluorin that is located on synaptic vesicles with high specificity. Here, live imaging of these probes at axon terminals demonstrated sorting of different cargos into morphologically distinct, non-overlapping hub compartments. This morphological distinction is also reflected by the protein machineries that differentially control sorting and degradation of distinct cargos. Although general membrane cargos are sorted and degraded by Rab7-dependent ubiquitous endomembrane degradation, synaptic vesicle cargos are sorted and degraded by previously identified neuronal sort-and-degrade mechanism operated by synaptic proteins n-Syb and V100 in a Rab7-independent manner. Given the fact that Rab7 is the key regulator of endosomal maturation from early endosome to late endosome/MVB in all cells including neurons (Guerra and Bucci, 2016), the question arises here: How are synaptic vesicle proteins specifically sorted into synaptic vesicle hubs? Synaptic vesicle protein sorting into distinct hub compartments is Rab7-independent suggesting that maturation of synaptic vesicle hubs bypasses the requirement of Rab5-to-Rab7 switch for normal maturation of endosomes in degradative route (Rink et al., 2005). One possibility of synaptic vesicle protein sorting in a Rab7-independent way is direct fusion of synaptic vesicles with the synaptic vesicle hub. Such mechanism might also require an intermediate endocytic sorting station downstream of synaptic vesicle retrieval from the plasma membrane. Recent reports on Rab35/Sky-dependent sorting mechanism into such intermediate endocytic compartments for synaptic vesicle rejuvenation might represent such a route. However, in our work, we observed similar overlap of Sky with both hub types implying that it may have role in both ubiquitous and neuron-specific pathways. Consistently, Sky-dependent synaptic vesicle turnover is affected by Rab7 loss-of-function and *sky* mutant affects turnover of some synaptic vesicle proteins including n-Syb (Fernandes et al., 2014; Uytterhoeven et al., 2011). Further work is still needed to identify molecular players regulating synaptic vesicle sorting into degradative pathways.

Autophagy is another possible route for degradation of general and synaptic vesicles cargos. Our co-localization experiments with autophagy marker Atg8 showed significantly higher co-localization with Rab7-dependent general cargo hubs than synaptic vesicle hubs. However, live observation of autophagosomes formed at axon terminals revealed that they are distinct from hub compartments based on dynamics. Following their formation at axon terminals, they directly enter the axon without initial involvement in any fusion or fission process. However, it is possible that autophagosomes can engulf hub compartments as a whole providing alternative degradation route for both types of proteins. Still, the different dynamics of autophagosomes compared to hub compartments urged us to investigate its possible roles at axon terminals of developing neurons, which will be discussed in the next section.

Filopodia dynamics restrict synapse formation and synaptic partner choice

Previous reports showed continuous, *de novo* formation of autophagosomes at axon terminals of primary mammalian neuron cultures and developing *Drosophila* R1-R6 photoreceptor terminals (Maday and Holzbaur, 2016; Maday et al., 2012; Okerlund et al., 2017). However, the possible functions played by developmental autophagy at axon terminals have remained unknown. One of the key findings in the second study (Chapter 2) was the observation of selective autophagosome formation at the tip of synaptogenic filopodia of developing R7 axon terminals and subsequent destabilization of these structures. Previously, our group demonstrated an active role of R7 axonal filopodia dynamics during synaptogenesis which led to the proposal of serial synapse formation model based on competitive distribution of synaptic building materials between synaptogenic filopodia (Ozel et al., 2019). Based on this model and our observation of autophagosome formation at the tip of synaptogenic filopodia, we showed that autophagy regulates axonal filopodial dynamics by keeping the amount of synaptic building materials at axon terminals in balance and consequently loss of autophagy leads to ectopic synapse formation during brain wiring. More importantly, using trans-synaptic tracing method ‘Trans-tango’ and GFP reconstitution across synaptic partners (GRASP), we showed that autophagy-deficient neurons connect to several aberrant synaptic partners causing neuronal miswiring.

Given the fact that loss of autophagy during brain wiring particularly affects axonal filopodial dynamics without affecting R7’s axon targeting to normal medulla layer target M6 but still leads to aberrant connections with wrong partners suggest that it kinetically restricts synapse formation with incorrect partners through regulation of filopodia dynamics. Previous studies have shown that when directed to ectopic locations, neurons readily form synapses with incorrect partners suggesting that synapse formation per se can be promiscuous (Hassan and Hiesinger, 2015; Kulkarni et al., 2016). Our findings in this study point to the fact that after normal axonal pathfinding to the correct target region, regulation of filopodia dynamics, i.e., speed and stability, might restrict or facilitate neuronal encounters between potential partners. Together with adhesive and repellent molecular interactions between potential neuronal partners, such dynamic interactions between axons and dendrites may sharpen synaptic specificity leading to proper neural circuit ensembles.

How does a ubiquitous degradation mechanism like autophagy regulate synaptic specificity? In one scenario, autophagy might be particularly triggered to remove immature synapses when two wrong partners attempt to form a synaptic connection. Alternatively, autophagy might set a global threshold on filopodial stability along axon terminals so that only partners in close proximity and with proper molecular affinity can form synapses. Our synaptogenic filopodia and synapse distribution data along R7 axon terminals in loss of autophagy showed a proportional increase in all medulla layers suggesting that autophagy is not differentially triggered in filopodia in distinct medulla layers. One interesting outcome of this global thresholding is that, in loss of autophagy, the aberrant partners R7s more frequently connect to have dendritic branches at medulla layers where R7s possess most of their filopodia and eventually form most of their synapses. Oppositely, aberrant partners with dendritic braches at medulla layers where R7s have very little filopodial activity during development form synaptic connections in a lesser extent. These findings suggest that synapse specificity between R7 photoreceptors and potential synaptic partners is established through combination of several layers of cellular processes: first, intrinsic developmental program of R7 photoreceptors control when and where at their axon terminals to form filopodia; second, cell biological mechanisms such as autophagy set thresholds to dynamic encounters between neuronal partners although these mechanism themselves carry no synaptic specificity information; and third, different adhesive and repellent molecular interactions might bias certain synaptic interactions over others. Based on this combinatorial model for synaptic specificity, we can speculate that many other biological mechanisms might play a role in establishing synaptic specificity and small changes in these biological mechanisms might be a driving force of evolutionary programming of neuronal circuits.

Our findings on filopodia speed and stability affecting synapse number and synaptic partner choice during development of neuronal circuits in an autophagy-dependent manner urged us to ask the question whether filopodia dynamics is a general strategy used by neurons to restrict which partners they get to see in time and space or is it caused by some other biological mechanism affected by loss of autophagy that we did not investigate in Chapter 2. Here, to generalize the idea that filopodia dynamics play an important role in synaptic partner selection, we took an unconventional way to affect filopodia dynamics during development. Instead of using a genetic manipulation, in Chapter 3, we exposed pupae to different environmental temperature during synaptogenesis phase and showed that temperature experienced by pupae during development affects filopodia speed and stability in an expected way: R7 axonal filopodia show slow and more stable filopodia at low temperature and oppositely, filopodia get faster and unstable at high temperature. Similar to autophagy-dependent changes in filopodia speed and stability affecting synaptic partner choice, here we also showed that low developmental temperature leads to aberrant synaptic connections between R7s and potential partners in close proximity. Collectively, these results demonstrate that filopodia kinetics play an important role in synaptic partner selection during formation of neuronal circuits.

Brain wiring with combinatorial role of several 'permissive' factors

To date, most efforts to explain synapse-specific brain wiring have focused on studying of molecularly encoded instructions that specify synaptic contacts. In this view, 'instructive' cues present on presumptive synaptic partners bring right partners together through attraction or exclude wrong connections through repulsion. Such an instructive mechanism can be described as a molecular key-and-lock mechanism so that synaptic connections would not form if the key does not fit the lock. In fact, over the years several examples of such molecular interactions have been found that bias certain synaptic interactions over the others (de Wit and Ghosh, 2016; Sanes and Zipursky, 2020). On the other hand, several other works demonstrated that neurons readily form synapses with incorrect partners when given the opportunity (Agi et al., 2020; Clements et al., 2008; Edwards and Meinertzhagen, 2009; Hassan and Hiesinger, 2015; Van der Loos and Glaser, 1972). Dm8 cell ablation experiments presented in Chapter 3 also favors this idea: In the absence of their main synaptic partner, R7 photoreceptors find alternative partners to synapse with. A molecular key-and-lock mechanism does not allow synapse formation between wrong partners but the fact that neurons can form promiscuous synapses when projected to wrong target areas or lose their normal synaptic partners suggest that synaptic promiscuity may be the integral part of the brain wiring process. Simply, restriction of neuronal encounters in time and space ensures only certain partners get to see each other with the exclusion of most, maybe in some cases all, incorrect partners even if the last synapse formation step is promiscuous. The results presented in this doctoral work also favor such a view of brain wiring. Autophagy as a general protein degradation mechanism and temperature as a physical property of outside world do not contain synaptic specificity information but yet lead to meaningful changes in synaptic partner selection. Therefore, we propose that proper brain wiring is the result of combinatorial action of several such ‘permissive’ factors, which do not instruct synapse specificity but collectively form composite instructions during growth program that give rise to specificity. Small changes in permissive mechanisms such as in level of autophagy may lead to subtle but selectable and heritable changes in brain wiring program that may be a means of evolutionary programming of neuronal circuits and behavior.

7. Outlook and future directions

The goal of this doctoral work was to identify possible strategies neurons use for synaptic partner selection and maintenance of these synaptic connections. The first work led to the discovery of two parallel endolysosomal degradation pathways operating locally at axon terminals with distinct molecular players and with distinct cargo specificity. Although we successfully showed degradation of plasma membrane and synaptic vesicle cargos in distinct local degradative hub compartments, the exact mechanism of how different cargos are sorted into distinct compartments for degradation still remains elusive. Screening for molecular players in this sorting process would be a good direction to address this question. Particularly, the large family of Rab GTPases and their effectors with many neuron-specific and neuron-enriched members would be ideal candidates to screen for regulators of synaptic vesicle hub sorting and degradation. In addition to intracellular local degradation mechanisms in neurons, recent evidence demonstrated degradation of cargos originated in neurons by neighboring cells, particularly glia (Han et al., 2014; Jin et al., 2018; Song et al., 2008; Yuyama et al., 2012). An unpublished observation we made during this study was the presence of degradative compartments outside of photoreceptor axon terminals where several different type of glial cells are located. Following this observation, it would be interesting to address the following questions: Are these compartments released by photoreceptor axon terminals? If so, what molecular machinery controls this release and capture by recipient cells? And what is the physiological importance of cargo degradation by neighboring cells during development and maintenance? Together with compartmentalized intracellular degradation mechanisms in neurons, future research on extracellular degradation mechanisms might progress our understanding of the role of these biological processes in neuronal development and maintenance.

Our observation of local generation of autophagosomes but their distinct dynamic behaviors compared to local endocytic hub compartments urged us to investigate the role of autophagy in developing axon terminals. This study led to the discovery of a highly specific role of autophagy to regulate axonal filopodial dynamics. Subsequent loss of function analyses demonstrated ectopic synapse formation and neuronal miswiring due to increased stability of axonal filopodia. Considering that autophagy is a bulk degradation mechanism and mostly unspecific in nature, one can assume that defects in several other biological processes might have a similar or opposite impact on filopodial stability and eventual impact on brain wiring. The anterograde transsynaptic circuit tracing method 'Trans-tango' can ideally be used to identify proteins and protein families affecting brain wiring via mutant or knockdown analyses of target genes. Strong candidates for such a screen would be actin regulatory proteins since they are known to regulate filopodia extension and retraction through polymerization/depolymerization of actin filaments. Furthermore, there are several Rab GTPase proteins known to be involved in formation/maturation process of autophagosomes that one can investigate localization of these protein in filopodia, whether and how they affect filopodia dynamics and subsequently if their loss- and/or gain-of-function leads to brain wiring defects.

8. Summary

The daunting complexity of the brain emerges from the large number of neurons it contains and their compartmentalized synaptic interactions at axon terminals and dendrites. Generation of functional neuronal networks requires robust, unambiguous developmental processes to ensure synapse-specific neuronal partner choice and subsequent maintenance mechanisms to keep neurons and particularly synapses healthy and functional over a long time. Defects in wiring and maintenance mechanisms are associated with neuropsychiatric and neurodegenerative disorders.

Having regard to the importance of protein quality control mechanism both during development and function of the nervous system, in this doctoral work, I investigated possible local roles of lysosomal degradation pathways including ubiquitous and neuron-specific endolysosomal degradation and autophagy at axon terminals. Using live imaging in intact *Drosophila* brains and novel acidification-sensing degradation probes, first, we reported a direct live observation of local protein degradation at axon terminals in large, acidified compartments. These acidic, degradative endocytic compartments undergo continuous flux of fusion and fission of smaller compartments that is reflected by their molecular composition at a given time. Therefore, we named these compartments 'local hubs' as they behave as sort-and-degrade stations for local protein turnover at axon terminals. Secondly, we reported differential, cargo-specific sorting of plasma and synaptic vesicle membrane proteins into distinct hubs via two molecularly distinct pathways. Although plasma membrane protein sorting and degradation depends on ubiquitous Rab GTPase, Rab7, synaptic vesicle membrane protein sorting and degradation is Rab7-independent and operated by previously characterized synaptic vesicle proteins V100 and n-Syb. V100, as a subunit of a proton pump, particularly affects acidification of synaptic vesicles hubs, whereas n-Syb is required for the delivery of golgi-derived microvesicles containing acidic hydrolases into synaptic vesicle hubs. Interestingly, autophagy does not overlap with any of these local degradation pathways. Following their formation at axon terminals, they enter in axons without engaging in any fusion/fission events, hence morphologically and dynamically distinct from local hub compartments.

Despite several reports on formation of autophagosomes at axon terminals, potential physiological roles it may exert still remain largely unknown, especially during neural circuit assembly. Live imaging of developing *Drosophila* photoreceptor axon terminals with autophagosome markers revealed their formation at the tip of synaptogenic filopodia followed by destabilization of these structures. Consistent with this observation, loss of function analyses of autophagy in developing *Drosophila* photoreceptors revealed increased stability of synaptogenic filopodia and subsequent increase in synapse numbers. More importantly, autophagy-deficient neurons connect to several aberrant synaptic partners causing neuronal miswiring. Finally, adult flies with miswired brains due to loss of autophagy show distinct and predictable behavioral phenotypes such as prolonged, repetitive visual attention to objects. Interestingly, development at colder temperatures exerts similar effect on filopodial stability as in loss of autophagy where axonal filopodia slow down and stabilize more synaptogenic filopodia. This effect on filopodia stability further leads to increased synapse formation and recruitment of aberrant synaptic partners changing brain wiring pattern. Collectively, these results demonstrate that filopodia kinetics play an important role to restrict or facilitate synaptic partnerships between neurons in close proximity during brain wiring.

In conclusion, my doctoral work contributed to better understanding of local functions of protein degradation machineries and developmental temperature during brain wiring and maintenance. Unexpected roles of such cellular mechanisms and external factors in establishing proper neuronal circuits point to the fact that combinatorial action of several factors in time and space during brain development contribute to the final outcome, a functional brain.

9. Zusammenfassung

Die ungeheure Komplexität des Gehirns ergibt sich aus der großen Anzahl von Neuronen, sowie die um mehrere Größenordnungen höheren Anzahl von synaptischen Verbindungen zwischen den axonischen und dendritischen Bereichen der Neuronen. Die Bildung funktioneller neuronaler Netzwerke erfordert robuste, eindeutige Entwicklungsprozesse, um die synaptische Spezifität bei der neuronalen Partnerwahl und nachfolgender Erhaltungsmechanismen zu gewährleisten, damit Neuronen und insbesondere Synapsen über lange Zeit gesund und funktionsfähig bleiben. Defekte in den Verdrahtungs- und Erhaltungsmechanismen werden mit neuropsychiatrischen und neurodegenerativen Störungen in Verbindung gebracht.

In dieser Doktorarbeit untersuche ich die lokale Rolle von lysosomalen Abbauwegen als Mechanismus zur Kontrolle von Proteinqualität sowohl während der Entwicklung als auch während der Funktion des Nervensystems. Hierbei konzentriere ich mich auf den ubiquitären und Neuronen spezifischen endolysosomalen Abbau sowie der Autophagie in Axonendigungen. Unter Verwendung von ‚live-imaging‘ in intakten Drosophila-Gehirnen und neuartigen optischen Proben, die durch die Messung der Azidität indirekt Aufschluss über den Degenrationszustand geben, berichteten wir zunächst, dass der lokale Proteinabbau an Axonendigungen in großen, sauren Kompartimenten stattfindet. Diese sauren, endocytische Kompartimente unterliegen einem kontinuierlichen Wechselspiel von Verschmelzung und Spaltung kleinerer Kompartimente, was sich in ihrer molekularen Zusammensetzung zu einem gegeben Zeitpunkt widerspiegelt. Diese Kompartimente nannten wir "lokale Hubs", da sie als lokale Sortier- und Abbaustationen für Proteine an den Axonendigungen fungieren. Desweitern berichteten wir über die differentielle Sortierung von Plasmamembranproteinen und synaptischen Vesikelmenbranproteinen in verschiedene ‚Hubs‘ über zwei molekular unterschiedlich Wege. Obwohl die Sortierung und der Abbau von Plasmamembranproteinen von der ubiquitären Rab-GTPase, Rab7, abhängt, ist die Sortierung und der Abbau von synaptischen Vesikelmembranproteinen Rab7-unabhängig und wird von den zuvor charakterisierten synaptischen Vesikelproteinen V100 und n-Syb betrieben. V100, Untereinheit einer Protonenpumpe, beeinflusst insbesondere die Azidifikation der synaptischen Vesikel-Hubs, während n-Syb für die Zufuhr von Mikrovesikeln aus dem Golgi Apparat, die azidifizierende Hydrolasen enthalten, in die synaptische Vesikel-Hubs erforderlich ist. Interessanterweise überschneidet sich die Autophagie mit keinem dieser lokalen Degradationswege. Nach der Bildung der Hubs an den Axonendigungen wandern diese in das Axon ein ohne an weitern Fusions- oder Spaltungsereignissen beteiligt zu sein, und unterscheiden sich daher morphologisch und dynamisch von ‚lokalen Hub'.

Trotz mehrerer Berichte über die lokale Entstehung von Autophagosomen an Axonendigungen ist ihre mögliche physiologische Rolle noch weitgehend unbekannt, insbesondere während der Entwicklung neuronaler Schaltkreise. ‚Live-imaging' von Autophagosomen-Markern in sich entwickelnden Axonendigungen von Drosophila-Photorezeptoren zeigte die Bildung von Autophagosomen an der Spitze synaptogener Filopodien und die anschließende Destabilisierung dieser Strukturen. Im Einklang mit dieser Beobachtung zeigten Analysen des funktionellen Verlust von Autophagie in sich entwickelnden Drosophila-Photorezeptoren eine erhöhte Stabilität der synaptogenen Filopodien und eine anschließende Zunahme der Synapsen Anzahl. Noch wichtiger ist, dass Neuronen mit verminderter Autophagie sich vermehrt mit atypischen synaptischen Partnern verbinden, was zu Fehlentwicklung neuronaler Netzwerke führt. Adulte Fliegen mit fehlentwickelten neuronalen Netzwerken, aufgrund des Verlusts der Autophagie, zeigen ausgeprägte und vorhersagbare Verhaltensphänotypen wie verlängerte, wiederholt auftretende visuelle Aufmerksamkeit auf Objekte. Interessanterweise hat die Entwicklung bei kälteren Temperaturen eine ähnliche Wirkung auf die Stabilität der Filopodien wie der Verlust von Autophagie, wie etwa die Verlangsamung der axonalen Filopodien die zu einer erhöhten Stabilisation der synaptogenen Filopodien führt. Dieser Effekt auf die Stabilität der Filopodien führt außerdem zu einer verstärkten Synapsenbildung und zur Rekrutierung von atypischen synaptischen Partnern, die das Verdrahtungsmuster des Gehirns verändern. Zusammengenommen zeigen diese Ergebnisse, dass die Filopodienkinetik eine wichtige Rolle spielt bei der Etablierung von synaptischen Verbindungen zwischen Neuronen während der Entwicklung des Nervensystems.

Abschließend möchte ich sagen, dass meine Doktorarbeit zu einem besseren Verständnis der lokalen Funktionen von Proteinabbaumechanismen und der Entwicklungstemperatur während der Entwicklung und Erhaltung des Nervensystems beigetragen hat. Die unerwartete Rolle solcher zellulären Mechanismen sowie externer Faktoren, wie die Entwicklungstemperatur, bei der Etablierung von funktionellen neuronalen Schaltkreisen deuten darauf hin, dass die synergistische Wirkung mehrerer Faktoren, in zeitlicher und räumlicher Abfolge, elementare zur Entwicklung eines funktionierenden Gehirnes beitragen.

10. References

Agi, E., Kulkarni, A., and Hiesinger, P.R. (2020). Neuronal strategies for meeting the right partner during brain wiring. Curr Opin Neurobiol *63*, 1-8.

Angilletta, M.J., Steury, T.D., and Sears, M.W. (2004). Temperature, growth rate, and body size in ectotherms: Fitting pieces of a life-history puzzle Integr Comp Biol *44*, 498-509.

Apitz, H., and Salecker, I. (2014). A challenge of numbers and diversity: neurogenesis in the Drosophila optic lobe. J Neurogenet *28*, 233-249.

Ashrafi, G., Schlehe, J.S., LaVoie, M.J., and Schwarz, T.L. (2014). Mitophagy of damaged mitochondria occurs locally in distal neuronal axons and requires PINK1 and Parkin. J Cell Biol *206*, 655-670.

Balaskas, N., Abbott, L.F., Jessell, T.M., and Ng, D. (2019). Positional Strategies for Connection Specificity and Synaptic Organization in Spinal Sensory-Motor Circuits. Neuron *102*, 1143-1156 e1144.

Bekkers, J.M., and Stevens, C.F. (1991). Excitatory and inhibitory autaptic currents in isolated hippocampal neurons maintained in cell culture. Proc Natl Acad Sci U S A *88*, 7834-7838.

Berger-Muller, S., Sugie, A., Takahashi, F., Tavosanis, G., Hakeda-Suzuki, S., and Suzuki, T. (2013). Assessing the role of cell-surface molecules in central synaptogenesis in the Drosophila visual system. PLoS One *8*, e83732.

Bezprozvanny, I., and Hiesinger, P.R. (2013). The synaptic maintenance problem: membrane recycling, Ca2+ homeostasis and late onset degeneration. Molecular Neurodegeneration *8*.

Bright, N.A., Davis, L.J., and Luzio, J.P. (2016). Endolysosomes Are the Principal Intracellular Sites of Acid Hydrolase Activity. Curr Biol *26*, 2233-2245.

Carrillo, R.A., Ozkan, E., Menon, K.P., Nagarkar-Jaiswal, S., Lee, P.T., Jeon, M., Birnbaum, M.E., Bellen, H.J., Garcia, K.C., and Zinn, K. (2015). Control of Synaptic Connectivity by a Network of Drosophila IgSF Cell Surface Proteins. Cell *163*, 1770-1782.

Chan, C.C., Scoggin, S., Wang, D., Cherry, S., Dembo, T., Greenberg, B., Jin, E.J., Kuey, C., Lopez, A., Mehta, S.Q.*, et al.* (2011). Systematic discovery of Rab GTPases with synaptic functions in Drosophila. Curr Biol *21*, 1704-1715.

Chedotal, A. (2019). Roles of axon guidance molecules in neuronal wiring in the developing spinal cord. Nat Rev Neurosci *20*, 380-396.

Chen, B.E., Kondo, M., Garnier, A., Watson, F.L., Puettmann-Holgado, R., Lamar, D.R., and Schmucker, D. (2006). The molecular diversity of Dscam is functionally required for neuronal wiring specificity in Drosophila. Cell *125*, 607-620.

Chen, W.V., Nwakeze, C.L., Denny, C.A., O'Keefe, S., Rieger, M.A., and Maniatis, T. (2017). Pcdhalphac2 is required for axonal tiling and assembly of serotonergic circuitries in mice. Science *356*, 406-411.

Cherry, S., Jin, E.J., Ozel, M.N., Lu, Z., Agi, E., Wang, D., Jung, W.H., Epstein, D., Meinertzhagen, I.A., Chan, C.C.*, et al.* (2013). Charcot-Marie-Tooth 2B mutations in rab7 cause dosage-dependent neurodegeneration due to partial loss of function. Elife *2*, e01064.

Choe, K., Prakash, S., Bright, A., and Clandinin, T.R. (2006). Liprin-alpha is required for photoreceptor target selection in Drosophila. Proc Natl Acad Sci U S A *103*, 11601-11606.

Clandinin, T.R., Lee, C.H., Herman, T., Lee, R.C., Yang, A.Y., Ovasapyan, S., and Zipursky, S.L. (2001). Drosophila LAR regulates R1-R6 and R7 target specificity in the visual system. Neuron *32*, 237-248.

Clandinin, T.R., and Zipursky, S.L. (2002). Making connections in the fly visual system. Neuron *35*, 827-841.

Clements, J., Lu, J., Gehring, W.J., and Meinertzhagen, I.A. (2008). Central projections of photoreceptor axons originating from ectopic eyes in Drosophila. Proc Natl Acad Sci U S A *105*, 8968-8973.

Courgeon, M., and Desplan, C. (2019). Coordination between stochastic and deterministic specification in the Drosophila visual system. Science *366*.

Darwin, C. (1872). The expression of emotions in man and animals.

Dascenco, D., Erfurth, M.L., Izadifar, A., Song, M., Sachse, S., Bortnick, R., Urwyler, O., Petrovic, M., Ayaz, D., He, H., *et al.* (2015). Slit and Receptor Tyrosine Phosphatase 69D Confer Spatial Specificity to Axon Branching via Dscam1. Cell *162*, 1140-1154.

de Wit, H., Lichtenstein, Y., Kelly, R.B., Geuze, H.J., Klumperman, J., and van der Sluijs, P. (2001). Rab4 regulates formation of synaptic-like microvesicles from early endosomes in PC12 cells. Molecular Biology of the Cell *12*, 3703-3715.

de Wit, J., and Ghosh, A. (2016). Specification of synaptic connectivity by cell surface interactions. Nat Rev Neurosci *17*, 22-35.

Deal, S.L., and Yamamoto, S. (2018). Unraveling Novel Mechanisms of Neurodegeneration Through a Large-Scale Forward Genetic Screen in Drosophila. Front Genet *9*, 700.

Drescher, U., Kremoser, C., Handwerker, C., Noda, M., and Bonhoeffer, F. (1995). In vitro guidance of retinal ganglion cell axons by RAGS, a 25 kDa tectal protein related to ligands for Eph receptor tyrosine kinases. Cell *82*, 359-370.

Edwards, T.N., and Meinertzhagen, I.A. (2009). Photoreceptor neurons find new synaptic targets when misdirected by overexpressing runt in Drosophila. J Neurosci *29*, 828-841.

Esposito, G., Ana Clara, F., and Verstreken, P. (2012). Synaptic vesicle trafficking and Parkinson's disease. Dev Neurobiol *72*, 134-144.

Falk, J., Konopacki, F.A., Zivraj, K.H., and Holt, C.E. (2014). Rab5 and Rab4 regulate axon elongation in the Xenopus visual system. J Neurosci *34*, 373-391.

Feinberg, E.H., Vanhoven, M.K., Bendesky, A., Wang, G., Fetter, R.D., Shen, K., and Bargmann, C.I. (2008). GFP Reconstitution Across Synaptic Partners (GRASP) defines cell contacts and synapses in living nervous systems. Neuron *57*, 353-363.

Fernandes, A.C., Uytterhoeven, V., Kuenen, S., Wang, Y.C., Slabbaert, J.R., Swerts, J., Kasprowicz, J., Aerts, S., and Verstreken, P. (2014). Reduced synaptic vesicle protein degradation at lysosomes curbs TBC1D24/sky-induced neurodegeneration. J Cell Biol *207*, 453-462.

Fischbach, K.F., and Dittrich, A.P.M. (1989). The optic lobe of Drosophila melanogaster. I. A Golgi analysis of wild-type structure. Cell Tissue Res *258*, 441-475.

Frampton, J.P., Guo, C., and Pierchala, B.A. (2012). Expression of axonal protein degradation machinery in sympathetic neurons is regulated by nerve growth factor. J Neurosci Res *90*, 1533-1546.

Gao, S., Takemura, S.Y., Ting, C.Y., Huang, S., Lu, Z., Luan, H., Rister, J., Thum, A.S., Yang, M., Hong, S.T., *et al.* (2008). The neural substrate of spectral preference in Drosophila. Neuron *60*, 328-342.

Goo, M.S., Sancho, L., Slepak, N., Boassa, D., Deerinck, T.J., Ellisman, M.H., Bloodgood, B.L., and Patrick, G.N. (2017). Activity-dependent trafficking of lysosomes in dendrites and dendritic spines. J Cell Biol *216*, 2499-2513.

Guerra, F., and Bucci, C. (2016). Multiple Roles of the Small GTPase Rab7. Cells *5*.

Haberman, A., Williamson, W.R., Epstein, D., Wang, D., Rina, S., Meinertzhagen, I.A., and Hiesinger, P.R. (2012). The synaptic vesicle SNARE neuronal Synaptobrevin promotes endolysosomal degradation and prevents neurodegeneration. J Cell Biol *196*, 261-276.

Hakim, V., Cohen, L.D., Zuchman, R., Ziv, T., and Ziv, N.E. (2016). The effects of proteasomal inhibition on synaptic proteostasis. EMBO J *35*, 2238-2262.

Hamilton, A.M., and Zito, K. (2013). Breaking it down: the ubiquitin proteasome system in neuronal morphogenesis. Neural Plast *2013*, 196848.

Han, C., Song, Y., Xiao, H., Wang, D., Franc, N.C., Jan, L.Y., and Jan, Y.N. (2014). Epidermal cells are the primary phagocytes in the fragmentation and clearance of degenerating dendrites in Drosophila. Neuron *81*, 544-560.

Hara, T., Nakamura, K., Matsui, M., Yamamoto, A., Nakahara, Y., Suzuki-Migishima, R., Yokoyama, M., Mishima, K., Saito, I., Okano, H., *et al.* (2006). Suppression of basal autophagy in neural cells causes neurodegenerative disease in mice. Nature *441*, 885-889.

Hassan, B.A., and Hiesinger, P.R. (2015). Beyond Molecular Codes: Simple Rules to Wire Complex Brains. Cell *163*, 285-291.

Hernandez, D., Torres, C.A., Setlik, W., Cebrian, C., Mosharov, E.V., Tang, G., Cheng, H.C., Kholodilov, N., Yarygina, O., Burke, R.E*., et al.* (2012). Regulation of presynaptic neurotransmission by macroautophagy. Neuron *74*, 277-284.

Hiesinger, P.R., Reiter, C., Schau, H., and Fischbach, K.F. (1999). Neuropil pattern formation and regulation of cell adhesion molecules in Drosophila optic lobe development depend on synaptobrevin. The Journal of Neuroscience *19*, 7548-7556.

Hiesinger, P.R., Zhai, R.G., Zhou, Y., Koh, T.W., Mehta, S.Q., Schulze, K.L., Cao, Y., Verstreken, P., Clandinin, T.R., Fischbach, K.F*., et al.* (2006). Activity-independent prespecification of synaptic partners in the visual map of Drosophila. Curr Biol *16*, 1835-1843.

Holbrook, S., Finley, J.K., Lyons, E.L., and Herman, T.G. (2012). Loss of syd-1 from R7 neurons disrupts two distinct phases of presynaptic development. J Neurosci *32*, 18101-18111.

Holguera, I., and Desplan, C. (2018). Neuronal specification in space and time. Science *362*, 176-180.

Hui, K.K., Takashima, N., Watanabe, A., Chater, T.E., Matsukawa, H., and Tanaka, M. (2019). GABARAPs dysfunction by autophagy deficiency in adolescent brain impairs GABA-A receptor trafficking and social behavior. Science Advances *5*.

Jackson, G.R. (2008). Guide to understanding Drosophila models of neurodegenerative diseases. PLoS Biol *6*, e53.

Jeon, Y., Lee, J.H., Choi, B., Won, S.Y., and Cho, K.S. (2020). Genetic Dissection of Alzheimer's Disease Using Drosophila Models. Int J Mol Sci *21*.

Jin, E.J., Kiral, F.R., and Hiesinger, P.R. (2018). The where, what, and when of membrane protein degradation in neurons. Dev Neurobiol *78*, 283-297.

Juhasz, G., Erdi, B., Sass, M., and Neufeld, T.P. (2007). Atg7-dependent autophagy promotes neuronal health, stress tolerance, and longevity but is dispensable for metamorphosis in Drosophila. Genes Dev *21*, 3061-3066.

Karuppudurai, T., Lin, T.Y., Ting, C.Y., Pursley, R., Melnattur, K.V., Diao, F., White, B.H., Macpherson, L.J., Gallio, M., Pohida, T*., et al.* (2014). A hard-wired glutamatergic circuit pools and relays UV signals to mediate spectral preference in Drosophila. Neuron *81*, 603-615.

Kim, H.J., Cho, M.H., Shim, W.H., Kim, J.K., Jeon, E.Y., Kim, D.H., and Yoon, S.Y. (2017). Deficient autophagy in microglia impairs synaptic pruning and causes social behavioral defects. Mol Psychiatry *22*, 1576-1584.

Kiral, F.R., Kohrs, F.E., Jin, E.J., and Hiesinger, P.R. (2018). Rab GTPases and Membrane Trafficking in Neurodegeneration. Curr Biol *28*, R471-R486.

Kiral, F.R., Linneweber, G.A., Mathejczyk, T., Georgiev, S.V., Wernet, M.F., Hassan, B.A., von Kleist, M., and Hiesinger, P.R. (2020). Autophagy-dependent filopodial kinetics restrict synaptic partner choice during Drosophila brain wiring. Nat Commun *11*, 1325.

Kolodkin, A.L., and Hiesinger, P.R. (2017). Wiring visual systems: common and divergent mechanisms and principles. Curr Opin Neurobiol *42*, 128-135.

Kolodkin, A.L., and Tessier-Lavigne, M. (2011). Mechanisms and molecules of neuronal wiring: a primer. Cold Spring Harb Perspect Biol *3*.

Komatsu, M., Waguri, S., Chiba, T., Murata, S., Iwata, J., Tanida, I., Ueno, T., Koike, M., Uchiyama, Y., Kominami, E*., et al.* (2006). Loss of autophagy in the central nervous system causes neurodegeneration in mice. Nature *441*, 880-884.

Kulkarni, A., Ertekin, D., Lee, C.H., and Hummel, T. (2016). Birth order dependent growth cone segregation determines synaptic layer identity in the Drosophila visual system. Elife *5*, e13715.

Langen, M., Agi, E., Altschuler, D.J., Wu, L.F., Altschuler, S.J., and Hiesinger, P.R. (2015). The Developmental Rules of Neural Superposition in Drosophila. Cell *162*, 120-133.

Lee, C.H., Herman, T., Clandinin, T.R., Lee, R., and Zipursky, S.L. (2001). N-Cadherin regulates target specificity in the Drosophila visual system. Neuron *30*, 437-450.

Lefebvre, J.L. (2017). Neuronal territory formation by the atypical cadherins and clustered protocadherins. Semin Cell Dev Biol *69*, 111-121.

Lim, L., Pakan, J.M.P., Selten, M.M., Marques-Smith, A., Llorca, A., Bae, S.E., Rochefort, N.L., and Marin, O. (2018). Optimization of interneuron function by direct coupling of cell migration and axonal targeting. Nat Neurosci *21*, 920-931.

Liston, C., Cichon, J.M., Jeanneteau, F., Jia, Z., Chao, M.V., and Gan, W.B. (2013). Circadian glucocorticoid oscillations promote learning-dependent synapse formation and maintenance. Nat Neurosci *16*, 698-705.

Lokmane, L., Proville, R., Narboux-Neme, N., Gyory, I., Keita, M., Mailhes, C., Lena, C., Gaspar, P., Grosschedl, R., and Garel, S. (2013). Sensory map transfer to the neocortex relies on pretarget ordering of thalamic axons. Curr Biol *23*, 810-816.

Ludwig, D., and Cable, R.M. (1933). The effect of alternating temperatures on the pupal development of Drosophila melanogaster Meigen. Physiological Zoology *6*, 493-508.

Macpherson, L.J., Zaharieva, E.E., Kearney, P.J., Alpert, M.H., Lin, T.Y., Turan, Z., Lee, C.H., and Gallio, M. (2015). Dynamic labelling of neural connections in multiple colours by trans-synaptic fluorescence complementation. Nat Commun *6*, 10024.

Maday, S., and Holzbaur, E.L. (2016). Compartment-Specific Regulation of Autophagy in Primary Neurons. J Neurosci *36*, 5933-5945.

Maday, S., Wallace, K.E., and Holzbaur, E.L. (2012). Autophagosomes initiate distally and mature during transport toward the cell soma in primary neurons. J Cell Biol *196*, 407-417.

Margeta, M.A., and Shen, K. (2010). Molecular mechanisms of synaptic specificity. Mol Cell Neurosci *43*, 261-267.

McGurk, L., Berson, A., and Bonini, N.M. (2015). Drosophila as an In Vivo Model for Human Neurodegenerative Disease. Genetics *201*, 377-402.

McLauchlan, H., Newell, J., Morrice, N., Osborne, A., West, M., and Smythe, E. (1997). A novel role for Rab5-GDI in ligand sequestration into clathrin-coated pits. Curr Biol *8*, 34-45.

Meinertzhagen, I.A., and O'Neil, S.D. (1991). Synaptic organization of columnar elements in the lamina of the wild type in Drosophila melanogaster. The Journal of Comparative Neurology *305*, 232-263.

Menon, K.P., Kulkarni, V., Takemura, S.Y., Anaya, M., and Zinn, K. (2019). Interactions between Dpr11 and DIP-gamma control selection of amacrine neurons in Drosophila color vision circuits. Elife *8*.

Mizushima, N. (2007). Autophagy: process and function. Genes Dev *21*, 2861-2873.

Morante, J., and Desplan, C. (2008). The color-vision circuit in the medulla of Drosophila. Curr Biol *18*, 553-565.

O'Keefe, L., and Denton, D. (2018). Using Drosophila Models of Amyloid Toxicity to Study Autophagy in the Pathogenesis of Alzheimer's Disease. Biomed Res Int *2018*, 5195416.

Okerlund, N.D., Schneider, K., Leal-Ortiz, S., Montenegro-Venegas, C., Kim, S.A., Garner, L.C., Waites, C.L., Gundelfinger, E.D., Reimer, R.J., and Garner, C.C. (2017). Bassoon Controls Presynaptic Autophagy through Atg5. Neuron *93*, 897-913 e897.

Osterhout, J.A., El-Danaf, R.N., Nguyen, P.L., and Huberman, A.D. (2014). Birthdate and outgrowth timing predict cellular mechanisms of axon target matching in the developing visual pathway. Cell Rep *8*, 1006-1017.

Ozel, M.N., Kulkarni, A., Hasan, A., Brummer, J., Moldenhauer, M., Daumann, I.M., Wolfenberg, H., Dercksen, V.J., Kiral, F.R., Weiser, M.*, et al.* (2019). Serial Synapse Formation through Filopodial Competition for Synaptic Seeding Factors. Dev Cell *50*, 447-461 e448.

Ozel, M.N., Langen, M., Hassan, B.A., and Hiesinger, P.R. (2015). Filopodial dynamics and growth cone stabilization in Drosophila visual circuit development. Elife *4*.

Petrovic, M., and Schmucker, D. (2015). Axonal wiring in neural development: Target-independent mechanisms help to establish precision and complexity. Bioessays *37*, 996-1004.

Powsner, L. (1935). The effects of temperature on the durations of the developmental stages of Drosophila melanogaster. Physiological Zoology *8*, 474-520.

Rink, J., Ghigo, E., Kalaidzidis, Y., and Zerial, M. (2005). Rab conversion as a mechanism of progression from early to late endosomes. Cell *122*, 735-749.

Sachdeva, R., Farrell, K., McMullen, M.K., Twiss, J.L., and Houle, J.D. (2016). Dynamic Changes in Local Protein Synthetic Machinery in Regenerating Central Nervous System Axons after Spinal Cord Injury. Neural Plast *2016*, 4087254.

Sanes, J.R., and Zipursky, S.L. (2010). Design principles of insect and vertebrate visual systems. Neuron *66*, 15-36.

Sanes, J.R., and Zipursky, S.L. (2020). Synaptic specificity, recognition molecules, and assembly of neural circuits. Cell *181*, 536-556.

Schmid, A., Hallermann, S., Kittel, R.J., Khorramshahi, O., Frolich, A.M., Quentin, C., Rasse, T.M., Mertel, S., Heckmann, M., and Sigrist, S.J. (2008). Activity-dependent site-specific changes of glutamate receptor composition in vivo. Nat Neurosci *11*, 659-666.

Schmucker, D., Clemens, J.C., Shu, H., Worby, C.A., Xiao, J., and Zipursky, S.L. (2000). Drosophila Dscam is an axon guidance receptor exhibiting extraordinary molecular diversity. Cell *101*, 671-684.

Schultz, M.L., Tecedor, L., Chang, M., and Davidson, B.L. (2011). Clarifying lysosomal storage diseases. Trends Neurosci *34*, 401-410.

Semerdjieva, S., Shortt, B., Maxwell, E., Singh, S., Fonarev, P., Hansen, J., Schiavo, G., Grant, B.D., and Smythe, E. (2008). Coordinated regulation of AP2 uncoating from clathrin-coated vesicles by rab5 and hRME-6. J Cell Biol *183*, 499-511.

Shen, W., and Ganetzky, B. (2009). Autophagy promotes synapse development in Drosophila. J Cell Biol *187*, 71-79.

Shirasaki, R., and Pfaff, S.L. (2002). Transcriptional codes and the control of neuronal identity. Annu Rev Neurosci *25*, 251-281.

Song, J.W., Misgeld, T., Kang, H., Knecht, S., Lu, J., Cao, Y., Cotman, S.L., Bishop, D.L., and Lichtman, J.W. (2008). Lysosomal activity associated with developmental axon pruning. J Neurosci *28*, 8993-9001.

Soukup, S.F., Kuenen, S., Vanhauwaert, R., Manetsberger, J., Hernandez-Diaz, S., Swerts, J., Schoovaerts, N., Vilain, S., Gounko, N.V., Vints, K*., et al.* (2016). A LRRK2-Dependent EndophilinA Phosphoswitch Is Critical for Macroautophagy at Presynaptic Terminals. Neuron *92*, 829-844.

Spencer, K.A., Belgacem, Y.H., Visina, O., Shim, S., Genus, H., and Borodinsky, L.N. (2019). Growth at Cold Temperature Increases the Number of Motor Neurons to Optimize Locomotor Function. Curr Biol *29*, 1787-1799 e1785.

Sperry, R.W. (1943). Visuomotor coordination in the newt after regeneration of the optic nerve.

Sperry, R.W. (1951). Regulative factors in the orderly growth of neural circuits. Reprinted from GROWTH Symposium *X*, 63-87.

Sperry, R.W. (1963). Chemoaffinity in the orderly growth of nerve fiber patterns and connnections. Proc Natl Acad Sci U S A *50*, 703-710.

Stavoe, A.K.H., Hill, S.E., Hall, D.H., and Colon-Ramos, D.A. (2016). KIF1A/UNC-104 transports Atg9 to regulate neurodevelopment and autophagy at synapses. Dev Cell *38*, 171-185.

Steward, O. (2002). mRNA at synapses, synaptic plasticity, and memory consolidation. Neuron *36*, 338-340.

Steward, O., and Schuman, E.M. (2001). Protein synthesis at synaptic sites and dendrites. Annu Rev Neurosci *24*, 299-325.

Stoeckli, E.T. (2018). Understanding axon guidance: are we nearly there yet? Development *145*.

Sudhof, T.C. (2004). The synaptic vesicle cycle. Annu Rev Neurosci *27*, 509-547.

Sudhof, T.C. (2017). Synaptic Neurexin Complexes: A Molecular Code for the Logic of Neural Circuits. Cell *171*, 745-769.

Takemura, S.Y., Xu, C.S., Lu, Z., Rivlin, P.K., Parag, T., Olbris, D.J., Plaza, S., Zhao, T., Katz, W.T., Umayam, L.*, et al.* (2015). Synaptic circuits and their variations within different columns in the visual system of Drosophila. Proc Natl Acad Sci U S A *112*, 13711-13716.

Talay, M., Richman, E.B., Snell, N.J., Hartmann, G.G., Fisher, J.D., Sorkac, A., Santoyo, J.F., Chou-Freed, C., Nair, N., Johnson, M.*, et al.* (2017). Transsynaptic Mapping of Second-Order Taste Neurons in Flies by trans-Tango. Neuron *96*, 783-795 e784.

Tan, L., Zhang, K.X., Pecot, M.Y., and Zipursky, S.L. (2015). Ig superfamily ligand and receptor pairs expressed in synaptic partners in Drosophila. Cell *163*, 1756-1769.

Tang, G., Gudsnuk, K., Kuo, S.H., Cotrina, M.L., Rosoklija, G., Sosunov, A., Sonders, M.S., Kanter, E., Castagna, C., Yamamoto, A.*, et al.* (2014). Loss of mTOR-dependent macroautophagy causes autistic-like synaptic pruning deficits. Neuron *83*, 1131-1143.

Tautz, J., Maier, S., Groh, C., Rossler, W., and Brockmann, A. (2003). Behavioral performance in adult honey bees is influenced by the temperature experienced during their pupal development. Proc Natl Acad Sci U S A *100*, 7343-7347.

Ting, C.Y., McQueen, P.G., Pandya, N., Lin, T.Y., Yang, M., Reddy, O.V., O'Connor, M.B., McAuliffe, M., and Lee, C.H. (2014). Photoreceptor-derived activin promotes dendritic termination and restricts the receptive fields of first-order interneurons in Drosophila. Neuron *81*, 830-846.

Treisman, J.E. (2013). Retinal differentiation in Drosophila. Wiley Interdiscip Rev Dev Biol *2*, 545-557.

Uytterhoeven, V., Kuenen, S., Kasprowicz, J., Miskiewicz, K., and Verstreken, P. (2011). Loss of skywalker reveals synaptic endosomes as sorting stations for synaptic vesicle proteins. Cell *145*, 117-132.

Van der Loos, H., and Glaser, E.M. (1972). Autapses in neocortex cerebri: Synapses between a pyramidal cell's axons and its own dendrites Brain Research *48*, 355-360.

Wang, B., Iyengar, R., Li-Harms, X., Joo, J.H., Wright, C., Lavado, A., Horner, L., Yang, M., Guan, J.L., Frase, S.*, et al.* (2018). The autophagy-inducing kinases, ULK1 and ULK2, regulate axon guidance in the developing mouse forebrain via a noncanonical pathway. Autophagy *14*, 796-811.

Williamson, W.R., Wang, D., Haberman, A.S., and Hiesinger, P.R. (2010a). A dual function of V0-ATPase a1 provides an endolysosomal degradation mechanism in Drosophila melanogaster photoreceptors. J Cell Biol *189*, 885-899.

Williamson, W.R., Yang, T., Terman, J.R., and Hiesinger, P.R. (2010b). Guidance receptor degradation is required for neuronal connectivity in the Drosophila nervous system. PLoS Biol *8*, e1000553.

Wu, K., He, M., Hou, Q., Sheng, A., Yuan, L., and Luo, Z. (2014). Semaphorin 3A activates the guanosine triphosphatase Rab5 to promote growth cone collapse and organize callosal axon projections. Science Signaling *7*, 1-13.

Xu, C., Theisen, E., Maloney, R., Peng, J., Santiago, I., Yapp, C., Werkhoven, Z., Rumbaut, E., Shum, B., Tarnogorska, D.*, et al.* (2019). Control of Synaptic Specificity by Establishing a Relative Preference for Synaptic Partners. Neuron *103*, 865-877 e867.

Xu, S., Xiao, Q., Cosmanescu, F., Sergeeva, A.P., Yoo, J., Lin, Y., Katsamba, P.S., Ahlsen, G., Kaufman, J., Linaval, N.T.*, et al.* (2018). Interactions between the Ig-Superfamily Proteins DIP-alpha and Dpr6/10 Regulate Assembly of Neural Circuits. Neuron *100*, 1369-1384 e1366.

Yamagata, M., and Sanes, J.R. (2008). Dscam and Sidekick proteins direct lamina-specific synaptic connections in vertebrate retina. Nature *451*, 465-469.

Yamaguchi, S., Desplan, C., and Heisenberg, M. (2010). Contribution of photoreceptor subtypes to spectral wavelength preference in Drosophila. Proc Natl Acad Sci U S A *107*, 5634-5639.

Yan, J., Porch, M.W., Court-Vazquez, B., Bennett, M.V.L., and Zukin, R.S. (2018). Activation of autophagy rescues synaptic and cognitive deficits in fragile X mice. Proc Natl Acad Sci U S A *115*, E9707-E9716.

Yi, J.J., and Ehlers, M.D. (2007). Emerging roles for ubiquitin and protein degradation in neuronal function. Pharmacol Rev *59*, 14-39.

Yuyama, K., Sun, H., Mitsutake, S., and Igarashi, Y. (2012). Sphingolipid-modulated exosome secretion promotes clearance of amyloid-beta by microglia. J Biol Chem *287*, 10977-10989.

Zuo, Y., Yang, G., Kwon, E., and Gan, W.B. (2005). Long-term sensory deprivation prevents dendritic spine loss in primary somatosensory cortex. Nature *436*, 261-265.

11. Appendix

11.1. List of publications from the doctoral work

Kiral, F.R., Linneweber, G.A., Mathejczyk, T., Georgiev, S.V., Wernet, M.F., Hassan, B.A., von Kleist, M., Hiesinger, P.R. (2020). Autophagy-dependent filopodial kinetics restrict synaptic partner choice during *Drosophila* brain wiring. *Nature Communications*, 11, 1325.

Ozel, M.N., Kulkarni, A., Hasan, A., Brummer, J., Moldenhauer, M., Daumann, I., Wolfenberg, H., Dercksen, V.J., **Kiral, F.R.,** Weiser, M., Prohaska, S., von Kleist, M., Hiesinger, P.R. (2019). Serial synapse formation through filopodial competition for synaptic seeding factors. *Developmental Cell*, 50, 447-461.

Kiral, F.R.*, Kohrs, F.E.*, Jin, E.J., Hiesinger, P.R. (2018). Rab GTPases and membrane trafficking in neurodegeneration. *Current Biology*, 28(8):471-486.

Jin, E.J.*, **Kiral, F.R.*,** Ozel, M.N., Burchardt, L.S., Osterland, M., Epstein, D., Wolfenberg, H., Prohaska, S., and Hiesinger, P.R. (2018). Live observation of two parallel membrane degradation pathways at axon terminals. *Current Biology*, 28(7):1027-1038.

Jin, E.J.*, **Kiral, F.R.*,** and Hiesinger. P.R. (2018). The where, what, and when of membrane protein degradation in neurons. *Developmental neurobiology*, 78(3):283-297.

* These authors contributed equally.

11.2. Curriculum Vitae

Ferdi Ridvan Kiral
ridvan.kiral@fu-berlin.de

Division of Neurobiology, Immenweg, 5a,
12169
Institute for Biology, Berlin,
Germany
Freie Universität Berlin,
Koenigin-Luise-Str. 1-3, 14195
Berlin, Germany
+49 30 838 59529

EDUCATION

Freie Universität Berlin
Ph.D., Neurobiology, expected July 2020
Dissertation: The development and maintenance of synaptic specificity in the fly visual system

Bogazici University, Istanbul
MSc, Neurobiology, 2015
Dissertation: Functional characterization of a novel hexosaminidase, dmHexDC, in *Drosophila* eye development.

Middle East Technical University, Ankara
BS, Molecular Biology and Genetics, 2012

Dissertation: Neuroprotective effects of rosmarinic acid on H2O2-induced oxidative stress mediated neuronal damage in Neuro-2a cell line.

RESEARCH EXPERIENCE

Freie Universität Berlin, 2015-present

Graduate Researcher, Advisor: Peter Robin Hiesinger

- Designed and cloned ‘acidification-sensing probes’ to investigate the role of ubiquitious and neuron-specific protein degradation pathways in neuronal maintenance with *ex vivo Drosophila* brain cultures.
- Analyzed the role of growth cone filopodia dynamics during synaptogenesis and neuronal circuit assembly using customized Amira plug-in FiloTracker.
- Revealed a previously unknown function of developmental autophagy during brain wiring using intact, developing *Drosophila* brain cultures.

Bogazici University, Istanbul, 2012-2015

Graduate Researcher, Advisor: Arzu Celik Fuss

- Characterized the roles of a novel glycosylation enzyme in *Drosophila* eye development using immunohistochemistry, confocal microscopy and biochemical methods.

KU Leuven, Leuven, 2013

Visiting Scholar, Advisor: Bassem A. Hassan

- Generated a mutant of a novel glycosylation enzyme, dmHexDC using CRISPR/Cas.

Gebze Technical University, Istanbul, 2011

Intern, Advisor: Ferruh Ozcan

- Investigated the role of salt-inducable kinase 2 (SIK2) in ER-stress pathways using Hek293FT and 3T3-L1 cell lines.

Middle East Technical University, Ankara, 2011-2012

Undergraduate Researcher, Advisor: Tulin Yanik

- Investigated antioxidant effects of Rosmarinic acid using neuronal cell cultures.
- Assisted master students with mice husbandry, handling, brain dissections and serum collections.

RELATED PROFESSIONAL EXPERIENCE

Cerebral organoids: Establishment, Culture and Manipulation course, Cambridge, UK

Participant, 2-day theoretical and practical course instructed by Dr. Madeline Lancaster

PUBLICATIONS

Autophagy-dependent filopodial kinetics restrict synaptic partner choice during *Drosophila* brain wiring. **Nature Communications**, (2020), 11, 1325.

First author

Serial synapse formation through filopodial competition for synaptic seeding factors. **Developmental Cell**, (2019), 50: 447-461.

Contributing author

Rab GTPases and membrane trafficking in neurodegeneration. **Current Biology**, (2018), 28: 471-486.

First author

Live observation of two parallel membrane degradation pathways at axon terminals. **Current Biology**, (2018), 28: 1027-1038.

Co-first author

The where, what, when of membrane protein degradation in neurons. **Developmental Neurobiology**, (2018), 78: 283-297.
Co-first author

Systematic functional analysis of Rab GTPases reveals limits of neuronal robustness in *Drosophila*, (2020), preprint at ***bioRxiv***.
Contributing author

CONFERENCE PRESENTATIONS

Autophagy-dependent filopodial kinetics restrict synaptic partner choice *Drosophila* brain wiring
Oral presentation at The Allied Genetics Conference, Washington, DC, 2020 (Cancelled due to COVID-19 pandemic).

Kinetic restriction of synaptic partner choice through autophagy in axonal filopodia
Poster presentation delivered at Cold Spring Harbor Laboratory, Neurobiology of Drosophila meeting, Cold Spring Harbor, NY, 2019.

Kinetic restriction of synaptic partner choice through autophagy in axonal filopodia
Poster presentation delivered at Circuit Development & Axon Regeneration meeting, Ali Cante, Spain, 2019.

Decreased filopodial dynamics at autophagy-deficient photoreceptor axon terminals lead to ectopic synapse formation and neuronal miswiring
Oral presentation delivered at 13th Gottingen Meeting of the German Neuroscience Society, Gottingen, Germany, 2019.

Autophagy restricts synapse formation in *Drosophila* photoreceptors
Poster presentation delivered at Cold Spring Harbor Laboratory, Molecular Mechanisms of Neuronal Connectivity meeting, Cold Spring Harbor, NY, 2018.

Live observation of two parallel endomembrane degradation pathways in *Drosophila* brain
Poster presentation delivered at 25th European Drosophila Research Conference meeting, Imperial College, London, UK, 2017.

Live observation of two parallel endolysosomal degradation pathways at axon terminals
Poster presentation delivered at 4th Protein Trafficking in Health and Disease meeting, Hamburg, Germany, 2017.

GRANTS AND AWARDS

DFG (Deutsche Forschungsgemeinschaft) graduate researcher grant, 2015-present
SFB 958: Scaffolding of Membranes: Molecular Mechanisms and Cellular Functions

TUBITAK (The Scientific and Technological Research Council of Turkey) graduate researcher scholarship, 2012-2015

TUBITAK (The Scientific and Technological Research Council of Turkey) undergraduate scholarship, 2007-2012
An award given to first 5000 students among over 2 million participants in University Entrance Examination.

TEACHING EXPERIENCE

Bogazici University, Istanbul

- Assisted undergraduate students in practical courses, 2012-2015
- Mentored two undergraduate students for their Bachelor theses, 2012-2015

Freie Universität Berlin

- Prepared handbooks and presentations for practical courses and assisted Master students for *Drosophila* brain dissections and confocal microscopy, 2016-2019.
- Mentored three Master students for their Master theses, 2016-2019.